Performance and Efficiency Analysis of a Centrifugal Compressor under Pulsating Flow

Aakeen Parikh

Department of Mechanical Engineering
Imperial College London

This dissertation is submitted for the degree of
Doctor of Philosophy

Imperial College London February 2024

Dedicated to and in loving memory of Jash Parikh

Declaration

Statement of Originality

I hereby declare that except where specific reference is made to the work of others, the contents of this dissertation are original and have not been submitted in whole or in part for consideration for any other degree or qualification in this, or any other university. This dissertation is my own work and contains nothing which is the outcome of work done in collaboration with others, except as specified in the text and Acknowledgements.

Copyright

The copyright of this thesis rests with the author. Unless otherwise indicated, its contents are licensed under a Creative Commons Attribution-Non Commercial 4.0 International Licence (CC BY-NC). Under this licence, you may copy and redistribute the material in any medium or format. You may also create and distribute modified versions of the work. This is on the condition that: you credit the author and do not use it, or any derivative works, for a commercial purpose. When reusing or sharing this work, ensure you make the licence terms clear to others by naming the licence and linking to the licence text. Where a work has been adapted, you should indicate that the work has been changed and describe those changes. Please seek permission from the copyright holder for uses of this work that are not included in this licence or permitted under UK Copyright Law.

Aakeen Parikh
February 2024

Acknowledgements

This thesis would not have been possible without the help and support from my supervisors, colleagues, friends and family. I would like to especially thank my supervisors Esperanza and Ricardo. Esperanza presented me with this opportunity and has supported me from the beginning. Ricardo imparted invaluable knowledge, guidance and mentorship. The calm presence of my supervisors, despite the turbulence we faced, provided me with the strength to persevere throughout. I would also like to acknowledge Mitsubishi Heavy Industries (MHI) for their industrial sponsorship, and, in particular, I would like to thank Yoshihiro, who worked with me on the MHI Theme 6 project and shared valuable expertise with me.

I have nothing but heartfelt gratitude for Chris and Harminder. Thank you for everything you do to help me - I am a better engineer because of your guidance. I don't know how you ingeniously fix problems and somehow, even manage to resurrect incinerated experimental facilities, but there is no research group without you. Thank you!

I am extremely grateful for my research team. In particular, Pablo, Oskar, and Eva have been amazing to me. Thank you for helping me navigate my thesis. The coffees, hikes and climbing sessions powered me through! Thank you also to Bijie, whom I have learned a lot from over these years.

Thank you to every one of my friends. You know who you are - There are no words to describe my gratitude. You have all helped me by listening to me and encouraging me. My special thanks to Hannah, who has always been by my side, Rik, who has always made me laugh, even during the toughest of PhD moments, and Stephen, who has been there since the day I got my Imperial College acceptance letter.

Above all, I want to thank my family. My parents, for their sacrifices and endeavours, my grandma, for always believing in me, and, my aunts and uncles, for their constant support and encouragement. Lastly, I could not be where I am today without my sisters, Rhea and Aayushi, who are funny and supportive in equal measures and for whom I am forever grateful.

Impact of COVID-19

This research was affected by the COVID-19 pandemic. I am grateful to Imperial College London and Mitsubishi Heavy Industries for supporting the completion of this research despite the difficulties incurred during the pandemic.

Abstract

The performance of a turbocharger centrifugal compressor is affected by the engine system in which it operates. This type of turbomachine experiences a pulsating backpressure caused by the opening and closing of the engine intake valves. This research studies the impact of these pulsating conditions on the behaviour of a centrifugal compressor and presents modifications to compressor designs to improve performance.

This research is conducted experimentally and computationally. The experimental facility is improved for increased accuracy in measurements and a prototype torque meter has also been developed to enable high speed measurements of compressor torque. The experimental results show that in pulsating conditions the largest drop in compressor efficiency (around 4% compared to steady conditions) takes place in the large mass flow rate conditions, as the fluctuating high-pressure amplitudes at the compressor exit lead to increased losses in the volute.

Computational investigation of the near surge operating point shows that, in pulsating flow, instantaneous changes in pressure allows the flow field near the impeller to stabilise despite low mass flow conditions that would otherwise trigger surge, resulting in the key benefit of extended operating range in low flow conditions. Further detailed computational assessments of the compressor model show that the volute and volute tongue regions are affected under pulsating flow. The volute tongue contributes to 20% of the losses on average in pulsating states.

Initial results from two compressor design modifications show an improved compressor performance, with efficiency improvement of 2% with a sharp tongue modification. This is a significant outcome from this research and has an influence on the design of turbochargers, as this improvement could indirectly impact the efficiency of the entire engine system. This would lead to greater fuel economy and reduced emissions from transport, which is necessary to address global climate change.

Table of contents

List of Figures **10**

List of Tables **20**

Nomenclature **21**

1 Introduction **25**

1.1 Motivation . . . 25
1.2 Background . . . 29
1.3 Industrial Project and Targets . . . 32
1.4 Research Aims and Objectives . . . 32
1.5 Thesis Outline . . . 33
1.6 Scholarly Output . . . 35

2 Background and Literature Review **37**

2.1 Centrifugal Compressor Background . . . 37
2.1.1 Compressor Characteristics . . . 39
2.1.2 Losses in a Centrifugal Compressor . . . 42
2.1.3 Off-Design Behaviour . . . 45
2.2 Compressor behaviour under Pulsating Flow . . . 50
2.2.1 Surge Margin Improvement . . . 52
2.2.2 Hysteresis Behaviour . . . 55
2.2.3 Evaluation of Unsteadiness . . . 59
2.2.4 Flow Phenomena . . . 60
2.2.5 Efficiency in Pulsating Conditions . . . 63
2.3 Design Concepts in Literature . . . 65
2.4 Measurement Techniques . . . 69
2.5 Closing the Gaps in Knowledge . . . 72

3 Experimental Facility and Methods **74**

3.1 Experimental Facility . . . 74
3.1.1 Original Experimental Facility . . . 74

3.1.2 Modifications to Experimental Facility . . . 78
3.2 Experimental Method . . . 94
3.2.1 Data Processing Methods under Pulsating Conditions . . . 98
3.2.2 Calculation method . . . 100
3.3 Results and Discussion . . . 103
3.3.1 Updated Facility . . . 103
3.3.2 Measurement Uncertainty and Reliability Assessments . . . 105
3.4 Chapter Summary . . . 108

4 Experimental Investigation of Compressor Under Pulsating Flow 110
4.1 Experiment Details . . . 110
4.1.1 Design of Instrumented Compressor . . . 111
4.1.2 Test Conditions . . . 113
4.2 Experimental Results . . . 115
4.2.1 Pressure ratio and efficiency for operating line . . . 115
4.2.2 Static Pressure Measurements . . . 120
4.3 Chapter Summary . . . 134

5 Computational Assessments on Compressor Performance 136
5.1 Computational Set Up . . . 137
5.2 Investigation One: Near Surge . . . 143
5.2.1 Operating Point . . . 143
5.2.2 Validation . . . 144
5.2.3 Results . . . 145
5.2.4 Discussion . . . 166
5.3 Investigation Two: Analysis at Key Operating Points . . . 168
5.3.1 Operating Points . . . 168
5.3.2 Validation . . . 169
5.3.3 Computational Results . . . 170
5.4 Chapter Summary . . . 187

6 Design Modifications to Centrifugal Compressor for Pulsating Flow 188
6.1 Modification 1: Cavity Treatment . . . 189
6.1.1 Computational Assessment . . . 190
6.1.2 Experimental Investigation . . . 200
6.2 Modification 2: Compressor Tongue . . . 210
6.2.1 Compressor Tongue . . . 210
6.2.2 Design Process for Compressor Tongue Modification . . . 211
6.2.3 Computational Results . . . 215
6.2.4 Experimental Investigation . . . 219

6.2.5 Discussion . . . 230
6.3 Chapter Summary . . . 231

7 Torque Meter Design, Development and Preliminary Results 233
7.1 Torque Meter Design and Development . . . 235
7.1.1 Torque Meter Design . . . 235
7.1.2 Static Calibration . . . 243
7.1.3 Experimental Method . . . 247
7.1.4 Limitations of Torque Meter . . . 250
7.2 Preliminary Results . . . 257
7.3 Chapter Summary . . . 270

8 Conclusion and Future Work 271
8.1 Conclusion . . . 271
8.2 Future Work . . . 279

References 285

Appendix A 291

Appendix B 296

List of Figures

1.1 Map of global temperature measurements for the year 2021 showing large regions of 'Much More Than Average' readings 26
1.2 Schematic illustration showing that the size and intensity of wildfires in California between 1970-2021 is dramatically increasing 26
1.3 Pie chart showing the global greenhouse gas emissions by sector 27
1.4 Pie chart showing emissions from different types of transport collected in 2021 28
1.5 Section view of a turbocharger showing the compressor, turbine and connecting shaft 30
1.6 Schematic of a turbocharger showing the IC engine, air cooler, intake and exit manifolds 31
1.7 Figure showing data for a 2500rpm, 40 mm 3/stroke engine 31

2.1 Section view of a centrifugal compressor showing the impeller, diffuser and volute regions. 38
2.2 Typical centrifugal compressor map showing the low and high mass flow limits (surge and choke), design line and efficiency contours 39
2.3 Schematic illustration of inlet recirculation 41
2.4 Schematic drawing of stall on a compressor blade 42
2.5 An illustrative schematic of secondary flow structures in a compressor impeller, as a result of flow separation in the boundary layer and flow formation perpendicular to primary channel flow 43
2.6 Locations and regions of loss within a typical impeller stage 44
2.7 Schematic of common incidence angles at off-design operating points on the performance map 45
2.8 Flow profiles at stable and for low-mass-flow unstable operating conditions 47
2.9 Internal volume of a compressor volute (volute negative) showing the location of the tongue 48
2.10 Schematic of the different velocity triangles and the relative size of the tangential velocity at design and off design conditions of the volute 49

2.11 Experimental results from Benson and Whitfield for a compressor system with a rotary valve for different orifice disc sizes and pulse frequencies in cycles/sec (c/s) 51
2.12 Experimental results from testing conducted by Galindo et al. for different pulsating frequencies showing the improvement in surge margin 52
2.13 Experimental results of pressure ratio vs. mass flow rate curve from Marelli et al. for two different frequencies (45Hz and 60Hz), with different operating speeds (60k rpm - 140k rpm) 53
2.14 Experimental results on the frequency and volume effect on a centrifugal compressor exposed to pulsating backpressure 55
2.15 Experimental findings of pressure ratio and flow rate showing instantaneous deviation from the steady operating line for different operating speeds for a given pulse frequency 56
2.16 Phase shift between the outlet static pressure signal and volume flow rate for key operating points 57
2.17 Experimentally captured phase shift in the inlet and outlet pressure and mass flow rate signals as a result of pulsation 58
2.18 Streamwise velocity vectors showing the reverse flow at the impeller wheel inlet and outlet positions for four different instantaneous mass flow rates (A - D) 60
2.19 Unsteady response of an impeller obtained through computational simulation of a compressor under pulsation 61
2.20 Simulation result of a single passage showing the size of the recirculation zone in pulsating conditions is lower than quasi steady conditions 62
2.21 Experimental results on efficiency reduction in pulsating conditions at peak efficiency and at different pulse frequencies (25k, 30k and 35k rpm) 63
2.22 Computational results showing efficiency in quasi-steady vs pulsating conditions (top) and loss distribution during a single pulse for quasi steady and pulsating conditions 64
2.23 Schematic of a casing treatment or bleed slot. The bleed slot is on the shroud surface 65
2.24 Schematic and description of the different cavity treatment designs tested by Martos 66
2.25 Efficiency deficit seen in the cavity designs experimentally tested by Martos at different pulsating flow conditions 66
2.26 Different experiments conducted on four different volute modifications by H. Okauchi et al. 67
2.27 Schematic showing two tongue shapes tested with different leading edges. . 68
2.28 Pressure ratio and efficiency results from Mohtar et al. for two different tongue fillet depths 69

2.29 Example of a phase shift torquemeter and the corresponding signal between the two measurement locations 71

3.1 Original compressor test facility built for surge testing of a centrifugal compressor under pulsating conditions. A section view of the plenum is detailed showing the maximum and minimum plenum volumes. 75
3.2 Comparison of 66.67Hz pulse generated by the pulsating device to a pressure pulse recorded in the engine system running at 2000rpm. This is measured data - the measurement is made at a set distance from compressor outlet in both measurements. A clear matching is seen. [Figure adapted from Barrera-Medrano [23]]. 76
3.3 The locations and measurements of the original sensors on the compressor rig facility 77
3.4 Photographs of thermal insulation placed on the compressor test facility . . 80
3.5 Schematic showing the recirculation region of the compressor rig and closeness of the original sensors to the recirculation region. The original position was too close to the recirculation region. 83
3.6 Section view of the new inlet pipe & outlet pipe showing the measurement plane locations 85
3.7 Differences in the measured mass flow rate of the hotwire probes in the two positions 86
3.8 CAD Schematic of the V-cone mass flow measurement device 87
3.9 A magnified view of a CTA Hot-wire probe from Dantec Dynamics 89
3.10 Calibration of the hot-wire. The mass flow rate measured at the v-cone (Y-axis) is plotted against the corrected voltage measurement (X-axis) and a calibration fit is obtained. The calculated mass flow rate after calibration is also plotted on the figure. 92
3.11 Comparison of mass flow measured at the hot-wire to the mass flow measured at the v-cone in steady conditions 93
3.12 Schematic showing change in flow area (not to scale) for different points on the speed line, estimated using the boundary layer assumption 94
3.13 Baseline compressor provided by Mitsubishi Heavy Industries as the reference compressor 95
3.14 Performance map of the baseline compressor showing the engine operating line (red) and the equivalent operating line for research (green) 96
3.15 Schematic of behaviour under pulsating flow 98
3.16 Example of time synchronous signal averaging process resulting in a single, representative signal after averaging 100

3.17 Compressor experimental test facility. 1 - Volute and Impeller, 2 - bellmouth and inlet pipe, 3 - Rotatry pulse generator, 4 - 16L Plenum, 5 - V-cone, 6 - butterfly valve, 7- Motor, 8 - Adapter 104
3.18 Pressure ratio against mass flow rate for steady and pulsating conditions with frequencies of 30Hz, 46.7Hz and 66.6Hz - including range error bars. 107
3.19 Efficiency against mass flow rate for steady and pulsating conditions with frequencies of 30Hz, 46.7Hz and 66.6Hz. 108

4.1 CAD model of the instrumented volute design showing the measurement positions within the compressor 111
4.2 Figure of the instrumented volute installed in the experimental facility . . . 112
4.3 Location of different static pressure sensors. P1 - impeller inlet, P2 - impeller midspan, P3 - impeller outlet, P4 - diffuser inlet near tongue, P5 - diffuser outlet near tongue, P6 – volute at clockwise location 3:00, P7 – volute at clockwise location 4:30, P8 – volute at clockwise location 7:30, P9 –volute at clockwise location 9:00, P10 – volute at clockwise position 12:00, P11 – volute at clockwise position 1:30, P12 – compressor outlet 112
4.4 Cycle average pressure ratio and efficiency results for all pulsating and steady flow conditions. The comparable range is shown in the figure. 116
4.5 Pressure ratio and efficiency curve at operating points OP A (near surge), OP B (peak pressure), OP C (peak efficiency for steady case; large flow for pulsating case) and OP D (Large flow for steady case) for the compressor system . . . 118
4.6 Pressure ratio against mass flow rate for compressor under pulsating operation, with pulse frequencies of 30Hz (Top) and 66Hz (Bottom) 120
4.7 30Hz (Top) and 66Hz (Bottom) Trace from static transducer locations 1 – 12. 1 -impeller inlet, 2 - impeller midspan, 3 - impeller outlet, 4 - diffuser inlet near tongue, 5 - diffuser outlet near tongue, 6 – volute at clockwise location 3:00, 7 – volute at clockwise location 4:30, 8 – volute at clockwise location 7:30, 9 – volute at clockwise location 1:30, 12 –outlet pressure 122
4.8 Ensemble average static pressure pulse for different positions along the volute for tested frequencies of 30Hz (Top) and 66Hz (bottom) 124
4.9 Schematic of pressure wave propagating through tongue gap and disturbing the main flow 125
4.10 Static pressure hysteresis behaviour for OP C for volute locations P12 – compressor outlet, P9 – volute at clock position 9.00, P10 – volute at clock position 12.00, P6 – volute at clock position 3.00 for 30Hz and 66Hz case 126
4.11 Exit static pressure at impeller stage and volute stage for Peak Pressure (OP A) and peak efficiency flow (OP C) operating points 128
4.12 Impeller Static Pressure Hysteresis at compressor with pulsating operating conditions with pulse frequencies of 30Hz (Top) and 66Hz (Bottom) 129

4.13 Instantaneous pressure ratio compared to Quasi-steady Pressure Ratio for operating point A (Peak Pressure) and operating point C (Peak Efficiency) . 131
4.14 Steady, quasi steady and unsteady average efficiency results for compressor under pulsation at frequencies 30Hz (Top) and 66Hz (Bottom) 133

5.1 Computational domains modelled in ANSYS-CFX for the two investigations. The domains are: D1 - inlet pipe and bellmouth, D2 impeller, D3 - diffuser and D4 - Volute. 138
5.2 Mesh of a single blade passage in the impeller domain. All other impeller blade passages identical. 140
5.3 Static pressure boundary condition applied at the outlet based on typical static pressure profile achieved in experiment. This is obtained at the experimental facility. 141
5.4 This figure showes the computational outputs for 4 different operating points under steady and pulsating boundary conditions- the operating lines are added on the schematic for clarity. The location of the near surge operating point is represented by the blue-square on the figure. 144
5.5 Hysteresis outlet pressure loop between predicted CFD data and measured experimental data (black loop). CFD average results are presented on the graph. 145
5.6 Impeller Outlet static pressure variation with inlet flow coefficient. 146
5.7 Flow coefficient and normalised static pressure at impeller outlet showing position of all transients obtained. The 6 transients of interest have been labelled by their timesteps. 148
5.8 Reference plane positions 1 and 3 corresponding to impeller inlet and blade inlet respectively, and front view of domain showing location of the tongue in Figures 5.9, 5.10, 5.11 149
5.9 Static pressure contours at Plane 1, impeller inlet, for instantaneous times A - F: A (High F_c, High but Rising BP_s), B (Average F_c, High BP_s) C (Low F_c, High BP_s), D (Low F_c, High but Falling BP_s), E (Average F_c, Low BP_s) and F (High F_c, Low but Rising BP_s) 150
5.10 Static pressure contour at Plane 3, blades inlet for all timesteps A-F: A (High F_c, High but Rising BP_s), B (Average F_c, High BP_s) C (Low F_c, High BP_s), D (Low F_c, High but Falling BP_s), E (Average F_c, Low BP_s) and F (High F_c, Low but Rising BP_s) 152
5.11 Mach Number contours at Plane 3, blade inlet, for timesteps A-F: A (High F_c, High but Rising BP_s), B (Average F_c, High BP_s) C (Low F_c, High BP_s), D (Low F_c, High but Falling BP_s), E (Average F_c, Low BP_s) and F (High F_c, Low but Rising BP_s) 153

5.12 Pitchwise average streamline velocity projection in three locations; blade inlet, midway through impeller and near impeller exit for timesteps A-F: A (High F_c, High but Rising BP_s), B (Average F_c, High BP_s) C (Low F_c, High BP_s), D (Low F_c, High but Falling BP_s), E (Average F_c, Low BP_s) and F (High F_c, Low but Rising BP_s) 155
5.13 Pitchwise average static entropy contours for timesteps A-F: A (High F_c, High but Rising BP_s), B (Average F_c, High BP_s) C (Low F_c, High BP_s), D (Low F_c, High but Falling BP_s), E (Average F_c, Low BP_s) and F (High F_c, Low but Rising BP_s) 157
5.14 Mach number contours at blade span 0.7 for timesteps A-F: A (High F_c, High but Rising BP_s), B (Average F_c, High BP_s) C (Low F_c, High BP_s), D (Low F_c, High but Falling BP_s), E (Average F_c, Low BP_s) and F (High F_c, Low but Rising BP_s) 160
5.15 Mach number contour at blade span 0.8 for timesteps A-F: A (High F_c, High but Rising BP_s), B (Average F_c, High BP_s) C (Low F_c, High BP_s), D (Low F_c, High but Falling BP_s), E (Average F_c, Low BP_s) and F (High F_c, Low but Rising BP_s) 161
5.16 Mach number contour at blade span 0.9 for timesteps A-F: A (High F_c, High but Rising BP_s), B (Average F_c, High BP_s) C (Low F_c, High BP_s), D (Low F_c, High but Falling BP_s), E (Average F_c, Low BP_s) and F (High F_c, Low but Rising BP_s) 162
5.17 Static entropy contour at blade span 0.8 for timesteps A-F: A (High F_c, High but Rising BP_s), B (Average F_c, High BP_s) C (Low F_c, High BP_s), D (Low F_c, High but Falling BP_s), E (Average F_c, Low BP_s) and F (High F_c, Low but Rising BP_s) 164
5.18 Static entropy contour at blade span 0.9 for timesteps A-F: A (High F_c, High but Rising BP_s), B (Average F_c, High BP_s) C (Low F_c, High BP_s), D (Low F_c, High but Falling BP_s), E (Average F_c, Low BP_s) and F (High F_c, Low but Rising BP_s).Location X and Y indicate high SE in areas of local flow acceleration at the inlet. 165
5.19 Schematic of the key operating points at the 40k rpm operating line 168
5.20 Pressure ratio against mass flow rate for OP B (Peak Pressure), OP C (Peak Efficiency) and OP D (Large Flow) for experimental and computational results; good matching of the results can be seen. 169
5.21 Hysteresis loops for key operating points in CFD results compared to experiments for OP B (peak pressure), OP C (peak efficiency) and OP D (large flow) 170
5.22 Inlet and outlet measurement planes in CFD positioned to match the experimental facility 171

5.23 Pressure ratio and mass flow rate results for peak pressure (OP B), peak efficiency (OP C) and large flow (OP D) - instantaneous outputs within a pulse cycle 172
5.24 Efficiency and mass flow rate results for peak pressure (OP B), peak efficiency (OP C) and large flow (OP D) - instantaneous outputs within a pulse cycle . 173
5.25 Static pressure rise in the volute component for operating points: OP B - Peak Pressure; OP C - Peak Efficiency, OP D - Large Flow 175
5.26 Entropy generation rate for operating points: OP B - Peak Pressure; OP C - Peak Efficiency, OP D - Large Flow 176
5.27 Entropy generation rate for peak pressure operating point (OP B) for domains (D1 - Inlet; D2 - Impeller; D3 - Diffuser; D4 - Volute) 178
5.28 Entropy generation rate for peak efficiency operating point (OP C) for domains (D1 - Inlet; D2 - Impeller; D3 - Diffuser; D4 - Volute) 178
5.29 Entropy generation rate for large flow operating point (OP D) for domains (D1 - Inlet; D2 - Impeller; D3 - Diffuser; D4 - Volute) 179
5.30 Total pressure drop in the volute and diffuser domain for large flow operating point (OP D) 180
5.31 Volute showing the isolation of the tongue volume 181
5.32 Pressure ratio against mass flow rate at nine instances in time for large flow operating point (OP D) 182
5.33 Location of the cut-plane in the volute component 183
5.34 This path schematic shows the flow vectors indicating the design flow path of the volute 183
5.35 Mach number and velocity vectors near the tongue for the volute domain . 184
5.36 Mach number and velocity vectors near the tongue in the diffuser domain . 185

6.1 Cavity treatment design developed by Barrera-Medrano and Martos. The baseline cavity position and size is shown in this Figure. 189
6.2 Impeller mesh without cavity and with cavity 191
6.3 Schematic of the operating point for the cavity flow analysis and design . . . 192
6.4 Impeller exit outlet conditions (static pressure and mass flow) for the cavity case at different instantaneous points in time (A-I) for the cavity case simulation. It can be seen that position H corresponds to the case of peak mass flow rate 192
6.5 Pressure ratio and efficiency results for baseline cavity and no cavity case for peak efficiency operating point (OP C) 194
6.6 Instantaneous compressor power cavity and baseline case 195
6.7 Instantaneous difference in efficiency for baseline cavity and no cavity case 196
6.8 Schematic flow vectors demonstrating the reversal mechanism of the cavity 196
6.10 Velocity Vectors for time **G**. Top - Baseline cavity case. Bottom - No cavity case198

6.11 Optimised shape of cavity based on CFD insights - the change to shape is based on the velocity vectors . . . 199
6.12 Cad model of the cavity insert and volute assembly . . . 200
6.13 Pictures of the cavity insert in the modified volute assembly . . . 201
6.14 Total to total pressure ratio for steady and pulsating (30Hz) cases . . . 203
6.15 Total to total pressure ratio for pulsating flow 46.7Hz and 66Hz cases . . . 204
6.16 Total to total efficiency for steady and pulsating (30Hz) cases . . . 205
6.17 Total to total efficiency for pulsating flow 46.7Hz and 66Hz cases . . . 206
6.18 Recirculation temperature ratio for steady and unsteady case of 30Hz . . . 208
6.19 Location of the tongue on the baseline compressor . . . 210
6.20 Design ideas for modifying the tongue shape to accommodate the flow at off-design conditions . . . 211
6.21 CAD screenshot of the key issues with modifying original MHI geometry . . . 212
6.23 Schematic showing the operating point . . . 215
6.24 Pressure ratio and efficiency computational results for large flow operating point (OP D) . . . 217
6.25 Instantaneous and average efficiency results against time for sharp tongue modification . . . 218
6.26 Instantaneous and average efficiency results against time for blunt tongue modification . . . 218
6.27 CAD assembly of volute geometry design with the new tongue fillets . . . 219
6.28 Section view of the CAD model showing the sharp tongue fillet radius . . . 220
6.29 Section view of the CAD model showing the sharp tongue fillet radius . . . 221
6.30 Picture of the printed perFORM volute . . . 222
6.31 Pictures of the damaged perFORM volutes after initial testing . . . 223
6.32 Baseline, Sharp and Blunt tongue compressor modification results for pressure ratio and efficiency in steady flow for 40k rpm . . . 226
6.33 Baseline, Sharp and Blunt tongue compressor modification results for pressure ratio and efficiency with pulse frequency of 30Hz for 40k rpm . . . 227
6.34 Baseline, Sharp and Blunt tongue compressor modification results for pressure ratio and efficiency with pulse frequency of 46.7Hz for 40k rpm . . . 228
6.35 Baseline, Sharp and Blunt tongue compressor modification results for pressure ratio and efficiency with pulse frequency of 66.7Hz for 40k rpm . . . 229

7.1 Bearing Housing assembly of the shaft indicating the shaft adapter location as the only plausible placement for the torque meter . . . 236
7.2 Front-view schematic of the shaft showing critical dimensions . . . 237
7.3 Shaft and Encoder Design Iterations . . . 238
7.4 Torque meter shaft and encoder assembly showing the encoder disc and encoder alignment . . . 240

7.5 Diagram representing two time measurements required for angular twist measurement - paper reference 241
7.6 Theoretical minimum resolvable angle as a function of shaft speed 243
7.7 Theoretical minimum resolvable torque as a function of shaft speed 243
7.8 Static Calibration Machine 245
7.9 Schematic static torque calibration for the torque meter 245
7.10 Results from the static calibration of torque meter 246
7.11 Data from low-speed compressor runs to determine zero offset of torque meter247
7.12 Torsional resonance issue at the operating speed - Result from C.Noon, internal report (2022) 251
7.13 FFT of signal for 40k rpm, Valve Opening - Fully Open, Steady operation, showing torsional resonance at 73Hz 252
7.14 FFT of signal for 40k rpm, Valve Opening - Fully Open, 30Hz and 66Hz operation 253
7.15 Time signals of the outlet static pressure and the torque signal 254
7.16 Time synchronous signal for 30Hz and 66Hz case showing the average pulse signal 256
7.17 Measured torque meter power compared to predicted thermodynamic power 258
7.18 Cycle average efficiency from torque meter compared to thermodynamic prediction for large flow operating point (OP D) at 66Hz 259
7.19 Cycle average power from torque meter compared to thermodynamic prediction for large flow operating point (OP D) at 66Hz 260
7.20 Phase difference in mass flow rate and static pressure measurement 260
7.21 Torque meter power and pressure ratio for steady and pulsating frequencies for full operating line 262
7.22 Torque meter power and pressure ratio for instantaneous behaviour at 30Hz for low flow (red) through to to high flow (blue) (from left to right) 264
7.23 Torque meter power and pressure ratio for instantaneous behaviour at 46.7Hz for low flow (red) through to to high flow (blue) (from left to right) 265
7.24 Torque meter power and pressure ratio for instantaneous behaviour at 66Hz for low flow (red) through to to high flow (blue) (from left to right) 266
7.25 Instantaneous power hysteresis for 30Hz, 46.7Hz and 66Hz pulse frequency cases at peak pressure operating point (OP A) 267
7.26 Instantaneous power hysteresis for 30Hz, 46.7Hz and 66Hz pulse frequency cases at large flow operating point (OP D) 268

8.1 CAD schematic of mass accumulation concept 282
8.2 Different cavity modifications for optimisation of baseline cavity 283

A.1 Current conceptualised mass accumulation concept using existing plenum 292

A.2 Experimental set-up to test the mass accumulation concept 292
A.3 Pressure ratio vs mass flow for Large flow (OP D) and peak efficiency (OP C) operating Points 293
A.4 Static pressure pulse reduction at compressor outlet 294

List of Tables

3.1 Sensors on original facility at the time of Barrera-Medrano's research 77
3.2 Mass flow rate sensors on the updated experimental facility 87
3.3 Selection of applied Frequencies for Design Points 97
3.4 Frequencies of Operating Points 97
3.5 Constants 101
3.6 Sensors on updated facility permanently installed 104

4.1 List of instrumentation for the detailed measurement test 114

5.1 Mesh Statistics for all the domains 139
5.2 Boundary Conditions 141
5.3 Reference conditions corresponding to points under study for flow coefficient F_c and backpressure BP_s 147
5.4 Entropy Generation Rate in volute region contribution from tongue 181

6.1 Design Modifications for improving the performance of the compressor under pulsating flow 189
6.2 Computational Set-Up 190
6.3 Efficiency difference at peak efficiency point (OP C) 202
6.4 Improvement of the modified tongue performance at peak pressure and peak efficiency operating points 230

7.1 List of instrumentation for the detailed measurement test 248

Nomenclature

Roman Symbols

A Area

a Acoustic Velocity

A_d Encoder Disc Diamater

A_w Wire Surface Area

B Greitzer B Parameter

BP_s Back Pressure

C_d Cone Discharge Coefficient

C_p Specific Heat Capacity of Air

C_θ Angular Velocity

D Pipe Diameter (Outer)

d Pipe Diameter (Inner)

d_m Deflection Distance

E Voltage

F Force

f Frequency

F_a Material Temperature Expansion Coefficient

G Shear Modulus

h Heat Transfer Coefficient

h_0 Stagnation Enthalpy

J Polar Moment of Inertia

K Unloaded Offset

k_1 Flow Coefficient

L Length

m Temperature Loading Factor

$\dot{m}$ Mass Flow Rate

MF_r Mass Flow Range

M Mach Number

N Speed (rpm)

P Static Pressure

$\bar{P}$ Cycle Average Pressure

P_{Lab} Lab Pressure

P_0 Total Pressure

P_{ref} Mean Pressure

Q Heat Transfer

R Gas Constant

R Radius

r Recovery Factor

SPr Stagnation Pressure Recovery Coefficient

S_t Strouhal Number

S_{xy} Shear Stress

T Static Temperature

t Time

T_{Lab} Lab Temperature

T_{meas} Measured Temperature

M_m Tip Mach Number

T_0 Total Temperature

$T_w - T_0$ Wire Over Temperature

U Velocity

W Power

Y Gas Expansion Factor

Greek Symbols

α_{cone} Cone Thermal Expansion Coefficient

α_{pipe} Pipe Thermal Expansion Coefficient

β Cone Beta Ratio

ΔP Pressure Range

η Efficiency

γ Ratio of Specific Heat Capacities

μ Dynamic Viscosity of Air

Ω Omega Number

Θ Encoder Disc Relative Angle (radians)

Θ_d Angle of Deflection

Π Stagnation Pressure Ratio

π pi = 3.14

Π_{PA} Pressure Amplitude Weighting Factor

ρ Density

σ Stress

υ Bulk Average Velocity

ω Angular Velocity

ω_h Natural Frequency

Acronyms / Abbreviations

BL Boundary Layer

CFD Computational Fluid Dynamics

CTA Constant Temperature Anemometry

DP Design Point

EGR Entropy Generation Rate

FRAP Fast Response Aerodnymic Probe

IPCC Intergovernmental Panel on Climate Change

LDV Laser Doppler Velocimetry

LES Large Eddy Simulations

MHI Mitsubishi Heavy Industries

NCEI National Center for Environmental Information

OEM Original Equipment Manufacturers

OP Operating Point

Q-S Quasi Steady Approximation

RANS Unsteady Reynolds Average Navier Stokes

RTD Resistance Temperature Detectors

SE Static Entropy

SMI Surge Margin Improvement

URANS Unsteady Reynolds Average Navier Stokes

Chapter 1

Introduction

1.1 Motivation

Climate change is a term used to describe long-term shifts of the Earth's temperature and weather patterns [1]. One of the key reasons for climate change is when carbon dioxide and other air pollutants, collectively known as 'greenhouse gases', are present in excess in the atmosphere. These gases absorb sunlight and other reflected solar radiation that would have otherwise escaped into space [2], trapping heat in the atmosphere. One of the key emitters of greenhouse gases are internal combustion engines, which utilise combustion of fuel with air for propulsion of a vehicle. The combustion products, carbon dioxide and water vapour, are released into the atmosphere in the engine exhaust stream.

In recent years, climate change has been occurring so rapidly, that it causes large-scale changes to the ecosystem and an increase of natural events such as droughts and floods [3]. The consequent increase in atmospheric temperature is threatening life on Earth as we know it and will lead to significant events of mass migration. An example of this can be seen in figures released by leading climate researchers. The National Centers for Environmental Information [NCEI] released a global map of the recorded temperatures in 2021, see Figure 1.1. It can be seen that record warmest temperatures were seen globally, with temperatures higher than average almost everywhere. A direct consequence of this can be seen through the study of wildfires. For example, Figure 1.2 shows that in California, there has been a rise in size and intensity of wildfires in the last 40 years; About 3% of the California's land surfaces were found to burn between 1970-1980 whereas, 11% were found to have burned down between 2010-2020 [4]. It is estimated that in order to reverse the aforementioned negative effects of climate change, the rise in core atmospheric temperature must be limited

to 1.5°C by 2040, which the Intergovernmental Panel on Climate Change [IPCC] estimate that without reduction in emissions is out of reach [5].

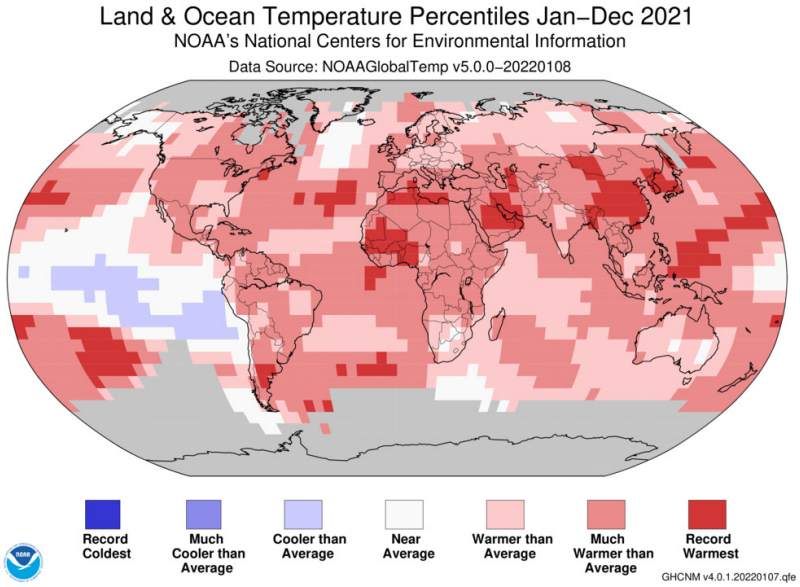


Fig. 1.1 Map of global temperature measurements for the year 2021 showing large regions of 'Much More Than Average' readings [Figure from NCEI [6]].

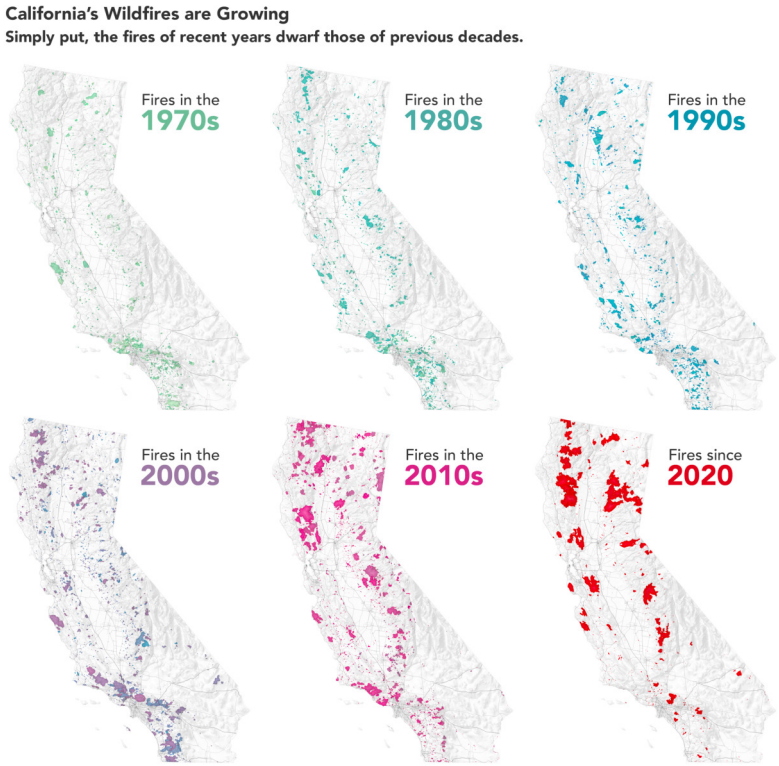


Fig. 1.2 Schematic illustration showing that the size and intensity of wildfires in California between 1970-2021 is dramatically increasing [Figure from Earth Observatory [4]].

There are many international efforts to collectively curb the greenhouse effect, one is 'Net Zero 2050', which aims to neutralise the carbon footprint. In 2019, the UK Government

modified the Climate Change Act to commit the UK to achieving net zero carbon emissions by 2050. Additionally, the UK government has also introduced a ban on all diesel and petrol car sales by 2035 [7]. Yet, despite efforts, emissions seem to have rebounded to their highest levels [8]. Some of the recent efforts include pushing towards electric vehicles (EV) - positively, EV sales in the UK reached all-time-high in 2023 [9]. There has also been a clear shift in consumer trends towards greener, less emitting means of transport.

The transport industry is one of the highest contributors of greenhouse gases in the atmosphere. According to the data gathered in 2021, transport was found to account for 20.2% of global carbon dioxide emissions [10], as can be seen in Figure 1.3. Within the transportation sector, road transport is the highest contributor to global greenhouse gases (77%) followed by shipping (11%), aviation (9%) and rail (3%) [11], as can be seen from Figure 1.4. For the UK alone, the department of BEIS show that in 2020, transport contributed to around 24% of the total emissions, which is higher than the global average [12].

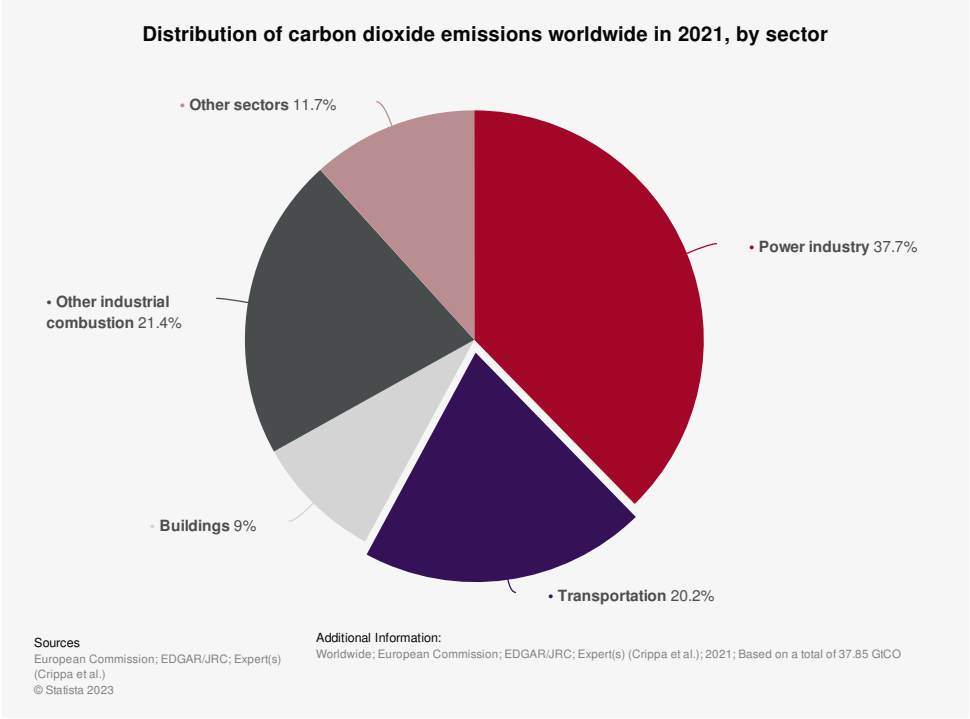


Fig. 1.3 Pie chart showing the global greenhouse gas emissions by sector. The emissions from transport are shown to be 20.2% and contribute to 1/5 of the emissions overall [Figure from Statista [10]].

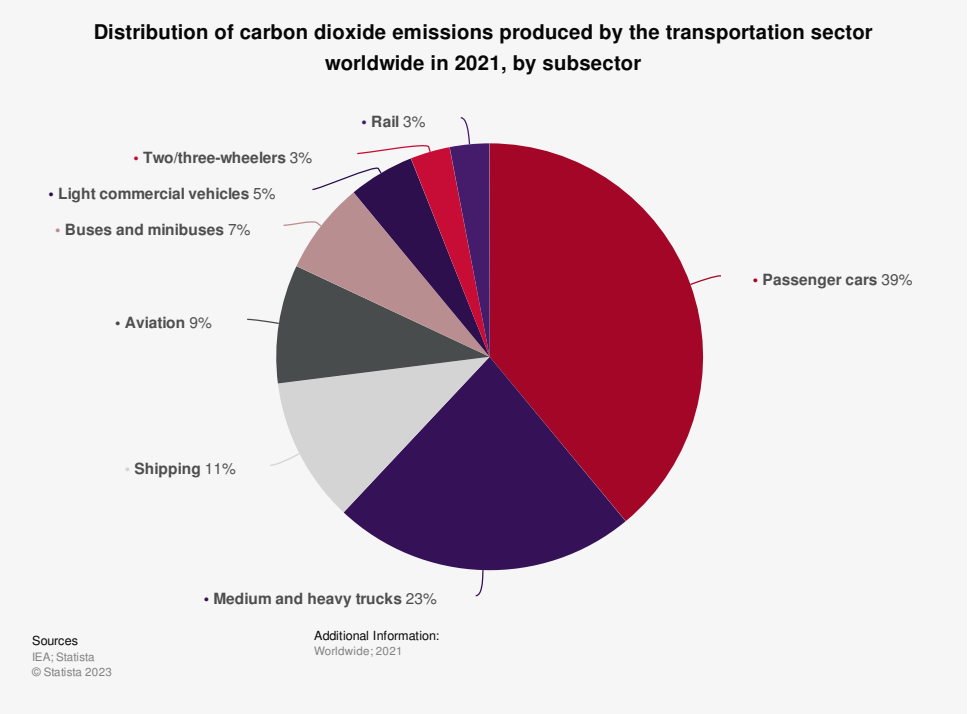


Fig. 1.4 Pie chart showing emissions from different types of transport collected in 2021. Road transport combining passenger cars, trucks and moped contribute to around 77%, followed by shipping (11%), aviation (9%) and rail (3%) [Figure from Statista [11]].

Impact of Turbocharger boosted IC engines on Climate Change

One of the ways the emissions from an engine can be reduced is through turbochargers. The role of the turbocharger is to recover waste heat energy in the exhaust. With a turbocharger, the engine can be downsized and thus achieve the same output with a smaller frictional loss and overall weight. The turbocharger increases the engine boost pressure by increasing the amount of air delivered to the engine. This is important because increasing the air to fuel ratio causes the engine to burn leaner, increasing combustion efficiency and reducing the formation of undesirable gaseous species. This results in an increase in the performance output of an an engine; carbon emissions are reduced as the engine converts more fuel into energy that would usually be lost through the exhaust system. By increasing engine performance through leaner combustion and engine downsizing, turbochargers effectively result in reduced specific fuel consumption and reduction in CO2 emissions, and maximise fuel efficiency. This means the vehicle uses less fuel per kilometer travelled, and in turn reduces the emissions of greenhouses gases to the atmosphere.

It is important that turbochargers are as efficient as possible to contribute to the overall engine system efficiency. There are a few factors that affect the efficiency of the turbocharger, some related to the process by which turbochargers are matched to the engine (system level), while others are related to the detailed aerodynamic performance of the compres-

sor and turbine (component level). When matching a turbocharger to the engine, the components are assumed to behave in a quasi-steady manner (i.e. operating as a sequence of steady state point), this not being the actual conditions encountered at engine operation. When placed within the engine environment, the operating conditions have unsteady dynamic effects induced by the engine intake valve that affect the efficiency of the turbocharger as well as the other performance parameters (i.e. mass flow, pressure).

What is clear is that the engine system has an impact on the performance of the turbocharger and that the performance of turbocharger within the engine environment is key to improving the overall efficiency of the engine system and reap the benefits of turbocharger boosted systems. This has a direct impact on the emissions profile of the vehicle. Therefore, understanding and improving the performance of the turbocharger in an engine environment will lead to maximising fuel efficiency of the vehicle, reducing emissions.

The turbocharger has two sub-components: the turbine and the compressor. There has been significant progress in this area on turbines however, the behaviour of turbocharger compressors under this dynamic, fluctuating environment is a relatively new and exciting area of research and although major developments have been made in the last few decades, much is left to be learned in order aid designers in developing a better performing design, for which studying the behaviour under engine conditions is vital. The intention of this research is to investigate the changes of performance under unsteady engine conditions and to develop the design of the turbocharger compressor, such that the compressor efficiency in an unsteady environment is increased. The reduced emissions from turbocharger boosted engine systems as a result will have a direct positive impact on climate change.

1.2 Background

Turbochargers enhance the boosting level of an engine system, achieved by feeding high density air into the engine with a compressor, thus allowing higher power density to be achieved. It is worth noting that from an engine application point of view, there are benefits of operating at optimum pressure ratio conditions or optimum efficiency conditions of the turbocharger. Optimum pressure ratio, or boosting pressure, increases the power density and allow for system to reach the same performance for a smaller engine, or even increase the performance of a given engine size. Depending on the operating point of interest, operation at peak pressure ratio or the peak efficiency of the turbocharger can be useful. The choice of operation at high pressure ratio or high efficiency conditions is dependent on the application of interest to the manufacturer and customer.

In essence, a turbocharger is a coupled compressor and turbine system in which the turbine is driven by the exhaust gases of the engine. A schematic of a turbocharger assembly is shown in figure 1.5. The air leaving the compressor passes through air cooler or inter cooler, as can be seen in figure 1.6. The inter cooler acts to reduce the temperature of the incoming air and further increase the air density to optimise the combustion of fuel in the engine. Although the inlet manifold is downstream of the compressor, it has an instantaneous effect on the way the compressor operates as the flow field changes in response to the opening and closing of the intake valves. As a result, the efficiency and stability of the compressor can be altered.

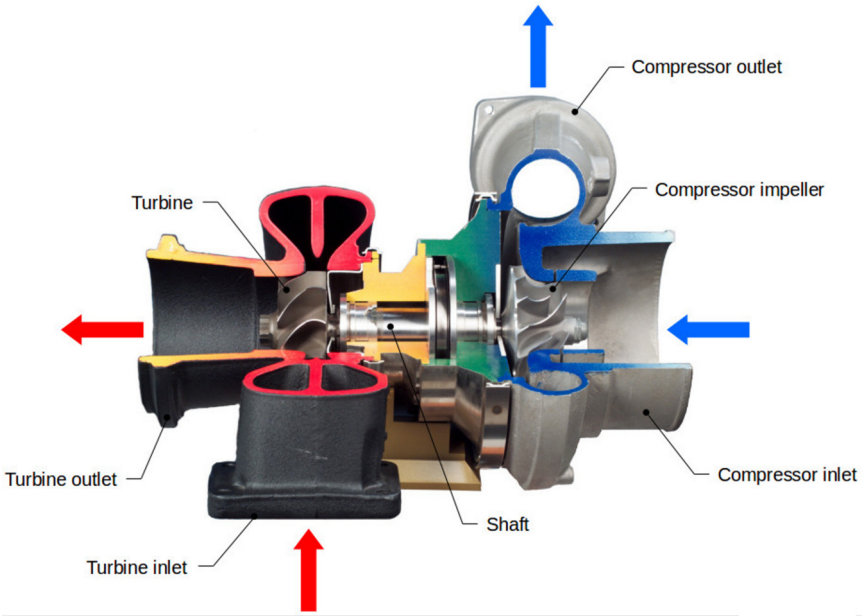


Fig. 1.5 Section view of a turbocharger showing the compressor, turbine and connecting shaft [Figure from x-engineer [13]].

The periodic opening and closing of the intake valve train of the engine cylinder arrangement can be seen as as pressure fluctuations. A typical pressure pulsation seen by the turbocharger is depicted in Figure 1.7. This figure is taken from a study conducted in 2004 on 3 stroke engine with a 2500rpm engine speed. This schematic shows the pressure fluctuations measured at the exit of a turbocharger. At the inlet of the turbocharger, a similar pressure fluctuation is seen.

It should be noted that in this thesis, the word '**pulsating**' will be used to describe the engine environment, where the compressor experiences pressure fluctuations from the opening and closing of the engine intake valves, and the word '**steady**' used when these pressure fluctuations are not present.

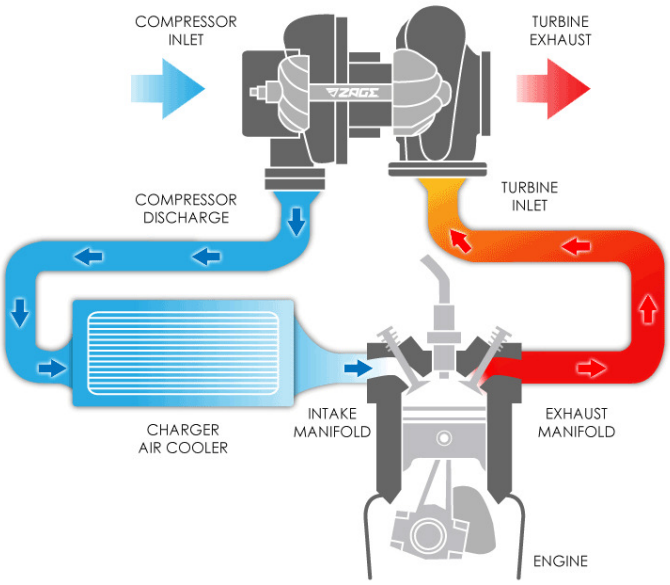


Fig. 1.6 Schematic of a turbocharger showing the IC engine, air cooler, intake and exit manifolds [Figure from Turbodynamics [14]].

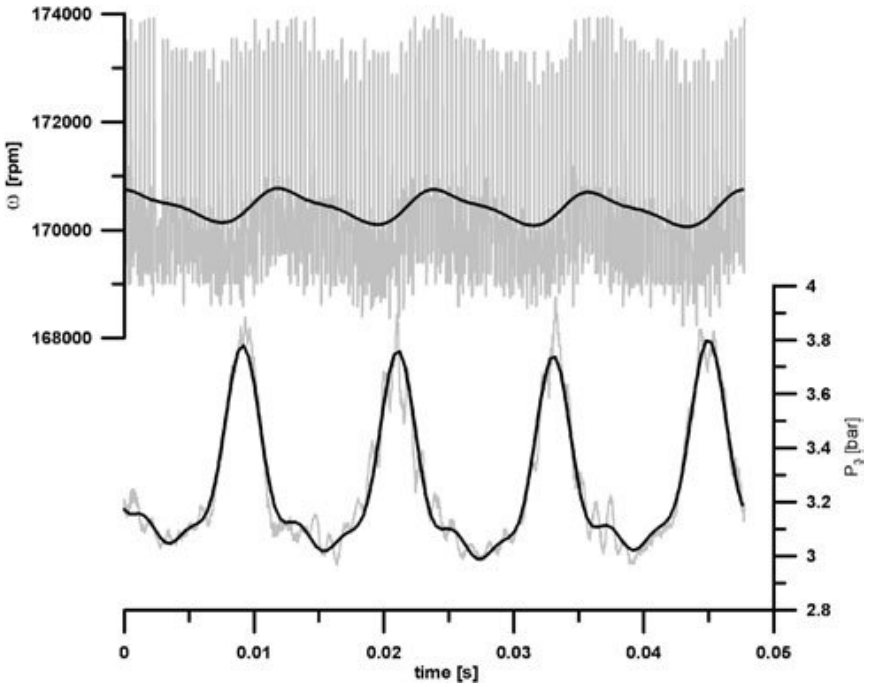


Fig. 1.7 This figure shows measured data for a 2500rpm, 40 mm 3/stroke engine. The turbocharger speed (top) and exhaust pressure (bottom) are shown. Two signals are displayed: original (light grey) and filtered (black) signal. It is clear to see pulsations in the static pressure signal resulting from the engine operation [Figure from Macián et al. [15]].

1.3 Industrial Project and Targets

Turbocharger manufacturers are interested in improving their understanding of components under engine conditions, particularly with respect to performance limits and efficiency. There is a gap in knowledge with regards to the compressor efficiency assessments under pulsating conditions, and this sets the basis of this research. The work has been sponsored by Mitsubishi Heavy Industries Ltd (MHI). MHI are a global turbocharger manufacturer with applications across many different sectors.

1.4 Research Aims and Objectives

The overall research aim is to design centrifugal compressors with improved performance under engine conditions - it is estimated that 1% in efficiency would be achievable. To achieve this aim, it is important to determine the behaviour of turbocharger compressors under the pulsating flow conditions experienced by compressors. This can be studied experimentally and computationally such that key sources of efficiency deficit can be identified. This assessment will ultimately help develop key design modifications that can improve performance, which will be a significant outcome for industry.

To achieve the overall aim of this research, the following key research objectives and milestones have been developed:

1. To increase the capability of the existing compressor rig testing facility for reliable efficiency measurements
2. To determine the performance differences of the baseline compressor at key operating points using detailed measurement data
3. To conduct computational investigations of the compressor under pulsating conditions and gather insights on the compressor loss mechanisms
4. To develop, test and evaluate modifications to compressor designs, such as the shape of the compressor tongue and shroud cavity, for improved efficiency in the pulsating flow environment
5. To enable torque measurements as part of the test facility and assess instantaneous, unsteady torque of the compressor

1.5 Thesis Outline

This thesis is divided into the following chapters:

Chapter 1: Introduction

This chapter introduces the thesis and provides motivation and background, states the research question and provides the chapter summary.

Chapter 2: Background and Literature Review

This chapter outlines a summary of related published work to the topics addressed in this thesis. It provides the background on a typical centrifugal compressor as well as the sub-components. Following on from the background, it covers the research into pulsed flow in turbocharger compressors, both experimentally and computationally, as well as the system influence on the stability limits of the compressor. Finally, this chapter emphasises the gap of knowledge that this thesis aims to fulfil.

Chapter 3: Experimental Facility and Methods

In this chapter, the experimental testing methodology of the compressor is discussed. The capabilities of the experimental facility and necessary improvements for increased accuracy in the measurement of compressor efficiency is outlined, such as improvements to the mass flow rate measurements. The updated test facility is presented, and the suitability of the updated test facility, including the reliability and uncertainty of measurement is discussed. Finally, the experimental method is described in brief before the chapter closes with a summary.

Chapter 4: Experimental Investigation of Compressor Under Pulsating Flow

In this chapter, the performance of the baseline compressor is assessed in detail through an experimental investigation. The baseline compressor and required modifications for measurements is outlined, and details about the instrumentation is also presented. The modified compressor has been designed and manufactured for specific measurements at various locations within the compressor. The experimental results are outlined and

insights are drawn on the state of flow inside the compressor by assessing static pressure and efficiency measurements.

Chapter 5: Computational Assessments on Compressor Performance

In this chapter, the baseline compressor is computationally investigated at key operating points. The computational method is validated against known experimental results; the state of flow inside the compressor is further studied using the ANSYS CFX package. The flow fields at different instances in time along a pulse are studied to provide further information about losses and loss mechanisms. The chapter focuses on two separate computational investigations. The first investigation is near surge conditions (low mass flow rates). The next investigation is looking at the three different operating points that are key to the research: peak pressure, peak efficiency and large flow conditions.

Chapter 6: Design Modifications to Centrifugal Compressor for Pulsating Flow

In this chapter, designs that could improve efficiency of the compressor under pulsating flow conditions are detailed, tested and evaluated. The design and manufacturing process for the modified designs are provided along with the initial results from the designs. Two key design modifications are detailed. Each of the designs are developed through different means. Where possible, experimental measurements provide further insight into the compressor design. Finally, the results from the tests are discussed.

Chapter 7: Torque meter Design, Development and Preliminary Results

In this chapter, a torque meter that is able to obtain instantaneous information about power and torque has been designed, manufactured and validated. The design process for manufacturing a working prototype of the torque meter has been outlined and the method of assessment is also detailed. The suitability of the designed torque meter for test purposes is discussed. Finally, some initial tests are conducted to assess the instantaneous behaviour of the compressor at different amplitudes and frequencies of the pulse experimentally.

Chapter 8: Conclusion and Future Work

In this chapter, the concluding remarks of this research are outlined with respect to the initial aims and objectives of the thesis, stating the key research outcomes. The thesis closes with a section detailing future works that would further the research in this area.

1.6 Scholarly Output

This research has contributed to a few publications, briefly detailed here for reference to the reader.

Parikh, A, Martos, P, Barrera-Medrano, E, Hayashi, Y, Martinez-Botas, R, "Computational Flow Field Assessment of the Inlet Region of Centrifugal Compressor Under Unsteady Flow Conditions Near Surge", Proceedings of ASME Turbo Expo 2022, Turbomachinery Technical Conference and Exposition GT2022, Rotterdam, June 13-17 2022

This conference paper was authored by Parikh, the co-authors Barrera-Medrano, Martos, Hayashi and Martinez-Botas provided key supervision. In this paper, the computational flow field of the inlet region of a centrifugal compressor under pulsating flow is studied. A full stage, 3D URANS model of a compressor exposed to pulsating backpressure is solved using ANSYS-CFX for the near surge operating point. The flow field is assessed using Mach number, static entropy, static pressure and local flow direction in the inlet region. Flow separation regions have been identified. This paper is one half of the computational research conducted within this thesis and is presented in Chapter 5.

Parikh, A, Singh, G, Noon, C, Flora, H, Martinez-Botas, R, "Design and Development of a Fast Response Torque Meter for Unsteady Flows in Turbocharger Applications", Proceedings of ASME Turbo Expo 2022, Turbomachinery Technical Conference and Exposition GT2022, Rotterdam, June 13-17 2022

This conference paper was authored by Parikh, and includes the work conducted by co-authors Singh, Noon and Flora. Martinez-Botas acts as a supervisory role. In this paper, the design and test procedure for a high-speed torque meter for turbocharger applications is presented. The torque meter operating methodology and working principles as well as the calibration process is detailed. The validation of the torque meter is conducted on the compressor testing facility by measuring the response of the pulses at different

frequencies and amplitudes The torque measurement is compared against static pressure measurements corresponding to the pulsating conditions. This paper is the preliminary work conducted on the torque meter, which is used for torque meter assessments in Chapter 7.

Parikh, A, Noon, C, Barrera-Medrano, E, Hayashi, Y, Martinez-Botas, R, "Detailed experimental performance and efficiency assessment of a turbocharger centrifugal compressor under steady and pulsating conditions", 15th International Conference on Turbochargers and Turbocharging, London, May 16-23 2023

This conference paper is authored by Parikh. Noon, Barrera-Medrano, Hayashi and Martinez-Botas take on key supervisory roles. The paper details the experimental analysis undertaken on an instrumented centrifugal compressor under compressor exit pulsating conditions. Instantaneous static pressure amplitudes for operating points and the corresponding hysteresis behaviour have been studied for the volute, diffuser, and impeller pulses. The region near the volute tongue region has been shown to be particularly critical due to its vicinity to the outlet changing (pulsating) boundary condition and has found to have an impact on impeller efficiency. This initial assessment leads to interesting insights in the response of the compressor to an unsteady pulsating environment thus allowing a better understanding on the real turbo-engine system performance. This paper is the primary outcome of the experimental research presented in Chapter 4.

Hayashi, Y, Parikh A, Barrera-Medrano, E, Martinez-Botas, R, "Hysteresis effect of volute to compressor performance under pulsating flow condition", Proceedings of ASME Turbo Expo 2023, Turbomachinery Technical Conference and Exposition GT2023, Boston, June 26-30 2023

This paper is co-authored by Hayashi and Parikh on the findings conducted by the industrial collaboration project betweeh Mitsubishi and Imperial College. Barrera-Medrano and Martinez-Botas take on a supervisory role. This paper focuses on the volute region, which was investigated computationally for loss regions after Parikh conducted the experimental investigation with the modified compressor. From the validated simulation results, the instantaneous velocity distribution and energetic loss profile have been obtained. Changes to the flow direction around the volute have been found depending on whether the instantaneous flow rate increases or decreases and the consequent loss regions have been identified. Some of the work conducted as part of this paper forms part of the computational research conducted within this thesis and is presented in Chapter 5.

Chapter 2

Background and Literature Review

Centrifugal compressors have been extensively studied over many years and the available literature on this topic is vast. Most of the literature focuses on steady flow operating conditions. However, as seen in the Introduction chapter (Chapter 1), operating conditions are altered when the compressor is connected to the engine. The study of true-engine conditions, where the flow is in a pulsating state, is a relatively new area of research. It is clear from studies conducted thus far that pulsating conditions have an effect on the performance of the compressor when compared to steady flow, but there is still much to be learned about the impact of the pulsating environment. More research in this area is critical for the understanding of performance of compressors under engine conditions.

This chapter provides an overview of the relevant literature and closes with a summary of the current gaps in knowledge. In the first section, a background on centrifugal compressor is provided as this knowledge is necessary to understand the influence of pulsating flow. Then, the current knowledge on the performance of centrifugal compressors under pulsating environments is reviewed. Finally, as a significant part of the research effort is experimental and design, additional literature guiding the design of compressors and background on experimental measurements is also provided.

2.1 Centrifugal Compressor Background

A centrifugal compressor is a device that is able to raise the pressure of a fluid medium by imparting energy through rotational motion. Centrifugal compressors are used in turbomachinery because they are compact, robust and can achieve high pressure ratios in a single stage application. The compressor's core function is to raise the density of the

fluid medium, by causing an increase of the fluid static pressure [16]. Figure 2.1 shows a section view of a centrifugal compressor. The three critical components namely the impeller, diffuser and volute, have been highlighted.

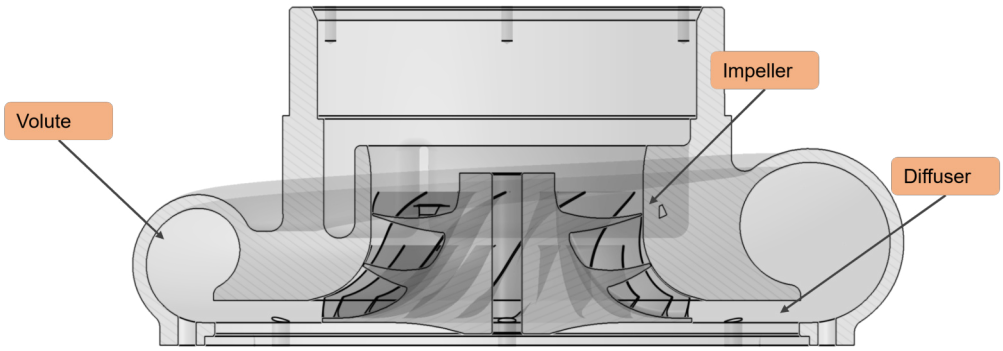


Fig. 2.1 Section view of a centrifugal compressor showing the impeller, diffuser and volute regions.

The performance of the compressor is connected to the tip Mach number, which is dependent on the rotational speed of the compressor. The tip Mach Number, M_m is the ratio of the outlet blade tip velocity, U_b, to the acoustic velocity at inlet conditions, a_1 [17].

$$M_m = \frac{U_b}{a_1} \tag{2.1}$$

The work done by the impeller on the fluid can be determined using the Euler turbomachinery equation shown in Equation 2.2 [18]. The work done by the impeller is a function of the blade speed, U, and the angular velocity, C_θ, at the inlet and exit of the impeller. In most centrifugal compressor stages, the flow often approaches axially through an inlet duct. Sometimes, geometrical changes can be made to include pre-swirl, resulting in non-zero values for $C_{\theta 1}$ [18].

$$W_x = U_2 C_{\theta 2} - U_1 C_{\theta 1} \tag{2.2}$$

To raise the density of the gas, the static pressure must be increased and therefore the impeller passage is designed to enable diffusive processes to take place by increasing the flow area between the inlet and outlet of the impeller passage. In addition, a diffuser normally follows the impeller and it is designed to allow the fluid to slow down further. The compressor volute or scroll collects the fluid as it leaves the diffuser and in this component, the static pressure is sometimes also increased further in the scroll.

The isentropic efficiency of a compressor is the ratio of the isentropic work (i.e. when the compression is adiabatic and reversible) to the actual work, it is indicative of the losses in the system. The losses generated in the compressor system result in a loss of total pressure.

2.1.1 Compressor Characteristics

The standard performance of a compressor is shown in the form of a compressor 'map' which plots the pressure ratio across the device against non-dimensional mass flow rate traversing the compressor for various fixed values of rotational speed.

Performance Map

Figure 2.2 provides an example of a typical compressor map showing the pressure rise versus mass flow rate. The operating range is indicated by the range of mass flows that the compressor can operate for a given compressor speed. This is otherwise known as the 'stable' operating region of the compressor. Constant efficiency contours are often also shown in the map to help identify the best efficiency operating regions.

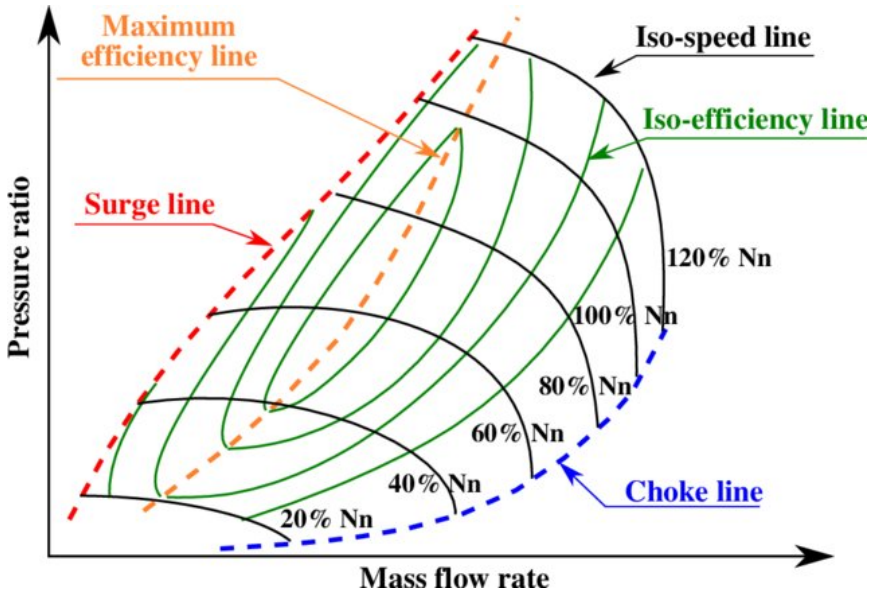


Fig. 2.2 Typical centrifugal compressor map showing the low and high mass flow limits (surge and choke), design line and efficiency contours [Figure from Zambonini [19]].

The peak pressure is the maximum pressure that the compressor can reach for given inlet conditions, this can be seen as the maxima of the pressure curve for any given speed. Sub-optimal conditions can result in increased aerodynamic losses and performance degradation. In extreme conditions, it can also result in damage to equipment and operational instabilities [20].

The four key non-dimensional parameters that define a compressor characteristic are shown in Equation 2.3 [21]. They are: stagnation pressure ratio, stagnation temperature ratio, non-dimensional mass flow rate and non-dimensional rotational speed. These non-dimensional parameters are calculated using total Pressure, P_0, Total Temperature, T_0, Mass Flow Rate, $\dot{m}$, and compressor speed, N.

$$F\left(\frac{P_{02}}{P_{01}}, \frac{T_{02}}{T_{01}}, \frac{\dot{m}\sqrt{T_{01}}}{P_{01}}, \frac{N}{\sqrt{T_{01}}}\right) = 0 \tag{2.3}$$

The stagnation pressure ratio, Π is defined by 2.4.

$$\Pi = \frac{P_{02}}{P_{01}} \tag{2.4}$$

The efficiency of a compressor system is calculated as a ratio of total-to-total isentropic enthalpy change for the whole stage over the actual enthalpy change, see equation 3.27.

$$\eta_{tt} = \frac{h_{02s} - h_{01}}{h_{02} - h_{01}} \tag{2.5}$$

One of the ways in which diffuser and volute performance is assessed is through the means of a static pressure recovery which estimates the amount of static pressure that has been achieved [22], see Equation 2.6. The static pressure, P_3 and P_2 refer to the static pressure at the outlet and inlet of the stator component. The stagnation pressure, P_{02}, refers to the inlet stagnation pressure of the stator component.

$$SPr = \frac{P_3 - P_2}{P_{02} - P_2} \tag{2.6}$$

Comparative Measures

In this research, comparisons in performance will be made between pulsating flow and steady flow. One of the ways to compare the performance is to assess the difference in the surge limit, or otherwise known as the Surge Margin Improvement (SMI). There are many definitions of Surge Margin Improvement. In this thesis, SMI is defined as per equation 2.7. This approach allows for continuation between current work and previous work conducted on this compressor system, see Barrera-Medrano [23].

$$SMI(\%) = \frac{\dot{m}_{steady} - \dot{m}_{pulsating}}{\dot{m}_{steady}} x100 \tag{2.7}$$

Another useful assessment is the difference in mass flow range. The mass flow range, MF_r, is calculated using equation 2.8 [18]. The mass flow range is a useful calculation to understand the shift in flow range under pulsating conditions compared to steady conditions.

$$MF_r = \frac{\dot{m}_{choke} - \dot{m}_{surge}}{\dot{m}_{choke}} \tag{2.8}$$

Performance limits

As can be seen in the performance map, there are two limitations to the operating range of the compressor: surge and choke. The choke limit is the aerodynamic maximum flow rate where the components reaches sonic conditions in the minimum area location. The low flow limit is called surge, where the compressor behaves in an unstable manner, causing oscillatory flow fluctuations and vibrations that damage the structural integrity of the system.

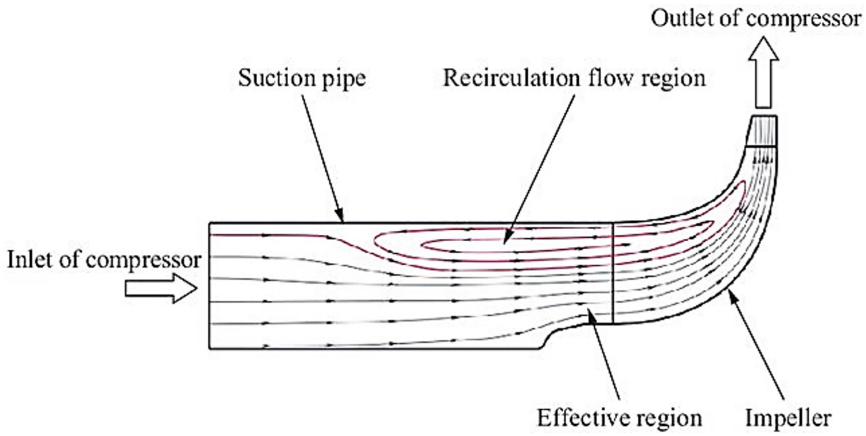


Fig. 2.3 Schematic illustration of inlet recirculation. The recirculated flow is shown at the walls of the suction pipe, near the impeller inlet region [Figure from Tamaki [24]].

During a surge cycle, the compressor experiences flow reversal in some or all the passage, Figure 2.3 shows a typical inlet recirculation region which is often a sign that the compressor is about to surge. The surge margin is affected in the case of pulsating flow as will be shown in the later sections.

Stall and Rotating Stall

Before surge is reached some of the channels begin to stall and a stall cell is formed leading to blocked flow. If the stall cell rotates, then it is called rotating stall or dynamic stall. Rotating stall cells can appear or disappear. When there is rotating stall, the average mass flow is steady and forward [23]. Even if there is slight oscillatory behaviour (mild surge), there is no bulk axial flow reversal as in the case of deep surge and some of the compressor blade passages are still able to generate pressure. Stall and rotating stall are mainly caused by flow separation regions in the main channel. If they are present, the efficiency of the compressor reduces.

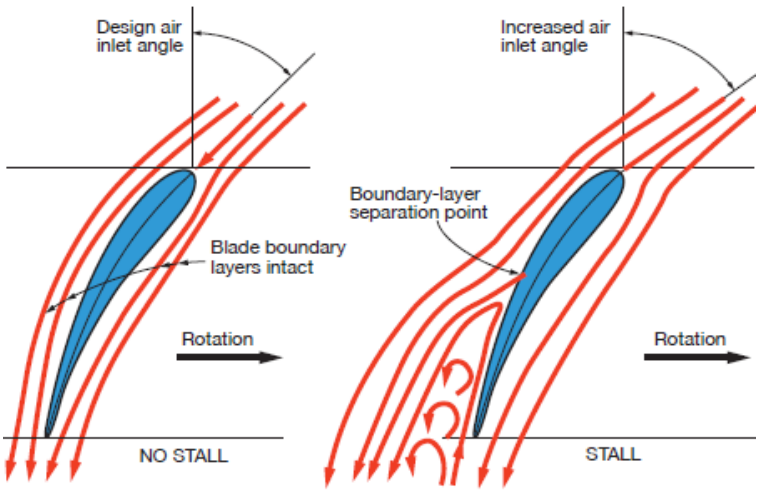


Fig. 2.4 Schematic drawing of stall on a compressor blade [Figure from Langston[**?**]].

2.1.2 Losses in a Centrifugal Compressor

The losses within the compressor can be summarised as one of four types, as noted by Cumpsty [25]; drag at solid surfaces that result in a loss of stagnation pressure, mixing loss from diffusion between high and low momentum flows, shock losses (particularly if the

boundary layer separates), and shear work losses due to viscous dissipation between shear layers.

Secondary Flow

The secondary flow term is used to describe any flow that is perpendicular to the primary channel [25]. A representation of secondary flow formation in an axial device is shown in Figure 2.5. Brun and Kurz [26] show that the secondary flow is always caused by an imbalance between static pressure field and kinetic energy in the flow. Secondary flow structures are one of the major sources of loss and lead to strong mixing. There are also sometimes small separation regions near the inducer inlet. In general, secondary flows increase significantly when the system approaches stall.

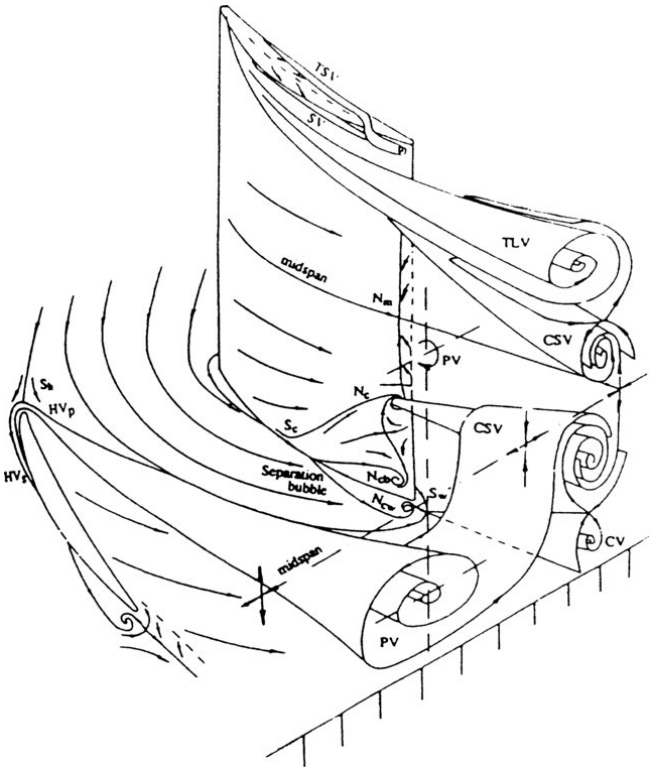


Fig. 2.5 An illustrative schematic of secondary flow structures in a compressor impeller, as a result of flow separation in the boundary layer and flow formation perpendicular to primary channel flow [Figure from Kang et al. [27]].

In the diffuser, there are large total pressure losses due to mixing and frictional losses at the flow walls. Impeller slip, a process by which the primary passage flow migrates from the pressure surface to the suction surface due to the effect of blade unloading at the airfoil exit, also affects the overall performance of the compressor [16]. This interface is one of the key regions affecting the performance of the impeller and diffuser and has a significant impact on overall impeller stability.

Loss Distributions in Steady Flow

Figure 2.6 shows some of the regions of detected losses in a typical compressor stage adapted from Abel et al. [28]. Positions 1 and 2 are upstream of the impeller, 3 to 16 occur within the impeller, 17 to 21 refer to diffuser region and 22 to 25 are in the volute. Majority of the losses are due to secondary flow formation, separation of the flow from the blade, mixing of high and low momentum fluid streams, tip leakage (when flow migrates from the pressure side to the suction side and leads to interactions) and reverse flow. In the diffuser (vaned), the losses are due to incidence on the blades and separation of the flow. This figure is presented here as reference to the reader for most common loss locations.

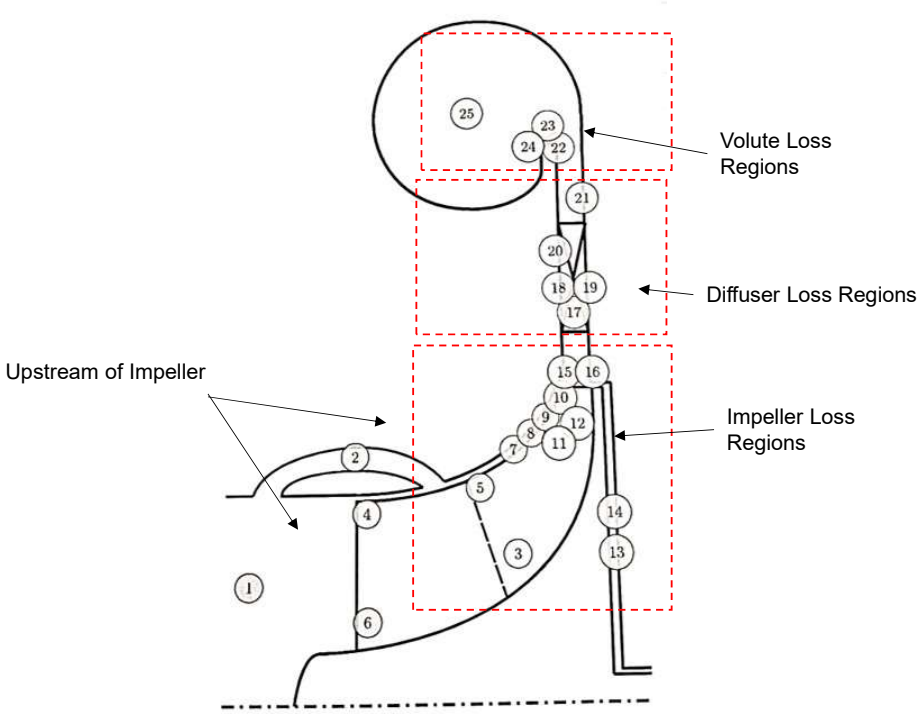


Fig. 2.6 Locations and regions of loss within a typical impeller stage [Figure from Abel et al. [28]].

To determine the loss mechanisms inside a compressor, 1D models or mean-line models are often used. The 1D models are created with empirical or theoretical mathematical functions, the results from which are verified with performance testing. It is then possible to use the 1D model to identify the dominating or most influential loss mechanisms. Mojaddam et al. [29] created a 1D model to study loss contributions from the different components of the compressor. The impeller, volute and diffuser regions were studied. It was found that that the impeller generated over 50% of the losses for operating speeds of 40k, 50k and 60k rpm, followed by the volute and lastly the diffuser. Gong and Chen [30] created a 1D model to estimate compressor performance by accounting for total pressure losses in the compressor. It was found that skin frictional losses were the most

dominant, followed by impeller incidence loss. The volute was shown to have a small effect on compressor performance. Similarly, Velásquez [31] show that impeller internal losses and diffuser losses were found to be the key locations for losses, with shock losses becoming relevant at high pressure ratios.

2.1.3 Off-Design Behaviour

When the compressor is operating under pulsating conditions, it instantaneously reaches operating points that differ from the intended design point.

Impeller off-design incidence angles

In off-design conditions, the incidence angles at the inlet change from the desired incidence angle. Figure 2.7 shows an illustration of the changing incidence angles along an operating line. In the schematic, the incidence angle changes from 10° to -5° when the compressor spans from low flow and high flow conditions. At the design point, the incidence angle is zero and the compressor operates with optimum efficiency. Variation from the incidence angle can be tolerated but results in losses.

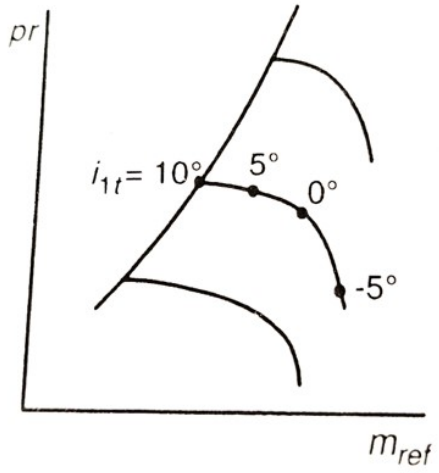


Fig. 2.7 Schematic of common incidence angles at off-design operating points on the performance map. An incidence angle of 0° occurs at design point as this is the optimum position of the blade [Figure from Japikse [16]].

Impeller inlet region near surge

It was shown above that surge is an unstable system phenomena that occurs at low mass flow conditions. The inlet region of the compressor is an important factor for compressor stability. Inlet flow leading to surge was studied using Large Eddy Simulations (LES) by Semlitsch & Mihaescu. Figure 2.8 shows the simulation result for three different flow conditions; $\dot{m} = 0.27$ (high flow), $\dot{m} = 0.105$ (medium flow) and $\dot{m} = 0.05$ (low flow - near surge). The top half of the figure shows a cut-view of the inlet pipe and the bottom half of the figure shows the meridional cut-view of the compressor. The plotted black lines are streamlines and the contour colours indicate flow velocity; Positive velocity contours show forward flow and negative velocity colours indicate reverse flow.

Comparing the results from $\dot{m} = 0.27$ with $\dot{m} = 0.05$ (the later corresponding to near surge conditions), it is clear that there are large differences in the flow. First, the flow in $\dot{m} = 0.27$ is much more uniform, and clear streamlines can be see, there is a small recirculation region at the impeller inlet (indicated by the small blue regions). All the flow otherwise collects in the volute in a uniform manner. In comparison, in $\dot{m} = 0.05$, the near surge condition, large recirculation regions can be seen,indicated by negative flow regions, the incoming flow is distorted and there are are secondary flow vortexes in the diffuser. The heavy inlet distortion in the near-surge region causes large changes in the incidence angles. The back flow in the tip clearance region for $\dot{m} = 0.05$ also induces large swirl effects in the incoming flow [32].

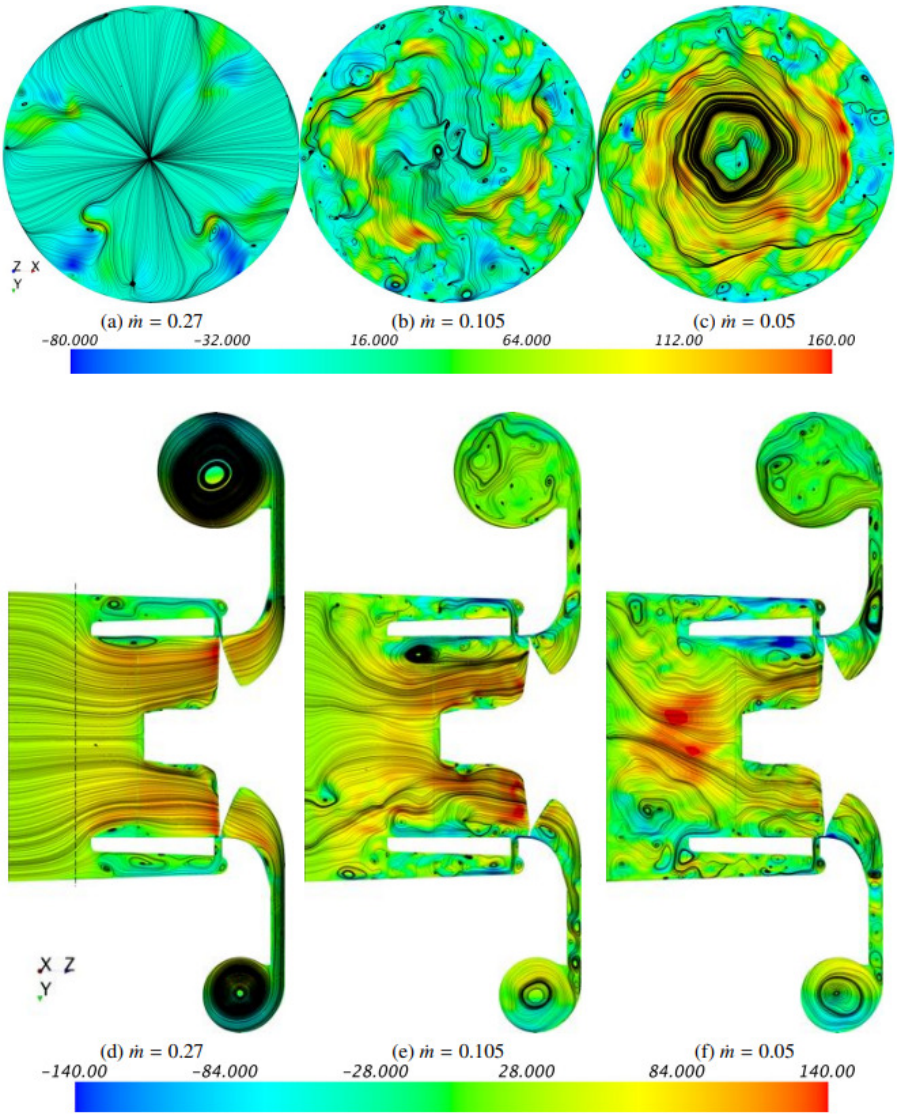


Fig. 2.8 Flow profiles at stable and for low-mass-flow unstable operating conditions. The top row shows streamlines on top of the tangential velocity (m/s) in cut plane (the location is indicated by a dashed line in the left figure on the bottom row). The bottom row shows streamlines on top of the instantaneous axial velocity (m/s) [Figure from Semlitsch & Mihaescu [32]].

Tosto et al. also studied the effects of the conditions at the inlet on the onset of surge. Their results also show separation of the flow from the blades, divergence of the streamlines from surface and pronounced recirculation [33]. Additionally, Zhang et al. [34] studied the stall inception at different circumferential positions for a compressor and observed tip-leakage vortices and separation of the suction side at the impeller. Other studies in literature also show that that inlet flow separation and inducer tip stall are likely precursors to surge [35–39].

Volute

The volute or scroll of the compressor is designed using one dimensional analysis assuming a free vortex flow from the volute inlet to the centre of the volute passage [40]. A schematic of the volute and volute tongue is shown in Figure 2.9.

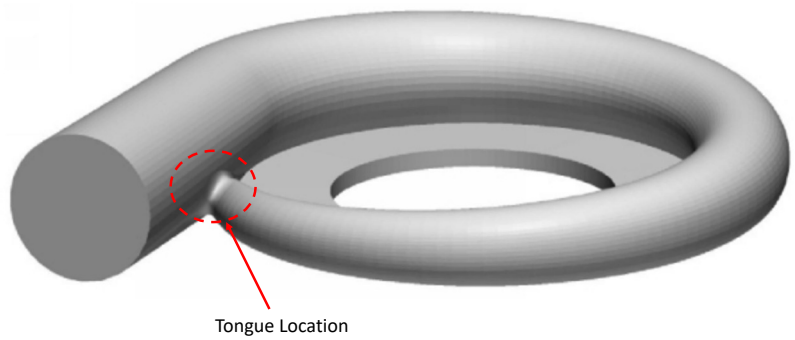


Fig. 2.9 Internal volume of a compressor volute (volute negative) showing the location of the tongue [Figure adapted from Heinrich & Schwarze [41]].

The design objective is to have uniform flow at the volute exit. This is usually obtained at the design flow rates only. In order to accommodate the increasing mass flow with the azimuth angle, the cross-sectional area of the volute increases. The volute and tongue have a significant impact on the overall compressor efficiency and loses [42]. The main losses in a volute tend to be friction, swirl, mixing, and expansion loss at low mass flow rates.

Volute tongue region

Ayder et al. [43] show that the pressure coefficient depends on length and angle of the tongue. A short tongue provides a higher efficiency at off-design conditions. Fluid entering the volute close to the tongue starts swirling around the centre of the cross section, giving rise to large velocity gradients and shear stresses. Periodic increase and decrease of swirl velocity results in extra diffusion and mixing losses. Pan et al [42] found that enlarging the flow passage area near the tongue region without changing the exit inlet area ratio of the volute led to improvement in the internal flow distribution at off-design conditions. Gulich [44] show blockage around the inlet due to the presence of the tongue resulted in a

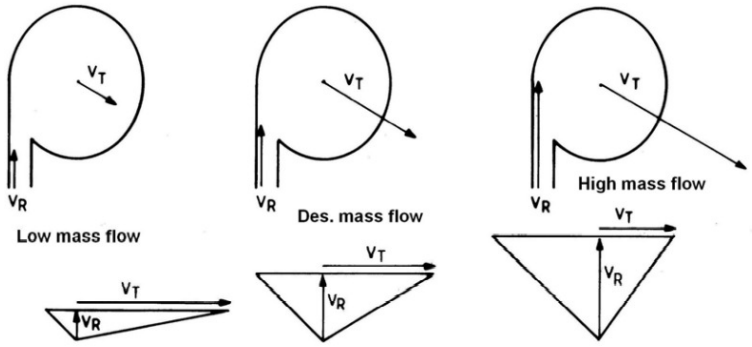


Fig. 2.10 Schematic of the different velocity triangles and the relative size of the tangential velocity at design and off design conditions of the volute [Figure from Braembussche [45]].

deviation of the otherwise uniform pressure distribution at the volute inlet, leading to flow separation at the outer wall of the volute inlet near the tongue. Whereas for high flow rates, the flow separation occurs at the pressure side due to a more radial velocity of the flow. At the tongue, this deviation from design point is critical, as it affects the overall efficiency of the impeller.

Volute at high or low flow conditions

Ayder et al. [43] analysed a centrifugal compressor volute and found that there is a rotational non-symmetric pressure distribution in the diffuser outlet at off-design conditions. When mass flow rates are lower than design mass flow rates, the volute acts as a diffuser. At high mass flow rates, decrease in static pressure along the volute periphery causes an increase in radial velocity at diffuser outlet. At high mass flow, volute outlet kinetic energy is higher than at the inlet, indicating accelerating flow; adding to the high total pressure loss in the volute and large negative static pressure recovery coefficient. A schematic of the velocity triangles that occur at lower and higher than design flow rates is shown in Figure 2.10.

Compressor System

The compressor system plays a large part in the onset of surge. Greitzer developed the lumped parameter model in 1976 to characterise surge in compressor systems [46]. It was found that, even for steady states, the point of instability was not defined by the compressor alone but depends on the system in which it operates. This can be categorised with the non-dimensional B parameter representing the ratio between pressure forces and inertia forces of a given compressor system. Although the lumped parameter model was designed for axial compressors, Hansen applied it to centrifugal compressors in 1981 [47].

$$B = \frac{U_t}{2\omega_h L} \tag{2.9}$$

Here, U_t is the tip speed at impeller exit, L is the characteristic length and ω_h is the natural frequency. Since the tip speed is proportional to the rotational speed of the compressor, at low speeds and large characteristic lengths, the B parameter is small and the system behaviour is inertia driven. When testing different B parameters, it was found that at large values of B, there was a larger loop in the hysteresis. Zheng et al. [48] also studied the compressor system with respect to Greitzer's lumped parameter model. For a small B, it was been found that the system experienced stall before entering deep surge, whereas stall was not required for surge at large values of B [48].

2.2 Compressor behaviour under Pulsating Flow

Experimental studies in recent literature have shown how the performance of an automotive turbocharger is affected by backpressure pulsations. The earliest assessments of pulsation on compressor performance date back to 1963. Yano [49] assessed the effect of pulsation on a centrifugal blower to understand how resonance in a system could affect the flow through the blower and power to the engine. It was concluded that it was possible to characterise the compressor system using a steady map to find momentary performance in pulsating case. Additionally, that in the case of a large reservoir placed after a rotary valve, it is possible to isolate or ignore any upstream effects after the rotary valve.

Yano and Nagata [50] conducted a theoretical study on the surging phenomena of a diesel engine in an air-charging system, with consideration of the pulsating flow effects induced by the opening and closing of the scavenging ports of an engine. Their research took into consideration different piping systems. The main objective of the study was to compare the theoretical model to the experimental findings. Detailed assessments of the onset of surge and the surge loop for different configurations of the piping system were conducted, and the results for the surging and non-surging characteristics of the compressor were compared. At the point of surge, the self-excited frequency of surge was found to have a greater effect than the rotary valve, although there was a clear influence of the rotary valve on the performance of the compressor.

Benson and Whitfield [51] conducted an experimental study into the unsteady flow characteristics on a centrifugal compressor with a rotary valve. A range of flow conditions were explored with different pulse frequencies and amplitudes. It was found that there were certain configurations where the surge margin was displaced to higher mass flow

conditions, and generally this was when the pulse frequency was the lowest. The orifices varied from smallest disc size (A3) to large disc size (A0). Figure 2.11 shows the results from a test conducted at 40,000 rpm for the different orifice sizes and different frequencies. The operating range is increased when a smaller orifice is used and there is a clear effect of frequency.

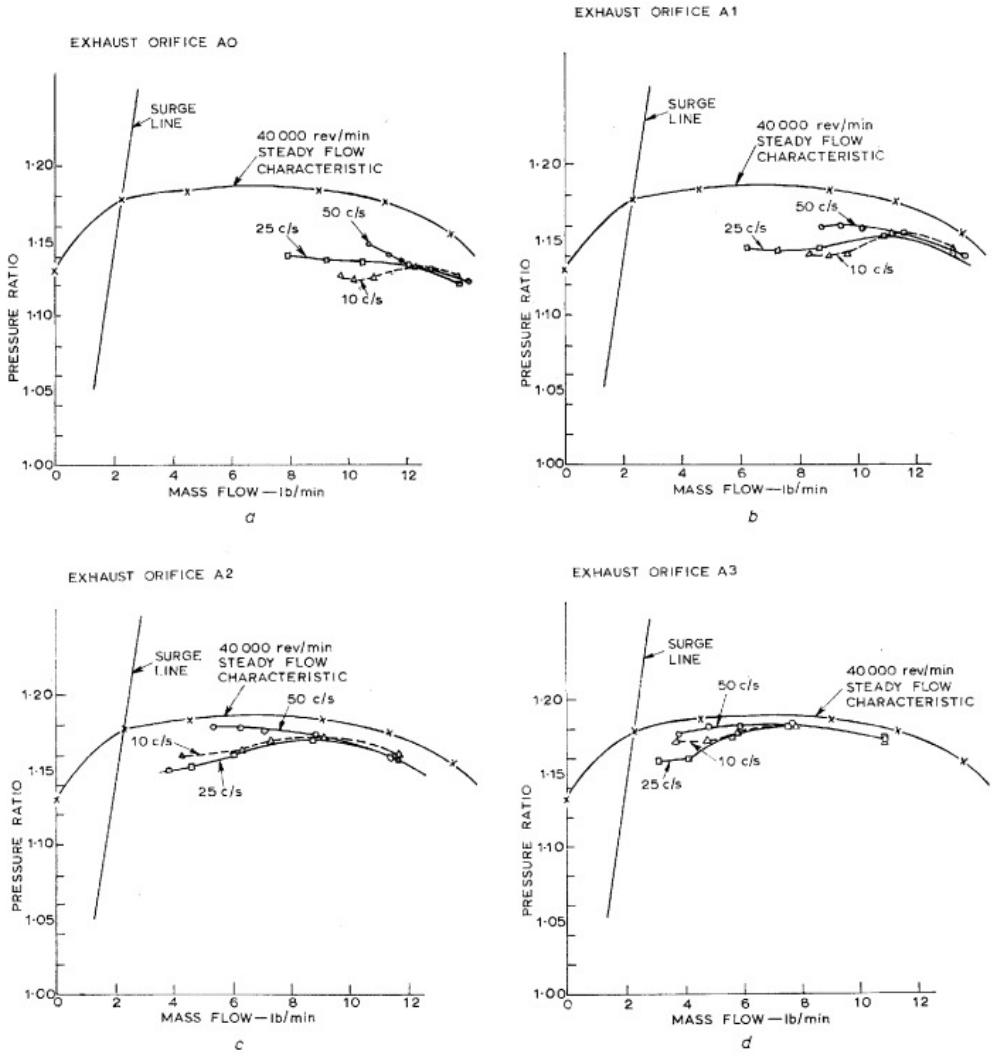


Fig. 2.11 Experimental results from Benson and Whitfield for a compressor system with a rotary valve for different orifice disc sizes and pulse frequencies in cycles/sec (c/s) [Figure from Benson & Whitfield [51]].

Benson and Whitfield [52] also conducted a theoretical study on the effect of a non-steady flow in a rotating duct to predict the non-steady flow in centrifugal compressor when exposed to pulsating conditions. The centrifugal compressor was replaced in the model by a rotating duct and a numerical model was developed to predict the behaviour of the compressor. There was some over-prediction in the theoretical model, however the increased computational time was discussed to be impractical. A valuable outcome was to

use the model to find the equivalent pipe length in a quasi-steady application to predict the onset of surge.

It can be concluded that the surging phenomena was of interest to early researchers as there was an influence of the system size on the onset of surge under pulsating conditions. Between 1960's and 1990's, the progress and research on compressor system behaviour slowed down. In this interim period, although the research effort on pulsating flow was albeit topical and relevant, the focus was dominated by turbines, as the performance of turbines was directly affected by pulsating flow from the exhaust valves.

2.2.1 Surge Margin Improvement

In recent years, the impact of pulsating flow on centrifugal compressor surge has resurfaced most notably with Galindo et al. [53]. Galindo et al. developed an experimental facility to study the surge phenomena in an automotive application and the corresponding 1D gas dynamics model. Galindo et al. used the model and experimental facility to assess the impact of pulsating flow on surge margin. It was found that at a pulsating flow of 40-67Hz, the surge margin increased by around 15% and that increase in surge margin was dependent on the amplitude of the pulse. In particular, the larger the amplitude of the pressure pulse the greater the shift in surge margin towards lower flow margins.

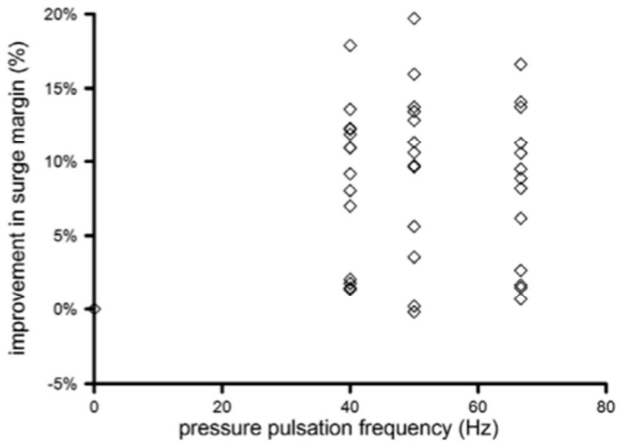


Fig. 2.12 Experimental results from testing conducted by Galindo et al. for different pulsating frequencies showing the improvement in surge margin. [Figure edited from Galindo et al. [53]].

The improvement in surge margin is shown in Figure 2.12. The effect of pulsation frequency was not noticeably detected within the tested range but the effect of pulsation amplitude

was clear. Additionally, it was found that modelling the compressor using Greitzer's lumped parameter model and surge using wave action was able to fully predict the onset of surge under pulsating flow.

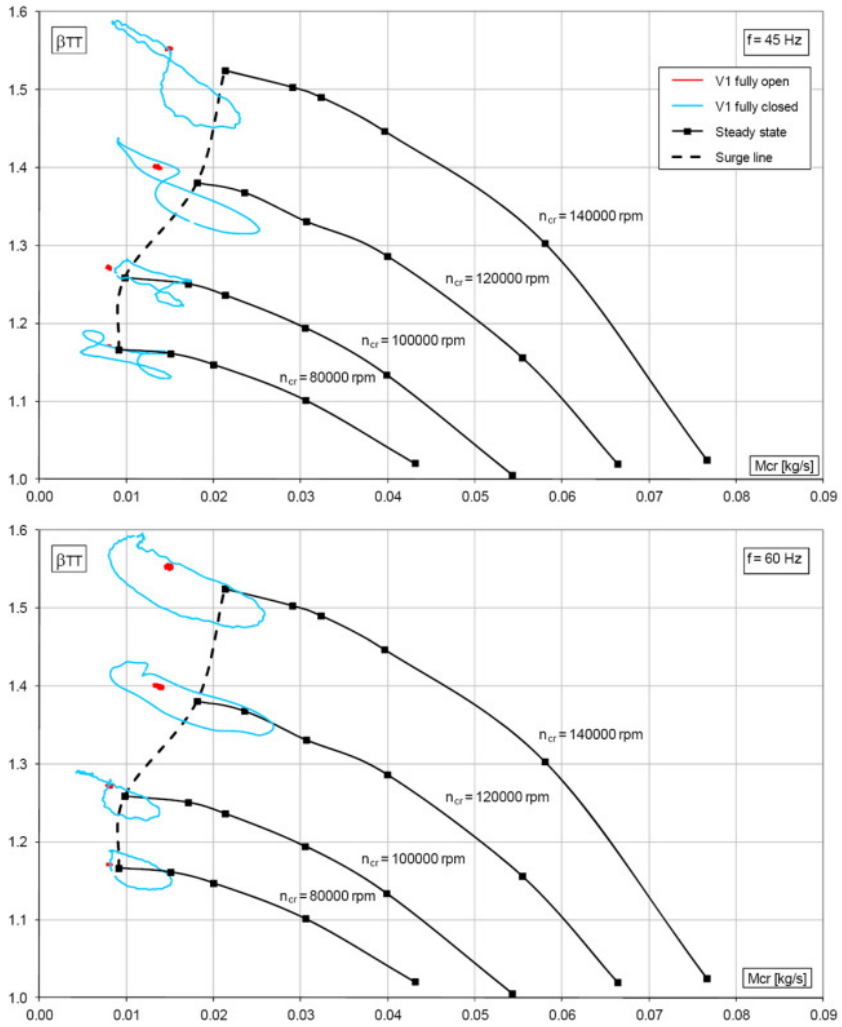


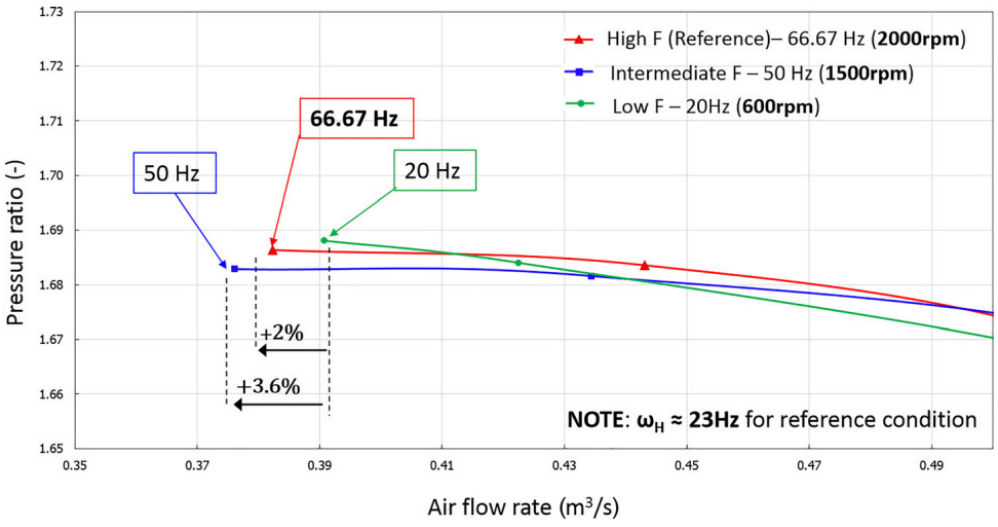
Fig. 2.13 Experimental results of pressure ratio vs. mass flow rate curve from Marelli et al. for two different frequencies (45Hz and 60Hz), with different operating speeds (60k rpm - 140k rpm). The blue line corresponds to a condition where the compressor sees a pulsating backpressure from the pulse generator; in this case hysteresis behaviour in surge margin is seen [Figure from Marelli et al. [54]].

Marelli et al. conducted detailed experimental studies on the effect on the pulsating flow effects near the surge limit. Figure 2.13 shows the results for two pulse frequencies, 45 Hz and 60 Hz for different speeds (80k - 140k rpm) of the compressor system. In the case of the experimental set-up titled 'V1', the rotary valve governing the flow condition was either closed (represented by red lines in the Figure) or fully open (represented by blue lines). When the valve was fully opened, the pulsations from the rotary valve were felt by the compressor and instead of there being a single operating point, the instantaneous behaviour spans multiple operating points. The surge margin shifted to left in pulsating condition compared to the steady case (represented by the black lines). The paper conclusively states

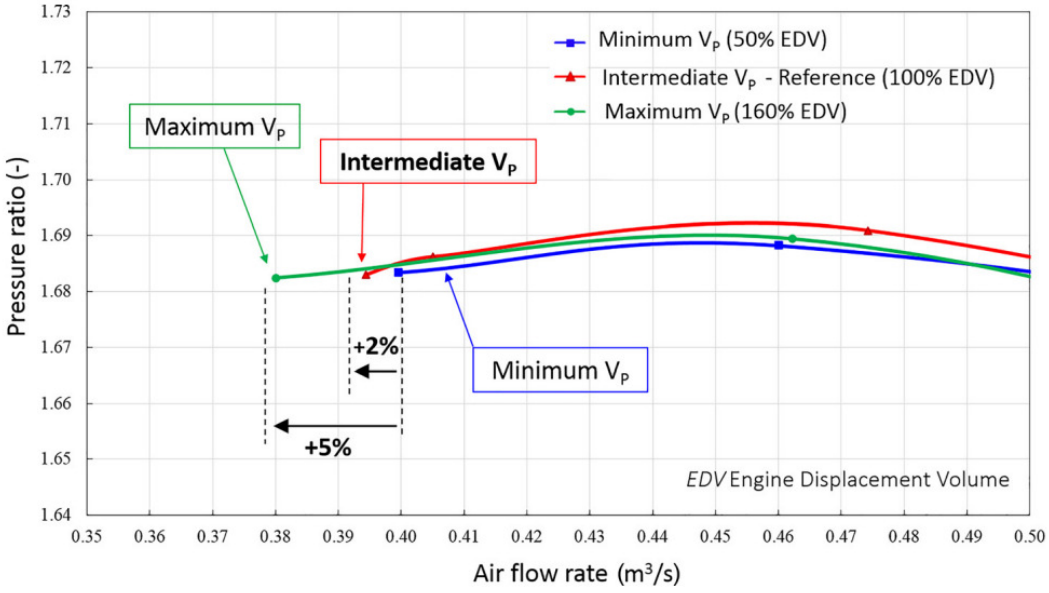
that the surge margin clearly shifts to the left and that under strong pulsating conditions, the compressor is capable of stable operation even if it instantaneously operates on the left of the surge line.

Barrera-Medrano also conducted a detailed study on the effects of pulsating flow on centrifugal compressors near surge [55, 56, 23]. The experimental facility developed by Barrera-Medrano et al. could modify the valve frequency, amplitude as well as system size to study the combined effects of the compressor system on surge - it was also able to capture instantaneous flow measurements.

Figure 2.14a shows the effect of pulsation frequency on the surge margin. A 3.6% improvement is found for the 50 Hz case. Whilst the increase in frequency generally improved the surge margin, there was an optimum frequency that was system dependent. At the resonant frequency of the system, the improvement in surge margin was the lowest. Barrera-Medrano also tested the impact of different sizes of the compressor system. In the earlier section of this chapter, it was shown that the compressor system size has an effect on surge, and the resonant frequency of surge is dependent on the compressor system, which Greitzer helped characterise with a lumped parameter model called the 'B parameter'. By modifying the system volume under pulsating conditions, Barrera-Medrano can test systems with different system sizes, in effect, different B parameters. Figure 2.14b shows the results obtained for three different volume conditions (maximum, intermediate and minimum) at a given frequency, overall a 5% improvement was found for the largest volume case compared to the smaller volume case. This was confirmed with Shu et al. [57], who show an improvement in surge margin when conducting experiments on a similar facility.



(a) Frequency effect



(b) Volume Effect

Fig. 2.14 Experimental results on the frequency and volume effect on a centrifugal compressor exposed to pulsating backpressure. The improvement in surge margin can be seen in both cases [Figure from Barrera-Medrano [23]].

2.2.2 Hysteresis Behaviour

One of the key findings on pulsating flow research is that there is a hysteresis in compressor response. A hysteresis is defined as a lag in the system response to a driving input. In this case, the pressure change caused by the opening and closing of the engine intake manifold is the 'driver' whereas the mass flow of the system exhibits the time delayed 'response'.

Marelli, Capobianco & Zamboni studied this concept by mapping the pressure path. Figure 2.15 shows their findings for four different operating speeds. The 'hysteresis' loops for certain operating points are shown in the performance maps. Each of the four maps are at different running speeds of the compressor. It is stated that the compressor is subject to the 'filling and emptying wave action' just as that of a turbine [58]. The filling and emptying wave action in this case refers to the system volume 'filling' and 'emptying' periodically. This is because there is a delay at which the system responds to the driving change. The time delay is said to be driven by the flow inertia of the compressor system [58].

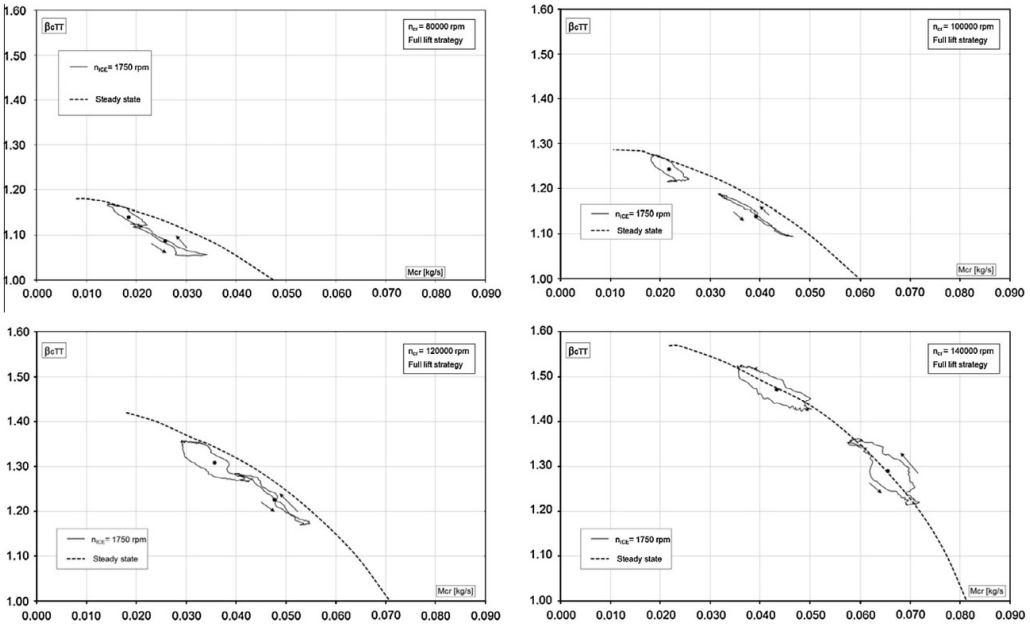


Fig. 2.15 Experimental findings of pressure ratio and flow rate showing instantaneous deviation from the steady operating line for different operating speeds for a given pulse frequency [Figure from Marelli et al.[58]].

During this assessment, the instantaneous performance of the compressor was compared to the steady performance. It was found that at the same mass flow rate, the mean pressure ratio was less than that of steady operation and that the swallowing capacity of the compressor was reduced. Additionally, it was found that there was an increase in the hysteresis loop at higher rotational speed levels. If the steady and unsteady values were compared, for the same mass flow rate, the mean pressure supplied by the compressor was found to be reduced. The results were still in line with those attained by Galindo et al. with respect to the improvement in surge margin.

Barrera-Medrano [55] also looked at the hysteresis behaviour in the pressure and mass flow signals. Figure 2.16 shows the instantaneous signals of static pressure and volume flow rate, and indicates that there is a clear shift in the signal. Additionally, although not shown here, they observed that the phase shift is dependent on the pulse frequency [23].

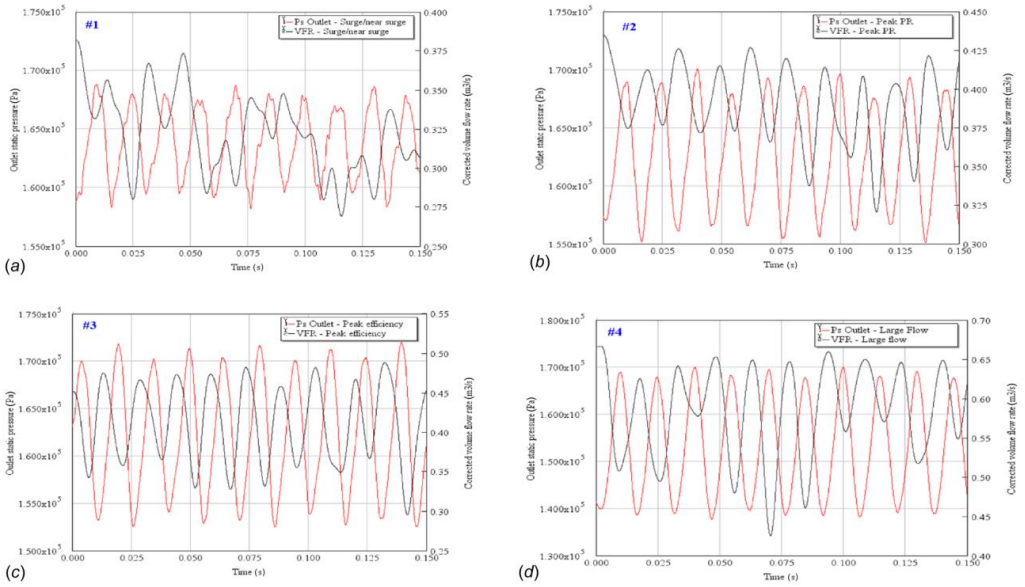


Fig. 2.16 Phase shift between the outlet static pressure signal and volume flow rate for key operating points (surge, peak Pressure Ratio (PR), peak efficiency and large flow) [Figure from Barrera-Medrano et al. [55]].

Barrera-Medrano [23] also finds that there is a tilt in the hysteresis behaviour and the hysteresis loop is found to change inclination. The hysteresis loop for a 100 Hz frequency was described as a narrow ellipse that was nearly vertical. At lower frequencies, such as between the 43 Hz and 20 Hz case, the loop became wider and more rounded. The 20 Hz hysteresis loop showed opposite trend to the 100 Hz case as it was found to be horizontal and narrower. Clearly, this also impacted the instantaneous performance at these different frequencies. With respect to the volume of the system, the hysteresis behaviour was found to be in accordance with Greitzer's model of transient system response for the 66 Hz frequency. The results for three operating points (surge, peak pressure and peak efficiency) show a trend of increasing loop size with increased volume.

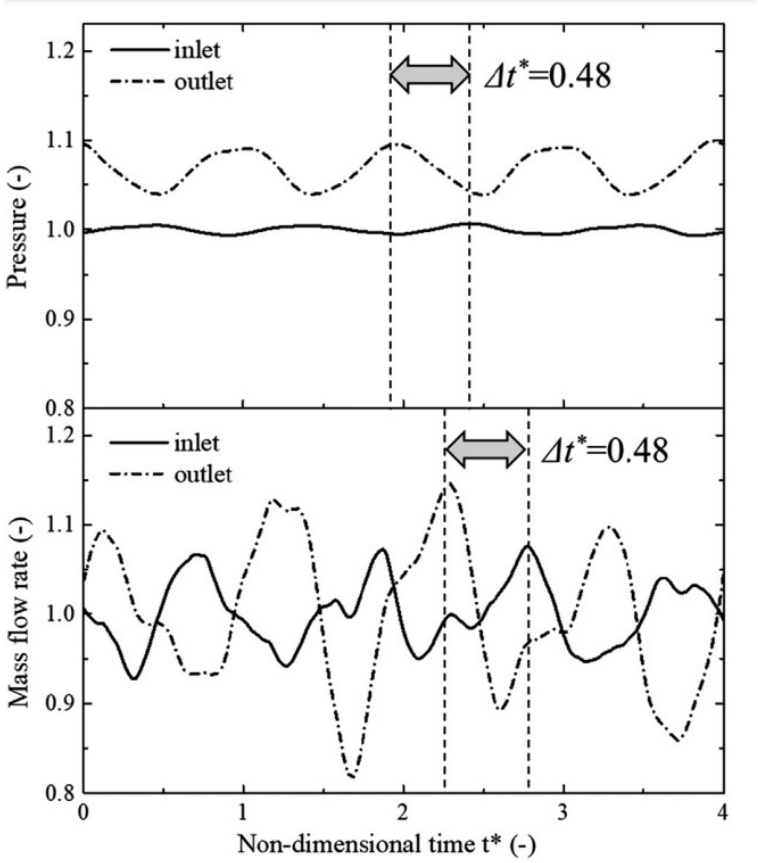


Fig. 2.17 Experimentally captured phase shift in the inlet and outlet pressure and mass flow rate signals as a result of pulsation [Figure from Shu et al. [57]].

Shu et al [59] studied the filling and emptying effect of a centrifugal compressor using a 1D model that had been validated through experimental data. The filling and emptying effect was compared to the wave dynamics of the system to see which was the driving behaviour (wave dynamics being a term used to describe the effects of the pressure wave propagation). It was found that at low pulse frequency conditions, the unsteadiness of the compressor was dominated by the filling-emptying effect. When the frequency was increased, the mass imbalance was weaker and wave dynamics effect was stronger, dominating the unsteadiness. It was also found that the pulse magnitude strongly influenced the filling and emptying effect but did not effect the wave dynamics.

Figure 2.17 shows the pressure and mass flow signals captured by Shu et al. The pressure pulse notably dampens between outlet and inlet of the compressor. There is a reduction in the mass flow rate amplitude between the inlet and the outlet, but it is still significant in comparison to the inlet pressure pulse, which is relatively stable. Additionally, there is a phase shift in the pressure and mass flow rate signals due to the time taken for the wave to propagate the length of the compression system.

2.2.3 Evaluation of Unsteadiness

At this point, it might be worth reviewing some non-dimensional parameters that are relevant to the assessments of pulsating flow, that have been used by researchers in the turbine and compressor fields to assess the level of unsteadiness of a system. One such non-dimensional parameter is the Strouhal number, named after Vincent Strouhal, who studied the effect of vortex shedding on wind flow [60]. In turbomachinery, it can be thought of as the ratio of timescales between the applied pulsating frequency of the throttle and the time taken for flow particle to traverse the flow domain. The Strouhal number is shown in Equation 7.3,

$$St = \frac{f.L}{U} \tag{2.10}$$

where f stands for frequency, L is the characteristic length of the impeller and U is the flow velocity. To calculate the Strouhal number of the impeller, the characteristic length L can be thought of as the length spanned by the flow, πD, and the flow speed, U, can then be taken as the blade tip speed, πND. Therefore, a close approximation for the St number is the ratio of excitation or applied frequency to the frequency of rotation of the impeller.

$$St = \frac{\pi D}{\pi DN\tau} = \frac{1}{N\tau} = \frac{f}{N} \tag{2.11}$$

Additionally, it can be seen above, that alongside the unsteadiness induced by the impeller rotation and the pressure pulsation, it is also important to take into consideration the inertial effects of the size and scale of the overall system.

Newton [61] researched the effects of inertial lag or mass storage within a system, discussing that unsteadiness was not just a function of the Strouhal number but also a function of pressure deviations from the mean pressure. Newton devised a pressure amplitude weighting factor, Π_{PA}, which could be used as an estimate for the level of mass storage in a given system, accounting for the inertial effects that drive the filling-and-emptying behaviour of that system. Equation 7.5 shows that the pressure amplitude weighting factor, Π_{PA}, is a function of the pressure range, ΔP_{in} and mean pressure, P_{ref}, and ratio of heat capacities, γ.

Newton developed a new parameter, Ω, to combine the Strouhal number with the pressure amplitude weighting factor. Therefore, if the Ω number is kept the same, then the level of unsteadiness as well as inertial effects are similar between the two systems. An assessment

of the Ω numbers has been conducted in order to calculate the level of unsteadiness in this system.

$$\frac{2\Delta P_{in}}{\gamma P_{ref}} St = \Pi_{PA} St = \Omega \tag{2.12}$$

$$St \Pi_{PA} = \Omega \tag{2.13}$$

2.2.4 Flow Phenomena

The flow phenomena in pulsating conditions has been of interest to researchers as well. Tomita et al.'s [62] conducted a computational study on a centrifugal compressor exposed to pulsating backpressure. The reverse flow streamwise velocity was studied for different instantaneous flow rates. Figure 2.18 shows the findings. The velocity contours were plotted for each unsteady time at points A to D. There is a development and reduction of the reverse flow at the impeller inlet. At Point C, where there is minimum flow rate, the impeller is found to fully stall, and there are high reverse flow vectors. When the flow rate increases again, the reverse flow velocity vectors start to reduce.

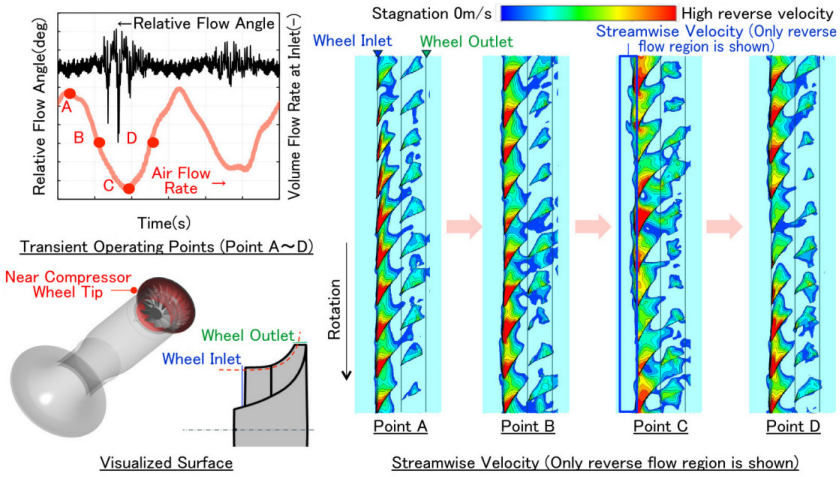
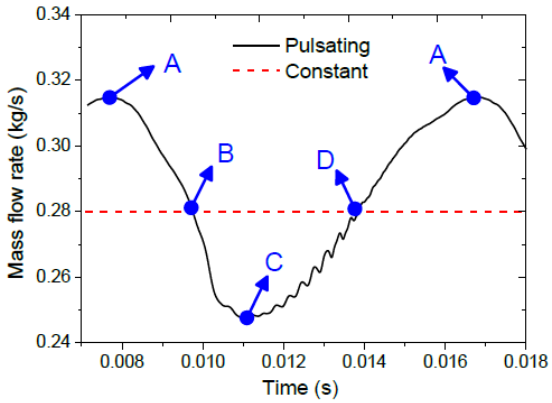


Fig. 2.18 Streamwise velocity vectors showing the reverse flow at the impeller wheel inlet and outlet positions for four different instantaneous mass flow rates (A - D) [Figure from Tomita et al. [62]].

Shu et al. [63] studied the evolution of the flow structure in the impeller at pulsating back pressure to further assess the improvement at surge. The flow structures were also found to vary instantaneously in time. Figure 2.19 shows the mass flow rate variation during one pulse.



(a) Four investigated points in a period

(a) Mass flow rate evolution during a pulse

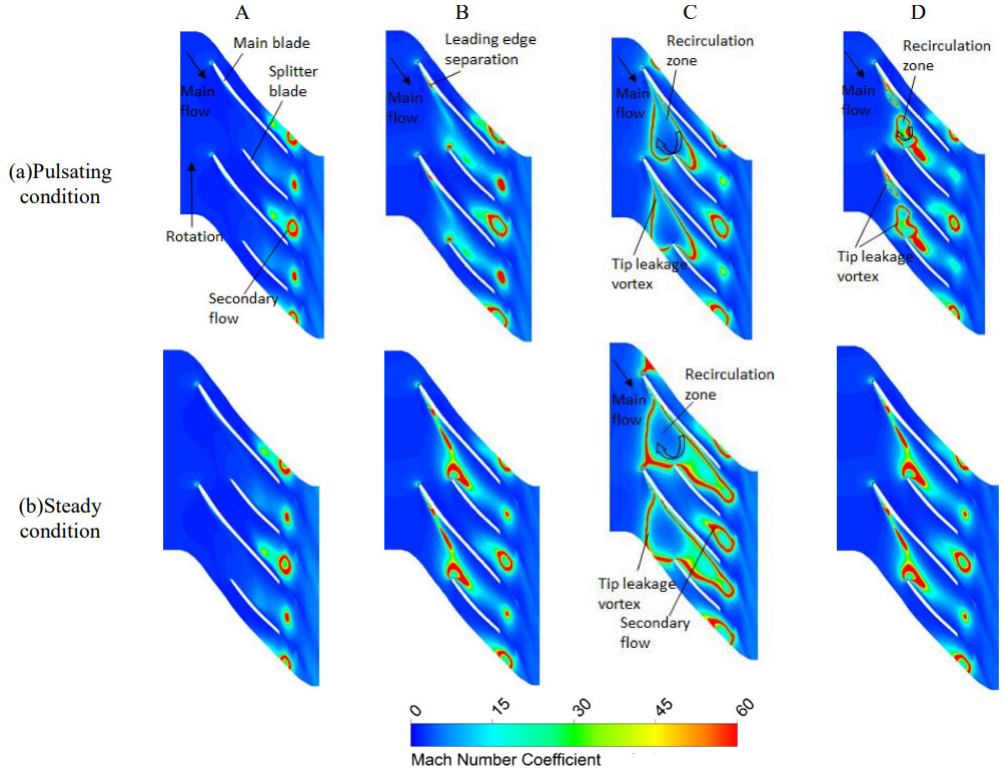


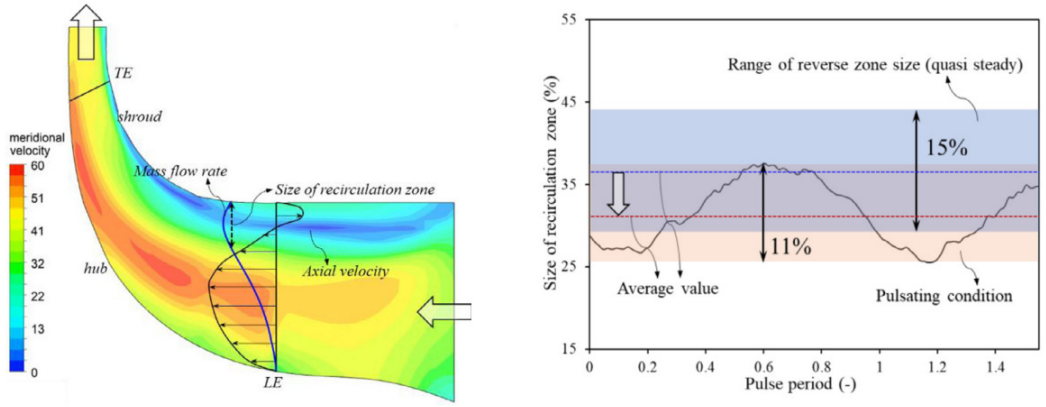
Figure 8. Mach number coefficient between pulsating and quasi-steady conditions at 95% blade height

(b) Impeller steady and pulsating entropy generation and secondary flow vortex formation

Fig. 2.19 Unsteady response of an impeller obtained through computational simulation of a compressor under pulsation [Figure from Shu et al. [63]].

Shu investigated how the flow varies at the different distinct points A, B, C and D for an impeller channel, as shown in Figure 2.19b, the flow structure at D is distinctly different to that at B, even though the mass flow rate in these points is the same. This is different to the comparative steady case, where the flow structures are similar if the mass flow rate is similar (points B and D, steady case) [63]. This was due to the aforementioned hysteresis effect of the compressor. At point C, secondary flow and tip vortex formation, normally seen at constant back pressure, was also not observed and it could be the main reason for the delay in instability of pulsating cases [**?**]. Shu et al. describe that this behaviour is due to dynamic stall rather than static stall seen in the steady flow conditions. In dynamic stall, the stall condition dissipates when the pressure pulse drops and there is an improvement in surge margin.

Yang et al. [64] found the entropy generation and secondary flow vortex formation at the impeller were reduced in pulsating cases compared to steady cases. There was a clear reduction in the size of the recirculation zone, see Figure 2.20. The blue box represents the recirculation zone size in quasi-steady conditions and it was found to be 15%. In pulsation, this recirculation zone was reduced to 11%. This was found to be due to the lagging flow field effect in pulsating flow conditions.



(a)Definition of recirculation zone size (b) Size of recirculation zone

Fig. 2.20 Simulation result of a single passage showing the size of the recirculation zone in pulsating conditions is lower than quasi steady conditions [Figure from Yang et al. [64]].

Additionally Tomita et al. [62] also conducted an analysis on the centrifugal compressor using ANSYS CFX with a SST-kw turbulence model. It was found that when the pressure pulsation was added, the inertial flow associated with the increase or decrease of flowrate suppressed the reverse flow associated surge. A study of the velocity fluctuations at the impeller inlet show the flow angle suddenly increased and decreased in accordance with the pressure fluctuation (and that these fluctuations were small at the diffuser). The flow angle at the impeller inlet indicated the development and reduction. The inlet velocity distribution cancelled out the effect of the reverse flow and the surge margin increased.

2.2.5 Efficiency in Pulsating Conditions

Only a limited number of studies have been performed on the impact of pulsation on compressor efficiency. Shu et al. [57] were able to obtain some insights on compressor efficiency when studying the performance of a centrifugal compressor experimentally. They found that at the peak efficiency, the performance dropped by around 3-7%. The experimental results are shown in Figure 2.21. At the different speeds, the peak efficiency decreased by 7%, 5% and 3% for 25, 30 and 35kRPM of the compressor. Other studies such as Marelli et al. [58] mention the deficit in performance.

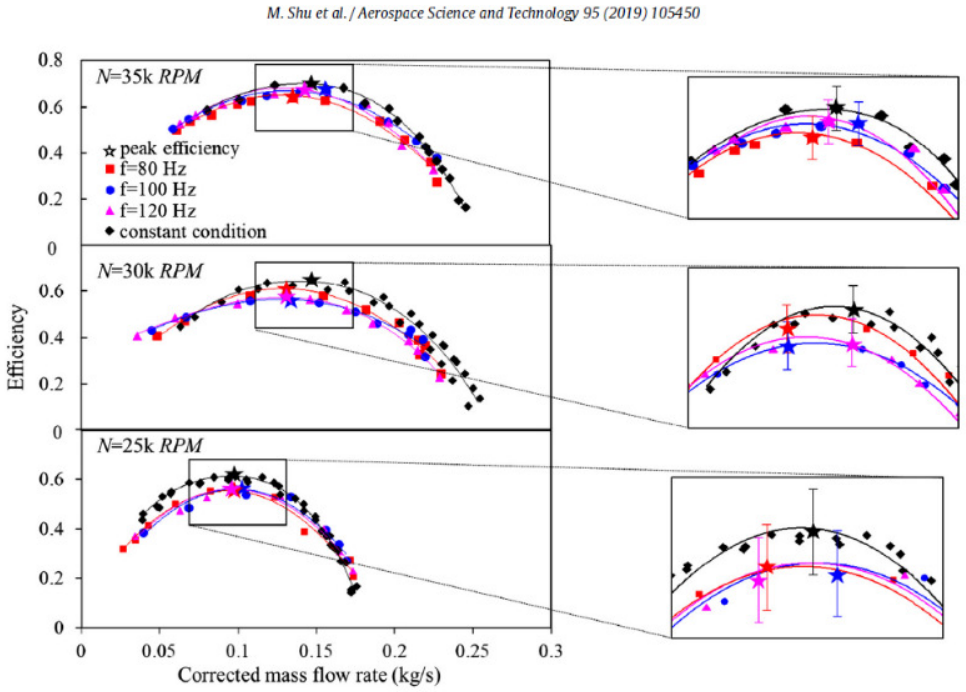


Fig. 2.21 Experimental results on efficiency reduction in pulsating conditions at peak efficiency and at different pulse frequencies (25k, 30k and 35k rpm) [Figure from Shu et al. [57]].

Most recently, a detailed computational study into centrifugal compressor efficiency was conducted by Yang et al. [64]. A 3-D full stage computational model that had been experimentally verified was used for the analysis. The impeller was found to be the leading source of loss, due to a change in the formation of secondary flows. Although the tip leakage vortex is alleviated under pulsating conditions, there is an increase in tip leakage at the splitter which results in greater wakes. The cycle average efficiency is found to be worse than the quasi-steady efficiency. Additionally, there is an additional pressure gradient along the circumferential direction due to the propagation of pressure pulsation in the volute. When there is a weaker circumferential distribution, there is a more even flow field in the impeller, and hence there is an improvement in the passage area downstream.

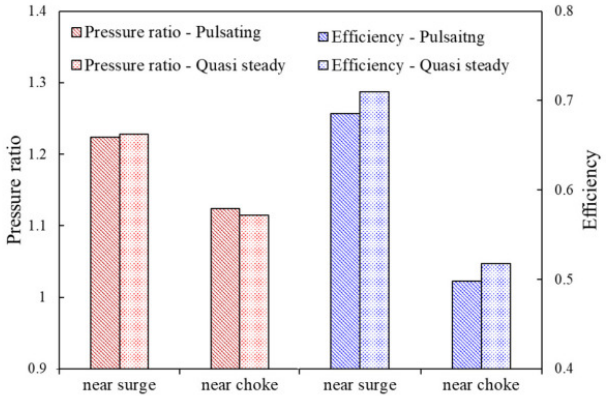
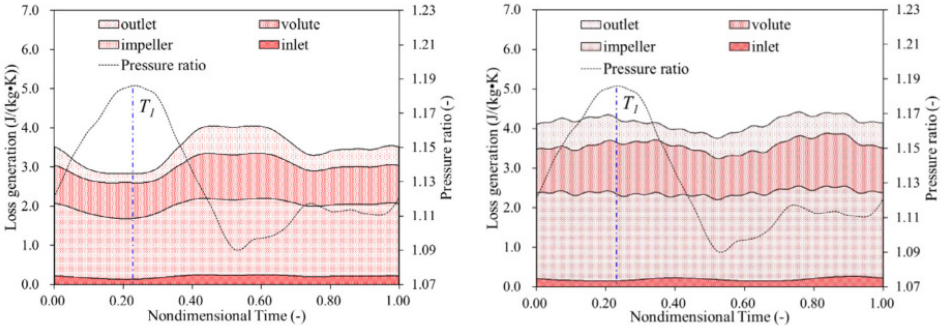


Fig. 5. Discrepancy of performance between pulsating and quasi-steady condition.



(a) Quasi-steady state (b) Pulsating backpressure condition

Fig. 2.22 Computational results showing efficiency in quasi-steady vs pulsating conditions (top) and loss distribution during a single pulse for quasi steady and pulsating conditions [Figure from Yang et al. [64]].

In summary, in pulsating conditions, there is a reduction in performance as the compressor is unable to reach the maximum or peak pressure as in steady conditions. The research so far has found that there is a change in the swallowing capacity of the compressor, and that there is an improvement in the surge limit, such that the compressor is able to sustain a more stable operation at mass flow rates lower than the surge point. Although there is a surge margin improvement, there is also a reduction in performance at critical operating points such as peak efficiency, which reduce the effectiveness of the turbocharger compressor when placed in engine conditions. There is a clear hysteresis effect that has been identified in the impeller inlet region as well as in other parts of the compressor.

2.3 Design Concepts in Literature

Impeller Inlet Concepts

As seen in the proceeding sections, the impeller inlet region is a key focus for compressor designers because at off-design conditions, such as low flow, the compressor suffers from inlet recirculation, stall, rotating stall or surge, all of which reduce the performance of the compressor in operation. As such, extending the lower limit of stable compressor operation is important as it has high commercial and research value. A variety of inlet designs have been developed to help increase the working limit of the compressors. This literature review provides an overview of some of the ideas that have been explored.

A common method to increase the operating range is to modify the compressor shroud with a casing treatment, otherwise known as a bleed slot. A schematic of a typical casing treatment is shown in figure 2.23. Casing treatments work by allowing some of the reverse flow to enter the bypass channel and re-enter through the inlet. This allows the bleed slot to help counteract the axial recirculation near the impeller blade tips.

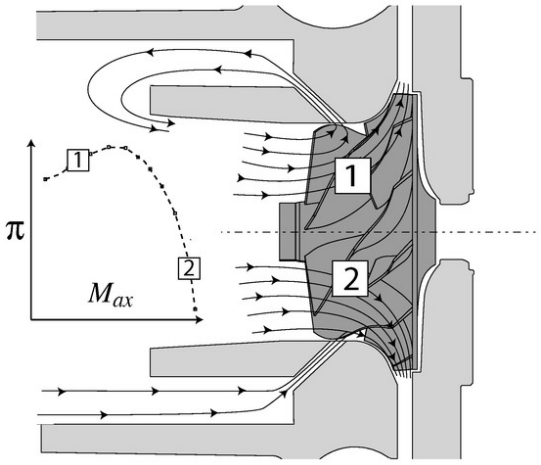


Fig. 2.23 Schematic of a casing treatment or bleed slot. The bleed slot is on the shroud surface. The flow pathway is illustrated for two operating points shown in the performance map. The performance map shows Pressure ratio, Π, on the y-axis and axial mass flow, M_{ax}, on the x-axis [Figure from Leichtfuß et al. [65]].

The cavity treatment concept has been developed by Barrera-Medrano & Martos [66]. The cavity treatment concept is a heart-shaped shroud cutout which was designed to collect the flow in the region of flow reversal; redirecting the flow back to the impeller in the inflow direction. The cavity treatment concept was researched in detail by Martos experimentally and computationally and it was found to show a high surge margin improvement but there was a deficit in performance. There was found to be an efficiency deficit. Martos then analysed four locations and shapes for the cavity concept using a RANS 3D full-stage

simulations and assessing the performance. Overall, it was found that stall propagation in the vicinity of the shroud was retarded by the cavity and that the presence of the cavity at the inlet delayed flow reversal, smoothing the incidence angle at the impeller blade loading edge. Of all the positions of the cavity, the 'Blade Mach' position was found to provide the best surge margin improvement. Figure 2.24 shows the four tested geometries and 6.1 shows the blade mach cavity in detail.

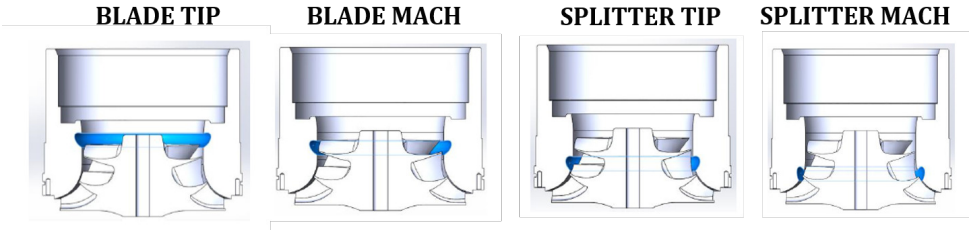


Fig. 2.24 Schematic and description of the different cavity treatment designs tested by Martos [Figure from Martos [66]].

In the experimental research conducted by Martos, the cavity positions were tested under different pulsating flow conditions. There was found to be an efficiency and performance deficit due to the cavity in pulsating conditions. The blade Mach position was found to have a 4% efficiency deterioration.

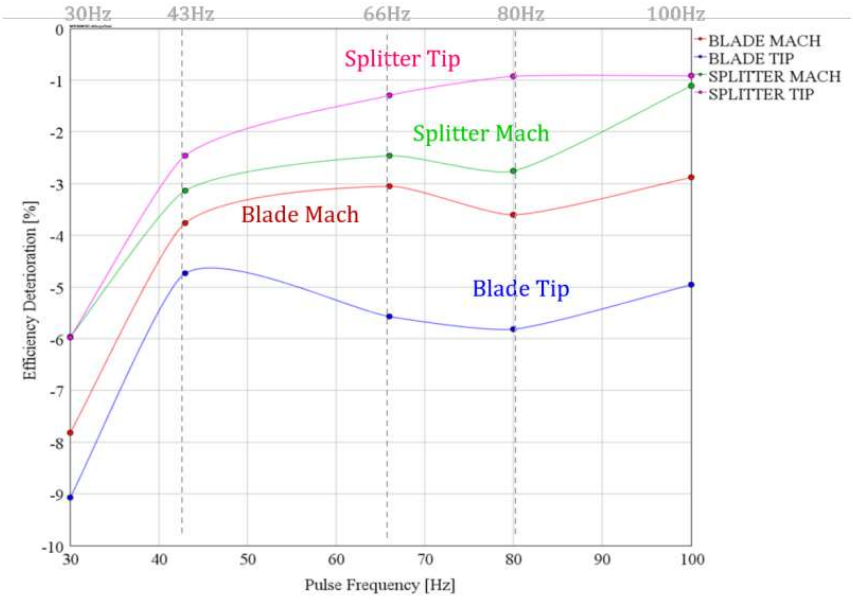


Fig. 2.25 Efficiency deficit seen in the cavity designs experimentally tested by Martos at different pulsating flow conditions [Figure from Martos [66]].

Volute Concepts

The volute is another key area for research; especially the volute tongue which was shown in Figure 2.9. When reviewing the off-design performance of the compressor, it was shown that the the tongue is a highly influential design feature as it affects the way the flow propagates and collects in the volute, and also has an influence on the stability of the impeller.

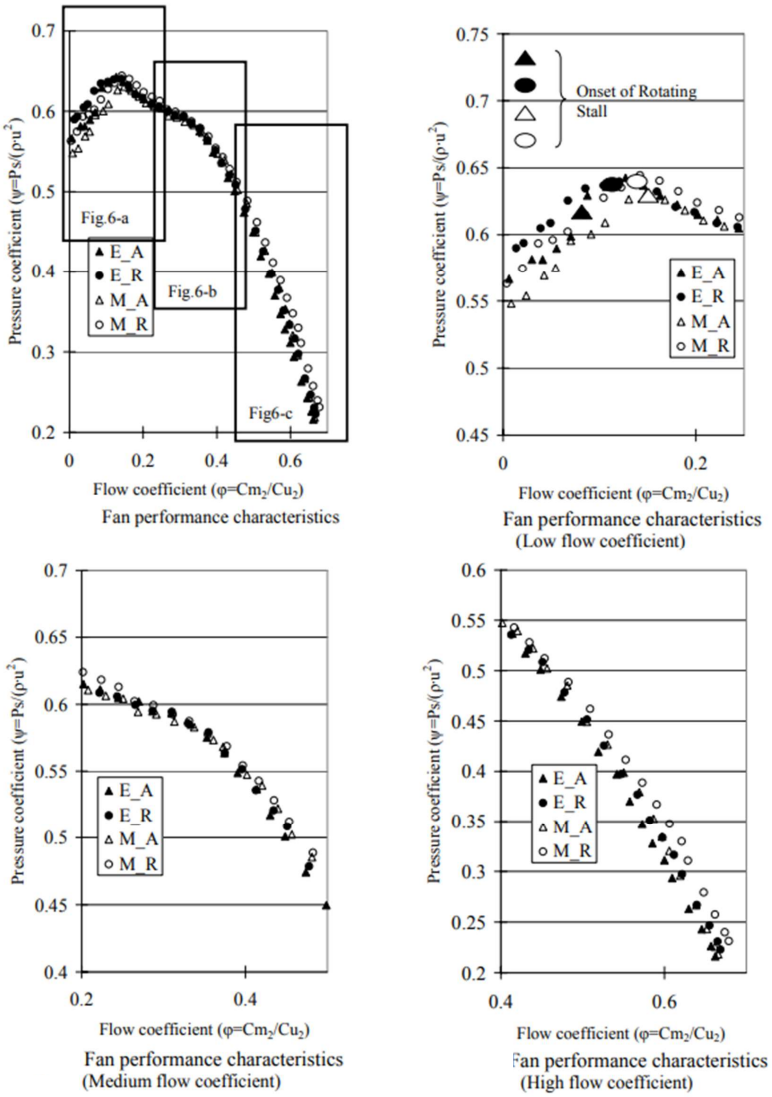


Fig. 2.26 Different experiments conducted on four different volute modifications by H. Okauchi et al. Volute. EA: standard volute, free vortex, ER; rounded tongue shape, MA; increased width of volute downstream of tongue, MR; combination of rounded tongue shape and increased width of tongue [Figure edited from Okauchi et al. [67]].

Okauchi et al. [67] studied the effect of the volute tongue for different types of centrifugal fans. The volute is normally designed assuming a free vortex flow path. Figure 2.26 shows the experimental results for reference. Okauchi compared the performance to a standard volute, labelled *EA*, designed with this procedure, to three other volutes. An experimental facility with measurements at different azimuth angles were tested. In the first modification, the tongue shape was more rounded, *ER*, next, the width of the volute downstream of the tongue was increased, *MA*. Lastly, a combination of the two effects was tested, *MR*. It was found that all three modifications improved the performance at moderate and high flow conditions, but had little affect on the flow stability at low flow conditions.

Xu and Muller studied the impact of different tongue geometries using computational simulations. The two main geometries that they tested had a very sharp tongue (no fillet), and a tongue with a round fillet radius. Figure 2.27 shows the geometry of the tested designs, and the velocity vectors at the intersection of the tongue. The CFD and experimental results show that the round tongue with a fillet of 0.3 has a better performance than a knife edge. Mohtar et al. [68] tested the effect of grooves, pinching and sharpness of the volute tongue on the compressor efficiency and performance for a high-speed compressor (greater than 90k rpm). The result for two tongue fillets, TG1 and TG2, is shown in Figure 2.28. The tongue fillet *TG1*, has a slightly higher efficiency than the fillet *TG2*.

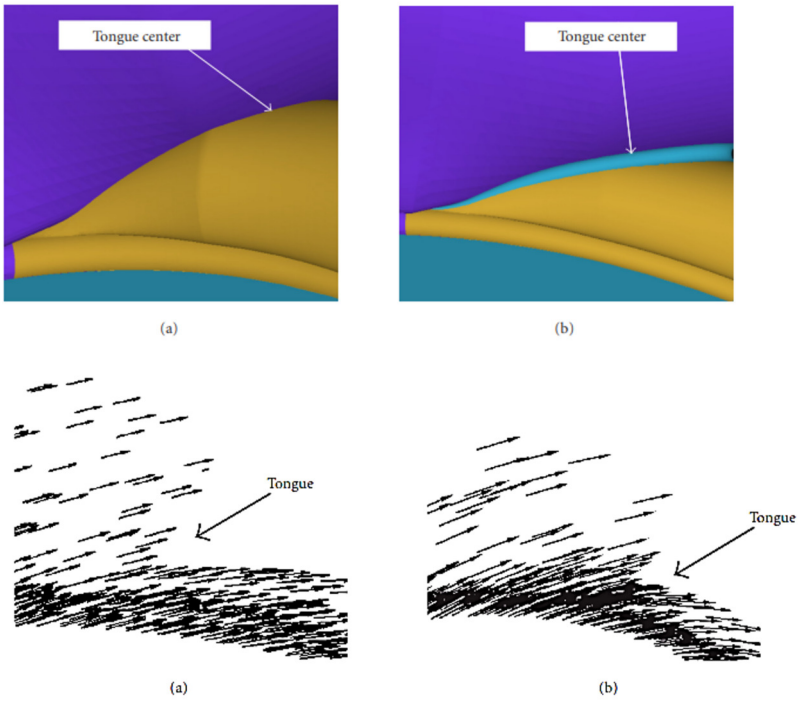


Fig. 2.27 Schematic showing two tongue shapes tested with different leading edges. (a) r/b = 0 (knife-edge). (b) r/b = 0.3. The vectors near the intersection between the mid-planes of the diffuser and tongue show the flow structure. The leading edge with a fillet radius of 0.3 (b) has a better performance than the knife edge [Figure from Xu & Muller [69]].

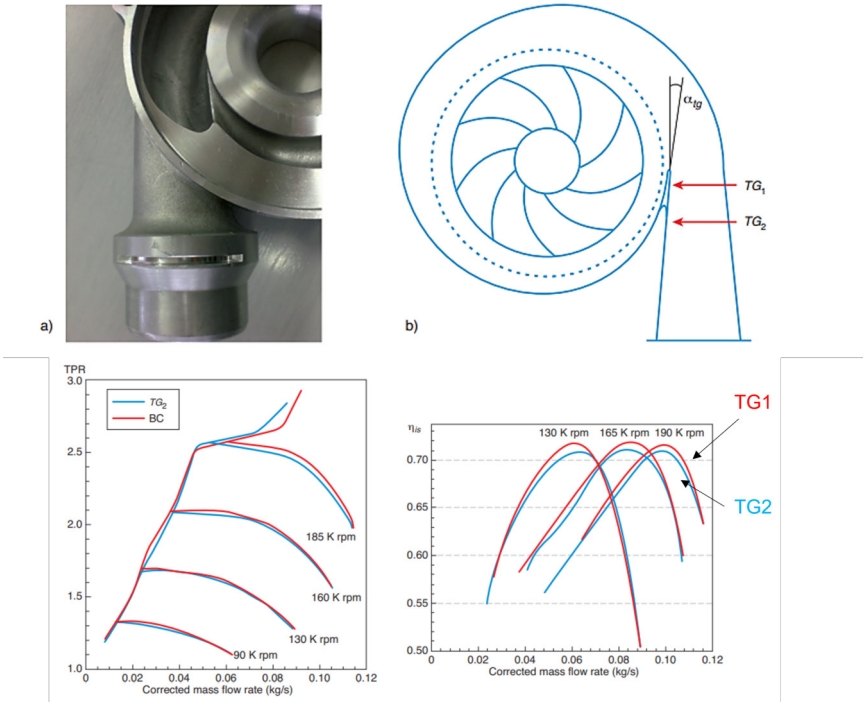


Fig. 2.28 Pressure ratio and efficiency results from Mohtar et al. for two different tongue fillet depths. The efficiency of *TG1* (sharper fillet) is found to be slightly higher than fillet *TG2* for all the speed lines tested [Figure from Mohtar et al.[68]].

By studying the design concepts for impeller and tongue modifications, insight has been drawn on the type of design concepts that have worked in the past and how they can be used for the development of high efficiency compressor designs under pulsating flow, which is one of the main objectives from this research.

2.4 Measurement Techniques

The most common guideline for experimental measurements on centrifugal compressors is based on the test code laid out by ASME PTC 10 [70]. ASME PTC 10 lays out the temperature measurement guidelines as well. It states that thermal convection & radiation needs to be minimised and negligible in comparison to the conductance between the sensor and the medium being measured, and that insulation is necessary.Temperature measurements need to extend a sufficient distance into the fluid stream and the instrumentation is required to be calibrated. The modifications to the facility are based on ASME PTC 10 guidelines so that efficiency measurements can be conducted.

Instantaneous temperature measurements are limited not only by the response time of the probe, but also the data acquisition system. There are only a few examples of instantaneous

temperature measurements in literature. A fast response total temperature probe was designed by Arenz et al. [71] but this was the only study of this kind.

Instantaneous flow measurements are difficult to conduct accurately. Springer's handbook of Experimental Fluid Mechanics [72] has a subsection on flow measurement techniques in turbomachinery, which details a number of different techniques that have been used in research and literature. Most often, Constant Temperature Anemometry (CTA) is used. In CTA measurements, the flow conditions are detected with a Hot-wire or film probe placed in stream of the moving fluid. Hotwire films are more rigid than hotwire probes but more expensive to replace. Other flow measurements are doppler velocimetry (LDV), particle image velocimetry (PIV) or specialised pressure probes such as 3/4/5 hole probes can also be used but these tools are often expensive and require additional installations.

Torque Measurements

One of the research objectives is to evaluate compressor performance is by assessment of torque. Torque measurements on the compressor facility would significantly improve the experimental capabilities. Torque measurements can be categorised as one of two types: direct or indirect measurements. Direct measurements are often in line torque transducers that are pre-calibrated by manufacturers [73]. Indirect methods use related parameters to assess torque. An early research study on automotive torque measurements was published by Fleming [74], who summarised seven different methods to study torque and their advantages and disadvantages. These were: strain gauge torque meters, torsional twist torque meter, magnetostrictive sensors, load-washers, load cells, crankshaft positional sensors and automatic transmission slip speed measurements. Of these, load-washers, crankshafts and load-cells are indirect and low accuracy methods, whereas strain gauge torque meters and torsional twist torque meters were found to be more common. Both strain gauge torque meters and torsional twist torque meters are indirect torque measurements.

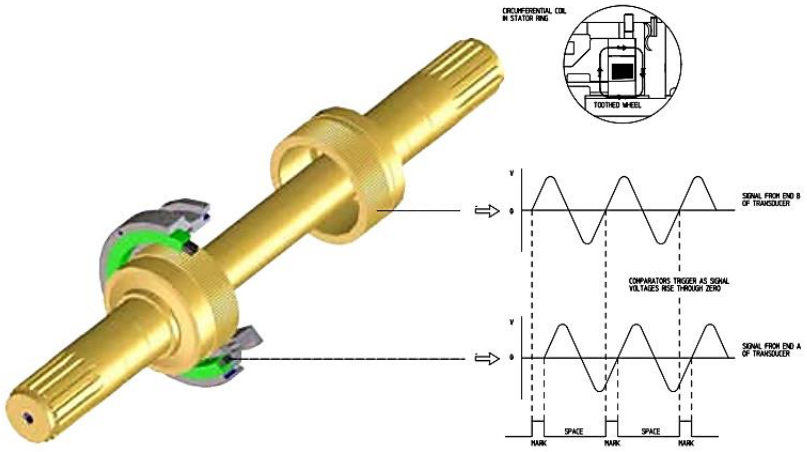


Fig. 2.29 Example of a phase shift torquemeter and the corresponding signal between the two measurement locations [Figure from Torquemeters [75]].

Figure 2.29 shows an example of torsional twist measurements. For torsional twist torquemeters, when a shaft is loaded in torsion, a torque, which is a moment applied about the axis of the shaft, generates shear stresses and shear strains, resulting in a 'twist. Torque is detected by relating the angular twist of the shaft to the applied torque. Encoders are placed on either ends of the drive shaft. Optical sensors pick up the signal from the encoders. The time delay in the two signals is used to detect a variation in torque. Shaft twist is directly proportional to applied torque. In this way, it is possible to detect torque in fast dynamic conditions such as under rotating unsteady applications. Whilst the angular twist of a shaft of known geometry is relatively easy to calculate, variations in tolerance and material properties can be removed by calibrating against a reference device, which also provides a route to measurement uncertainty and traceability.

Due to their compactness and size, torsional twist torque meters can be relatively simple to install. Some early principles and designs were developed by Milligen et al [76] Toothed gears, axially and radially constrained, were placed on a long shaft. By placing, magnetic coils in the vicinity of a toothed gear, it was possible to generate a current in the coil when the tooth is passed. The time delay between the two current signals was then used to relate the twist of the shaft to the torque. Other researchers such as Ward [77] and Ohigashi [78] have also created torsional twist torque meters for such applications.

2.5 Closing the Gaps in Knowledge

The contributions of this research address the key gaps in knowledge identified in literature. The detailed experimental and computational analysis conducted in this work increases the understanding of pulsating flow behaviour on compressor performance, and particularly aids the understanding of compressor behaviour at different operating points. The experimental and computational assessments of performance in the high mass flow region, which has not been studied in detail up to now, leads to valuable insights as it is found to be a key area for efficiency deficits in pulsating flow.

A combination of approaches is applied in this work to further the knowledge in this field. In particular, the use of an instrumented volute allows for detailed pressure measurements at different locations within the compressor. Computational models with pulsating boundary conditions for different operating points provide key insight, such as flow behaviour in critical regions and an assessment of losses within the compressor. In addition, a bespoke torque meter to study instantaneous compressor performance leads to a unique torque meter design for turbomachinary applications. Furthermore, the development of new designs to improve performance under pulsating flow addresses a key industrial demand. The experimental results from the initial prototypes are promising, leading to optimised designs in the future that will improve the overall turbocharger efficiency under engine conditions.

In summary, the gap in knowledge is identified to be in four key areas identified below.

Limited Research in Pulsating Flow Efficiency

The findings in this section show two research studies that have looked deeply into compressor efficiency under pulsating conditions ([57], [64]). This is partially due to the difficulties in estimating efficiency in pulsating conditions and there is clearly much more work required in estimating efficiency and losses under pulsating flow. Additionally, the second study provided a computational estimate of loss at the impeller but since computational environments are ideal, further assessment of efficiency are required to support the findings. In this thesis, compressor efficiency results are provided for experimental and computational research outcomes in each of the chapters.

Limited Research on Performance at Different Operating Points

Whilst a number of researchers have already looked at pulsating flow performance, this research is primarily focused on surge. Many studies have focused on the near surge operating point as pulsating conditions have found to improve the surge margin. Other operating points have not been studied in detail as yet and not enough data is available on the performance at other operating conditions. Additionally, it is not clear to see how the filling and emptying effect is changing the behaviour of the compressor - with respect to mass accumulation. Detailed experimental findings could help with this. Chapters 4 and 5 provide the assessment of compressor performance at different operating points. It is seen that the large flow regions have the greatest drop in efficiency from pulsating conditions.

Limited designs for improved performance under pulsating flow

The design concepts explored in literature have not yet been tailored towards pulsating flow. More research and investigation on the flow structures inside the compressor in pulsating conditions, will lead to new design modifications for the compressor, such as changes in geometry or material that will aid to minimise losses. Chapter 6 details two modifications to compressor designs tailored to improve compressor efficiency under pulsating flow. Efficiency improvements are seen in both modifications, with a 2% improvement seen in the sharp tongue modification.

Limited Research on Instantaneous Efficiency

Due to the limitations in sensor capabilities, it is difficult to estimate experimental efficiency instantaneously. Most experimental data is presented as a signal average. Additionally, there have not been enough detailed experimental assessments and the behaviour near the compressor tongue is unknown. Torque measurements of the compressor could help increase the understanding of instantaneous efficiency. The development of a bespoke torque meter shown in Chapter 7 details an experimental methodology for assessing compressor performance instantaneously and presents initial findings.

Chapter 3

Experimental Facility and Methods

The experimental research is conducted using a compressor testing facility. The test facility that is used was originally developed by Barrera-Medrano [23] for the assessment and characterisation of surge behaviour under pulsating conditions. The current research aims to explore the compressor performance in further detail. To do so, the original compressor experimental facility has been upgraded to enhance the accuracy and robustness of the measurement and data acquisition system.

This chapter details the developments to this experimental facility and the corresponding experimental method, and is divided into three sections. In the first section, the original experimental facility and corresponding modifications are outlined, including the development of new instrumentation. In the second section, the analytical method and data processing techniques are detailed. The last section discusses the results from the updated facility, such as the experimental reliability and uncertainty.

3.1 Experimental Facility

3.1.1 Original Experimental Facility

The original compressor test facility was initially developed for research conducted by Barrera-Medrano [23] to test the behaviour of the compressor system and study the changes to the onset of surge under pulsating flow. The facility was designed to have a number of key components such as a pulse generator that could create pulsating flow conditions and an adjustable plenum that could vary different compressor system sizes. A schematic of the original testing facility is shown in Figure 3.1. The variable plenum and pulse generator

is also shown. The plenum height has been fixed at the minimum depth position for all experiments conducted, as the plenum is not required for this research.

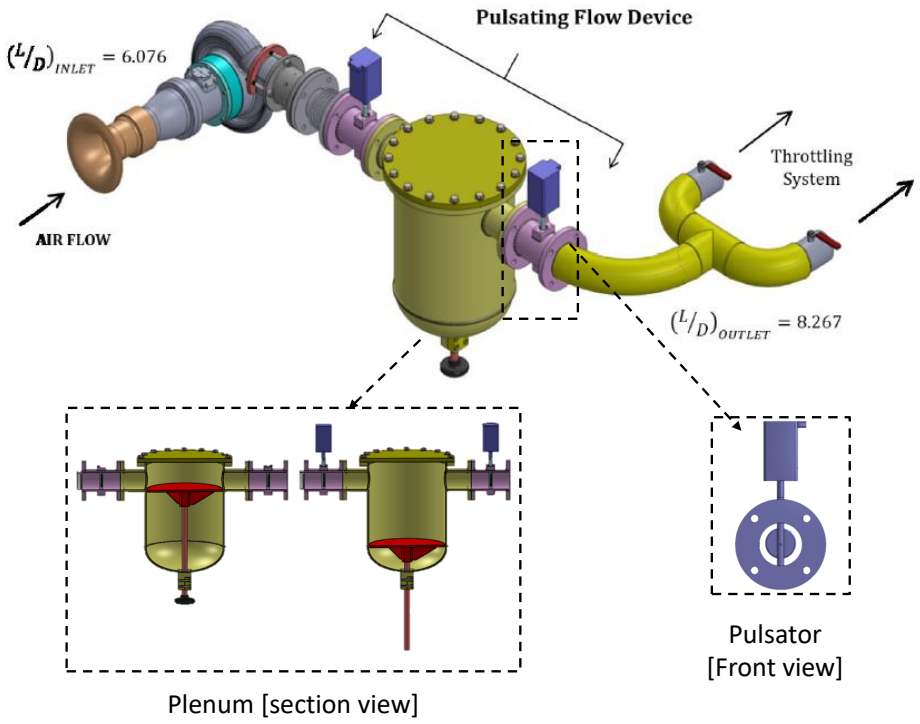


Fig. 3.1 Original compressor test facility built for surge testing of a centrifugal compressor under pulsating conditions. A section view of the plenum is detailed showing the maximum and minimum plenum volumes. A front view of the pulsator is shown with the pulsating discs [Figure adapted from Barrera-Medrano [23]].

The compressor is driven with a 110kW ABB electric motor and a 27:1 step-up double epicyclic gearbox. It is directly mounted onto a bearing housing. There are two oil systems that are crucial to the safe operation of the compressor rig: these provide cooling and lubrication to the gearbox and bearing housing respectively. The compressor operates in an open system and the working fluid is ambient air. The flow rate is controlled by a throttling valve system, which is composed of a 3" butterfly valve. The compressor inlet draws air from the test lab and the compressed air is dumped back into the lab. The lab is ventilated to allow for ambient conditions to remain constant, however, there are still variations in ambient conditions, so the lab ambient temperature and pressure are recorded for every test. The mass flow rate through the compressor system is controlled by opening and closing the butterfly valve at the exit of the piping system.

It is worth noting that most compressor rigs use a turbines to drive the system in what is commonly known as an engine gas-stand. The use of a motor drive in this test facility was deliberate: The isolation of the compressor from the turbine allows full control on its

operation. It also eliminates the uncertainties that arise from speed variations and loading unbalances, which are commonly encountered when a compressor is driven by a turbine.

Pulse generator

The pulsating flow effect is generated by a rotary valve that is placed downstream of the compressor outlet and simulates the opening and closing of the engine intake manifold by the means of a disc that blocks a proportion of the pipe as it rotates, see Figure 3.1. By doing so, it results in a sinusoidal build-up and release of backpressure, which will be referred to as a pressure pulse. This pressure pulse profile has been previously compared with the true pulse from the engine and it is considered representative of the engine environment. Figure 3.2 shows the comparison between these two measurements. Although it is difficult to obtain true likeness, the magnitude and frequency of the pressure profile generated by the rotary valve are similar to the engine pulse and therefore, the rotary valve system is deemed suitable for use in pulsating flow testing.

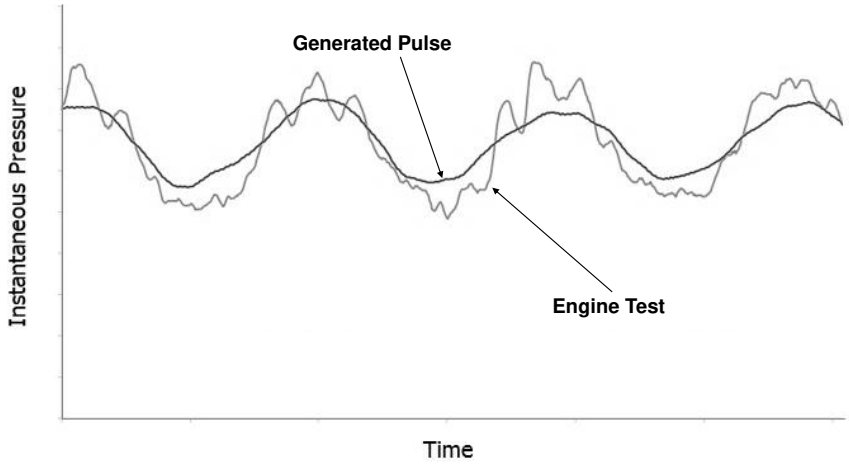


Fig. 3.2 Comparison of 66.67Hz pulse generated by the pulsating device to a pressure pulse recorded in the engine system running at 2000rpm. This is measured data - the measurement is made at a set distance from compressor outlet in both measurements. A clear matching is seen. [Figure adapted from Barrera-Medrano [23]].

The original test facility has the following sensors: 2 Resistance Temperature Detectors (RTDs) on each measurement plane, 1 pressure transducer for instant pressure reading and 4 pressure taping to get average static flow measurements. Mass flow is measured with a hot-wire CTA probe at the inlet of the compressor. The original measurement plane is 105mm before the inlet and 88mm after the outlet respectively. The quantity and location of instrumentation is shown in Figure 3.3 and further details are provided in Table 3.1.

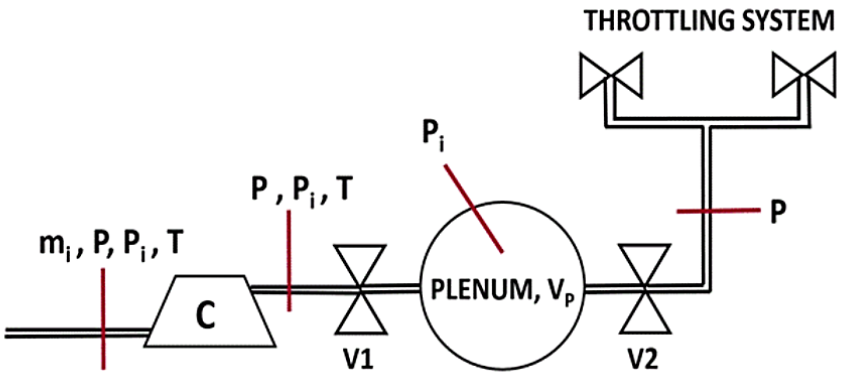


Fig. 3.3 The locations and measurements of the original sensors on the compressor rig facility. m_i - instantaneous velocity probe, P - static pressure probe, P_i instantaneous pressure probe, T - temperature probe, V_1 and V_2 - valve positions [Figure from Barrera-Medrano [23]].

Table 3.1 Sensors on original facility at the time of Barrera-Medrano's research [Details from Barrera-Medrano [23]]

Sensor	Details	Range	Uncertainty
Ambient pressure	PTB110 Vaisala type barometer	80kPa-110kPa	± 30Pa
Ambient temperature	K-Type thermocouple	-270 to +2,320° C	± 2.2° C
Static pressure	Scanivalve DSA3016/8D in rack enclosure DSAENCL4000	0-7 bar (gauge)	± 0.05% of full scale, ± 354Pa
Static temperature	Resistance Temperature Detectors (RTDs)	-240 to +650° C	± 0.15° C
Rotational speed	Magnetic speed sensor	8 pulses per revolution	± 1rpm at running speed of 40krpm
Mass flow sensor	Platinum plated tungsten 10 micron wire, CTA (hotwire) 51.7 mm from lower wall	0-10V	
Instantaneous pressure	Omega PX321B	0-7 bar	± 0.025% of full scale, ± 173Pa

3.1.2 Modifications to Experimental Facility

The baseline compressor investigated within this research is of the same size and dimensions to the one tested in previous research projects, therefore, the majority of the test facility has largely remained the same. Readers interested in the design and development of the rest of the test facility are recommended to read Barrera-Medrano [23], as this section details the key modifications from the original facility for the purposes of this investigation.

Required upgrades & improvements

The original facility was evaluated thoroughly to identify the areas of improvement. The evaluation was focused on increasing the key capabilities of the facility as well as identifying areas of improvement, particularly with respect to accurate efficiency measurements. After the evaluation was completed, a number of changes were identified and implemented. These relate to the placement of instrumentation, location of measurement planes, insulation and the development of new sensors.

Modifications for accurate efficiency measurements

Static temperature measurements

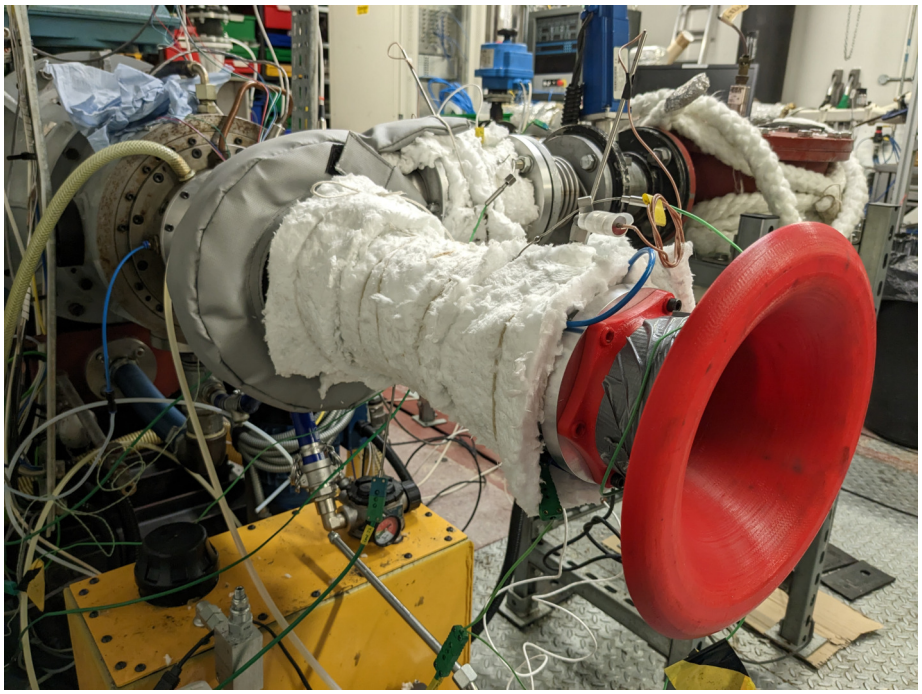
There are generally three common temperature measurement devices; thermistors, resistance temperature detectors (RTDs) and thermocouples. All of the above measurement types have similarities and differences with respect to their capabilities and limitations [79]. The original instrumentation set-up uses RTDs as they are widely known to have a good, stable response. However, RTDs generally also have larger probe diameters and therefore a higher heat capacity. On the other hand, thermocouples can be made with much smaller probe diameters and thus can respond to the changing flow conditions faster due to their smaller size. Because of this feature, the RTDs are replaced with thermocouples so that they can respond to the rapid changes under pulsating conditions. The smaller the size of the bead, the faster the theoretical response. The smallest thermocouples tested had a 0.8mm bead size [Product code: *5SC-TT-KI-40-1M* from Omega [80]]. Unfortunately, when using these thermocouples in the experimental facility, it was found that because of their very small diameter, they were bending in the flow stream and caused the measurement location to change between measurements. Therefore, despite the slightly higher heat capacity of a larger bead, a 1.5mm diameter beaded K-type thermocouple is used, that has

a stiff metallic wire so it does not deviate from the measurement plane ensuring robustness and repeatability on the results throughout the experimental campaign.

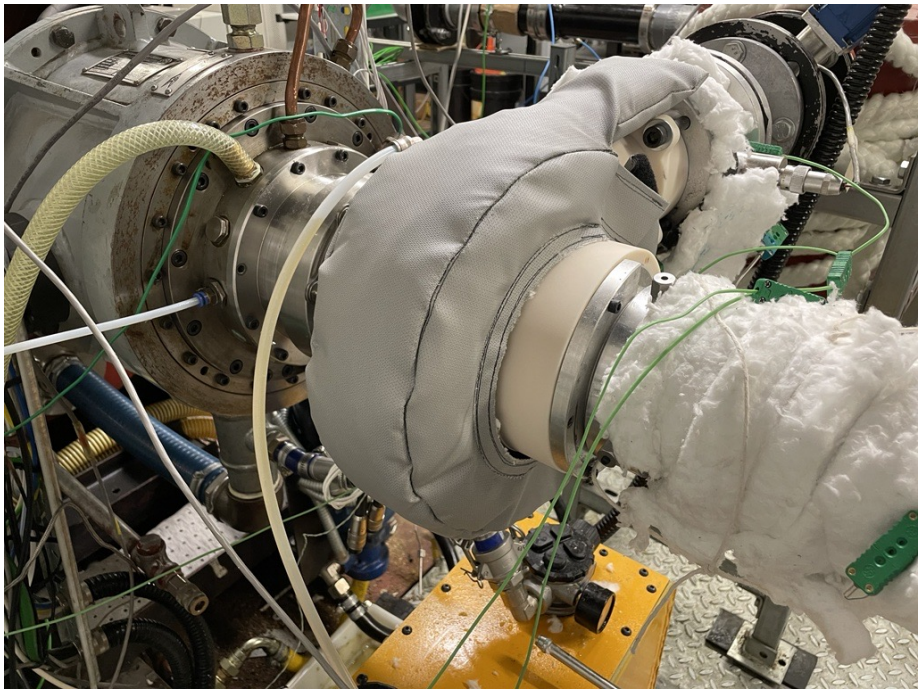
Two thermocouples are placed at the inlet and outlet measurement planes and an average reading of the plane is taken. The temperature recorded by the thermocouple is a function of the measured flow temperature, the static temperature of the fluid and an additional factor, known as the recovery factor. This is because even if the experiment aim is to measure static temperature, the measurement probe causes the flow to stagnate around it, resulting in an increase in temperature around the probe. To account for this a recovery factor is often used to obtain static temperature from the measured temperature. The choice of recovery factor depends on the average flow stream velocities. It has been found that for the range of temperatures used in this test, a recovery factor, r, of 0.97 can be used, as stated by the international standardised code for turbo compressor performance [81].

Thermal insulation

As mentioned above, it is important to minimise heat losses to the environment. To do so, thermal insulation has been placed over the experimental set-up, covering the length of pipework between the two measurement planes. The thermal insulation is intended to limit the heat transfer through the walls and allows the system to operate close to adiabatic conditions. Although it does not limit heat transfer completely, it minimises the heat loss and allows for better accuracy on the estimation of efficiency. A figure of the experimental facility with the insulation is shown in the figure 3.4a. The insulation is a super wool fibre thermal insulating sheet with a 25mm thickness and thermal conductivity of 0.69W/mK [82]. Although the installation process over the pipes is possible with this sheet, it is difficult to place the sheet over the compressor volute due to the complex geometry. The difficulty in installation makes the insulation process time consuming and inconsistent. To ensure that the heat transfer is uniformly minimised throughout the compressor, a bespoke sleeve has been manufactured for insulation over the volute. The bespoke sleeve allows for a snug fitting around all the exposed areas around the volute, see Figure 3.4b.



(a) Fully insulated facility with bespoke insulation sleeve and the thermal insulation SuperWool fibre sheets for the pipework.



(b) Close up view of bespoke insulation sleeve installed on the compressor.

Fig. 3.4 Photographs of thermal insulation placed on the compressor test facility

Thermal equilibrium

Additional to the insulation, it is necessary to reach thermal equilibrium during the experimental tests as the compressor test system is a large body of mass, and it takes time for the temperature to settle between runs. These heat transfer characteristics are very important as they affect the instrumentation and the measurement readings. A hot-running-rig and a cold-running-rig have different thermal parameters which affect the measurements of pressure ratio and efficiency of the compressor. Temperatures at three key locations are monitored for thermal equilibrium: bearing housing, inlet plane and outlet plane. As the bearing housing face is also the hub-face of the diffuser, and is relatively dense in comparison to the volute, it acts as a heat sink. It is important that the temperature at the bearing housing stabilises and heat transfer between the volute surface and bearing housing is minimised. Once it stabilises, it also takes longer for the heat to leave the dense material and hence, it allows for the subsequent tests to reach equilibrium faster. To account for thermal equilibrium, sensors are allowed to stabilise before readings are recorded. This is assessed by studying the time-history of the reading, which is displayed live during the test process. It is assumed that the temperature has stabilised when the reading does not change in 30 seconds, and the live display of the temperature change is flat (indicating no change).

Intake air parameters

The intake air temperature, pressure and humidity and cooling water temperature affects the performance of the centrifugal compressor [83]. If the inlet temperature is higher on a given day, compared to the previous day, the calculated efficiency of the compressor changes because the intake air conditions affects the performance. A lower intake air temperature is beneficial and raises the performance curve, increases the flow capacity and also increases the power consumption. The opposite happens if intake air temperatures increase. A decrease in the air inlet pressure decreases the density of the air and consequently reduces the performance. To account for these effects, the pressure ratio and efficiency is corrected, so that the inlet density effects are taken into consideration. However, it is also important to keep the operating facility at the same temperature throughout. To do this, the lab pressure and temperature is monitored and it is ensured that the tests are conducted in similar intake air conditions.

Pressure transducer offsets for thermal drift

Pressure transducers have a temperature dependency, and the readings vary depending on the ambient temperature conditions. This thermal dependency is unavoidable and often an inherent factor of the design of the transducer. Therefore, all pressure transducers have a thermal residence time. A common practice when using pressure transducers is to offset the transducer based on the deviation from ambient conditions at 'hot' conditions. This accounts for any thermal pressure inside the transducer which causes it to read higher than ambient pressure, even when the transducer is exposed to ambient conditions. Offsetting then resets the pressure to ambient conditions. Differences in offsets should not theoretically affect the results however, in practice, the particular transducers used for the test have been found to vary between runs, even if no other condition has been modified. This affects the reliability and repeatability of the results. For the purposes of this thesis, and because there are multiple comparisons that are conducted within the scope of this work, a fixed offset has been applied to all measurements so that they can be compared. The offset is based on the test conditions achieved during the testing, as this ensures that the pressure readings are as close to the true readings as possible.

Modifications to measurement plane location

In the original installation, the inlet pipe was designed with a measurement plane at around one diameter (1D) away from the impeller inlet. This resulted in a limitation to measurements under deep surge as the flow close to surge was disrupted, resulting in inaccurate mass flow rate and temperature readings. Upon investigation, it was found that flow recirculation effects were affecting the measurements in this region. Flow recirculation was introduced in the literature review as the flow reversal that takes place at the shroud as high back pressure gradients can reverse the flow entering the impeller. This recirculating flow is hotter than the incoming flow as it has gone through some compression the system before it turns backwards. When a temperature sensor was placed in the original measurement plane, high recirculation temperatures was measured, indicating that this measurement plane was too close to the impeller inlet.

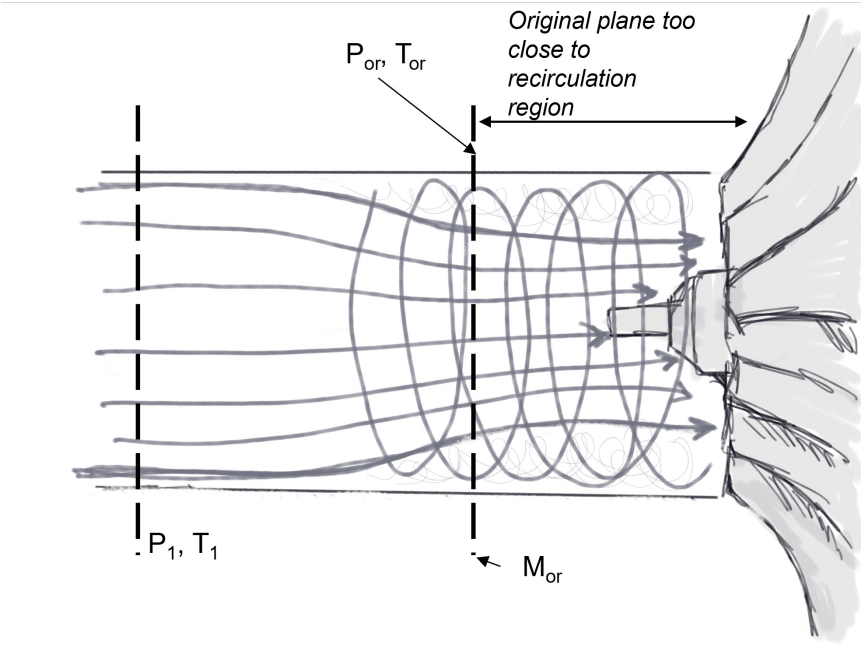


Fig. 3.5 Schematic showing the recirculation region of the compressor rig and closeness of the original sensors to the recirculation region. The original position was too close to the recirculation region.

Figure 3.5 shows a schematic of the changing flow field in the vicinity of the impeller inlet when there is flow recirculation. The schematic shows that when flow is reversed, some of the flow area is blocked when the reverse flow affects the near-wall regions of the pipe, the effective flow area is thus reduced, consequently the velocity at the centre of the pipe increases. When a flow sensor for mass flow rate measurements is placed in the centre of the flow field, it picks up the high velocity. If this velocity were to be used to estimate the mass flow rate, it would predict a mass flow rate that is higher than the actual flow

rate. To overcome this limitation, the inlet measurement plane needs to be moved further upstream to avoid the recirculation inlet region.

It is worth stating that the choice of measurement position depends on the measurement data of interest. The high-velocity fluctuations near the impeller inlet provide insight into the pulsating and recirculating effects near surge, and can be used to characterise the pulsation at the impeller inlet. Especially since a real engine system would not have long inlet pipes. Therefore, the measurement location was retained but not used for this testing. Due to the number of tests and operating points studied in this research, the assessment of mass flow rate was more important and hence, the mass flow rate sensor was placed away from the impeller inlet.

Modifications to the inlet piping

There are two main pipes that connect into and away from the compressor. The inlet pipe directs the flow uniformly into the compressor, the outlet pipe is placed between the compressor and the pulse generator. A bell mouth inlet is 3D printed and installed before the inlet pipe. The bell mouth is a common device used for allowing the flow entering the compressor to uniformly develop.

In the previous section, it was shown that the inlet measurement plane had to be moved further away from the compressor inlet as it was being affected by flow recirculation. To do this, a longer inlet pipe was designed and manufactured. The longer pipe moved the inlet measurement plane an approximate distance of 3 diameters away from the inlet region. Whilst this is sufficient for measurements, it is ideal that an even longer distance is attained between the measurement plane and the impeller inlet. However, there were physical limitations to the length of the inlet pipe. As the inlet pipe was cantilevered to the volute, increasing the length of the cantilevered arm increased the vibration at the far upstream region. The vibrations resulted in uncertainty and instabilities at the point of measurement. The compromise on the length of the pipe was reached through analysis of computational simulations of a very long inlet pipe; the manufactured length of the pipe was determined when the mass flow field was unaffected in simulation. The outlet measurement plane was deemed suitable for measurement and stayed constant. The measurement distances for the inlet and outlet planes are shown in figure 5.22.

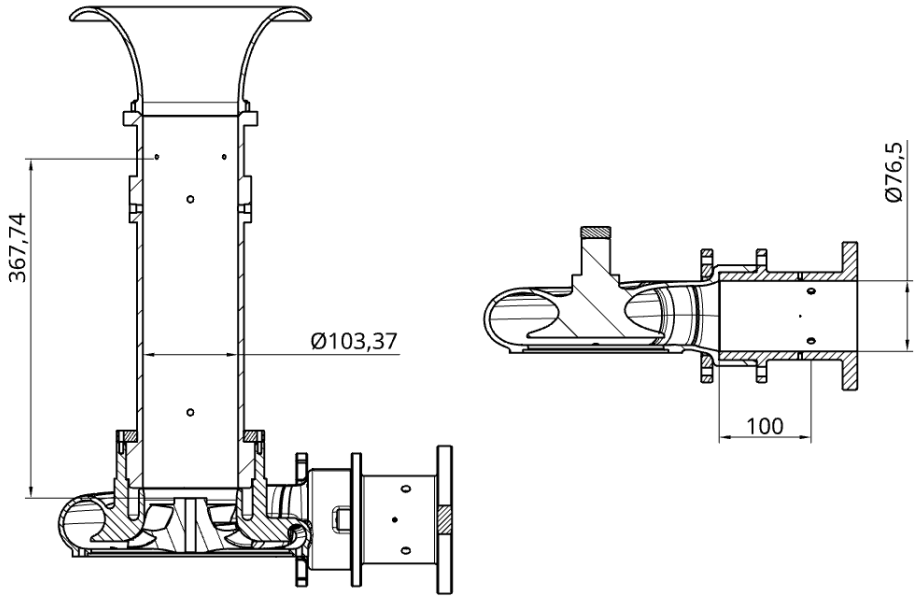


Fig. 3.6 Section view of the new inlet pipe & outlet pipe showing the measurement plane locations

Figure 3.7 shows the differences in the flow measurements before and after the repositioning of the mass flow rate sensor. The results show that the new position is sufficiently away from the recirculation region, as the correct flow rate is being captured. Additionally, the suitability of the new inlet plane was also validated with the installation of a temperature probe at the original plane. When the compressor system sees recirculation close to surge, this temperature probe can detect the change. When the surge operating condition is reached, the recirculation probe shows high temperatures, whereas the inlet temperature measurement remains steady, showing that recirculation was not affecting the new measurement location.

It can also be seen that the mass flow measurements before and after the repositioning of the sensor have different absolute values for the full operating line, see Figure 3.7. This is because the new facility and original facility has different calibration procedures. Additionally, some of the pipework has been modified so the overall system has a slightly different mass flow range, leading to the absolute mass flow rates being different. This system change was necessary to accommodate the new additions to the experimental facility.

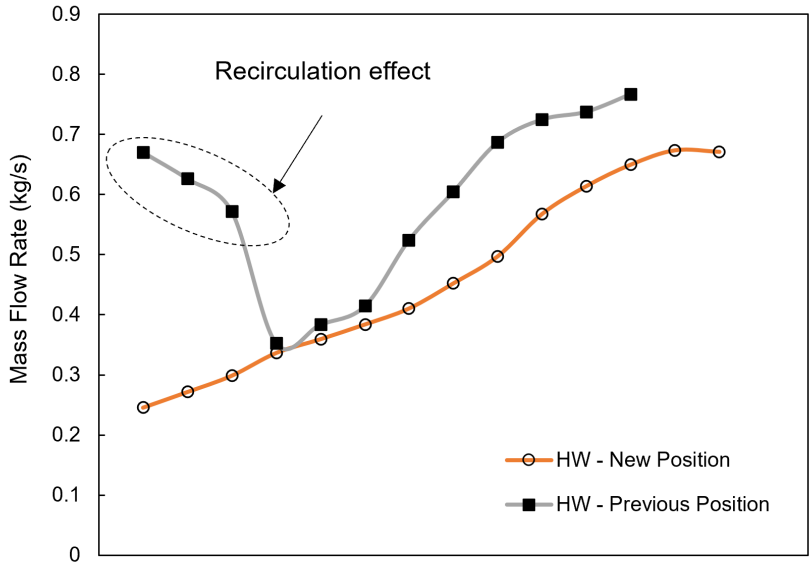


Fig. 3.7 Differences in the measured mass flow rate of the hotwire probes in the two positions

Mass flow rate sensors

In the original facility, the mass flow rate was calibrated using an external system, provided by supplier DANTEC. Since it was difficult to recreate the conditions for accurate calibration in an external system, many times the calibrations differed between different measurements - leading to inconsistencies in the calculation of mass flow rate. Due to the fragility of the device, the sensor broke often and the calibration constants changed between the readings. Subsequently, it was decided that the hot-wire probe will be calibrated in situ, using a secondary mass flow measurement, when operating in steady conditions.

The secondary mass flow measurement needed to be robust, repeatable and accurate for the calibration process. Some of the devices that are often used for these types of readings are pitot tubes, orifice plates and v-cones. These devices are accurate and straightforward for steady measurements but are not responsive enough for fast changing, pulsating conditions. This is why the hot-wire sensor, once accurately calibrated, is useful. For this reason, there are two different mass flow measurements on the updated facility in order to meet these two needs.

The following section describes the two mass flow rate measurements in detail. The description of the mass flow sensors is shown in Table 3.2.

Table 3.2 Mass flow rate sensors on the updated experimental facility

Sensor	Details	Position
V-Cone	V-cone flow meter (range (0-1 kg/s))	Exit piping (after plenum)
Hot-wire	Platinum plated tungsten 10 micron wire, CTA (hotwire)	Inlet pipe (new measurement position)

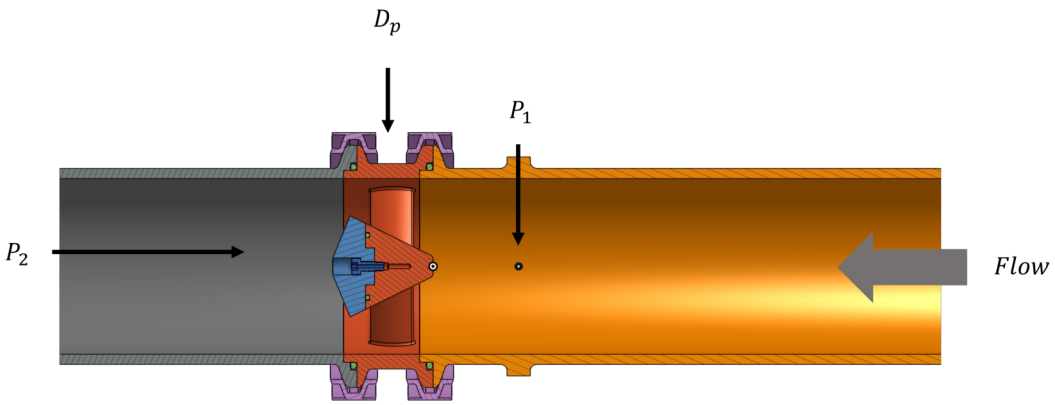


Fig. 3.8 CAD Schematic of the V-cone mass flow measurement device

V-Cone Flow Sensor

The steady flow rate is measured with a v-cone. The v-cone is a standard measurement device that uses the Bernoulli principle to measure bulk flow after the flow is straightened by the device. V-cones can be purchased as 'off the shelf' products by flow measurement specialists such as McCrometer. However, because of the high accuracy & reliability of the device, they are expensive and have a limited range of operation. Since the experimental facility is frequently used for experiments on different devices, it was more cost-effective to design a modifiable v-cone than to purchase multiple v-cones with different ranges. Therefore, the mass flow rate is measured with a bespoke v-cone measurement device that was designed to meet the expected flow rate of the testing.

The v-cone has been placed downstream of the compressor. The placement of the v-cone is determined largely by the manufacturing and assembly constraints of the experimental facility. Theoretically, a v-cone can be placed at the inlet or outlet of the compressor but the lab conditions available space limited the upstream placement. Placement after the compressor resulted in one key limitation; due to the conical restriction at the cone, which generates a small backpressure that restricts the mass flow rate through the compressor system, the maximum flow rate of the compressor system was reduced. However, several iterations of v-cone size have been trialled to ensure that the range of mass flow through

the compressor system is sufficient for the operating conditions required for the test, and therefore its placement and use is considered acceptable.

The v-cone mass flow rate is calculated using a set-of-equations available from the McCrometer [84], which is based on the ISO standard ISO: 5167-5:2022 for cone meters [85]. The V-cone can measure bulk mass flow rate using differential pressure between the high pressure port, P_1 and the low pressure port P_2, see Figure 3.8. A v-cone works by measuring the flow speed from the difference between total and static pressure, i.e. the dynamic pressure in the pipe that is proportional to flow velocity. Mass flow rate through the v-cone is calculated using Equation 3.1,

$$\dot{m}_2 = \sqrt{\rho} F_a C_d Y K_1 \sqrt{\Delta P} \tag{3.1}$$

where ρ is the density, F_a is the material temperature expansion coefficient, C_d is the discharge coefficient of the cone, K_1 is the flow coefficient and Y is the gas expansion factor. Y is dependent on other variables such as the thermal expansion coefficient and the local temperature. The local temperature is measured with the K-type thermocouple at the inlet of the V-cone. Two pressure measurements are required for the calculation. The absolute high pressure is measured using a Scanivalve pressure system, the differential pressure between the ports is measured with a differential pressure transducer.

The gas expansion factor Y is given by,

$$Y = 1 - (0.649 - 0.649\beta^4)\frac{U_1 \Delta P}{\gamma P} \tag{3.2}$$

Here, β is the beta ratio which depends on the cone geometry, see Equation 3.3, showing the calculation of β from cone diameter, d and pipe diameter, D. As the v-cone is placed after the compressor, a large cone size causes flow blockage through the region induces a backpressure on the compressor - this limits the mass flow rate that can be observed on the rig. For the range of mass flows expected for this compressor, 0-0.1 kg/s the recommended beta ratio is 0.82.

$$\beta = \sqrt{1 - \frac{d^2}{D^2}} \tag{3.3}$$

The material thermal expansion factor, F_a is calculated using the equation, 3.4, where D and d is the diameter of the pipe and cone inlets respectively, T is the temperature of the

incoming flow stream of the v-cone and α_{pipe} and α_{cone} are thermal expansion coefficients for the pipe and cone respectively.

$$Fa = \frac{D^2 - d^2}{((1-\alpha_{pipe}(T-528))D)^2 - ((1-\alpha_{cone}(T-528))d)^2} \tag{3.4}$$

K_1 is the flow constant and it is calculated with Equation 3.5. U_3 and U_2 are constants that can be obtained from McCrometer's technical brief [84]

$$k1 = \frac{\pi\sqrt{2U_3}}{4U_2}\frac{D^2\beta^2}{\sqrt{1-\beta^4}}; \tag{3.5}$$

CTA probe

A Constant Temperature Anemometry (CTA) measurement technique is used to detect instantaneous flow. This is done by placing a CTA 'hot-wire' probe at the pipe inlet such that the probe faces the free stream. For this experiment, since it is calibrated to bulk flow conditions, it is placed in the middle of the inlet pipe duct.



Fig. 3.9 A magnified view of a CTA Hot-wire probe from Dantec Dynamics

A magnified image of a hot-wire probe is shown in Figure 3.9. A thin tungsten wire can be seen in between two metal prongs. CTA works on the principle that the rate of heat loss through convection of a heated body is proportional to the velocity of the flow stream, $Q \propto U$. The convective heat transfer, Q, for a wire placed normal to the flow stream is given by Equation 3.6 and is derived from Newtons law of cooling [86].

$$Q = (T_w - T_0)A_w h = A + BU^n \tag{3.6}$$

Where $T_w - T_0$ is the over temperature of the wire, A_w is the wire surface area, h is the heat transfer coefficient and U is the flow velocity. A and B are constants.

During a run, the hot-wire is kept at a constant temperature, which is a predefined hot temperature. The resistance of the wire is known and the current through the wire is required to be kept constant, therefore as heat is lost through the wire from convection effects, the temperature of the wire drops and the voltage across the wire has to change correspondingly to return the wire to hot temperature. The hot-wire measures a change in the signal voltage that is required to keep the hot-wire at the hot temperature. As mentioned before, heat is being convected at a rate that is proportional to the changing flow velocity, therefore, the change in voltage, E, is also proportional to the heat transfer, $Q \propto E$.

The basic relation between Q and E for a wire placed normal to the flow can be seen in Equation 3.7 [87] and shows the operating principle of a CTA measurement.

$$(T_w - T_0) A_w h = A + BE^n \tag{3.7}$$

Temperature Correction of Voltage

The voltage at the hot-wire needs to be corrected for the temperature of the flow stream as the measurement signal is also affected by the free stream ambient temperature. The corrected voltage is calculated by Equation 3.8 where E_{corr} is the corrected voltage, E_1 is the raw voltage signal, T_w is the fixed hot temperature the hot-wire, T_0 is the reference temperature at the point of the hot-wire set up, T_1 is the ambient temperature of the flow stream during the calibration and m is the temperature loading factor, calculated for air using Equation 3.9, a function of the ambient flow stream and material coefficients (specified by McCrometer manual).

$$E_{corr} = E_1 \frac{T_w - T_0}{T_w - T_1}.^{0.5(1+m)}; \tag{3.8}$$

$$m = 2x10^{-5} + 5x10^{-8} T_1 + 3x10^{-11} T_1^2; \tag{3.9}$$

CTA Probe Calibration

Once the corrected voltage, E_{corr} has been obtained, it is now possible to calibrate the hotwire such that the readings of voltage are proportional to some aspect of the flow. A calibration where readings of voltage are taken at different expected flow conditions, will result in a mathematical expression for proportionality. A power law or a polynomial fit is often used to find the coefficients and constants.

The change in signal voltage, V, is proportional to the changing flow conditions, however, it is important to correctly decide what to calibrate against. For example, one could calibrate against known values of velocity and find coefficients that equate voltage to velocity. However, since the CTA probe is placed in the middle of the flow stream, it is only picking up the velocity in that location. If this value of velocity is used, it overestimates the bulk average velocity. Additionally to do this requires knowledge of the bulk average flow velocity or the velocity profile in that location under those flow conditions. This is difficult to measure without detailed velocity measurements of the whole measurement plane.

Instead, it is easier to estimate velocity from calibrating against a known value of mass flow rate. Since the test rig has an additional measurement of mass flow rate from the v-cone, it is possible to use this sensor. Therefore, it is possible to calibrate the hot wire voltage with the mass flow measurements from the V-cone. Later, it will be shown how the bulk average velocity is estimated from the mass flow rate readings.

The calibration of the hot-wire is done under steady flow conditions (without the pulse generator being on) and mass flow conservation is assumed.

$$\dot{m_{cta}} = \rho_1 U_1 A_1 \tag{3.10}$$

During the steady flow calibration runs, the compressor is taken from the theoretical maximum flow rate (valve fully open) to surge (valve closed to surge condition) a number of times. Mass flow rate at the v-cone is recorded for all runs and the voltage at the hot-wire is also recorded. The average recorded voltage is corrected for ambient temperature. The mass flow rate at the v-cone is given by:

$$\dot{m_{cone}} = \sqrt{\rho} F_a C_d Y K_1 \sqrt{\Delta P} \tag{3.11}$$

By plotting the relationship between the temperature corrected voltage and the mass flow rate at the v-cone over a steady operating condition of the compressor, it is possible to obtain the calibration constants. The calibration curve for the baseline results is shown in Figure 3.10. The Y axis the mass flow rate measured by the V-cone. A polynomial fit can be used to find the relationship between the v-cone mass flow rate and the voltage measured by the CTA probe.

Figure 3.10 shows the calculated mass flow values indicated by the black crosses. The calculated values of mass flow from the calibration fit closely match the measured values at the v-cone. After calibration, it is now possible to use the hot-wire signal to calculate the mass flow rates. More specifically, it can now also be used to calculate dynamic mass flow that is fast changing, which was previously not be possible to capture with just the v-cone. Figure 3.11 shows the difference in mass flow rate calculation if the mass flow rate is calculated at the v-cone compared to the hot-wire, there is a near perfect linear relationship between the two mass flows, with the hotwire mass flow being that of around 0.99 v-cone mass flow. This difference is found to be minimal for the measurement purposes for this research.

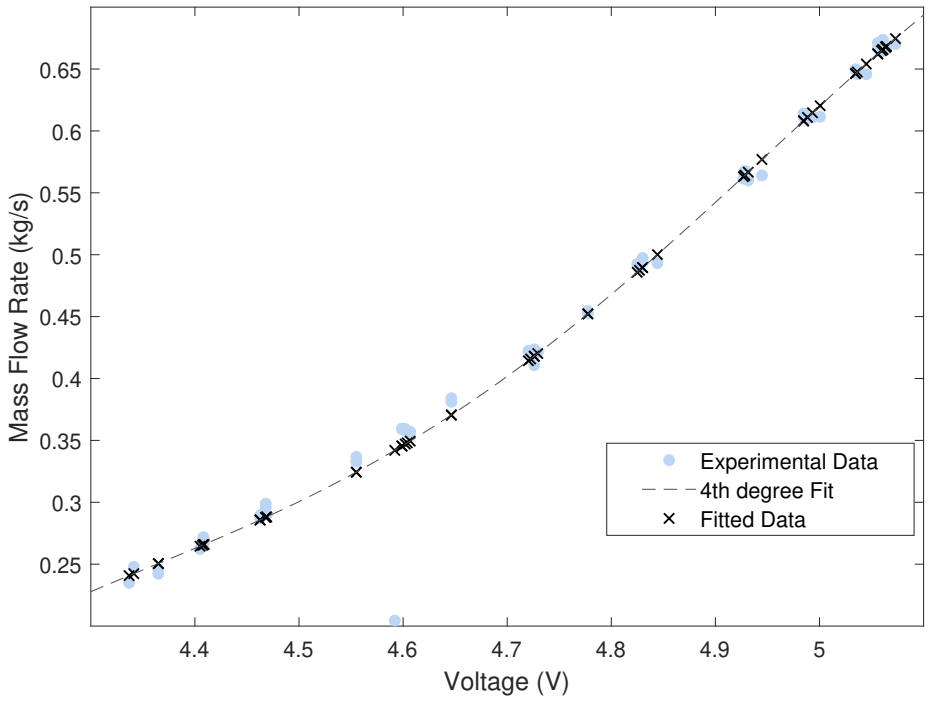


Fig. 3.10 Calibration of the hot-wire. The mass flow rate measured at the v-cone (Y-axis) is plotted against the corrected voltage measurement (X-axis) and a calibration fit is obtained. The calculated mass flow rate after calibration is also plotted on the figure.

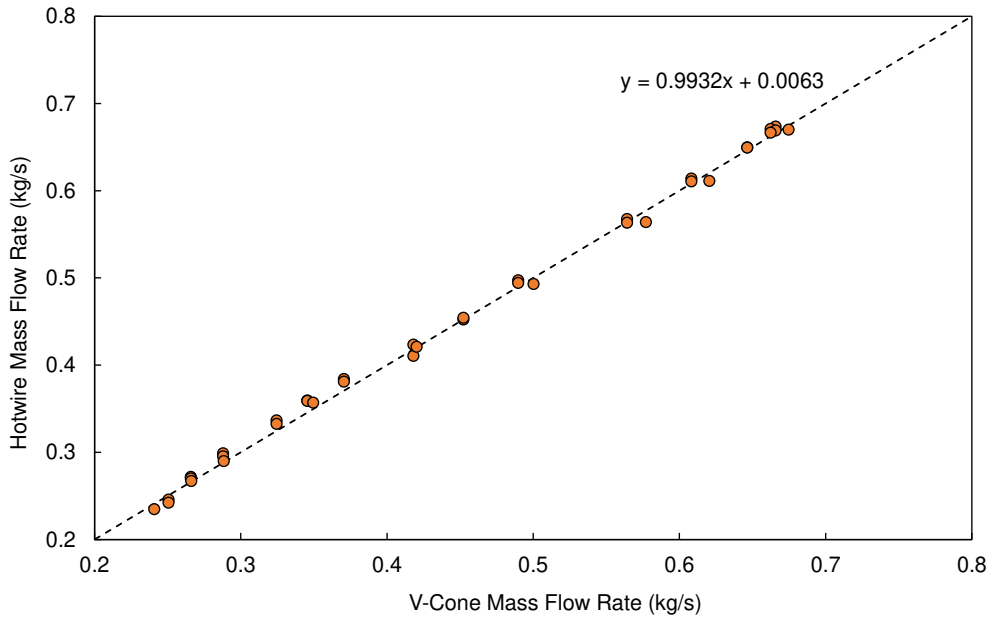


Fig. 3.11 Comparison of mass flow measured at the hot-wire to the mass flow measured at the v-cone in steady conditions

Velocity from Mass Flow

To calculate the velocity from the mass flow rate at the inlet and outlet, a number of assumptions are made. First, it is assumed that the shape of the actual velocity profile is not required. The reason for this is that the absolute value of the flow velocity is not of the greatest concern for this research, a generally close estimate is sufficient. The most important aspect of the work is the instantaneous deviation from bulk flow under pulsating conditions rather than the detailed specific flow profile and variation within a single flow profile (at least in experiments). Therefore, mapping the effective flow profile is not required and an estimate of the profile is sufficient.

Although the flow in a pipe is usually a parabolic profile, for calculation purposes, a square velocity profile with a reduction in flow area to account for boundary layer, BL has been assumed, see Figure 3.12. At the BL, the velocity is assumed negligible. This results in the true flow area being smaller than the available pipe area, to account for BL effects. This is indicated by the reduced diameter of the flow, D_{flow} compared to the true pipe area D_{pipe} in the Figure.

In order to calculate the boundary layer, BL, height, as a first estimate, it is assumed that the flow area is the same as the internal cross sectional area of the pipe, D_{pipe}. This is the value used for calculating the Reynolds number. It is found that the Reynolds number

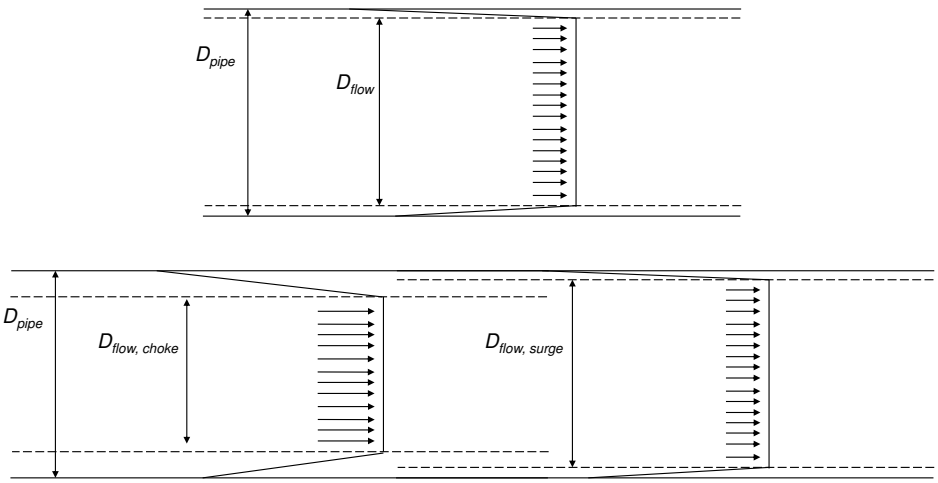


Fig. 3.12 Schematic showing change in flow area (not to scale) for different points on the speed line, estimated using the boundary layer assumption

is predicted to be turbulent for all points on the speed line. Therefore, it is possible to estimate that a turbulent BL is formed. The calculation for a turbulent BL is shown in Equation 3.12. It can be seen that the $BL = f(Re) \sim f(u, \rho, L, \mu)$, where u is the flow speed, ρ is density, L is the characteristic length, in this case pipe length, and μ is the dynamic viscosity of air. Since L and μ stay constant, and ρ at the inlet is approximately constant and close to ambient, the BL scales with flow velocity. At the highest flow condition, close to choke, the boundary layer height is 3mm for the given D_{pipe} of 103mm, and the reduction in flow diameter is around 11% of the pipe area near choke. Clearly, this is significant, therefore, for calculations, it is assumed that the flow area changes between surge and choke in correspondence to the flow velocity, see Figure 3.12, with the change calculated using an estimate for the boundary layer, from Equation 3.12.

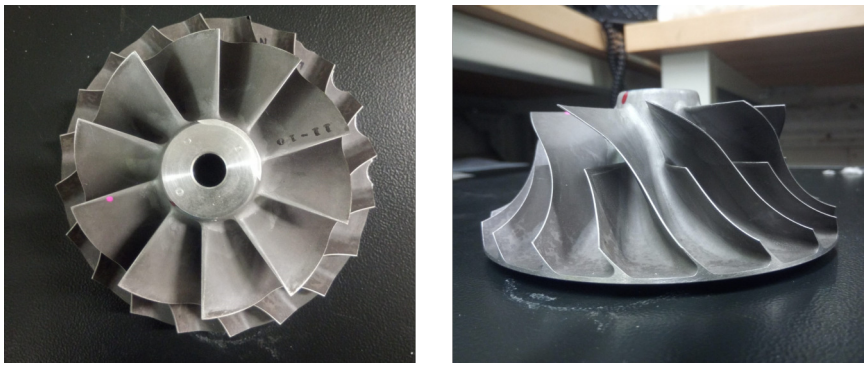
$$\delta_{gg} = 0.37 \frac{x}{Re^{\frac{1}{5}}} \tag{3.12}$$

3.2 Experimental Method

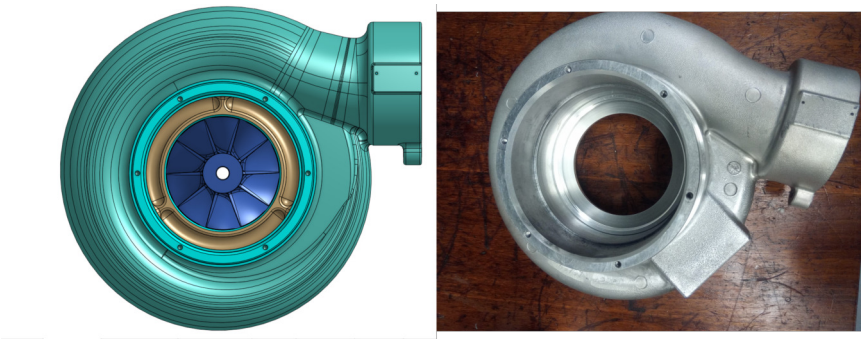
The experimental technique principally involves loading the compressor by controlling the compressor throttling system and taking static pressure and temperature measurements at each operating condition to estimate the thermodynamic state of the fluid before and after compression, at inlet and outlet measurement planes, respectively. With these measurements, it is possible to determine the work done to compress the fluid. Since it is also

possible to estimate the theoretical work that the compressor should have required, which is usually less than the actual work, the efficiency of the compressor can be determined as well.

The *MHI* turbocharger automotive compressor of interest in this study has an outlet diameter of 51mm. In operation, it is subject to engine speeds of 2000-5000rpm (66Hz-166.7Hz) and compressor operating speeds of 75,000-161,000rpm. In practice, a 51mm diameter compressor is too small for detailed measurements and has been scaled up to 136mm in diameter for measurement simplicity. All other parameters are also scaled such that the experiments conducted on this compressor can be transferred to the real application. The 136mm diameter compressor, as supplied by the manufacturer, is the baseline compressor for the performance assessment in this research. The baseline compressor impeller and volute assembly is shown in Figure 3.13a and 3.13b.



(a) Baseline impeller (Exit diameter: 136mm)



(b) Compressor volute and impeller assembly. CAD schematic (left), Cast-ally baseline volute (right)

Fig. 3.13 Baseline compressor provided by Mitsubishi Heavy Industries as the reference compressor

The baseline turbocharger centrifugal compressor performance map and the equivalent operating line is presented in Figure 3.14. The operating line of the original turbo compressor is shown with the red line, corresponding to the full operating range if the original compressor. In this research, three operating point of interest have been defined - OP1, OP2 and OP3, which correspond to peak pressure, peak efficiency and large flow condition, respectively. The equivalent engine operating line for the scaled compressor under study is

shown in green (see Figure 3.14). Instead of a range of operating speeds seen by the compressor when placed in an actual engine, a single constant operating speed of 40,000rpm has been selected. The equivalent design points at this speed are shown as DP1, DP2 and DP3 in Figure 3.14, corresponding to the new equivalent peak pressure, peak efficiency and large flow conditions. The investigations conducted in this research are with respect to these design points.

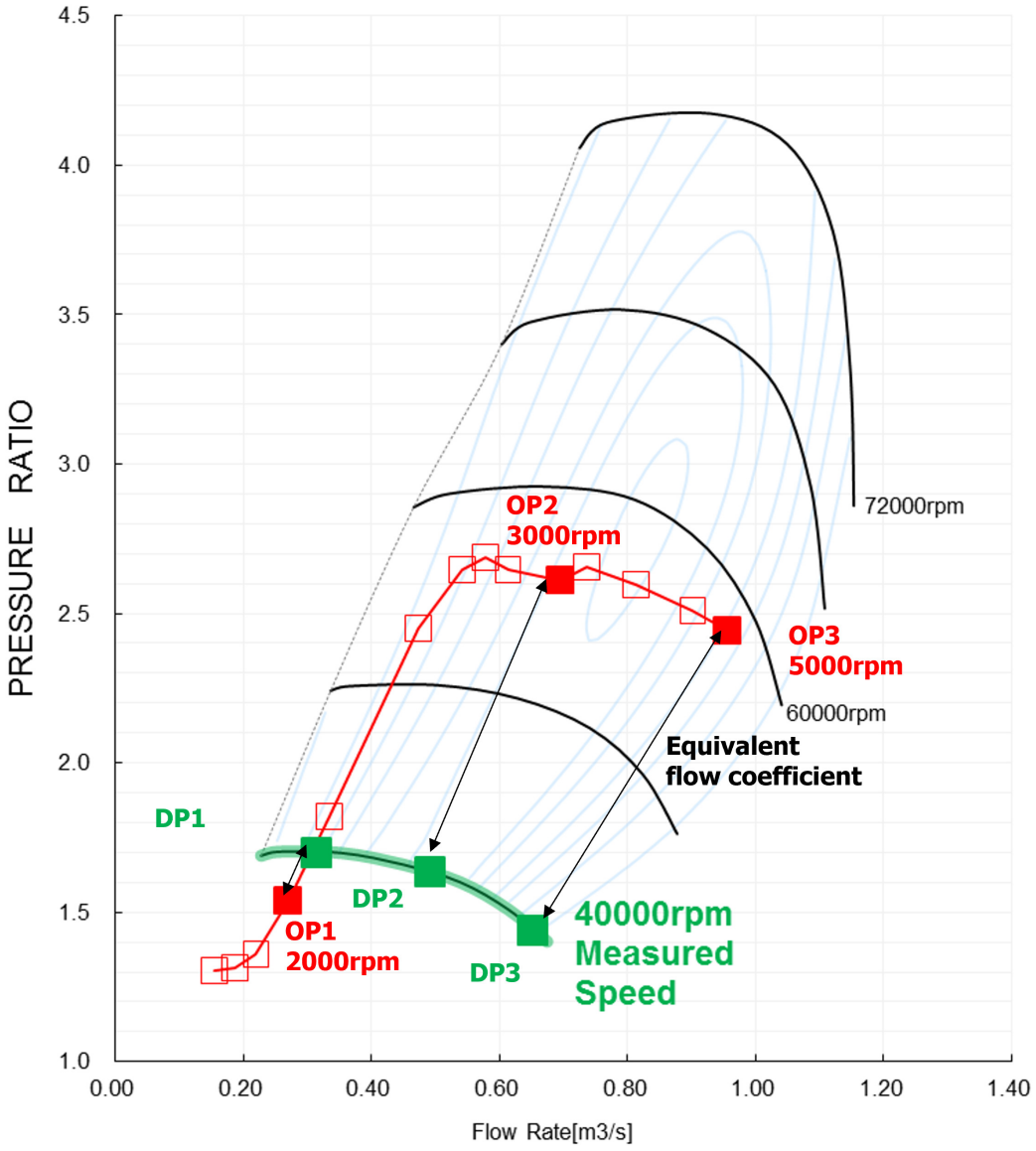


Fig. 3.14 Performance map of the baseline compressor showing the engine operating line (red) and the equivalent operating line for research (green)

Equivalence of Unsteady Conditions

As the compressor running speed changes with the engine speed, so does the throttle frequency. The operating point pulsating frequencies can be seen in Figure 3.14 and are 2000rpm (66Hz), 3000rpm (100Hz) and 5000rpm (166.7Hz) for the key operating points of interest. However, since the baseline compressor is scaled up and not the original size, it is important that the level of unsteadiness is the same so that the design points are comparable. The selection of the design point frequencies is driven by a number of key factors: one, the frequency range achievable by the servomotor on the test facility, data and knowledge of compressor performance on previously tested frequencies, and the similarity of unsteadiness. This would enable the learning and research on the design points to be applicable to engine applications.

It is important to reiterate that the original turbocharger is much smaller and resides in a smaller system, than the lab test set-up. This system is much smaller than the compressor system and hence the unsteady environment is different. Therefore, to ensure that the testing is done on similar unsteady environments, the design point frequencies have been selected such that the Ω numbers are similar, such that the frequency of pulsation as well as the system size effect are taken into consideration. Readers are reminded that the calculation of the Ω number was described in the literature review section. Table 3.3 and 3.4 show the final design points for the corresponding operating points respectively. The final test frequencies are 30 Hz (1800 rpm), 46.7 Hz (2802 rpm) and 66.6 Hz (4000 rpm). These frequencies will be used for the remainder for the analysis on pulsating flow.

Table 3.3 Selection of applied Frequencies for Design Points

Design Point	**DP1**	**DP2**	**DP3**
Frequency of Pulsation (RPM)	1800	2802	4000

Table 3.4 Frequencies of Operating Points

Operating Point	**OP1**	**OP2**	**OP3**
Frequency of Pulsation (RPM)	2000	3000	5000

Engine operating environments

As shown in the literature review, the engine operating environment is different to the operating environment centrifugal compressors are designed for. Due to the resulting pressure pulsations in the system, the compressor constantly operates in off-design operating states. Rather than a specific operating point, the compressor sees multiple 'operating

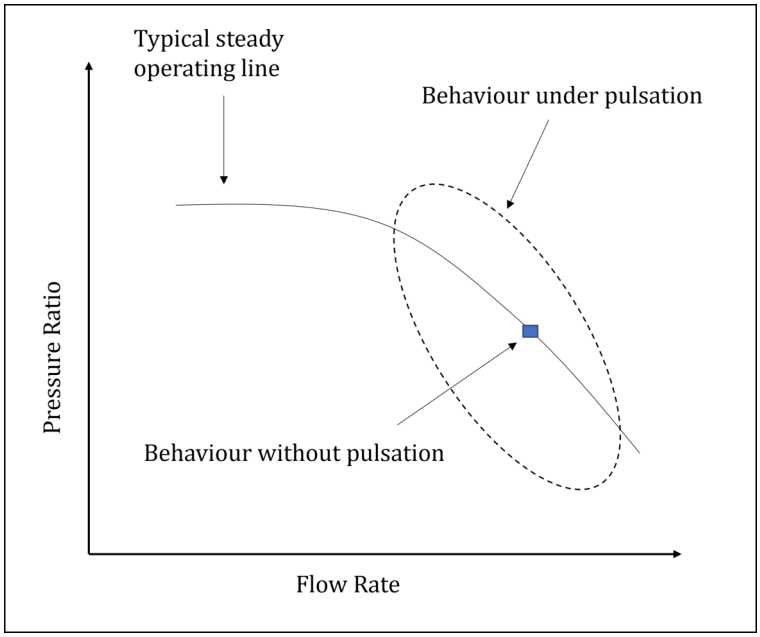


Fig. 3.15 Schematic of behaviour under pulsating flow

points'. Figure 3.15 shows a schematic of a typical representation of the behaviour of the compressor under engine pulsation.

3.2.1 Data Processing Methods under Pulsating Conditions

There are two main data processing methods that are used for evaluation: Cycle average and Ensemble Average. The two methods are useful for attaining average performance as well as capturing instantaneous data where possible and will be described below.

Cycle Average

When performance characterisation is carried out in pulsating conditions, the pressure ratio and efficiency measurements in pulsating flow are often reported as cycle average measurements. The cycle average result is the mean result of a given instantaneous condition. Cycle average results are an indicative measure of performance, even though they are not real values or real-measurement conditions. In pulsating cases, the true operating point is constantly moving with respect to the position of the pulse generator, and so the average value is never obtained in practice. Nonetheless, cycle average results are useful as they are an approximate representation of the operating points, and often provide information that of interest to manufacturers and designers.

The cycle average results for the measurements are taken over a total of 10,000 data points collected over 0.8 seconds. This means that for the lowest frequency case of interest, 30Hz, the average is taken over 24 pulses. The measurement time has been kept the same as 0.8s even in the larger frequency cases and in the steady cases for simplicity of data processing.

The cycle average results for the data points of any given parameter is calculated using Equation 3.13, where p are all the recorded values, n is the number of data points in the data set, in this case 10,000 points, and $\bar{p}$ is the time average result.

$$\bar{p} = \frac{\sum_0^n p}{n} \tag{3.13}$$

The cycle average mass flow rate, $\dot{m}$, is the average mass flow rate calculated at the v-cone. The time average pressure ratio, Π, is calculated as a ratio of the average total pressure at the inlet, P_{01} and average total pressure at the outlet P_{02} respectively, as seen in Equation 3.14.

$$\Pi = \frac{P_{02}}{P_{01}} \tag{3.14}$$

The efficiency is calculated with the isentropic temperature calculated from the obtained pressure ratio in the numerator and the average temperature at the outlet in the denominator. This is an average result and can only be obtained as an average due to the rate at which temperature information can be gathered.

$$T_{02,ad} = T_{01}\Pi^{\frac{k-1}{k}}; \tag{3.15}$$

$$\eta = \frac{C_{p,in}(T_{02,ad} - T_{01})}{C_{p,out}(T_{02} - T_{01})} \tag{3.16}$$

Ensemble Average

Another common representation is to present data using an ensemble average of the performance or time synchronous average. This allows a time signal of multiple different pulses to collapse into a signal pulse that represents the data from all the pulses. This representation is often useful in pulsating flow analysis. An example of the resulting 'ensemble average' is shown in Figure 3.16. The ensemble average is the average pulse over

a cycle of pulses; and is used to represent the signal in one wavelength. In this research, a type of ensemble averaging function, known as 'Time Synchronous Averaging', is used for all calculations.

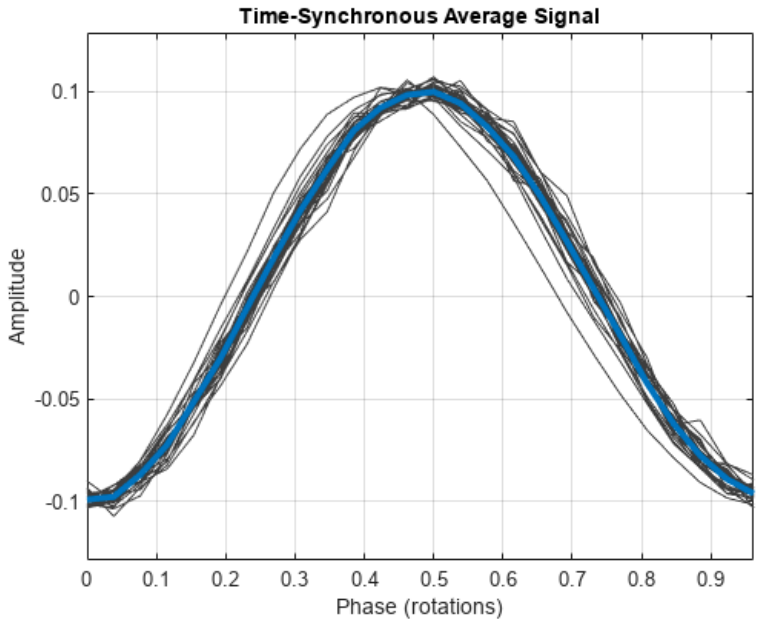


Fig. 3.16 Example of time synchronous signal averaging process resulting in a single, representative signal after averaging

3.2.2 Calculation method

This section describes the calculation method for obtaining the parameters for pressure ratio and efficiency assessment of the centrifugal compressor using the data obtained from the compressor testing facility. As described previously, the testing facility is equipped with static pressure transducers, thermocouples, and two mass flow measurement sensors on each plane. This, along with the lab sensors, allow estimations of thermodynamic states for calculation of performance. The procedure is outlined below.

Key Assumptions

Stated first are some key assumptions for the performance assessment.

1. The static temperature at the thermocouples is estimated using a recovery factor, as the measured temperature is a function of the static temperature, total temperature and recovery factor

2. The recovery factor is taken to be 0.97. This is the value specified by BS 5389-2005 as one that can be taken for a bare thermocouple with insulation, such as the one being used in the experiment.
3. No leakages in the compressor between inlet and exit take place.
4. The flow field at the inlet has a square velocity profile

The known constants are shown in Table 3.5:

Table 3.5 Constants

Standard Atmospheric Pressure, P_0,	101325	Pa
Standard Atmospheric Temperature, T_0	293.15	K
Inlet Area	0.008397	m^2
Outlet Area	0.00456	m^2
Gas Constant	287	-
Ratio of specific heats, γ (inlet)	1.4	-
Ratio of specific heats, γ (outlet)	1.39	-

The known values are: inlet static pressure, P_1, outlet static pressure, P_2, measured inlet temperature, T_{meas1}, measured outlet temperature, T_{meas2}, lab pressure, P_{Lab}, lab temperature T_{Lab}, mass flow rate from v-cone $\dot{m}$.

The following general equations apply for calculating the total conditions at the defined inlet and outlet states. The density is calculated using Equation 3.17, where P_s and T_s are the static pressures and temperatures at the state.

$$\rho_1 = \frac{P_s}{RT_s} \tag{3.17}$$

The inlet and outlet velocities are obtained using density ρ and mass flow rate, $\dot{m}$. The flow area is obtained from the Boundary Layer assumption as explained in Section 'Mass Flow Rate'. Once the flow area is obtained, the bulk average flow velocity is given by Equation 3.18, where A_f refers to the actual flow area.

$$v = \frac{\dot{m}}{\rho A_f} \tag{3.18}$$

The measured temperature is estimated to lay between between the static and total temperature. To work out the static temperature at the outlet, a recovery factor, $r = 0.97$ is used based on BS 5389-2005. The relationship between measured temperature, T_{meas} and static temperature, T_s, is given in Equation 3.19

$$T_s = \frac{T_{meas}}{(1+\frac{1}{2}(k-1)rM^2)} \tag{3.19}$$

The speed of sound, α is estimated using specific heat constant, K, gas constant of air, R and static temperature, T_s, which, with knowledge of the bulk average flow velocity is then used to estimate the Mach number M, see Equation 3.20 and 3.21.

$$\alpha_= \sqrt{kRT_s} \tag{3.20}$$

$$M = \frac{v}{\alpha} \tag{3.21}$$

With knowledge of the above, the total pressure, P_0, and total temperature, T_0, is given by Equation 3.22 and 3.23.

$$P_0 = P_s(1+\frac{k-1}{2}M^2)^{(\frac{k}{k-1})} \tag{3.22}$$

$$T_0 = T_s + \frac{v^2}{2C_p} \tag{3.23}$$

where C_p is the specific heat capacity of air, and it is calculated by,

$$C_p = a_0 + a_1.T + a_2.T^2 + a_3T^3 + a_4T^4 + a_5T^5 \tag{3.24}$$

where T is the average temperature between the inlet and outlet.

The specific heat constants for air are: a_0=1083.1165; a_1 -0.68388122; a_2=0.001787514; a_3 = -1.13237E-06; a_4 = -8.29433E-10; a_5 =1.11002E-12.

Using this theoretical procedure, the total pressures at the inlet and outlet state lead to the estimation of compressor performance which is a ratio of the total pressure ratio at the inlet and outlet:

$$\Pi = \frac{P_{02}}{P_{01}} \tag{3.25}$$

To calculate efficiency, adiabatic temperature is required. The adiabatic temperature is the temperature at the outlet that the compressor would have achieved in the case of adiabatic compression. However, in a real machine there are thermal losses which mean that the observed temperature is higher than the adiabatic temperature. The compressor efficiency is a function of the adiabatic temperature rise over the actual temperature rise, as shown by equation 3.27.

$$T_{02,ad} = T_{01}(PR^{\frac{(k_2-1)}{(k_2)}}) \tag{3.26}$$

$$\eta = \frac{C_{p,in}(T_{02,ad} - T_{01})}{C_{p,out}(T_{02} - T_{01})} \tag{3.27}$$

Mass flow rate calculations

Once the key information is obtained, the mass flow rate data is corrected to account for the differences in lab ambient conditions during the test. All mass flow rate results presented in this thesis are corrected to allow for comparison of results obtained on different days. Additionally, it is worth noting that mass flow rate, volume flow rate and flow coefficient are used for different analysis. This is because some results of this thesis have been externally published and in these instances the mass flow rate values have been normalised to protect propriety information of the research sponsor.

3.3 Results and Discussion

3.3.1 Updated Facility

The updated schematic of the general facility can be seen in figure 3.17. A longer inlet pipe, thermal insulation and the use of a v-cone for bulk mass flow readings are some of the key changes to the modified facility. The modified facility is detailed below. Table 3.6 describes the instrumentation on the updated facility, in particular, the main changes to instrumentation include the addition of the v-cone flow meter and the change of temperature sensors from resistance temperature detectors to thermocouples.

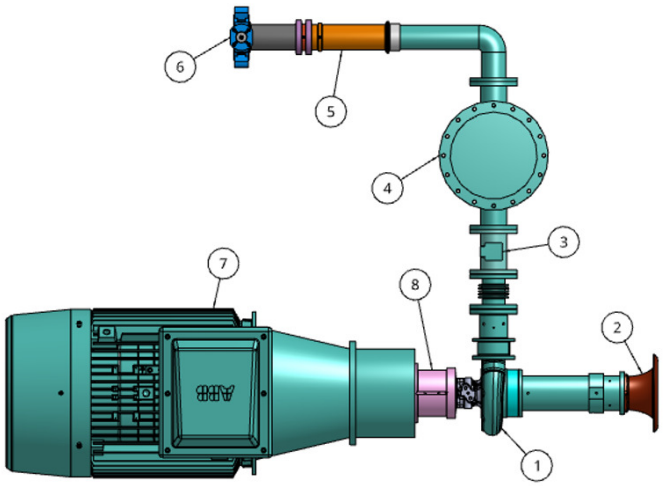


Fig. 3.17 Compressor experimental test facility. 1 - Volute and Impeller, 2 - bellmouth and inlet pipe, 3 - Rotatry pulse generator, 4 - 16L Plenum, 5 - V-cone, 6 - butterfly valve, 7- Motor, 8 - Adapter

Table 3.6 Sensors on updated facility permanently installed

Sensor	**Details**	**Range**	**Uncertainty**
Ambient pressure	PTB110 Vaisala type barometer	80kPa-110kPa	± 30Pa
Ambient temperature	K-Type thermocouple	-270 to +2,320° C	± 2.2° C
Static pressure	Scanivalve DSA3016/8D in rack enclosure DSAENCL4000	0-7 bar (gauge)	± 0.05% of full scale, ± 354Pa
Static temperature	K-Type Thermocouple, 1.5D diameter	-270 to +2,320° C	± 2.2° C
Rotational speed	Magnetic speed sensor	8 pulses per revolution	± 1rpm at running speed of 40krpm
Instantaneous Mass flow	Platinum plated tungsten 10 micron wire, CTA (hotwire) 51.7 mm from lower wall	0-10V	
Average Mass Flow	V-Cone	range	uncertainty
Instantaneous pressure	Omega PX321B	0-7 bar	± 0.025% of full scale, ± 175Pa
Surface temperature	K-Type thermocouple	-270 to +2,320° C	± 2.2° C

3.3.2 Measurement Uncertainty and Reliability Assessments

Measurement uncertainty

The measurement uncertainty is based on the precision error as well as systematic errors introduced by the experimental method. The precision errors are dependent on the measurement capabilities. If a measurement is used on its own without additional calculations, such as the measurement of temperature with a thermocouple, the measurement uncertainty is the combined uncertainty of measurement which includes the precision error as well as systematic or zero errors. If two temperature measurements are taken into consideration for a calculation, for example the determination of a temperature ratio, the uncertainty is the combined uncertainty of the individual temperature measurements, which can be calculated using the Root Sum Square (RSS) Method. The RSS method states that the uncertainty for any given parameter will be the root square sum of the dependent parameters [88].

$$\delta y = \left[\left(\delta x_1 \frac{\delta y}{\delta x_1} \right)^2 \left(\delta x_2 \frac{\delta y}{\delta x_2} \right)^2 + \ldots \left[(\delta x_n \frac{\delta y}{\delta x_n} \right)^2 \right]^{0.5} \tag{3.28}$$

Pressure Ratio

The pressure ratio is a function of the inlet and outlet pressure, $\Pi = \frac{P_{out}}{P_{in}}$ and is commonly used in this investigation as a measure of compressor performance. Both these measurements were taken with pressure transducers. The measurement uncertainty stated by the manufacturer is 0.025% for the full scale, which is 175 Pa. For the range of pressure ratios, (1.2 - 1.6), the measurement uncertainty is around 0.2%.

Temperature measurements

The temperature measurements are taken with thermocouples. K-Type thermocouples are stated to have an accuracy of 1.5°C in the range of 0-100°C This is known as the thermocouple error and is an inherent offset of the thermocouple. Since it does not change, the error is removed by calibration against known conditions, such as the lab temperature.

One additional error is introduced by the measurement system. This is the system error which is a sum of the error introduced by the thermal EMF of the instrumentation system and the error introduced by the cold junction temperature sensor. The system error for the

range of temperatures is found to be 0.5 $^{\circ}C$. Overall, this means that there is a 2$^{\circ}C$ error in the thermocouple measurement and the temperature measurement deviates from the true reading by 2$^{\circ}C$.

Based on this it is possible to conduct a sensitivity analysis. The performance of the compressor is determined mainly by the temperature rise through the system, roughly 70$^{\circ}C$ between the inlet and outlet. The mentioned 2$^{\circ}C$ error means that the maximum inaccuracy would be of $\pm$4$^{\circ}C$ and maximum if both temperatures were reading higher than nominal or lower than nominal. A quick estimation of efficiency can be conducted at the peak pressure and peak efficiency positions for some common temperature measurements, gives an error range of around 0.5-3% in the efficiency estimation depending on the combination of errors in the two thermocouples in the worst case scenario.

For this calculation, the errors introduced by the pressure transducers have been excluded as they are small, but it is worth noting that there will be a small error introduced by the pressure measurement. On top of this, it is worth noting as well that there is a heat loss through the system that is not consistent. This means that the outlet temperature measurement deviates not only by the thermocouple error but also because the system is not adiabatic and does not have the same heat loss each time the test is conducted (as it is dependent on the atmospheric conditions and the insulation).

However, this error in efficiency estimation of 0.5-3% applies only in a few cases and does not appear in most tests because the thermocouple sensor is never replaced. It is only replaced if there is a break - if there is a break, the experiments are repeated to ensure all comparisons are made to the same thermocouple. Additionally, the inlet thermocouple is always compared to the lab temperature sensor during tests to ensure that the thermocouple is working properly.

Mass flow sensors - v-cone

The uncertainty in the mass flow measurement is dependent on the scanivalve system as well as the differential pressure port that the v-cone mass flow system uses. The differential pressure port has an error of around 0.075% for the full range which is less than 0.5 mBar. The combination of errors gives an uncertanty of 0.1%.

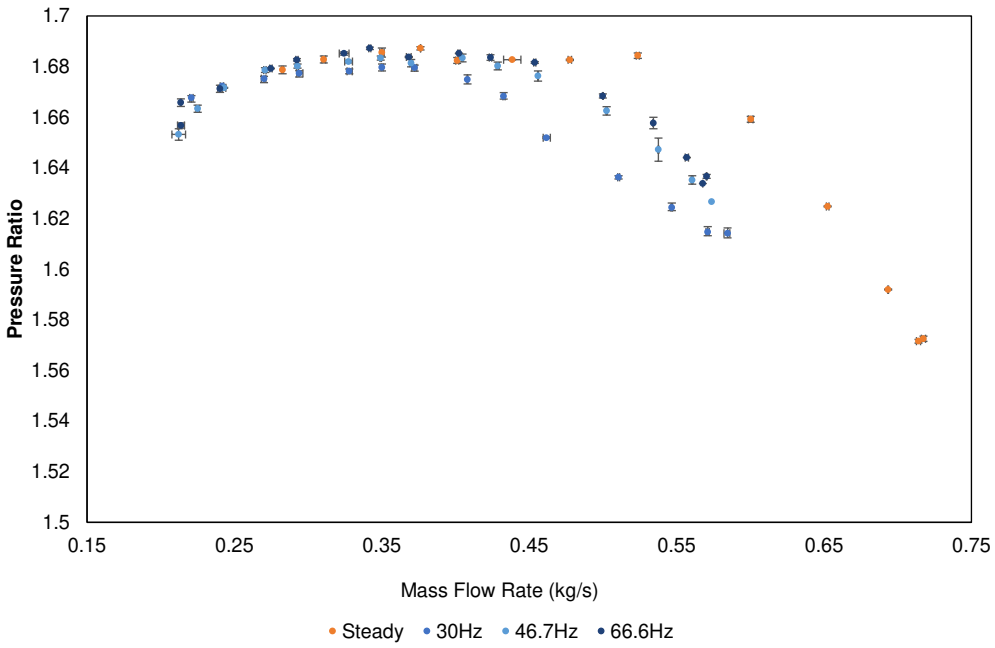


Fig. 3.18 Pressure ratio against mass flow rate for steady and pulsating conditions with frequencies of 30Hz, 46.7Hz and 66.6Hz - including range error bars.

Mass flow sensors - hot-wire

The uncertainty in the mass flow calculation at the hotwire is dependent on the calibration of the hot-wire. An example of the calibration process of the hot-wire was presented in Figure 3.11 - it can be seen that there is 1% difference in the mass flow values and hence the uncertainty in the mass flow measurement from the hot wire is taken to be 1%. As a calibration is done before every set of tests against the v-cone measurement, other errors, such as the error caused by the voltage drift is considered negligible.

Experimental reliability

As uncertainties are estimates, another way of assessing the experimental reliability is to check for repeatability. In order to check that this is in fact the true performance of the baseline compressor under steady, the experiments are repeated three times. Figure 3.18 and 3.19 show the range bars in pressure ratio and efficiency for the three steady and three pulsating runs at different frequencies (12 runs in total). It can be seen that there are almost no horizontal error bars, showing that the mass flow rate reading is highly repeatable and consistent. Similarly, the vertical range bars are small with some exceptions indicating that there is high repeatability in the experimental procedure.

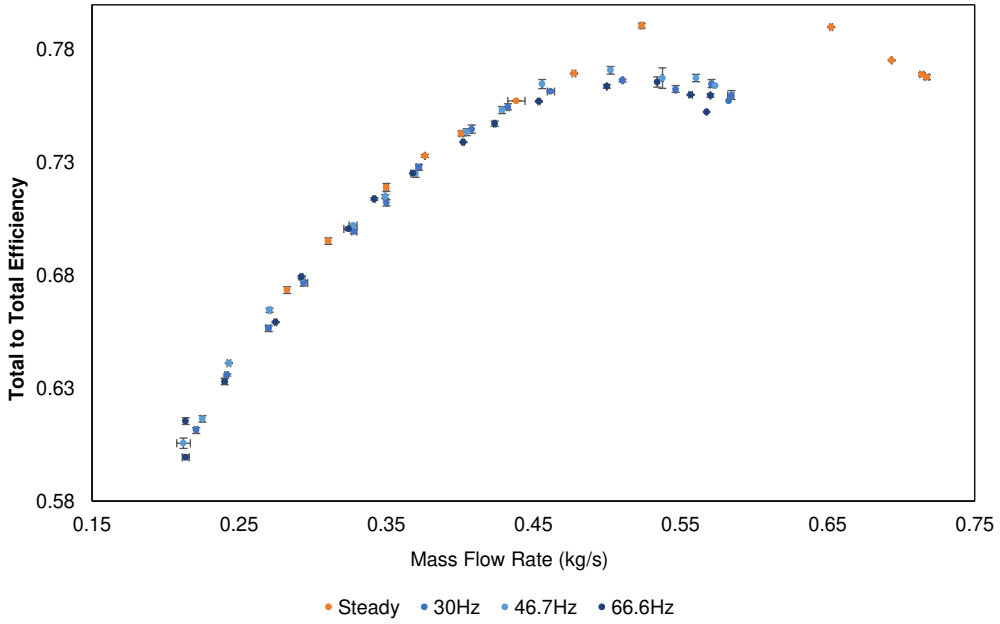


Fig. 3.19 Efficiency against mass flow rate for steady and pulsating conditions with frequencies of 30Hz, 46.7Hz and 66.6Hz.

3.4 Chapter Summary

The focus of this chapter was the improvement of an existing experimental facility, the capabilities of which had to be modified for the experimental facility to be suitably equipped to conduct this research. In the first section, the original experimental facility and the required modifications were described. Majority of the experimental facility was kept the same, including the pulse generator which generates the required throttle conditions. The summary of the modifications is detailed here: The original test inlet plane was found to be too close to the impeller inlet, and a new inlet pipe was designed and manufactured to move the inlet measurement plane further upstream. The instrumentation was kept largely similar but the RTD temperature probes were replaced with thermocouples for faster response to pulsating flow conditions. Thermal insulation was added and operating procedures were modified to account for thermal equilibrium and pressure transducer drift. Mass flow rate measurements were found to be unreliable between different test days. To improve this, a bespoke v-cone flow measurement device was developed and installed. The v-cone was also used to calibrate the hotwire so that the calibration process is consistent. Additional details such as the development of the boundary layer were also included into the calibration process.

The experimental method was discussed and key operating points for the research focus were found based on the operating line of interest. The equivalent design points in the compressor test rig were identified to simulate equivalent unsteady conditions. Two data processing techniques: cycle average and time synchronous averaging (or ensemble averaging) were described as the main two data processing techniques that will be used in this research. The calculation methodology was briefly outlined.

Lastly, the experimental results were obtained to assess the experimental uncertainty and reliability. The measurement uncertainty was calculated for each of the parameters of interest, and the greatest uncertainty was seen in the thermocouples at near $2°C$, in the worst case scenario however, careful experimental procedures, such as ensuring that all measurements are taken with the same thermocouple, minimised the systematic error. The pressure ratio and efficiency assessments for the repeated runs show that there is high repeatability in the experimental set-up, and the facility is suitable for further assessments.

Chapter 4

Experimental Investigation of Compressor Under Pulsating Flow

As briefly introduced in chapter 2, the compressor performance under pulsating conditions noticeably differs from reference steady flow conditions - under pulsating flow, the compressor sees many instantaneous off-design states for a given operating point, as the pressure at the compressor outlet is rising and falling which pulls the compressor into different operating states continuously. For certain compressor systems, the surge margin also improves, in other words, shifts towards lower mass flow rates. The percentage of improvement is dependent on different parameters such as the system size and frequency of the pulse flow. Additionally, as a result of the pulse at the compressor outlet, there is an inertial 'filling and emptying' effect on the overall compressor system that the system response is not only dependent on the propagation of the pulsating wave but also on the inertia of the mass within the compressor system. This results in a hysteresis in the response of the compressor - the corresponding mass flow response of the compressor is out of phase with the pressure pulse at the outlet.

4.1 Experiment Details

This section details the design of the instrumented compressor, the experimental set up and corresponding instrumentation and the test conditions.

4.1.1 Design of Instrumented Compressor

The modifications to the compressor for placement of instrumentation is shown in Figure 4.1. The details of the instrumented compressor showing the the different measurement positions is provided as a manufacturing drawings in the appendix. Figure 4.2 shows the instrumented volute installed in the facility.

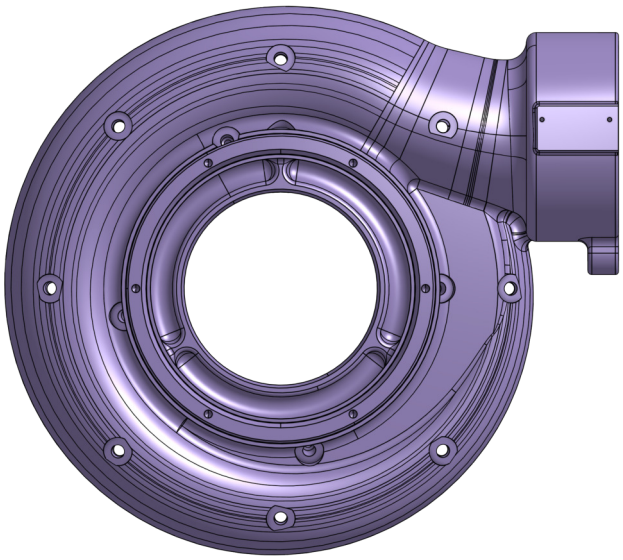


Fig. 4.1 CAD model of the instrumented volute design showing the measurement positions within the compressor

The measurement locations are shown in Figure 4.3. Three measurements are taken at the impeller inlet, mid-span and outlet locations. The access to the compressor shroud due to the gaps of the casing treatment, as seen in Figure 4.1, was a key manufacturing constraint. This meant it was not possible to take all measurements in the same plane as shown - instead, they have been staggered around the impeller. These ports are used for instantaneous pressure measurements at the shroud surface and they are as normal to the shroud surface as possible given the manufacturing constraints in this location. At the diffuser, measurements are taken at circumferential positions and around the tongue. The diffuser inlet and outlet position is highlighted in the figure as it will be used for analysis. At the volute, measurements are taken approximately every 45 ° circumferential locations. The measurements are taken at the top surface of the volute as it is a standard measurement location for experimental measurements in the volute. All ports are adapted to take instantaneous pressure measurements. All sensors are placed flush with the surface to avoid disturbing the flow field.

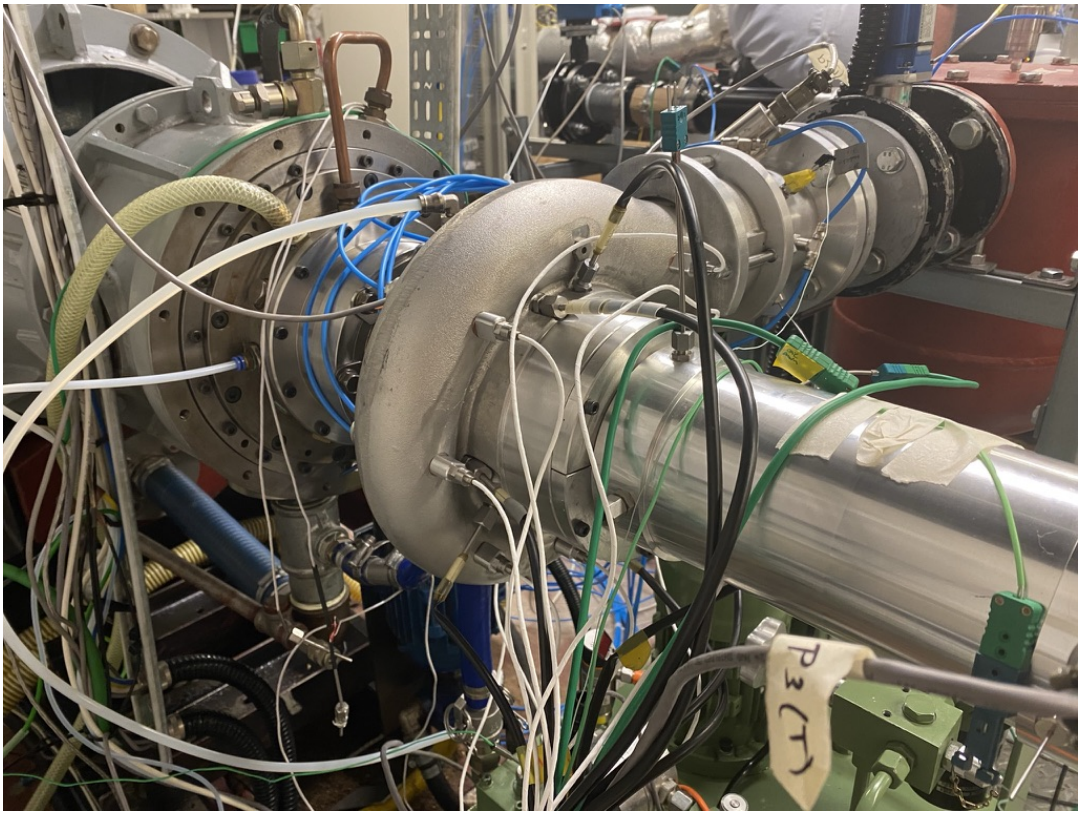


Fig. 4.2 Figure of the instrumented volute installed in the experimental facility

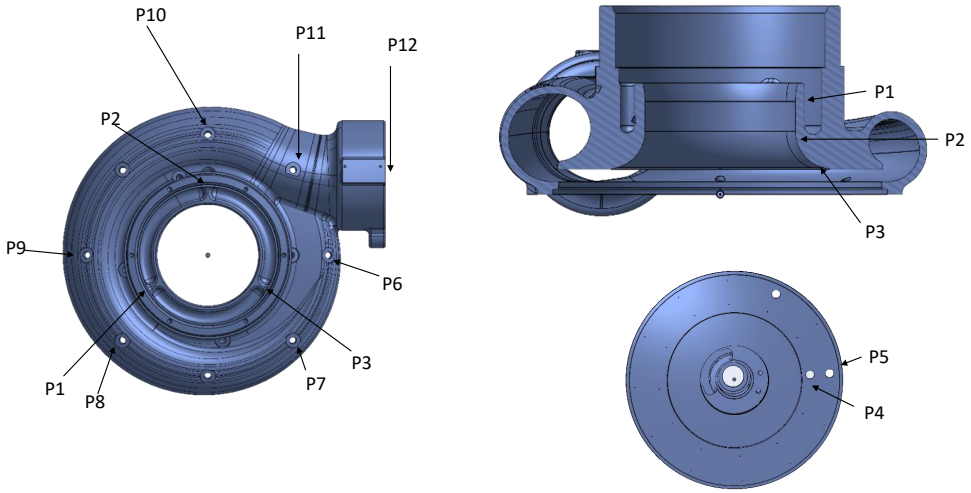


Fig. 4.3 Location of different static pressure sensors. P1 - impeller inlet, P2 - impeller midspan, P3 - impeller outlet, P4 - diffuser inlet near tongue, P5 - diffuser outlet near tongue, P6 – volute at clockwise location 3:00, P7 – volute at clockwise location 4:30, P8 – volute at clockwise location 7:30, P9 –volute at clockwise location 9:00, P10 – volute at clockwise position 12:00, P11 – volute at clockwise position 1:30, P12 – compressor outlet

The details of all the instrumentation used in the experimental set-up is shown in Table 4.1.

4.1.2 Test Conditions

The experiments have been conducted with steady flow conditions and at the required test frequencies which correspond to the near surge, peak pressure, peak efficiency and large flow operating points. The tested frequencies for the outlet pulsing boundary condition are 30Hz, 46.7Hz and 66Hz. The compressor runs at 40,000 rpm. The compressor test system is insulated to ensure adiabatic conditions. The modifications from Chapter 3 such as longer inlet pipe, thermal insulation and the use of a v-cone for bulk mass flow readings are all applied. The same pulsator disc size is used throughout all the experiments so that the pulse amplitude is consistent throughout.

Table 4.1 List of instrumentation for the detailed measurement test

Measurement	Sensor	Location	Type	Range
Ambient Pressure	PTB110 Vaisala Barometer	Lab	Absolute	80kPa-110kPa
Ambient Temperature	K Type Thermocouple	Lab		
Inlet Temperature	K Type Thermocouple	Inlet Plane (Far upstream)		
Inlet Pressure	PX419 Omega	Inlet Plane (Far upstream)	Differential	0-1Bar
Instantaneous Mass Flow	Platinum plated tungsten 10micron wire, CTA, 51.7mm from lower wall - DANTEC	Inlet Plane (Far upstream)		
V-cone differential pressure	Seitrans pressure transducer	differential ports at v-cone	Differential	600mBar
V-cone high pressure	Scanivalve DSA3016/8D in rack enclosure DSAENCL4000; module 16 pressure sensors	upstream of cone	Absolute	0-100PSI
V-cone Temperature	K Type Thermocouple	upstream of cone		
Outlet Temperature	K Type Thermocouple	Outlet measurement plane		
Outlet Pressure	MMV5A Omega	Outlet measurement plane	Absolute	0-3.5Bar
Impeller Pressure Transducers	XCE-062 Kulites	Impeller casing treatment	Absolute	0-3.5Bar
Diffuser Temperatures	K Type Thermocouple	4 diffuser locations		
Diffuser Pressure Transducers	XCE-062 Kulites	2 diffuser locations	Absolute	0-3.5Bar
Diffuser backplate transducers	HEL-375CO Kultie	bearing housing	Absolute	0-7Bar
Scroll Temperature	K Type Thermocouple	Volute		
Volute pressure transducers	XTEL-190L Kulite	volute surface	Absolute	0-6.9Bar

4.2 Experimental Results

4.2.1 Pressure ratio and efficiency for operating line

Figure 4.4 shows the cycle average results of pressure ratio and efficiency for steady, and pulsating frequencies of 30Hz, 46.7Hz and 66Hz.

The first thing that can be noticed is that as the flow rate is reduced, the compressor is able to operate in a stable manner for lower mass flow rates, compared to the steady flow conditions. This is in line with previous studies shown in the literature review; the increase in swallowing capacity of the system is due to the change in the system size and dynamics [55]. In the pulsating case, the system operates in a different range of flows and a much lower flow rate is reached before the system experiences surge. It can also be seen that there is a marginal advancement in pressure ratio at low mass flow rate conditions for pulsating flow frequencies as well.

It can also be seen that for this compressor system, the flow is also choked earlier when pulsating. In the high flow rate region, there is a decrease in the maximum mass flow rate that can be achieved by the experimental facility when the pulsator is enabled. This can be seen because the results in the pulsating cases do not reach the high flow rates achieved in steady conditions. The main reason this occurs is because the available pipe-duct area has been reduced when the pulse generator is running and the flow is restricted by the disc, effectively 'choking' the mass flow and reducing the operating region of the compressor.

In order to compare the performance between steady and pulsating conditions, it is important that comparisons are made for similar operating points. An operating point is determined by the pressure ratio or efficiency that a given mass flow rate can achieve. So, by fixing the mass flow rate, it is possible to compare the difference between steady and pulsating operating conditions. The comparable range has been highlighted in Figure 4.4 as the region between the dashed lines. Within this comparable range, it is possible to compare the performance between steady and pulsating flow as they have similar or same mass flow rates. Outside these boundaries, the operating points cannot be compared because there are no overlapping operating points outside this range.

The top figure in Figure 4.4 maps the performance and shows the cycle average steady results compared to pulsating frequencies results of 30, 46.7 and 66Hz, respectively. The cycle-average pressure ratio, Π, is plotted with respect to flow coefficient, F_c. For all pulsating conditions, the pressure ratio drops at high mass flow rates. There is a frequency dependency on the result as seen in the literature review [55, 23, 89]. At low mass flow rates, the performance appears to be similar at all tested operating conditions (pulse).

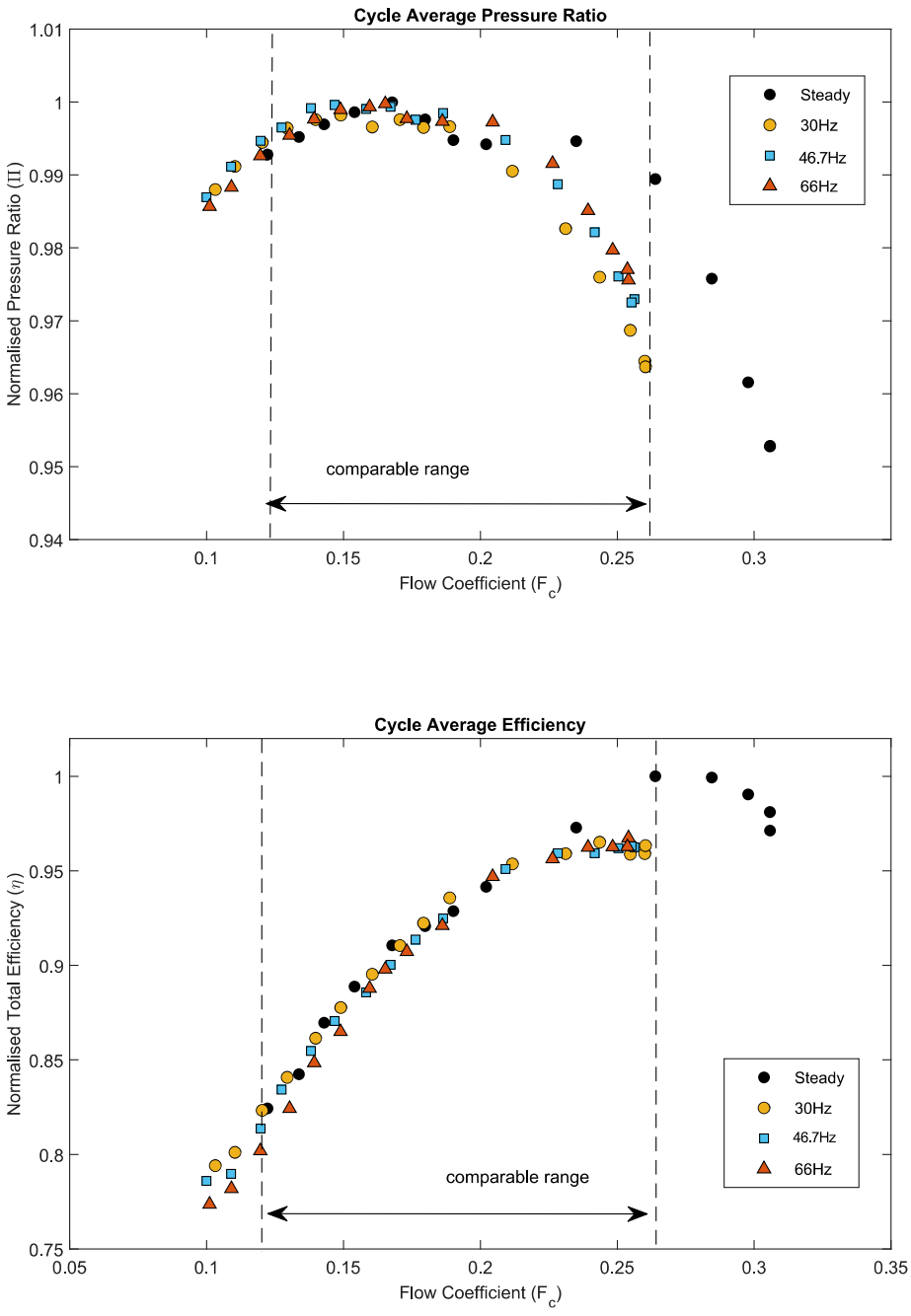


Fig. 4.4 Cycle average pressure ratio and efficiency results for all pulsating and steady flow conditions. The comparable range is shown in the figure.

Lower figure in Figure 4.4 shows the cycle average efficiency. There is a clear drop in the cycle average efficiency as the flow rate increases. It can be seen that the efficiency at low mass flow rates is similar to that of steady conditions.

Detailed assessment at key operating points

Four key operating points are selected for comparison, labeled as OP A, OP B, OP C and OP D corresponding to near surge, peak pressure, peak efficiency and large flow operating points, respectively. Figure 4.5 shows the performance of the compressor system for the reference steady flow conditions at three operating points and the equivalent cycle-average pulsating flow operating points for the three frequencies 30Hz, 46.7Hz and 66Hz.

Note that the large flow operating point (OP D) has only been recorded in steady conditions, as it was not possible to obtain this operating point in pulsating conditions. This is because the throttling of the flow reduces the maximum swallowing capacity of the compressor system. Operating point 'OP D' has been plotted on the Figure to show that operating point C corresponds to the equivalent peak efficiency condition if the flow was steady.

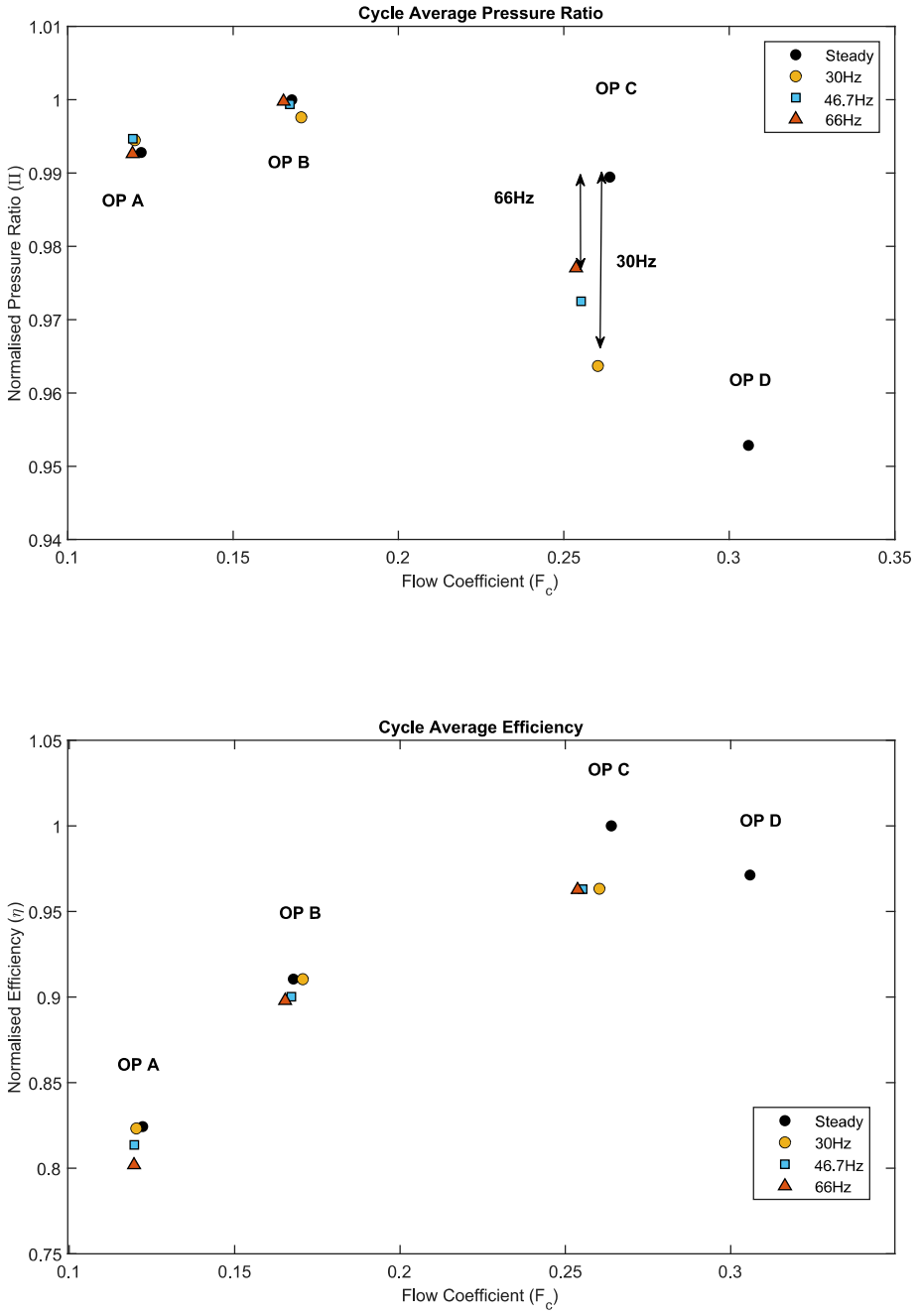


Fig. 4.5 Pressure ratio and efficiency curve at operating points OP A (near surge), OP B (peak pressure), OP C (peak efficiency for steady case; large flow for pulsating case) and OP D (Large flow for steady case) for the compressor system

Observing the pressure ratio curve, it is clear that there is a drop in performance at operating point C (peak efficiency - OP C) for the three pulsating frequencies, with the largest drop in

performance seen for the 30Hz frequency. At operating points A and B, the performance is similar or equivalent to the reference steady conditions. In Figure 4.5, it can be seen that there is a drop in the cycle-average efficiency for operating point C (OP C) but this drop in efficiency is independent of the frequency, on average.

At the near surge operating point (OP A), the cycle-average performance for the pulsating conditions is similar to the steady reference conditions however, the cycle-average efficiency drops with an increase in exit pulse frequency and it is worst for the 66Hz case. At the peak efficiency operating point (point B), the difference in cycle average pulsating and steady flow efficiency is smallest relative to points OP A and OP C. At operating point 'OP C', the performance deficit for pulsating exit conditions is most evident, with the largest drop in performance being the 30Hz frequency. What can be immediately inferred from Figure 4.5 is that there is a frequency effect on the performance of the compressor system when compared to a given reference operating point, which is in line with previous studies on pulsating flow [55, 23, 89].

The difference between the 30Hz and 66Hz case is worth further investigation. For detailed assessment, the remainder of the analysis focuses on these two frequencies in order to highlight the differences. The instantaneous and cycle average pressure ratio against mass flow for 30Hz and 66Hz is shown in Figure 4.6 for all operating points from surge (OP A) to choke (OP D) limits, at a constant compressor speed of 40k rpm. The difference between the instantaneous pressure ratio between the 30Hz and 66Hz can be seen in the figure. In the large flow region, the hysteresis loops in the 30Hz case case are wider and rounder, whereas the 66Hz case has narrow hysteresis loops. Comparatively, in the lower flow rate regions, the difference is less visible.

In order to gain further understanding on the differences observed in these operating conditions, a detailed analysis, including a static pressure measurement trace has been carried out and is presented in the next sections.

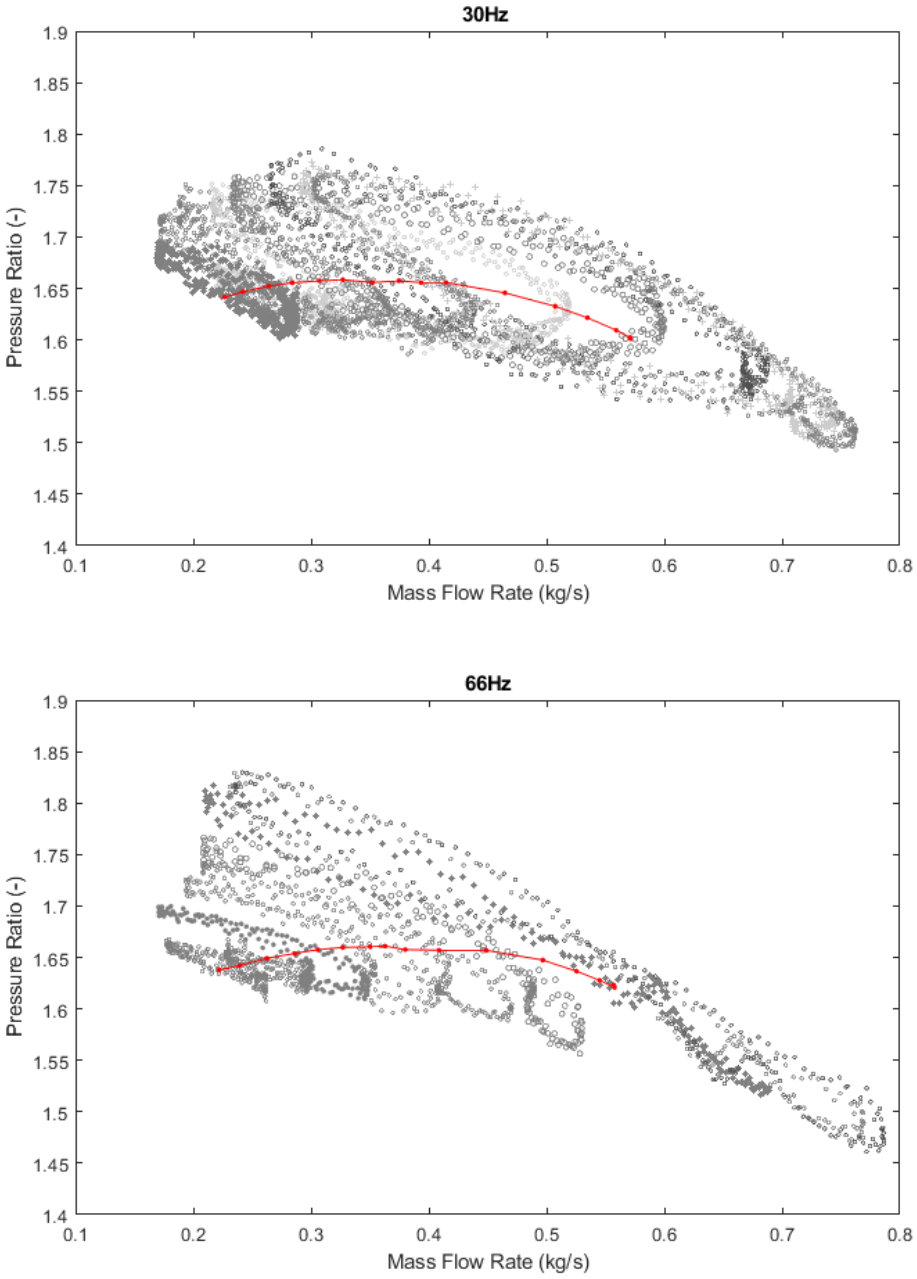


Fig. 4.6 Pressure ratio against mass flow rate for compressor under pulsating operation, with pulse frequencies of 30Hz (Top) and 66Hz (Bottom)

4.2.2 Static Pressure Measurements

The static pressure propagation has been measured at different positions (refer to Figure 4.3 for the positions of measurement). Figure 4.7 shows the static pressure results for the different measurement positions for 30Hz and 66Hz and OP A (near surge), OP B (peak pressure) and OP C (peak efficiency).

Figure 4.7 (top) shows 30Hz results whereas Figure 4.7 (bottom) shows 66Hz results for the three operating points under study (OP A - OP C). The static pressure for all measurement locations (P1 – P12) have been mapped on one figure, volute measurements P10 and P11 have not been included for simplifying the figure; The first measurement, position 1, is at the impeller inlet and the measurement at position 12 is at the compressor outlet. From position 1 (P1) to position 12 (P12), the pressure measurements track the static pressure rise through the compressor. Note, the figure shows one average pulse profile which is an average of all the pulses recorded during data acquisition.

It is possible to notice that at operating point C (peak efficiency) for 30Hz and 66Hz the static pressure traces in the diffuser and volute section of the compressor (P4-P8) do not follow the imposed static pressure at the compressor exit (P12). Additionally, this variation from the imposed static pressure at the outlet is affected differently in the 30Hz case vs the 66Hz case; the deviations for the different frequencies with respect to the outlet static pressure is highlighted with the red line.

Figure 4.7 showed that at operating point C (OP C), for the same swallowing capacity or mass flow rate, the compressor system with exit pulsating conditions was unable to match the steady performance, and that the pressure ratio attained was lower for the imposed frequency of 30Hz compared to 66Hz. In contrast, at operating point A there was a similar performance for both pulsating frequencies and the pressure ratios were close to the reference steady conditions. This drop in performance can be immediately attributed to a few factors. First, the difference in pressure trace at OP A and OP C is that the pulse is of a higher amplitude in OP C compared to OP A; the pulse amplitude reduces as the operating point shifts towards lower mass flow rates for all frequencies. This is because the amplitude of the backpressure wave is dependent on the amount of flow that is being periodically blocked by the valve; at high flow rates, as the mass flow rate is higher. When the valve closes, a large amount of mass is instantaneously stopped which creates a large localised static pressure; instantaneously a large deviation from mean pressure takes place resulting in a backpressure wave of high amplitude. At low flow rates, the backpressure wave does not have a high amplitude because there is less mass to create the backpressure and therefore there is less deviation from mean pressure. As the only controlled change has been the reduction of the flow capacity from valve closure, this pressure wave must be a function of the flow rate in the system.

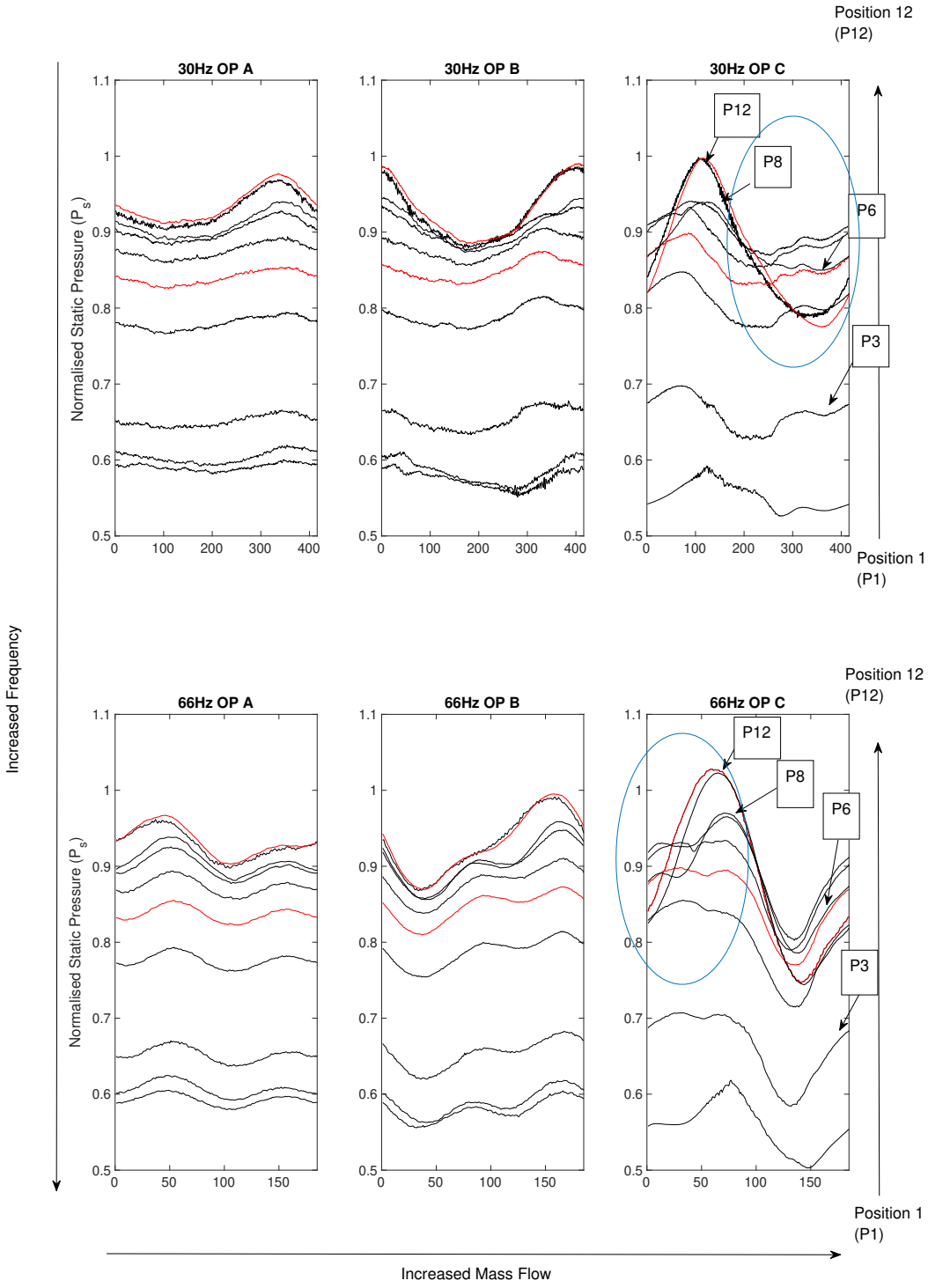


Fig. 4.7 30Hz (Top) and 66Hz (Bottom) Trace from static transducer locations 1 – 12. 1 -impeller inlet, 2 - impeller midspan, 3 - impeller outlet, 4 - diffuser inlet near tongue, 5 - diffuser outlet near tongue, 6 – volute at clockwise location 3:00, 7 – volute at clockwise location 4:30, 8 – volute at clockwise location 7:30, 9 – volute at clockwise location 1:30, 12 –outlet pressure

It is also possible to see that between OP B and OP C there is a transition in the way the pressure wave propagates through the volute internally, see Figure 4.7. For and between OP A and OP B the pressure wave propagation at all positions within the compressor follows the imposed pressure profile closely and at OP A, there is a distinct pressure rise for both 30Hz and 66Hz case throughout the compressor. However, between OP B and OP C, the static pressure within the volute does not uniformly rise. There appears to be a transition point after which static pressure measurements at P4-P8 are visibly different from the static pressure measurement at P12, suggesting that the pressure wave propagation has been altered.

A closer look at the static pressure variation in the volute for operating point 'OP C' (peak efficiency) is shown in Figure 4.8 for 30 and 66Hz for an average pulse. The azimuth positions along the volute are shown. There is a clear difference in the static pressure deviation at 30Hz compared to 66Hz.

It is possible that this difference in pressure changes between 30Hz and 60Hz for operating point 'OP C' is related to pressure reflections taking place. These reflections for 30Hz lead to worse internal pressure distribution and ultimately performance internally within the volute, see Figure 4.5. For the 66Hz case, the reflection reduces the wave peak at the near tongue measurements but has little impact on the wave trough (lowest pressure instance in the wave). For the 30Hz case, it appears that although the pressure wave trough is significant at the outlet (P12), when the waves reach the tongue they do not follow the outlet pressure; the pressure is unable to instantaneously reduce with the outlet pressure. Figure 4.9 shows the pressure wave propagation through the volute; the two waves could experience reflection near the tongue. Due to the different frequency of the imposed pulse, the reflected pressure wave affects the main pressure wave in different locations as it is propagating forward. Therefore, there is a phase shift in the position the interaction takes place. This would disturb the normal pulse propagation through the volute and disturb the main flow. This disturbance then leads to a local blockage, the effect of which could be disturbance of the main pulse profile.

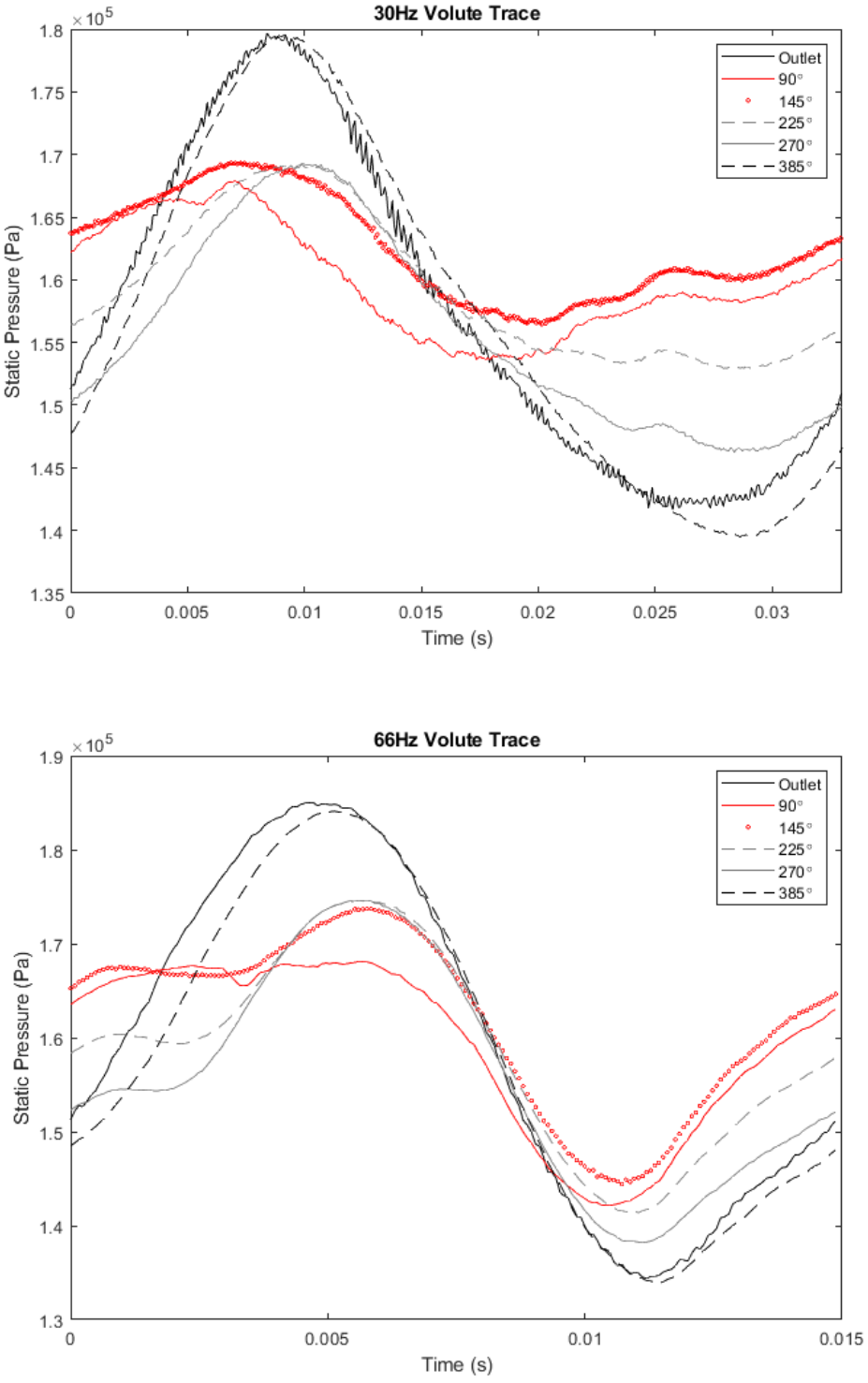


Fig. 4.8 Ensemble average static pressure pulse for different positions along the volute for tested frequencies of 30Hz (Top) and 66Hz (bottom)

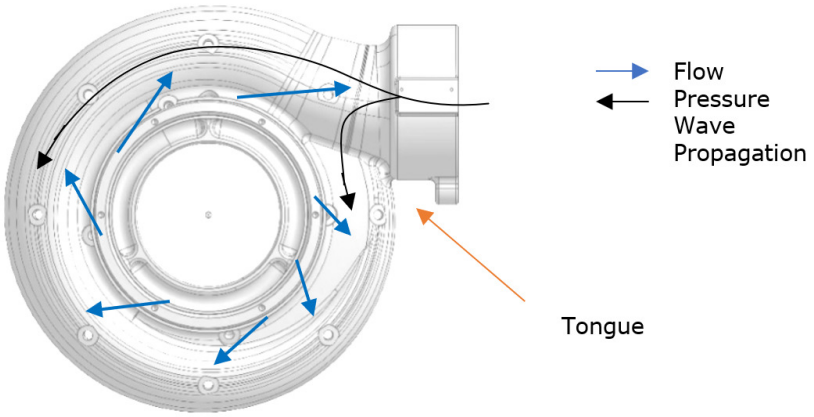


Fig. 4.9 Schematic of pressure wave propagating through tongue gap and disturbing the main flow

OP C 'filling and emptying' effect near volute

The static pressure and mass flow instantaneous response can be seen in Figure 4.10, this is characterised by a hysteresis behaviour, well established in the literature, refer to Figure 4.3 for the location of the different pressures. It can be seen that there is a 'filling and emptying' effect of the volume where the volume accumulates and releases mass locally. The static pressure is normalised to the maximum static pressure obtained during the 30Hz pulse. The x-axis shows the mass flow range that is swept instantaneously during this operating point. There are four positions tracing back the static pressure from the outlet imposed static pressure. As mentioned before, a hysteresis behaviour is more 'rounded' if the inlet mass flow rate takes a longer time to respond to the imposed static pressure, otherwise known as a 'lagging' response of the system and indicative of more localised filling and emptying of the volume. It is interesting that Figure 4.10 shows a difference in the location of a more rounded hysteresis behaviour for the 30Hz and 66Hz case. In position 12 which is at compressor exit, 66Hz shows less lag or filling and emptying in that location; the mass flow rate drops and rises in response to the rising and falling of the static pressure at the outlet. However in contrast position 12 for the 30Hz case shows that there is more lag in the mass flow response to the outlet static pressure.

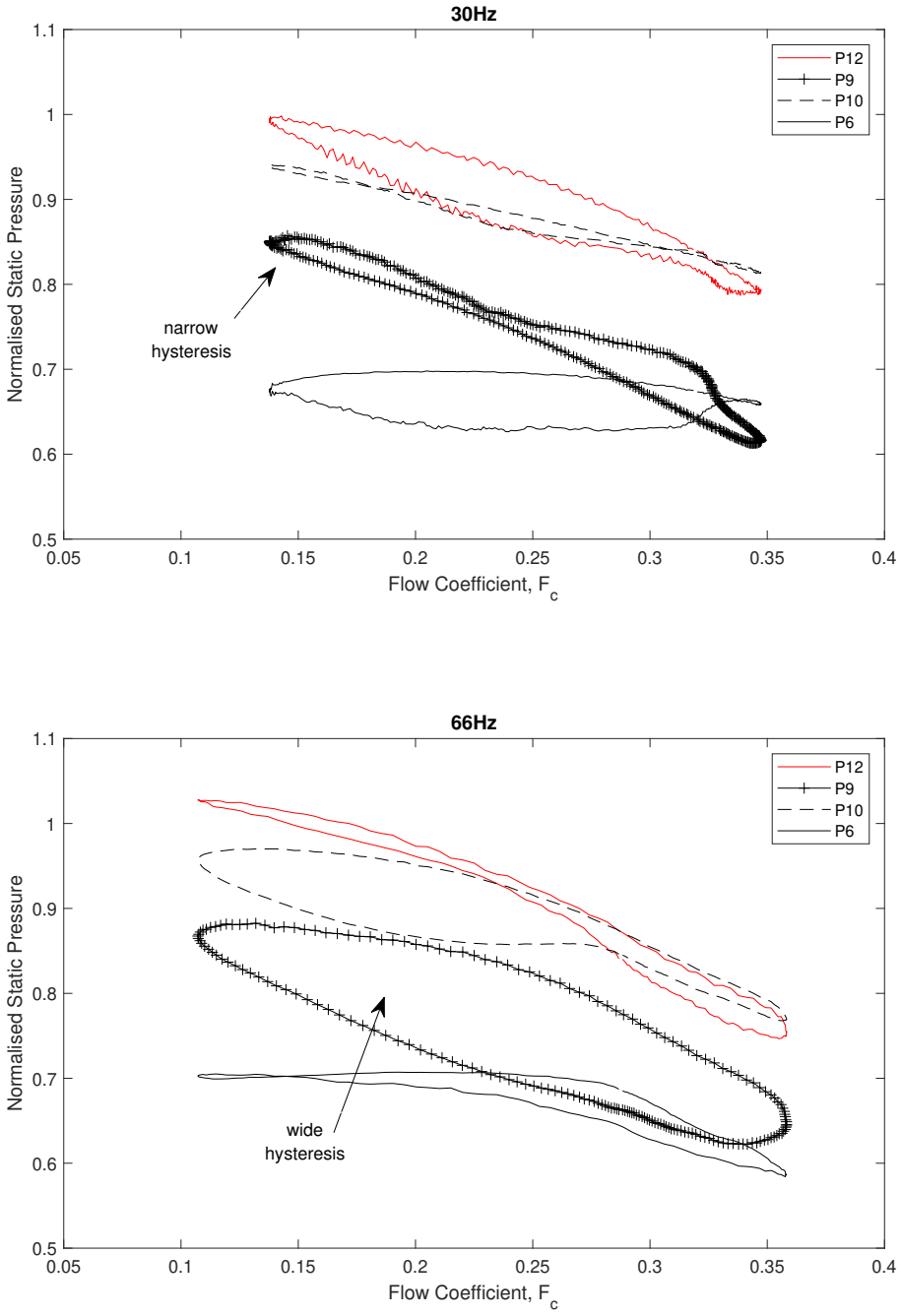


Fig. 4.10 Static pressure hysteresis behaviour for OP C for volute locations P12 – compressor outlet, P9 – volute at clock position 9.00, P10 – volute at clock position 12.00, P6 – volute at clock position 3.00 for 30Hz and 66Hz case

At position 10, shown in Figure 4.10, the static pressure at 30Hz shows almost no lag to the inlet flow coefficient whereas the 66Hz case shows a more significant lag. At position 11, which is around 180 degrees away from the compressor outlet and the half-way point of the collecting duct, the hysteresis loop is bigger and rounder in 66Hz case compared to 30Hz case, showing that the inlet mass flow rate does not coincide with the static pressure variation in this region. Interestingly, position 6, which is just before the compressor tongue, shows two distinct features for the 66Hz case. First, the static pressure trace for 66Hz shows less hysteresis behaviour than the 30Hz case. In this position the mass flow rate follows the static pressure variation as seen by the narrower hysteresis loop. However, there is a clear flat region of the pulse. This same flat region corresponds to the flat region shown in Figure 4.9 and is due to the pressure wave being effected at that location.

It is clear that filling and emptying of the flow is taking place within the volume, however, it appears that it is occurring at different positions within the volume for the different frequencies. For the 30Hz case, it is occurring more near the compressor exit and around the tongue, whereas for the 66Hz case it is occurring more away from the compressor exit. This is interesting because if the static pressure varies along the volute, different passages of the impeller also perform differently. The overall performance reflects this as the overall performance of the compressor is impacted by the internal static pressure distribution at the exit of the impeller passage. The difference in performance for the two frequencies can be seen in 4.5.

Additional to the location of the 'filling and emptying', the 66Hz case may be performing better than the 30Hz case because the pulse acts for a shorter time. It is worth noting that since 30Hz is near half the frequency of 66Hz, it has double the time period. The time period can be thought of as the residence time of the pulse. As the mass in the system has flow inertia, if the pressure changes faster than the flow can respond to the changing pressure, then the flow is less affected by the changing pressure conditions. Therefore, the instantaneous pressure propagation could be a function of the flow inertial response. Since the 30Hz case shows localised 'filling and emptying' at the exit of the compressor, it is an indication of localised flow inertial response that could be a reason for the larger drop in performance for 30Hz case.

Effect on impeller

Figure 4.11 shows the detailed internal response of the impeller at near surge (OP A) and peak efficiency (OP C). The dotted red lines show the average static pressure pulse at the measured impeller exit location (P3 on Figure 4.3). It can be seen that the static pressure at

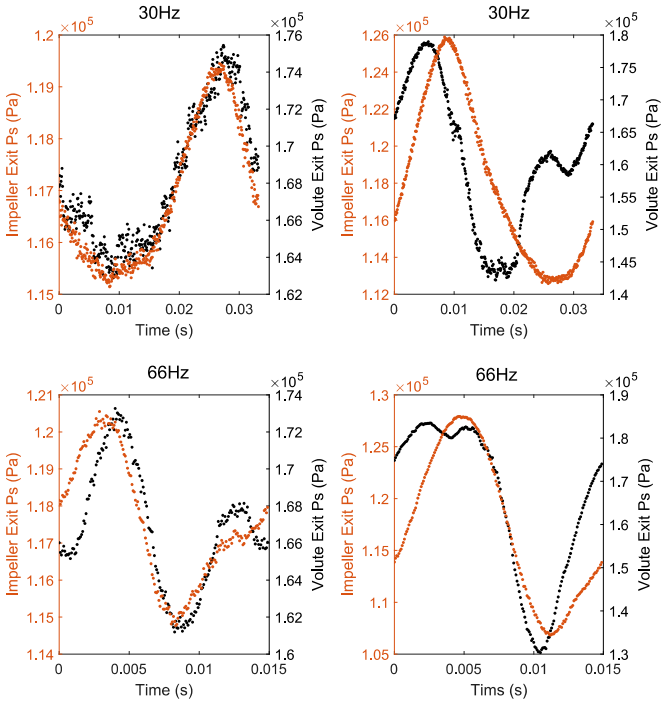
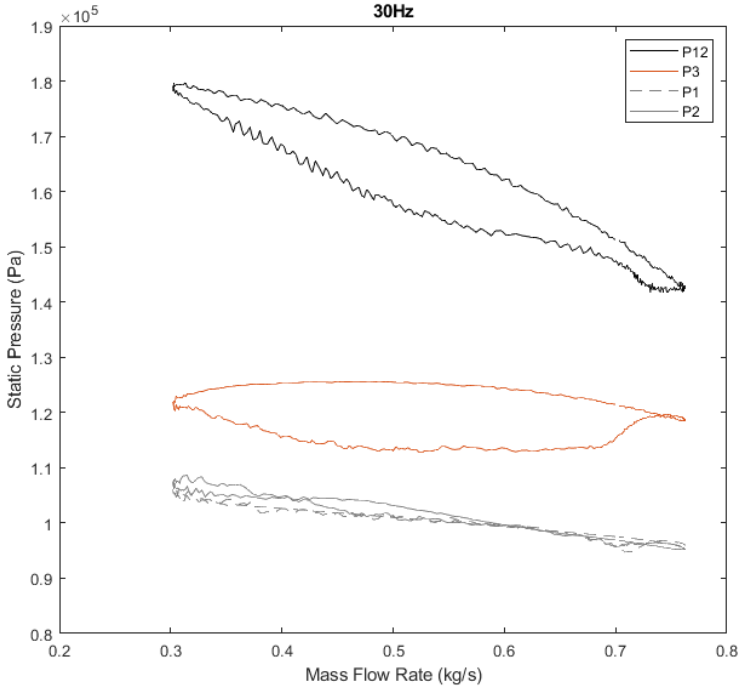


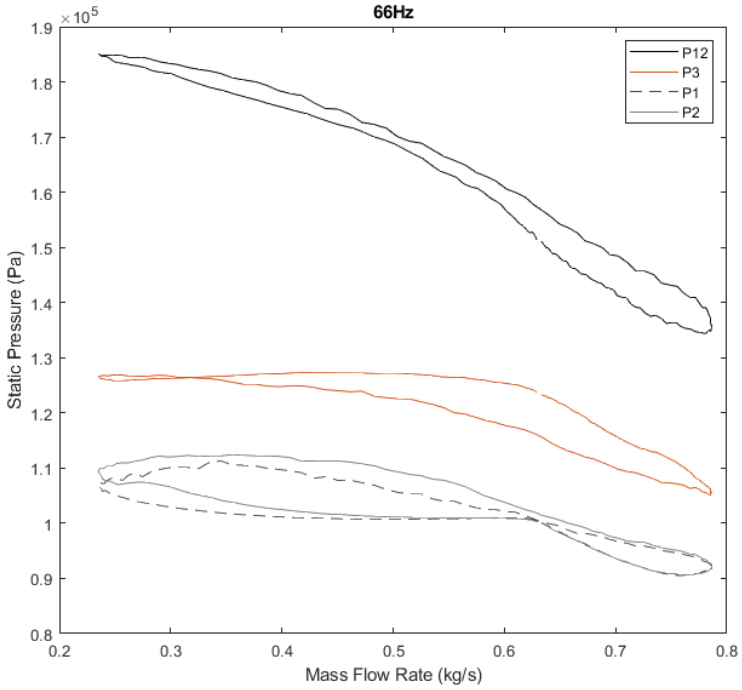
Fig. 4.11 Exit static pressure at impeller stage and volute stage for Peak Pressure (OP A) and peak efficiency flow (OP C) operating points

the impeller exit is distorted at the 30Hz and 66Hz case at OP C compared to OP A, where the impeller exit pressure matches the imposed outlet pressure much more closely.

At peak pressure (OP A), the impeller exit static pressure (P3), follows the imposed exit pressure (P12), there is no deviation in the pulse. This means that the impeller response is in phase with the compressor exit pressure, and there is no localised variation in static pressure for a given pulse. In comparison, at peak efficiency (OP C), the static pressure at the impeller exit (P3) has a different profile and phase to the imposed static pressure at compressor exit (P12). This is likely to lead to a performance deficit due to the resulting localised changes mass flow. Figure 4.12 shows the hysteresis behavior for 30Hz and 66Hz. The static pressure at the different impeller measurement positions is plotted against the inlet mass flow rate. From this hysteresis, it can be inferred that there is a localised filling and emptying effect for the 30Hz case because the mass flow rate is changing internally. Position P3 in Figure 4.12b shows that there is a greater lag in the 30Hz case compared to 66Hz case, where the lag is only for half the cycle.



(a) Impeller Static Pressure Hysteresis for P1 - Impeller Inlet, P2 - Impeller Mid, P3 - Impeller Outlet and P12 - Compressor Outlet for operating condition with 30Hz pulse



(b) Impeller Static Pressure Hysteresis for P1 - Impeller Inlet, P2 - Impeller Mid, P3 - Impeller Outlet and P12 - Compressor Outlet for operating condition with 66Hz pulse

Fig. 4.12 Impeller Static Pressure Hysteresis at compressor with pulsating operating conditions with pulse frequencies of 30Hz (Top) and 66Hz (Bottom)

Quasi-steady and unsteady comparison for OP A and OP C

As previous research has shown [55, 89], the instantaneous performance under exit pulsating flow conditions for a centrifugal compressor is different to the steady performance. For a single operating point, instantaneously, the pressure drops and rises within a single pulse and the mass flow rate rises and falls accordingly. Depending on the physical size of the compressor system, there is a filling and emptying effect which affects the hysteresis behaviour. The inlet mass flow and outlet pressure are out of phase. For any given compressor system, the hysteresis behaviour differs depending on the frequency of pulsation, as the time to react to the imposed pressure reduces with increased frequency.

Figure 4.13 shows the instantaneous hysteresis of compressor performance, given by the instantaneous pressure ratio, at operating points OP A and OP C. Also indicated on the figure is the quasi steady (QS) approximation of the performance for the same operating point. The QS approximation is the performance of the system if the compressor was behaving under steady conditions for the corresponding imposed pressure ratios. It can be seen that, for both operating points A and C the instantaneous behaviour in the 30Hz case differs from the 66Hz case. In the 66Hz case, the hysteresis behaviour is narrower than the 30Hz case; this indicates that the phase shift between the mass flow and the pressure is smaller in 66Hz than the 30Hz case This is much more evident at OP A than at OP C. In the 66Hz case, the instantaneous behaviour is almost similar to the QS behaviour and for 30Hz case, the instantaneous behaviour deviates evenly.

It can also be seen that at OP C, for both frequencies the instantaneous pressure ratio is much higher than QS pressure ratio. When the instantaneous mass flow rate drops to the low-mass flow rate region, the instantaneous pressure ratio is larger than expected compared to QS approximation, so instantaneously, it is possible for the compressor system to generate a pressure ratio that is higher than would be achieved in steady. This high instantaneous pressure achieved under pulsating conditions is what leads to a higher cyclic average calculation of pressure ratio compared to the Q-S approximation. In contrast, in the low flow rate conditions at OP A, the 30Hz and 66Hz instantaneous behaviour spans a much smaller flow range instantaneously compared to OP C.

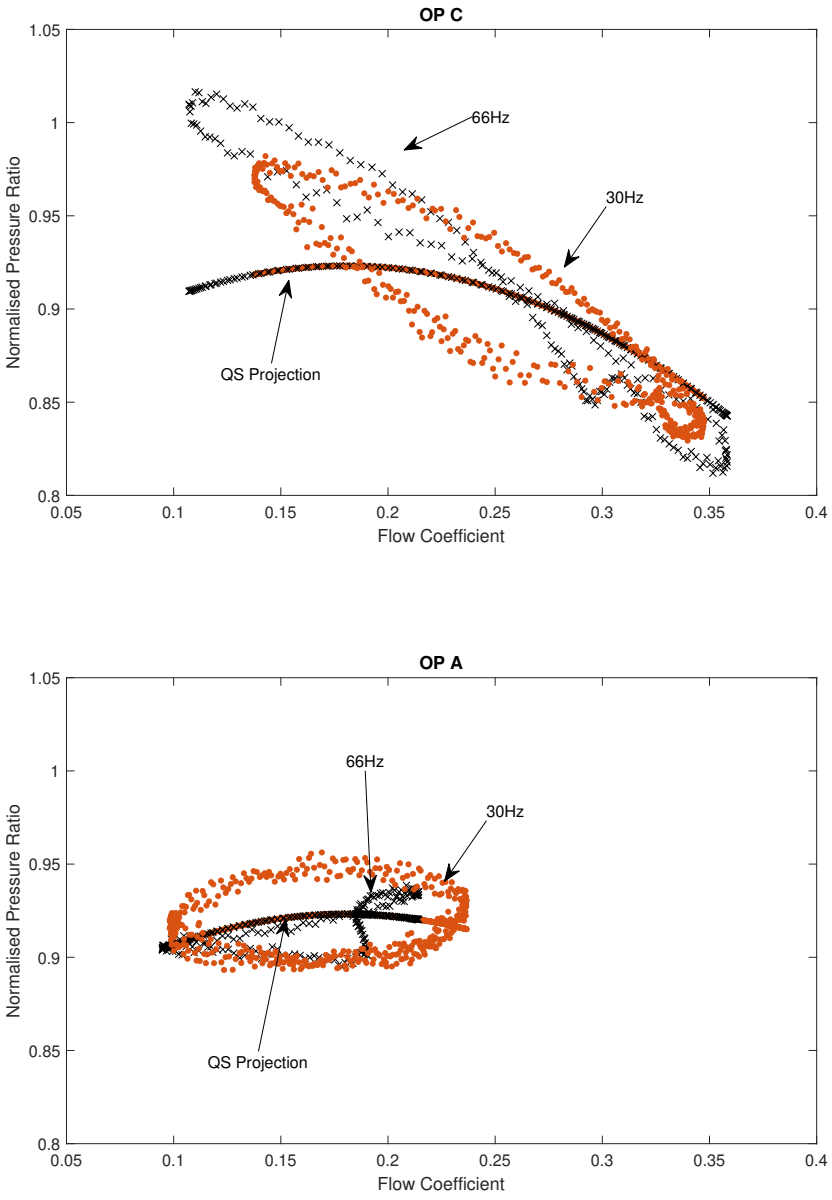


Fig. 4.13 Instantaneous pressure ratio compared to Quasi-steady Pressure Ratio for operating point A (Peak Pressure) and operating point C (Peak Efficiency)

Steady, Quasi-Steady and Unsteady Cycle Average Efficiency

Figure 4.14 shows the steady, average quasi steady and pulsating cyclic average efficiencies for near surge (OP A) and peak efficiency operating point (OP C) As before, the cycle average is representative of the pulsating performance but does not exist in practice. First, it can be seen that at low mass flow rates, the efficiencies predicted by the QS approximation match

the unsteady average efficiency for both 30Hz and 66Hz case. In comparison to steady flow efficiency obtained for this compressor system, the QS efficiencies predicted are all lower than the actual unsteady cyclic average. This can be explained by the instantaneous large pressures achieved at large flows pulling the average up, as seen in Figure 4.14.

It is clear to see the benefit of pulsation with respect to the instantaneous effect on the pressure rise in the system. If behaving in the QS manner, as a result of the large amount of mass flow swept for each instantaneous operating point, the average performance would be much lower. However, in reality, the performance instantaneously is higher than quasi steady performance, pulling the average efficiency for high mass flow rate conditions. In low mass flow rate conditions, the behaviour of compressor system is close to quasi steady because the mass flow swept by the compressor system is much lower. The compressor feels the benefit of the pulsation without the efficiency being compromised. At high flow rates, the efficiency is compromised because the compressor is less capable of producing a work output in the pulsating state.

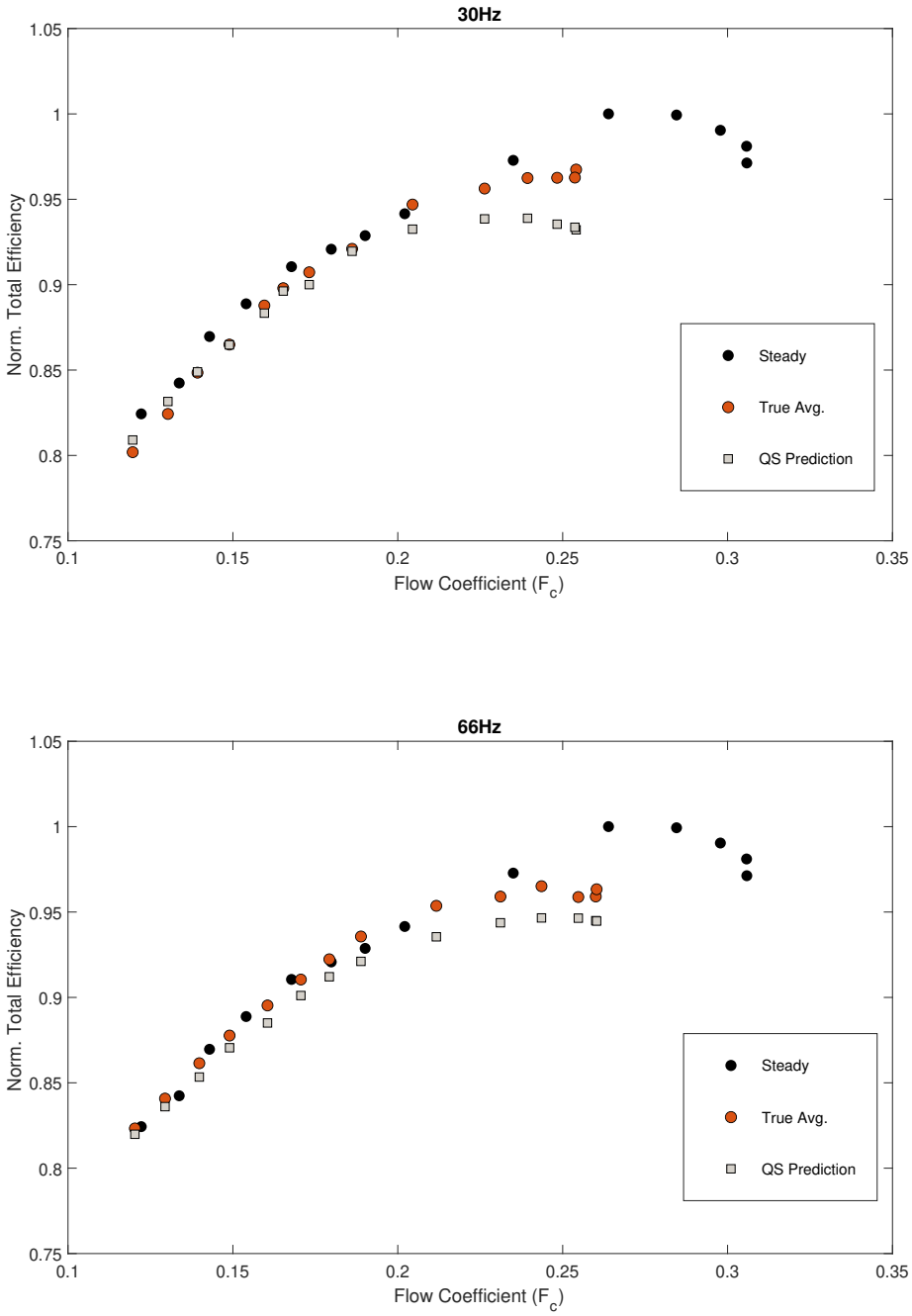


Fig. 4.14 Steady, quasi steady and unsteady average efficiency results for compressor under pulsation at frequencies 30Hz (Top) and 66Hz (Bottom)

4.3 Chapter Summary

In this chapter, the performance of a centrifugal compressor adapted for internal measurements has been studied in detail. The compressor measurement capabilities are briefly described before the results are discussed.

The full operating lines for steady and pulsating flow conditions of 30Hz, 46.7Hz and 66Hz at the target speed of 40,000rpm are compared. When comparing the results at key operating points, it is found that there is a frequency dependence on the performance when cycle average calculations are made. The efficiency drop is greatest for the 66Hz case at the near surge condition, corresponding to operating point A. The greatest performance drop in pulsating conditions occurs at peak efficiency operating point 'OP C' at the large flow rate conditions; the drop is greatest for 30Hz case.

The key findings from this chapter are detailed below.

- As expected, both 30Hz and 66Hz pulses suffer from the drop in efficiency under pulsating flow as well as a drop in performance because the compressor is unable to produce the same amount of work. The performance drop is dependent on the frequency; it is largest when the frequency is the lowest.
- The drop in efficiency is much more significant as mass flow increases due to an increase in system flow inertia. When the compressor flow rate increases, the compressor system has more mass, as the valve closes, a larger amount of flow is halted resulting in an increase in localised pressure, which generates the backpressure wave. This pressure wave amplitude is much larger compared to lower efficiency.
- The cycle average performance shows a deviation from the quasi-steady (QS) predictions as the mass flow rate increases for the 30Hz and 66Hz cases. In both cases for high flow conditions, the cyclic average performance is higher than the QS predictions because instantaneously the pressure rise exceeds the steady performance, resulting in a higher average than predicted. At low mass flow rates, the cycle averaged behaviour closely matches quasi-steady approximations as the mass flow spans a smaller range and the cycle behaviour , if present, is uniformly distributed around the QS prediction.
- The filling and emptying effect of the flow within the volute occurs in different positions depending on the frequency of the pulse. For the 30Hz case, it is occurring near the compressor exit and around the tongue, whereas for the 66Hz case it is occurring further away from the compressor exit. The filling and emptying for the 66Hz case may not be significant because the pulse acts for a shorter time than the 30Hz case, therefore the flow has less time to respond.

- The internal static measurements show that the static pressure trace within the compressor volute at high flow conditions deviate from the outlet imposed pulse and this deviation occurs in different positions for the 30Hz and 66Hz case. The reflection of the pressure wave affects the performance of the impeller in the vicinity of the tongue.

In summary, the average performance at 30Hz and 66Hz is different because of a few differences in the way the volute responds to the imposed pressure, and how it carries this information downstream. It is expected therefore that different passages of the impeller will perform differently and the overall performance (based on the volute exit alone) reflects this difference in performance for the different frequencies. At peak efficiency (OP C) and 30Hz frequency, the stage has the worst performance compared to the other two frequencies due to more significant effects the tongue and the wave reflections that follow.

Chapter 5

Computational Assessments on Compressor Performance

In this chapter, two computational assessments of centrifugal compressor performance are presented. In the first investigation, the near surge operating point is investigated in detail in the impeller inlet region, a critical region for the surge response of a compressor with a vaneless diffuser. The objective of this investigation is to understand the detailed behaviour of the compressor inlet region on the approach to surge. Assessing the differences in flow features in the inlet region can be used to provide insight into why surge is delayed under pulsating conditions in some compressor systems.

In the second investigation, three operating points, corresponding to peak pressure, peak efficiency and large flow points, are computationally investigated. These points are chosen because they correspond to the key operating points of a compressor. Therefore, computationally studying these design points will lead to valuable insights on the compressor behaviour of a pulsation in these different operating states. Similar to the experimental investigation discussed in Chapter 4, this computational investigation highlights the significance of the large flow operating point (OP D) as a drop in efficiency is seen. The flow field for the large flow operating point is analysed in greater detail to identify loss regions in pulsating conditions.

Background

Computational Fluid Dynamics (CFD) has been used for the assessments. CFD is a tool to solve complex physical problems that are theoretically characterised by the Navier Stokes equations. The complex physical problems are mathematically governed by a set of partial

differential equations (PDEs). These PDEs are transformed into algebraic equations that can be numerically solved by discretising the solving domain. It is important to ensure that the solving domain is as representative as possible. This is done by imposing boundary conditions and making sure the discrete elements, i.e. computational mesh, are of the appropriate size.

The CFD analysis for this project is conducted on ANSYS-CFX version R19. The computational model used in this investigation has been pre-validated through previous projects in the research group (see Barrera-Medrano([23]) and the mesh sensitivity studies were also conducted in previous investigations, therefore a mesh sensitivity study has not been recreated. The timesteps and discretisation of the domain is chosen such that the the results are satisfactory for trend studies and insights whilst keeping the simulation time low, this is based on findings from previous investigations on this geometry, see Martos [66] and Barrera-Medrano [23] for further details. The solver is run on the computational facilities of the sponsor of this research, Mitsubishi Heavy Industries Ltd (MHI), all the analysis has been done by the author.

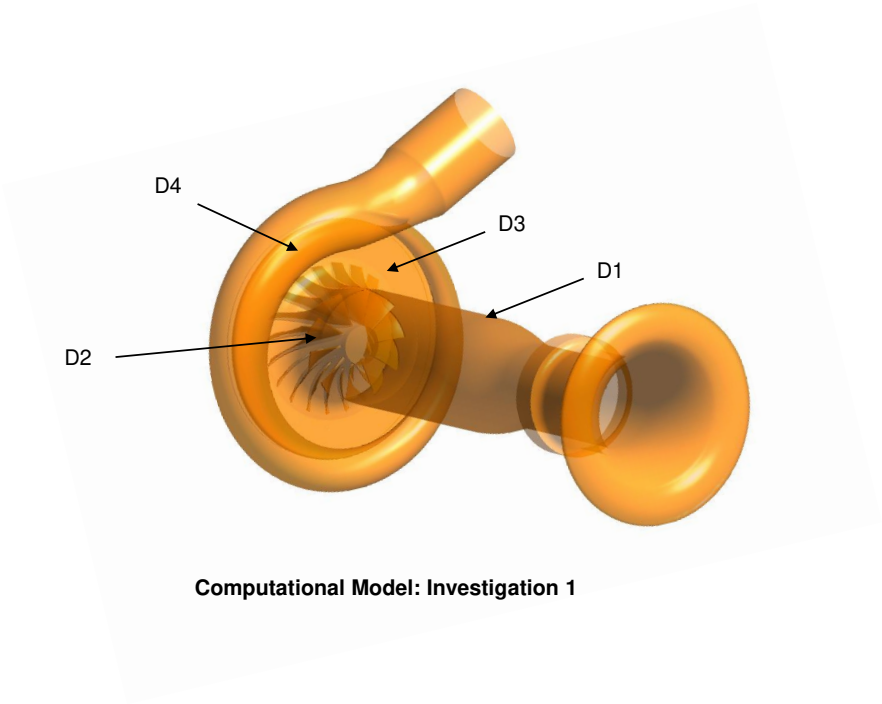
Research limitations

At this stage it is worth highlighting the computational research limitations with respect to the available computational time and resources. Dynamic, unsteady computational simulations are computational resource intensive and as such, only limited operating points that can be studied in the given time-frame of the research project. Additionally, computational simulations also have limitations of the solving method that is used, the discretisation method, and the way boundary conditions or fluid dynamic models are applied. This is overcome through experimental validation of the computational model. Initial assessments based on the computational results can be made and the insights on the detailed flow conditions can lead to new concept designs for the compressor. Because of the limitations to experimental and computational research, a combination of experimental and computational approaches are used to study the compressor behavior and develop the design modifications.

5.1 Computational Set Up

For the computational assessments, a computational model is created of the centrifugal compressor system. The main computational domains for the compressor are the inlet pipe, impeller, vaneless diffuser and scroll, as depicted in figure 5.1. The figure shows two

different inlet pipes analysed. The longer pipe was computed after the experimental facility was modified to enable a better conditioned flow to the impeller.



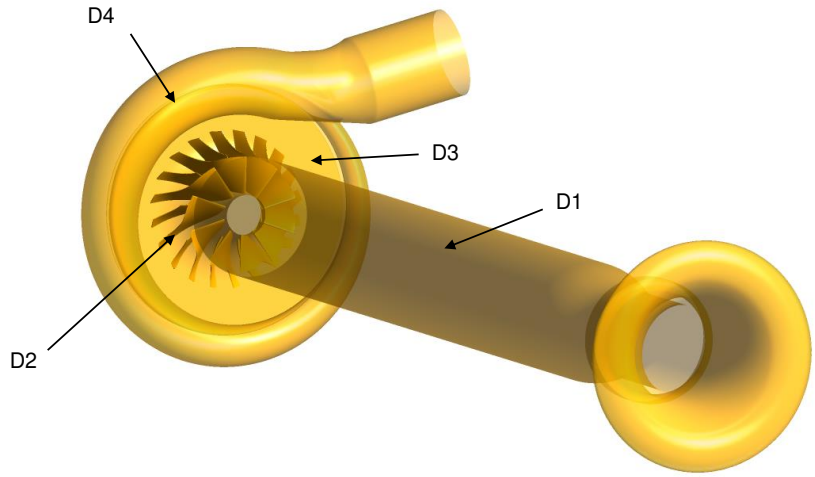


Fig. 5.1 Computational domains modelled in ANSYS-CFX for the two investigations. The domains are: D1 - inlet pipe and bellmouth, D2 impeller, D3 - diffuser and D4 - Volute.

The impeller has 10 main blades and 10 splitter blades. A full stage URANS 3D simulation is conducted in ANSYS CFX. This is a common CFD software used for turbomachinery, as it has imbedded software like 'Turbogrid' which creates meshes specifically for turbomachines. The fluid is set to air as an ideal gas. The walls are modelled as adiabatic, non-slip

Table 5.1 Mesh Statistics for all the domains

Domain	Element Number	Element Type
Inlet (Investigation 1)	3,422,425	Prism/Tetrahedron
Inlet (Investigation 2)	5,484,209	Prism/Tetrahedron
Impeller	6,230,440	Prism/Hexahedron
Diffuser	2,006,385	Prism/Tetrahedron
Volute	2,642,433	Prism/Tetrahedron

and smooth. Transient rotor-stator interfaces are applied between the inlet pipe-impeller inlet and the impeller exit-diffuser inlet. The other interfaces are standard interfaces modeled as fluid to fluid. The rotor is set as a rotating domain with an angular velocity of 40,000rpm. A SST with wall function (k-ω SST) turbulence model is used. The k-ω SST turbulence model is a two equation model that is most commonly used in turbomachinery because it most accurately models the free-stream behaviour within the blade passages as well as the boundary layer close to the blade surfaces. This is because the k-ω SST model is a combination of the k-ω and k-ϵ models, and uses a blended function based on wall distance. The wall distance acts like a switch which allows the turbulence calculations to use k-ϵ models in the far field and k-ω near the target geometry [90].

The global mesh statistics for all the domains are shown in Table 5.1.

It should be noted that a mesh density convergence has been evaluated for three different mesh sizes, coarse (0.1 M Nodes/Pitch), medium (0.6 M Nodes/Pitch) and fine (2.3 M Nodes/Pitch). The observed differences in efficiency values after analysis were less than 0.5 % between the medium and fine mesh density, which lead to the selection of the medium mesh size for the simulations carried out in this research.

The blade passage mesh is shown in Figure 5.2. The mesh is generated in CFX-Turbogrid from hub, shroud and blade profiles. The wall mesh is highly refined in order to obtain accuracy in the shear layer near the walls. For the impeller, the average Y+ of walls is 4.06 and is considered sufficient for use with the k-ω SST turbulence model.

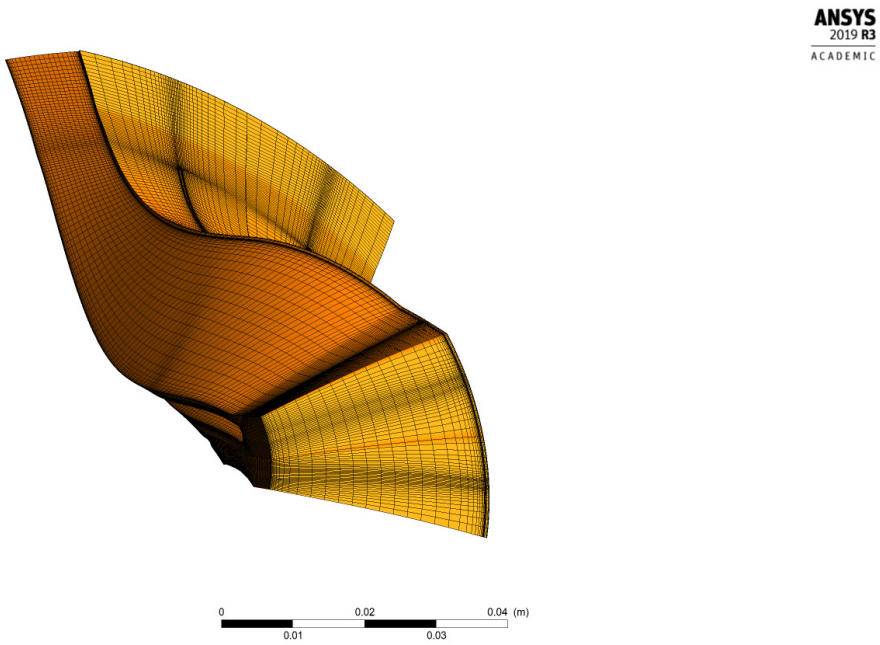


Fig. 5.2 Mesh of a single blade passage in the impeller domain. All other impeller blade passages identical.

For the solver, a time step of 3.75×10^{-5}s is used in order to capture the unsteady phenomena created at the operating speed of the compressor. As it is an unsteady simulation, the simulation does not converge per say, however, a convergence criteria for RMS residuals of each time step (inner loop) has been set to be 10^{-4}.

Boundary Condition

The inlet conditions are set as atmospheric pressure and temperature. The outlet boundary conditions are determined by the data gathered from experiments. To model the outlet conditions, an “opening” boundary condition is applied at the compressor exit. The compressor exit location in the computational model corresponds to outlet measurement plane in the experiment facility. The selection of "opening" as the outlet boundary condition allows the flow to the forward and backward (pulse travelling). This is representative of the real boundary condition seen at the real system (ICE).

The pressure at the compressor exit is captured by the static pressure transducer placed at the measurement plane before the pulse generator. In Chapter 3, it was shown that the pulse generator on the experimental facility recreated engine-like conditions, and the generated pulse at the point of measurement was similar in magnitude ant frequency to the engine pulse. The obtained pressure pulse is shown in Figure 5.3. Since it is directly captured in experiment, the measured static pressure can be applied as the pulsating boundary

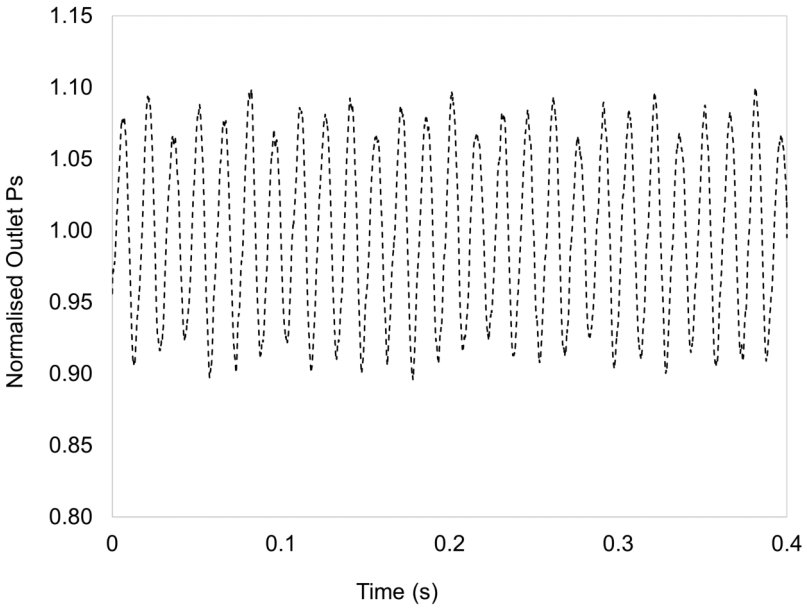


Fig. 5.3 Static pressure boundary condition applied at the outlet based on typical static pressure profile achieved in experiment. This is obtained at the experimental facility.

condition in the computational set-up. The pulsating boundary data is implemented as a User Defined Function (UDF). In each case, the UDF is defined by the data obtained for the design points at the representative pulsating frequencies.

Table 5.2 summarises the boundary conditions for the steady and pulsating flow simulations.

Table 5.2 Boundary Conditions

Simulation Type	Inlet Boundary	Rotor-Stator Interface	Outlet Boundary	Walls
Steady	101325Pa, 293.15K	Frozen rotor (Impeller passages fixed in time)	Fixed Mass Flow	Adiabatic, Non-slip
Pulsating	101325Pa, 293.15K	Transient	Static pressure UDF waveform	Adiabatic, Non-Slip

Calculation Method for Computational Results

Calculation of pressure ratio (PR)

The pressure ratio is calculated from the mass average total pressure at the compressor exit measurement plane over the mass average total pressure at the compressor inlet measurement plane. As it is a simulation, these values are directly available from ANSYS CFX-Post files.

$$\Pi = \frac{P02}{P01} \tag{5.1}$$

Calculation of Efficiency

Efficiency calculations should be conducted in phase with the pressure ratio. To do this, the compressor efficiency is calculated from the power, W, on the impeller blades and the hub.

$$W = \tau\omega = \dot{m}C_p(T_{02} - T_{01}) \tag{5.2}$$

where ω is the rotational speed in radians per second, $\dot{m}$ is the mass flow rate, C_p is the heat capacity at constant pressure, T_{02} is the total temperature at the outlet and T_{01} is the total temperature at the inlet. It can be seen that the power can be written in terms of torque and in terms of temperature rise.

$$\tau = \tau_{blades} + \tau_{hub} \tag{5.3}$$

Therefore, it is possible to estimate an equivalent T_{02}, as the T_{02} measured at the outlet in CFD is often out of phase with the mass flow and is therefore it is inaccurate to use during instantaneous calculations.

$$T_{02} = \frac{P}{\dot{m}C_p} + T_{01} \tag{5.4}$$

The efficiency is therefore,

$$\eta = \frac{T_{02,ad} - T_{01}}{T_{02} - T_{01}} \tag{5.5}$$

Where $T_{02,ad}$ is the adiabatic temperature at the outlet, calculated from:

$$T_{02,ad} = T_{01}(PR)^{\frac{k-1}{k}} \tag{5.6}$$

5.2 Investigation One: Near Surge

This section details the results for the computational flow field assessment of the compressor inlet region when the mass flow rate is reduced to low flow rate conditions near surge. This section is adapted from the publication A.Parikh et al. (2021a).

5.2.1 Operating Point

For this study, the compressor runs at 40,000rpm and the pulse generator at the compressor outlet mimicking the corresponding engine condition runs at a pulse frequency of 66Hz. This corresponds to a Strouhal number or non-dimensional frequency of 0.1 and a non-dimensional pulse amplitude of 0.03. In other words, this means that impeller rotates 10 times during the full cycle of the pulse and varies from mean backpressure by 3.5%. This is the pulse variation at the near surge operating point at low mass flow conditions. The machine Mach number is 0.82.

Figure 5.4 shows the mean performance of the compressor obtained in the aforementioned experimental facility for this speed at steady and pulsating conditions. The operating point of interest is shown on the figure in blue and the surge limit is also highlighted in orange. As it can be seen, the operating point is at low flow rate, high pressure ratio and it is achieved by closing the throttling system to achieve the desired compressor loading conditions. This operating point corresponds to the near surge location which is before deep surge is reached and the performance is still relatively stable; i.e. the dynamic response is a result of the pulse only and does not yet contain any natural frequencies from surge (which would have otherwise caused a coupled response that is difficult to distinguish). The near surge operating point is the last stable operating point. The flow rate results are normalised by volume flow rate, as required by the industrial sponsor to enable publication without sharing commercially sensitive information.

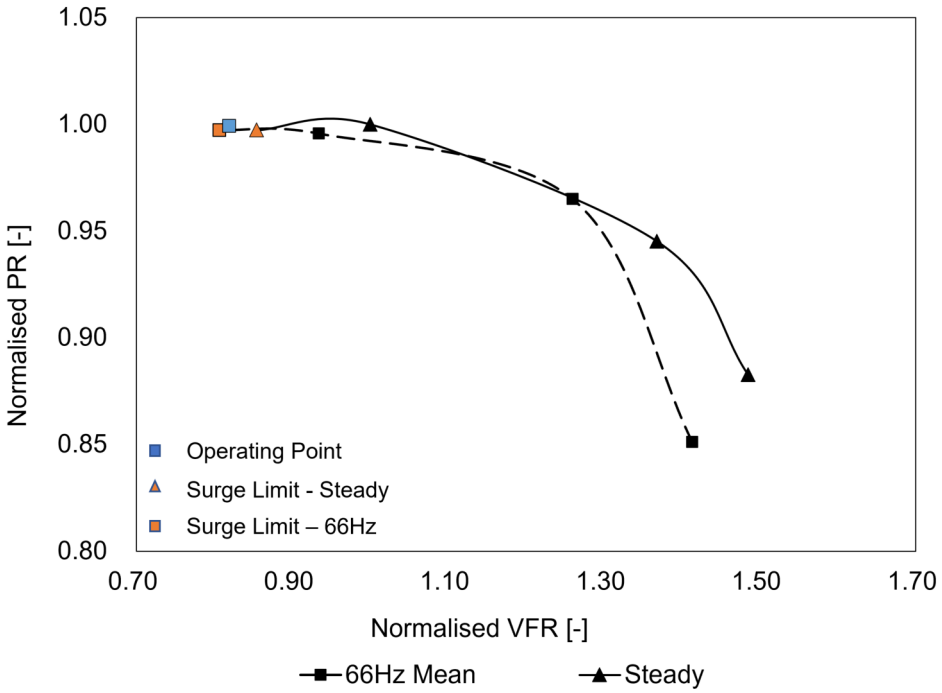


Fig. 5.4 This figure showes the computational outputs for 4 different operating points under steady and pulsating boundary conditions- the operating lines are added on the schematic for clarity. The location of the near surge operating point is represented by the blue-square on the figure.

It was discussed in the literature review that pulsating conditions results in a surge margin improvement (SMI) in some cases and compressor systems. See Equation 2.7 in Chapter 2 for the definition of SMI calculation in this research. The mass flow range also shifts to the left. These results compare well to the previous studies on this compressor, extensively researched by Barrera-Medrano. In effect, there is a noticeable shift in the position of the surge margin. Figure 5.4 shows the difference in the flow rate at which surge initiates in steady conditions vs the pulsating conditions of 66.6Hz. As it can be seen by the figure, the operating point in the 66Hz case moves to the left, towards lower flow rates.

5.2.2 Validation

For the simulated operating point, the difference between the experimental pressure ratio hysteresis and computationally obtained pressure ratio hysteresis is shown in Figure 5.5. This difference is expected because experimental and computational environmental environments are different. For one, the computational environment is adiabatic whereas the experimental environment is not and there are losses. Additionally, the results differ because it is difficult to model all the effects computationally, such as back disk friction. Lastly, the the running speed of compressor facility is usually slightly below 40,000 rpm by around 1000 rpm due to an imposed safety limit to avoid a resonance.

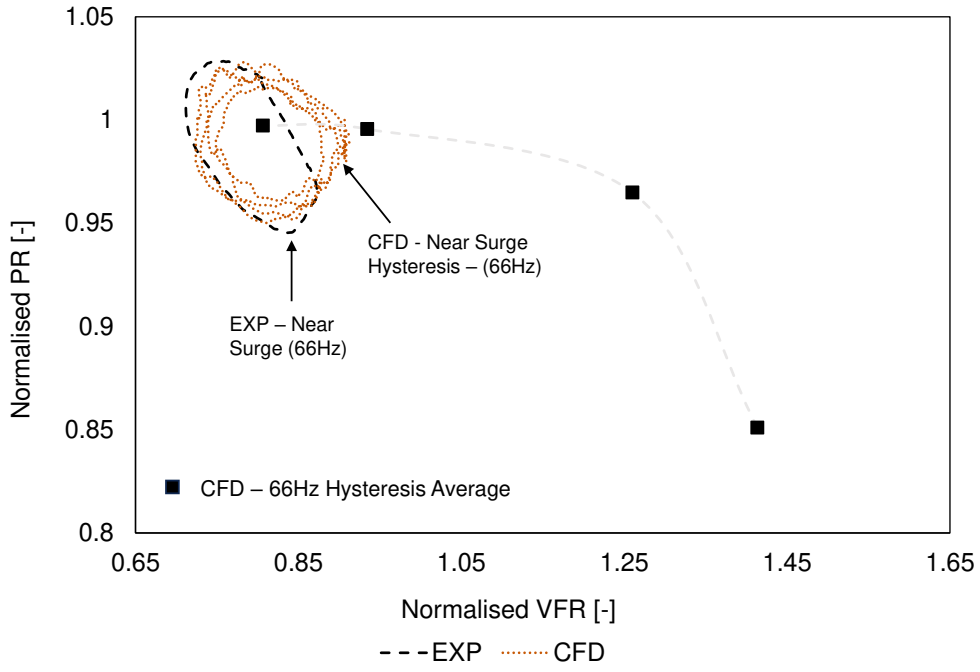


Fig. 5.5 Hysteresis outlet pressure loop between predicted CFD data and measured experimental data (black loop). CFD average results are presented on the graph.

Furthermore, there is flow inertia in the experimental system which is is larger than the computational simulation, as the computational system does not include the piping and plenum. The inertia of the system allows the experimental systems to extend into dynamic states that are difficult to achieve in computational simulations.

In Figure 5.5, even though there is a difference, this is within 2% in performance. The volume flow rate appears to vary in some cases by around 5%; this is due to the aforementioned differences in the compressor system size and system inertia - therefore it is expected that the instantaneous flow rates will not match exactly. The differences in in the CFD results are considered small as they nonetheless follow the trend seen in experimental data, and the hysteresis is of a similar magnitude to the experimental data. Therefore, it is possible to proceed with the computational analysis of the flow field.

5.2.3 Results

As seen in Figure 5.5, there is a an overall hysteresis behaviour stemming from the imposed boundary condition. This hysteresis behaviour is also seen by the impeller. Figure 5.6 shows the variation of the the static pressure at the outlet of the impeller with respect to flow coefficient at the operating point under study. It can be seen that the flow coefficient

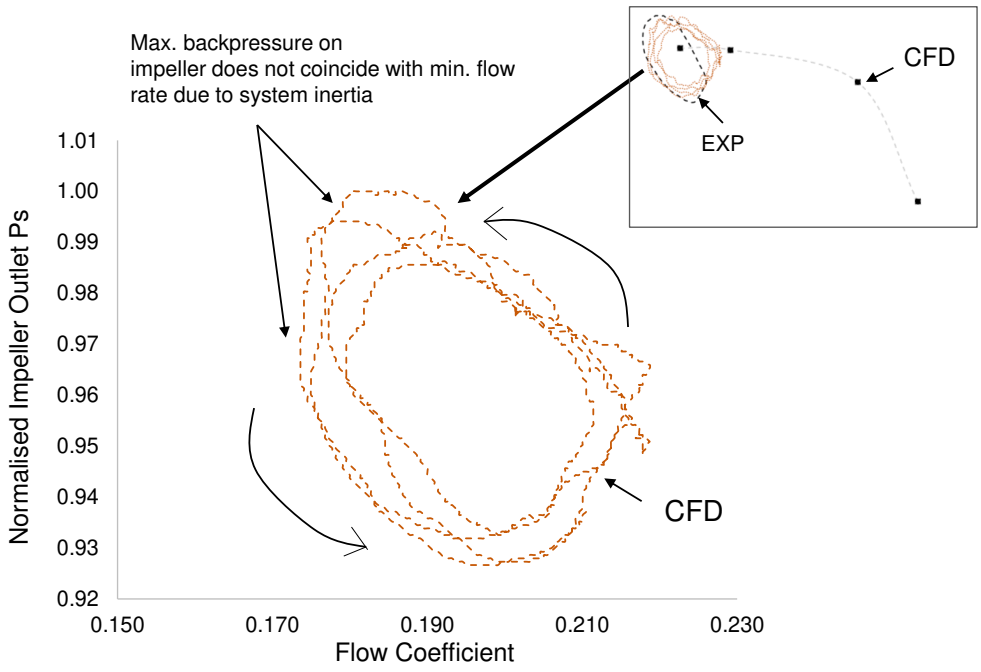


Fig. 5.6 Impeller Outlet static pressure variation with inlet flow coefficient.

and the pressure at impeller outlet are not in phase, this lag is due to the inertia of the system in which the compressor operates, and thus, does not instantaneously respond to the changing back pressure, this is referred to as flow inertia in this thesis. Phase lag was also seen in literature in previous studies on compressor flow.

When looking at this characteristic, it is worth remembering that the back pressure is artificially controlled with a pulse generator and hence the flow adjusts to it; consequently as the back pressure rises, the flow starts to slow down, soon after the back pressure begins to fall and the flow coefficient rises once more. This can also be described qualitatively as a 'filling and emptying' behaviour, that is naturally governed by the size of the system and the amount of mass flow. For this system, and at the operating point of assessment, the inertia of the flow creates a lag of around 30% and the maximum pressure of the pulse does not match the minimum point of the flow, see Figure 5.6. If there was no flow inertia, one would expect these two components to be exactly out of phase, however it is clear that there is a lagging effect. This behaviour of the compressor system to the pulsating backpressure is important as it is the primary indication of the dynamic behaviour and inertial influence that governs the impeller response, and hence, the compressor performance.

Table 5.3 Reference conditions corresponding to points under study for flow coefficient F_c and backpressure BP_s

Label	Timestep	Time	F_c	BP_s
A	825	0.033	High	High but Rising
B	875	0.035	Average	High
C	925	0.037	Low	High
D	975	0.039	Low	High but Falling
E	1075	0.043	Average	Low
F	1175	0.047	High	Low but Rising

Comparison points of the pulse under study

To obtain further details of the flow behaviour, it is important to assess different instances in time during the unsteady cycle. These are termed as transient events which correspond to different backpressure and inlet flow coefficient combinations at a given time. Figure 5.7 shows the backpressure and inlet flow coefficient variation with time. Six critical points corresponding to high, average and low values of the backpressure, BP_s, and inlet flow coefficient, F_c, are compared, as can be seen in Figure 5.7. The six points are referred to by labels A to F. Details for the six instances in time are given in Table 5.3. The selected transient points fall at different backpressure and inlet flow coefficient values so that a comparative assessment of the compressor behaviour at these specific instances in time can be made. Note that, the transient points during one pulse are obtained during the run at intervals of 50 timesteps, each timestep is 0.4μs. These six points are selected as they cover the range of a pulse cycle, and hence, it covers the range of flow and backpressure conditions that the impeller experiences when it is subject to this operating condition.

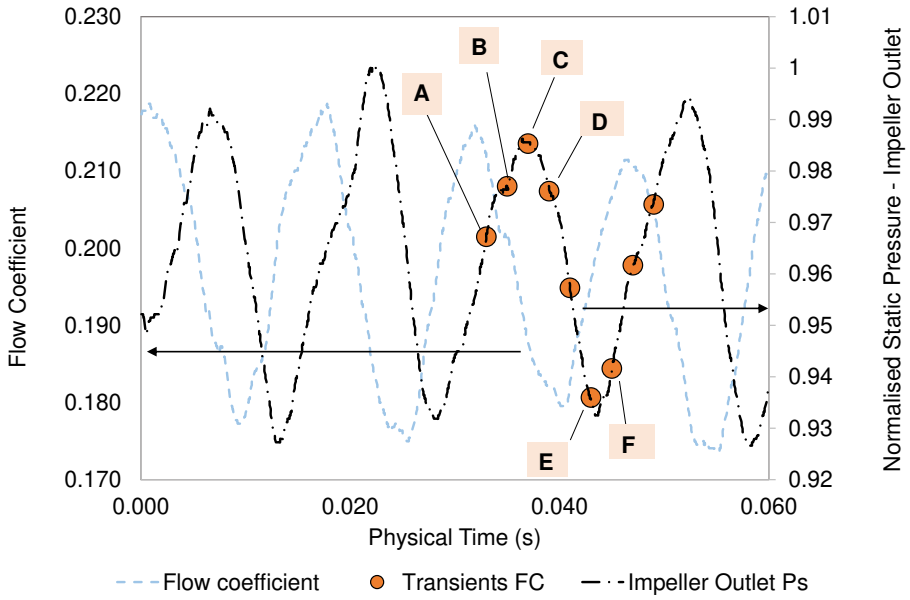


Fig. 5.7 Flow coefficient and normalised static pressure at impeller outlet showing position of all transients obtained. The 6 transients of interest have been labelled by their timesteps.

Inlet Static Pressure Contours

This section discusses the inlet static pressure and Mach number contours at the inlet to the impeller, see Figure 5.8 for reference. Two planes are selected, Plane 1 which falls just before the impeller wheel and Plane 3, which is a short distance from the leading edge, respectively. The tongue location is also shown on the left hand side of the figure for reference.

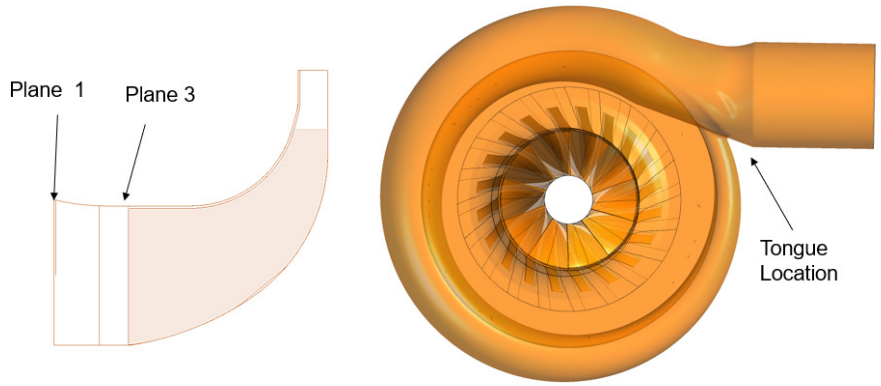


Fig. 5.8 Reference plane positions 1 and 3 corresponding to impeller inlet and blade inlet respectively, and front view of domain showing location of the tongue in Figures 5.9, 5.10, 5.11

Figure 5.9 shows the static pressure contours at Plane 1 for the six time locations described in Figure 5.7. The first difference that can be noticed is the difference in pressure contours between the high backpressure case B and the low backpressure case E (Figure 5.7 for reference). At B, in this plane, the static pressure, P_s, is over 1 Bar for over 50% of the impeller inlet, as indicated by the orange and red contours. In contrast for the E, the majority of the inlet region is below 1 Bar, as indicated by the light green and blue contours. The inlet P_s appears to mirror the backpressure; when the backpressure is low, it is low and the reverse is true when the backpressure is high. It was shown in the literature review that when flow coefficient changes from the design flow coefficient for a given operating point, the incoming flow angle also changes. The static pressure contours show that at the impeller inlet, the flow coefficient and pressure is changing for a given pulse cycle and it can be deduced that the inlet flow angles are also changing from the design intend. At B, the large orange region indicates that a large amount of incoming flow is seeing a high pressure, and this affects majority of the flow entering the compressor.

The second difference in Figure 5.9 are the circular-like regions of low pressure contours, these indicate local regions of acceleration of the flow. These circular regions appear in all instances but they are bigger and more uniform in some, such as D (High but falling BP_s) and E (Low BP_s). In timesteps A and B, these circular flow acceleration contours are smaller and they appear at the tip regions and and have a distorted appearance. As these regions are smaller than the average blade passage, this indicates that they could lead to secondary flows within the blade passage. Additionally, in time instances B, C and D, there are high P_s regions near the tip (red contours above 1 Bar). This high inlet pressure contour is indicative of a region where flow reversal or blockage from stalled flow could be taking place, forcing the flow to locally accelerate around the blockage. For the timestep F (Low BP_s, high F_c), this is not seen.

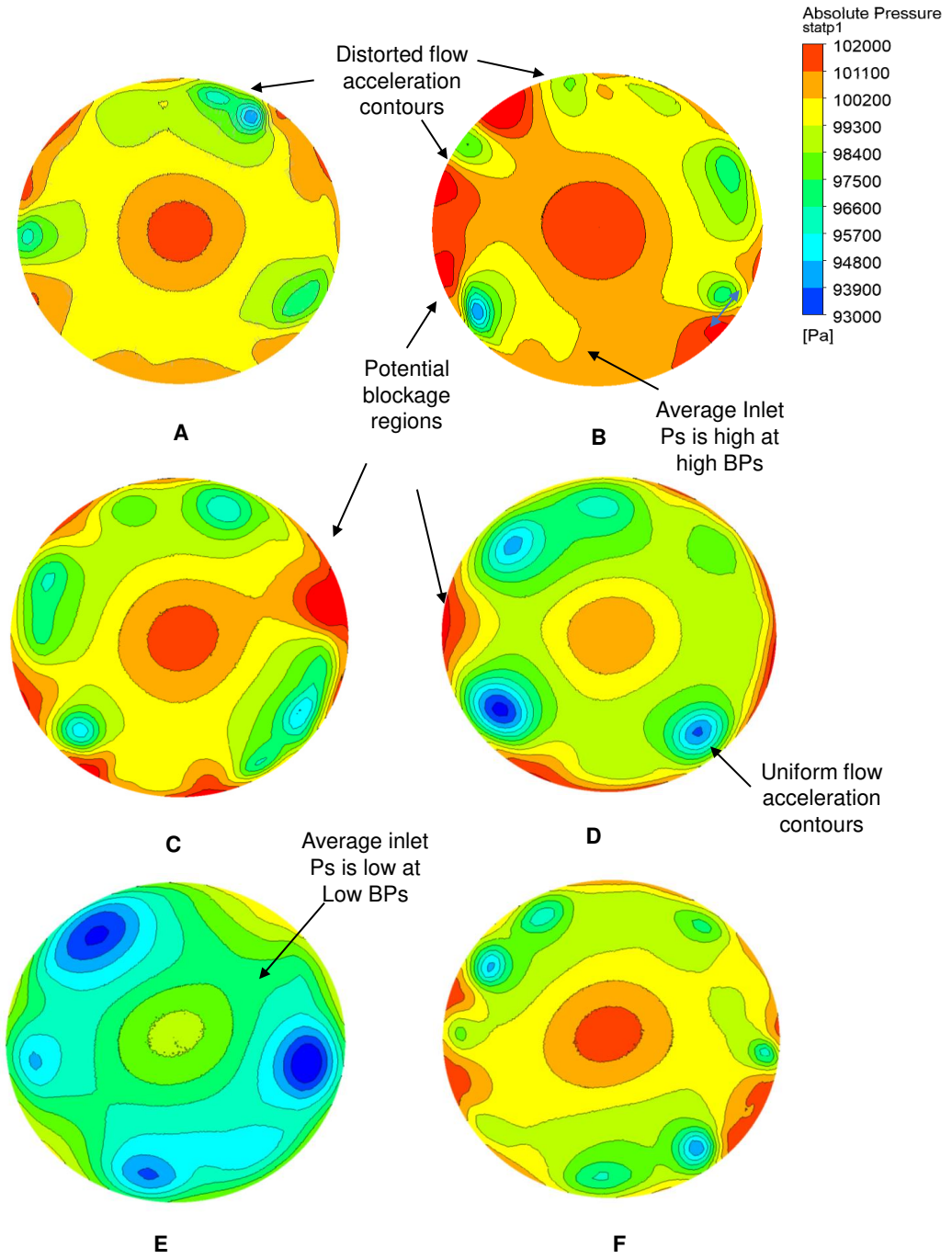


Fig. 5.9 Static pressure contours at Plane 1, impeller inlet, for instantaneous times A - F: A (High F_c, High but Rising BP_s), B (Average F_c, High BP_s) C (Low F_c, High BP_s), D (Low F_c, High but Falling BP_s), E (Average F_c, Low BP_s) and F (High F_c, Low but Rising BP_s)

For the plane very near the impeller leading edge, Plane 3 (Figure 5.8), it is possible to gather more details about the flow behaviour. Figure 5.10 shows the static pressure contours, the suction and pressure surfaces have been annotated. In all the time instances, the suction and pressure surface are similar except in E (Low BP_s), where the suction side has a larger area at a lower absolute pressure than other time instances (indicated by the larger blue region). At some timesteps, such as A and C (high back pressure cases), it is possible to see localised pressure drops near the tip region in the pressure side, these are annotated in the diagram for clarity.

An interesting feature appears near the tongue side for time instances A, B and C (all high back pressures), in A the backpressure is rising, at B it is maximum and at C it is dropping. In one blade passage (refer to the figure), there is a blockage or stall region that appears to grow at A, when the BP_s is rising. In this same region, at B when the BP_s is at its maximum, the blockage is most prominent (indicated by the orange absolute pressure contour). In C, the blockage appears to have dissipated in this section of the passage. The blockage arises from the compressor working against high pressure at the outlet and the flow reversal or stall is triggered in this situation. As the pressure is instantly alleviated, the blockage or flow reversal is reduced.

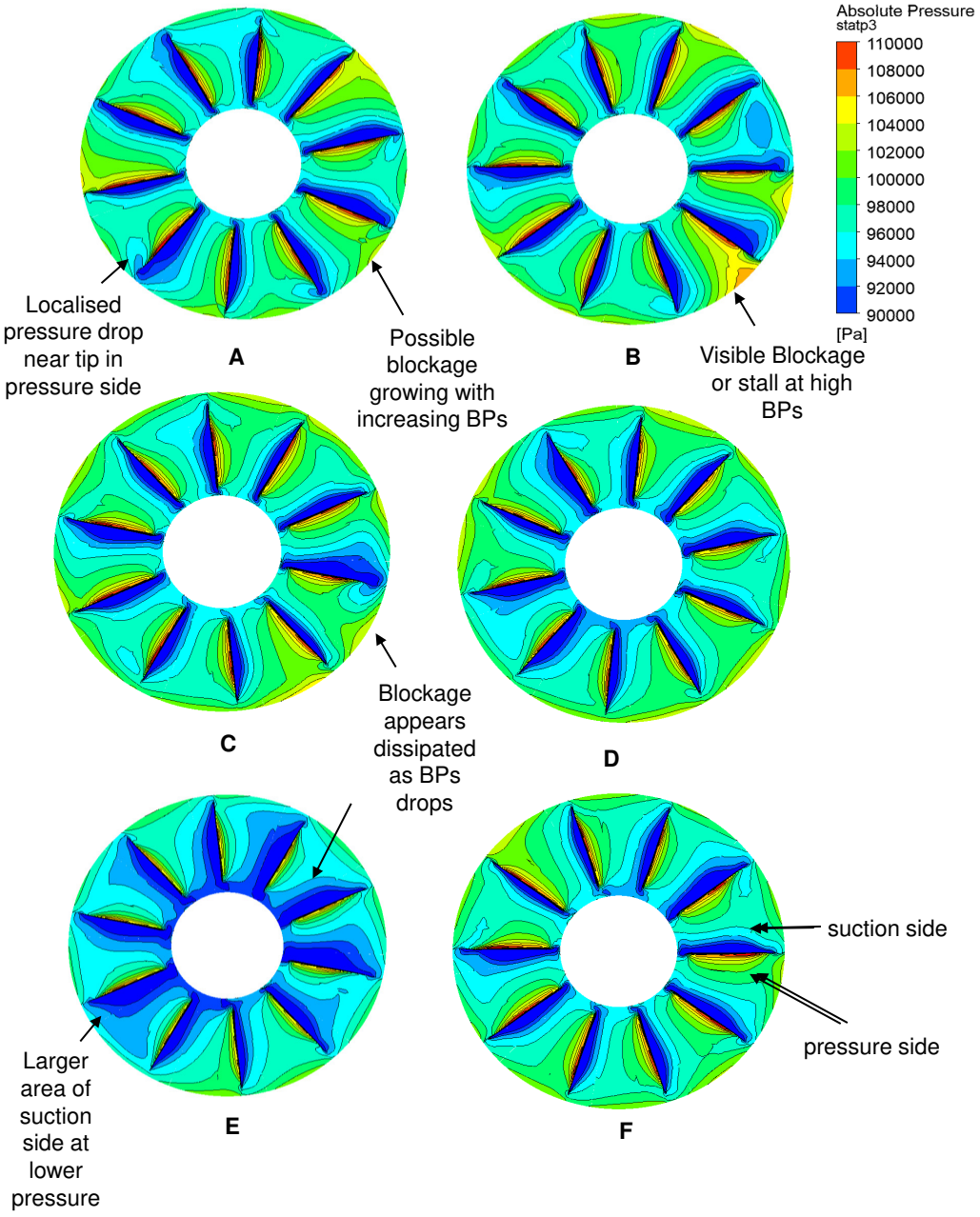


Fig. 5.10 Static pressure contour at Plane 3, blades inlet for all timesteps A-F: A (High F_c, High but Rising BP_s), B (Average F_c, High BP_s) C (Low F_c, High BP_s), D (Low F_c, High but Falling BP_s), E (Average F_c, Low BP_s) and F (High F_c, Low but Rising BP_s)

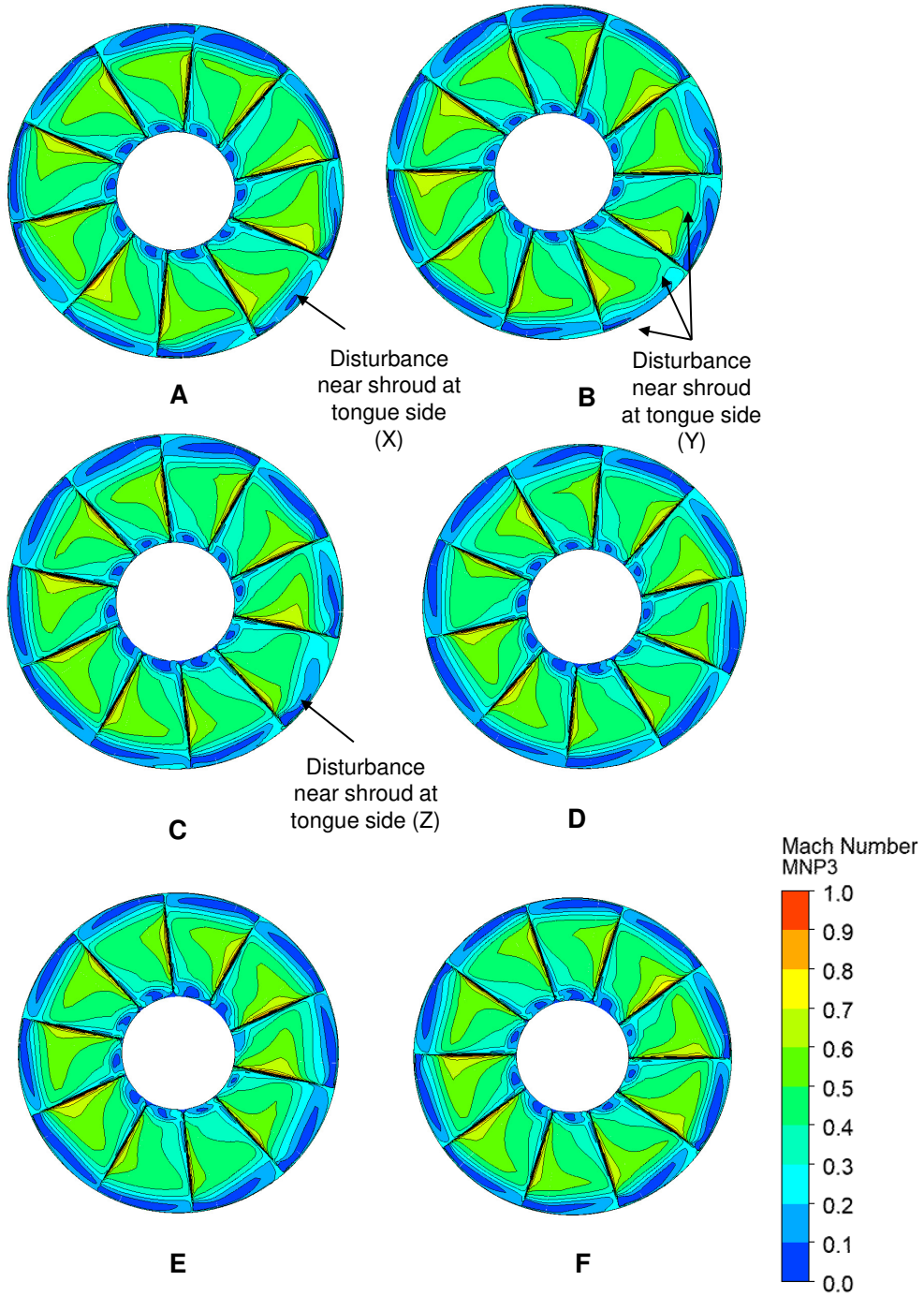


Fig. 5.11 Mach Number contours at Plane 3, blade inlet, for timesteps A-F: A (High F_c, High but Rising BP_s), B (Average F_c, High BP_s) C (Low F_c, High BP_s), D (Low F_c, High but Falling BP_s), E (Average F_c, Low BP_s) and F (High F_c, Low but Rising BP_s)

Figure 5.11 shows the absolute Mach number contours at the blade inlet (Plane 3). There is a low Mach number region at the tip for all instances, this is indicative of stalled and/or reversed flow. Despite of the different flow coefficients for all the points, on average, the Mach number contours are all are very similar. However, in the high backpressure timesteps (A, B and C), it is possible to see the flow disturbance features in the same position as the blocked flow identified in Figure 5.10 shown as features X, Y and Z. This region is on the tongue side of the compressor which is particularly exposed to the change in outlet boundary condition, the disturbances only appear near the shroud.

In summary, Figures 5.9, 5.10 and 5.11 show that there are slight difference in impeller response depending on the variation of backpressure, BP_s, and flow coefficient, F_c. As seen in Figure 5.6, the pressure leads and the flow lags. Therefore, the maximum pressure does not coincide with the minimum flow coefficient. When the backpressure is reduced to a minimum, it is instantaneously less than the mean backpressure by around 3%. The compressor responds as if it were further away from surge as the pressure that was previously building up is alleviated. This could explain why the contour at E (lowest backpressure) is on average at a lower inlet static pressure (indicated by the large blue regions) than the other instances and why the growing blockage in B is dissipated when the pressure drops, allowing the flow field to stabilise again. The performance of the compressor is instantaneously reduced when this happens but it is at the benefit of a pressure relief.

Pitchwise Average Flow Development

Figure 5.12 shows the pitchwise average streamwise velocity projection along the impeller. There is a flow reversal near the tip for all cases, with the majority of flow reversal taking place in the region from the leading edge to 50% location. The high backpressure cases show a greater flow reversal (see A). This near tip recirculation corresponds to the blockage mentioned when discussing Plane 1 static pressure contours (Figure 5.9).

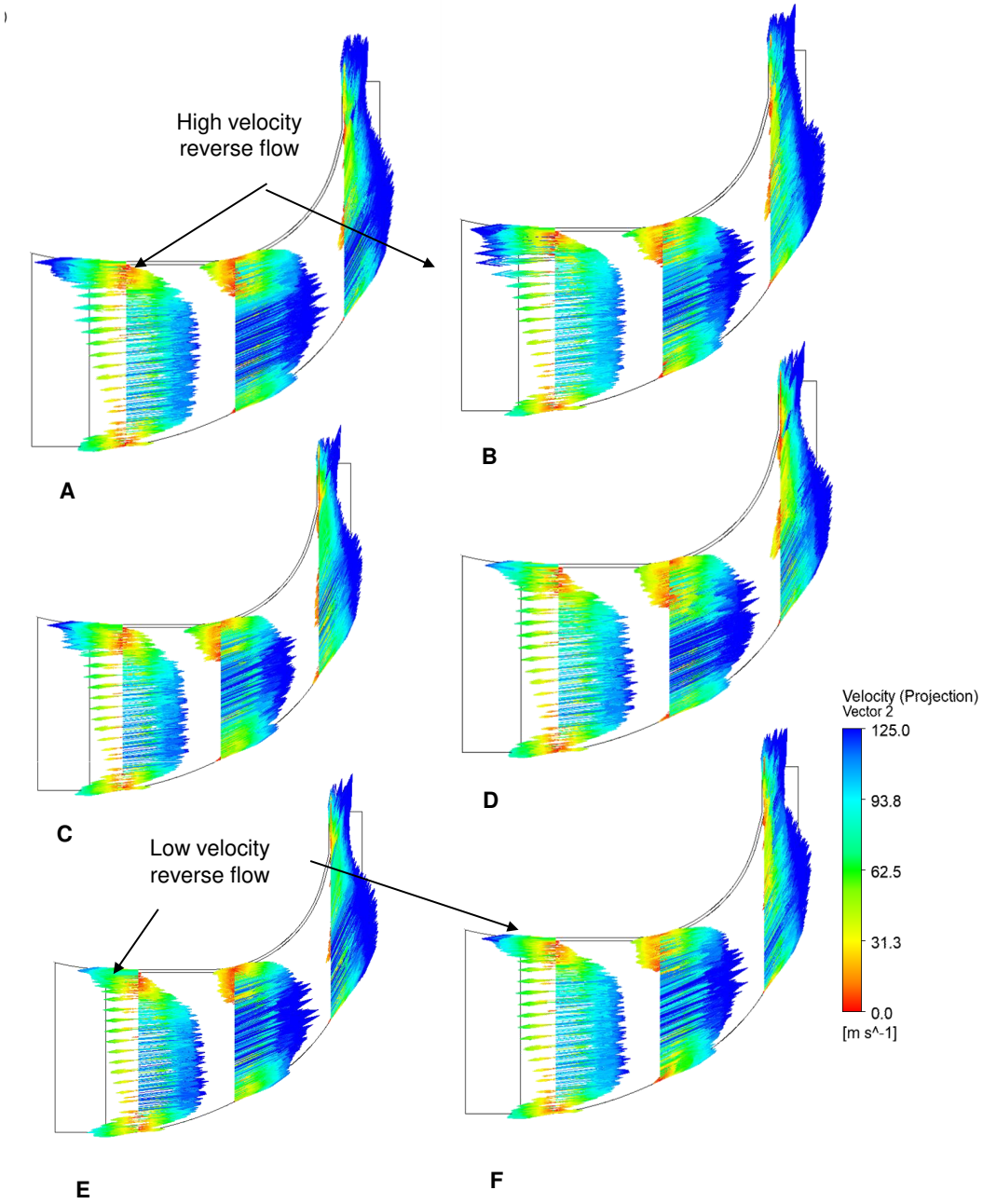


Fig. 5.12 Pitchwise average streamline velocity projection in three locations; blade inlet, midway through impeller and near impeller exit for timesteps A-F: A (High F_c, High but Rising BP_s), B (Average F_c, High BP_s) C (Low F_c, High BP_s), D (Low F_c, High but Falling BP_s), E (Average F_c, Low BP_s) and F (High F_c, Low but Rising BP_s)

Figure 5.13 shows the average static entropy, high value regions correspond to the regions of reverse flow shown in Figure 5.12. It can be seen that the static entropy distribution is similar all time instances. In the low back pressure cases, E and F, there is slightly higher static entropy due to the higher flow velocity of the incoming flow.

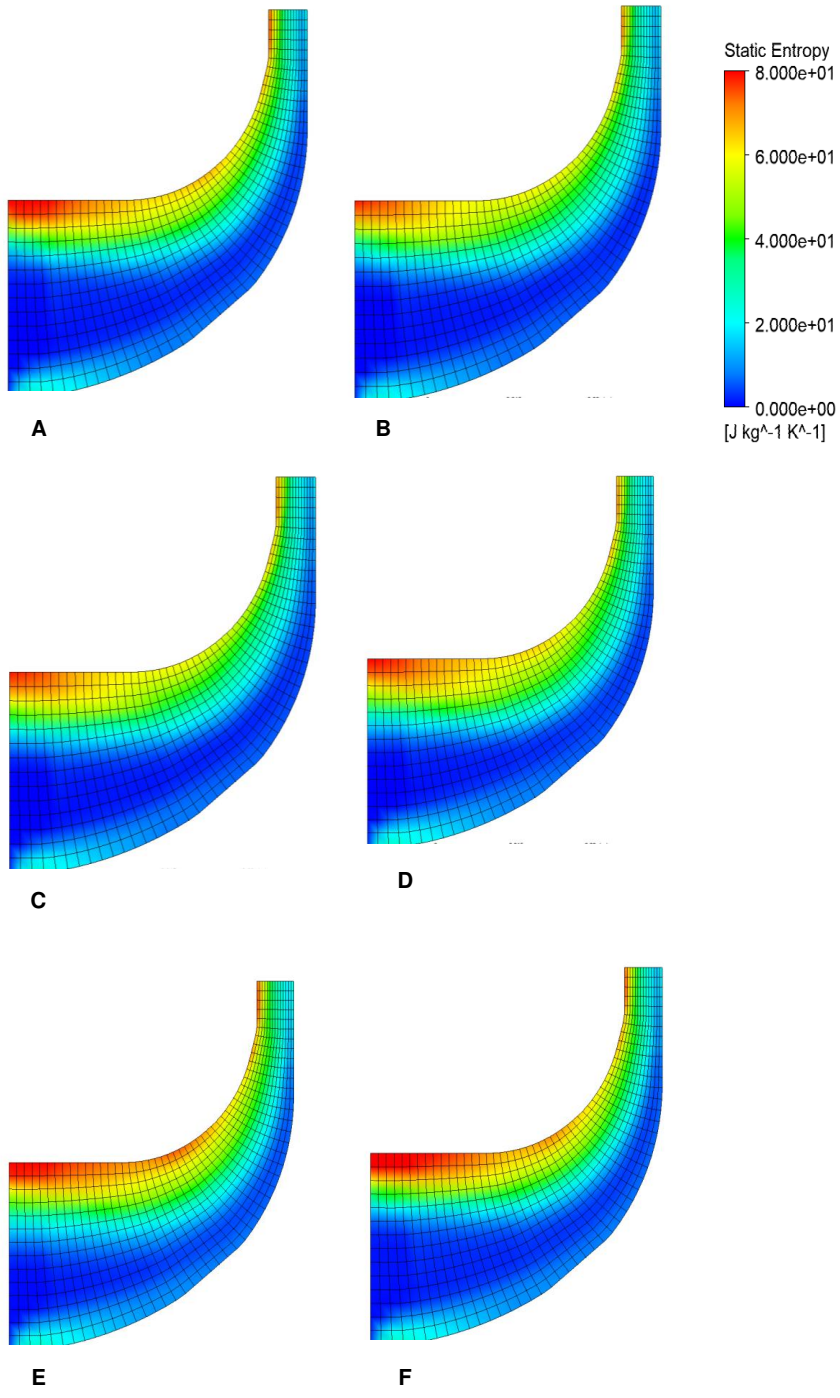


Fig. 5.13 Pitchwise average static entropy contours for timesteps A-F: A (High F_c, High but Rising BP_s), B (Average F_c, High BP_s) C (Low F_c, High BP_s), D (Low F_c, High but Falling BP_s), E (Average F_c, Low BP_s) and F (High F_c, Low but Rising BP_s)

Blade Span Flow Development Near Shroud

In order to further assess the flow and response to the unsteady changes near the shroud, Mach number (MN) and static entropy (SE) are plotted along the span from inlet to exit and displayed in a blade-to-blade view for three spans locations; corresponding to 70, 80 and 90% of the distance from hub to shroud (referred to 0.7, 0.8 and 0.9 respectively in the following discussion).

Figures 5.14 to 5.16 show the variation of Mach number at the six instances. The flow can be seen as highly disturbed, with many areas blocked or stalled. This is indicated by the low Mach number regions at the suction surface of the blade towards the trailing edge of the blade. As the span increases from 0.7 to 0.9, the blade passage gets more and more blocked, with 0.9 span appearing to be completely blocked (as seen by the blue).

The Mach number contour at 0.7 span appear very similar in all cases. In this region, the impeller does not feel the effects of the pulse and the behaviour appears quasi-steady. The Mach number contours for 0.8 and 0.9 span have two key differences between the high backpressure cases, such as A and B and low backpressure case E. Firstly, in the high backpressure cases, the flow is more disturbed. In contrast, at E, for 0.8 and 0.9 spans, the blade passage has a similar appearance for all passages. As mentioned before, the drop in backpressure is favourable for the compressor as it pulls the overall system behaviour away from the surge point, to a higher flow rate and a lower pressure ratio. When this happens, the inlet flow angles change correspondingly and the reverse flow reduces. Therefore, a more favourable flow alignment to the blade passage is obtained. The fact that the backpressure at the impeller outlet is directing the flow angle is further supported by the contours at A (High BP_s and F (Low BP_s). It is clear that for 0.8 and 0.9 spans, the flow field is different despite the flow coefficient of both instances being the same; F is much more uniform, whereas A is more disturbed. Within the inlet region of A and B, there are clear areas of local flow acceleration indicated by the green Mach number contours (Mach number of around 0.5-0.55).

As was seen in Figure 5.10 earlier in this section, around the tongue location, there are blockages in some blade passages. The flow has to accelerate around these blockages. These blocked sections cause the flow to divert and accelerate at a different span location. The fast flowing flow at the inlet interacts with the stalled field downstream in the passage. This could explain why the stalled regions for A and B have a disturbed appearance and vary from blade passage to blade passage, in comparison to D and E.

There are also some signs of separated flow near the suction side directly after the flow acceleration region (B in Figure 5.15). This indicates that there could be an interaction

between the accelerated flow and the separated flow on the suction surface. Although in all timesteps, the flow on the suction surface is similarly separated and the blade passage is blocked, the Mach Number contours show that the main difference seems to be the variation in stalled regions between blade passages and presence of local flow acceleration. The primary effect of this to affect the stability of the flow within the blade passage. If the flow is subject to high recirculation, flow acceleration and the interaction, it leads to instabilities, which can grow and further destabilise the flow field.

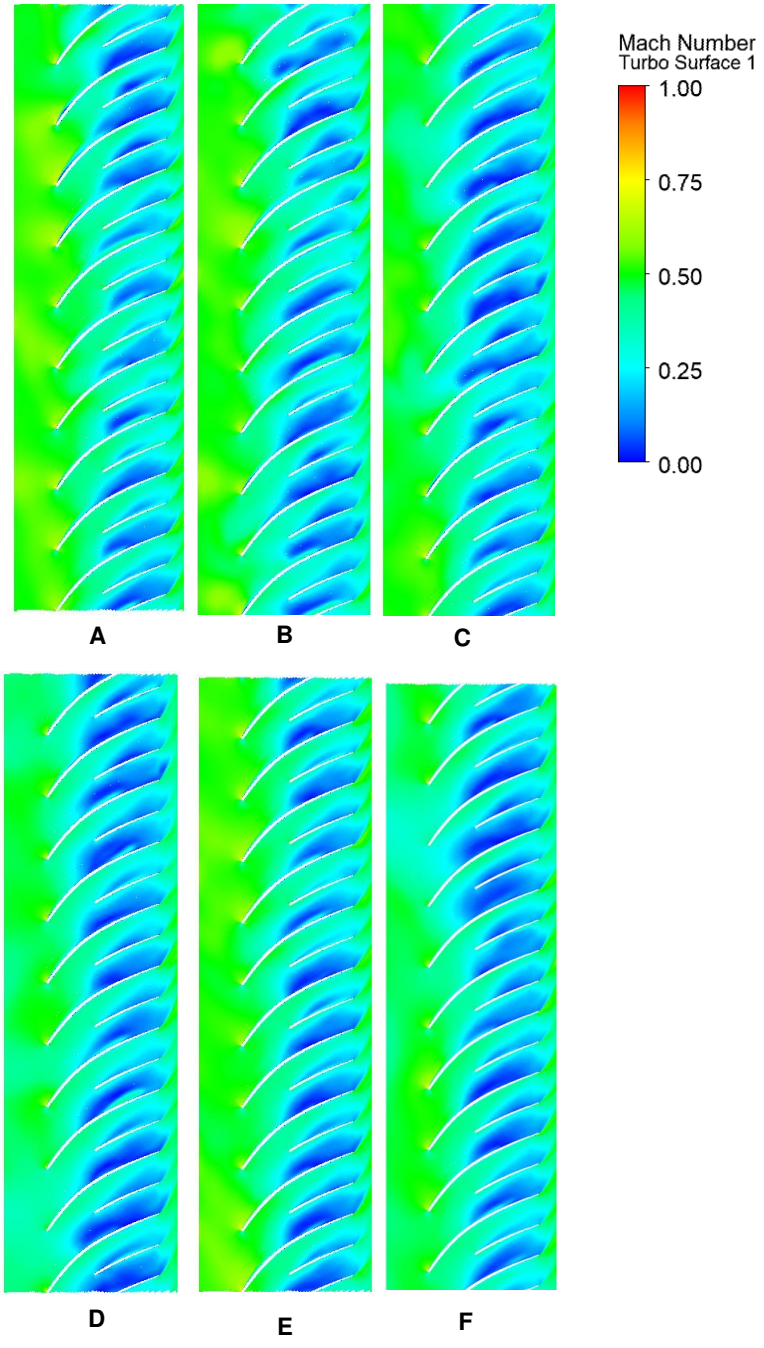


Fig. 5.14 Mach number contours at blade span 0.7 for timesteps A-F: A (High F_c, High but Rising BP_s), B (Average F_c, High BP_s) C (Low F_c, High BP_s), D (Low F_c, High but Falling BP_s), E (Average F_c, Low BP_s) and F (High F_c, Low but Rising BP_s)

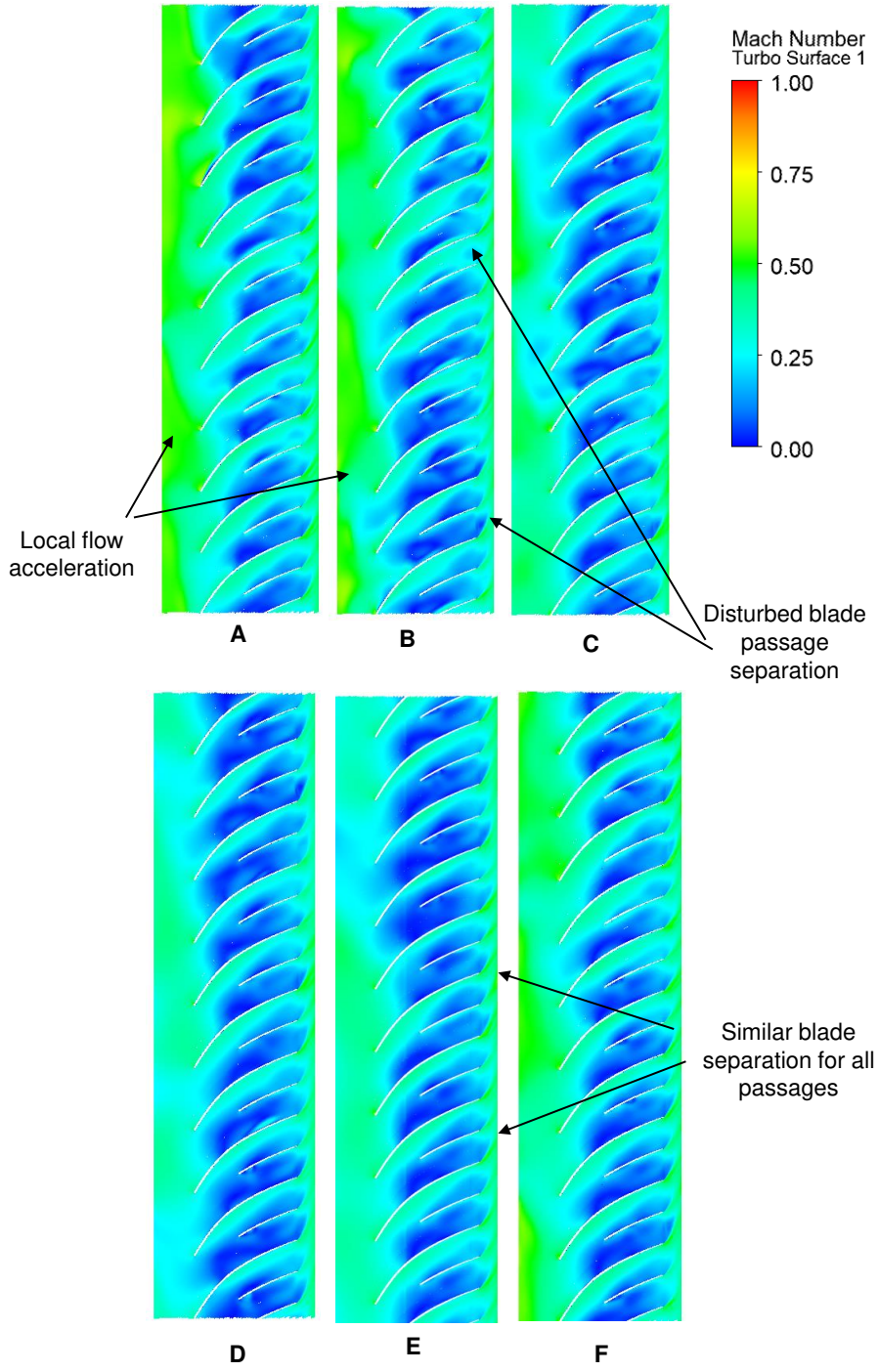


Fig. 5.15 Mach number contour at blade span 0.8 for timesteps A-F: A (High F_c, High but Rising BP_s), B (Average F_c, High BP_s) C (Low F_c, High BP_s), D (Low F_c, High but Falling BP_s), E (Average F_c, Low BP_s) and F (High F_c, Low but Rising BP_s)

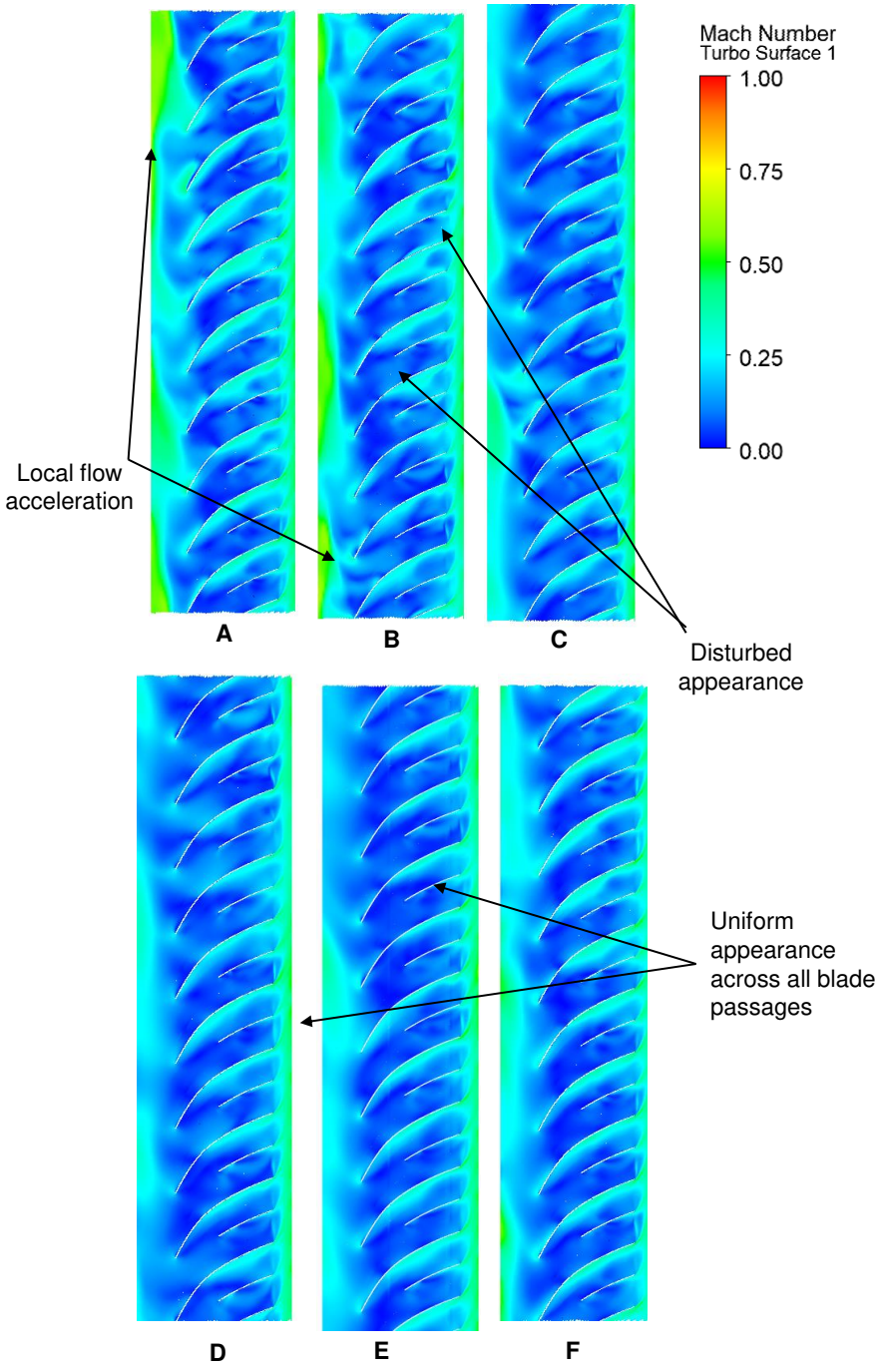


Fig. 5.16 Mach number contour at blade span 0.9 for timesteps A-F: A (High F_c, High but Rising BP_s), B (Average F_c, High BP_s) C (Low F_c, High BP_s), D (Low F_c, High but Falling BP_s), E (Average F_c, Low BP_s) and F (High F_c, Low but Rising BP_s)

Static Entropy in Blade Passage Near Shroud

Figures 5.17 and 5.18 show the variation in static entropy (SE) in the impeller domain from inlet to outlet using the blade to blade view for 0.8 and 0.9 span. There are visible regions of relative high SE that are mainly at the suction surface and near the trailing edge for all timesteps.

Generally, there is higher entropy throughout all the blade passages in the low backpressure case, as seen in Figure 5.13. In the 0.9 span, A shows the most visible static entropy variation, as the static entropy in some blade passages varies from 0 to 100. It is possible that this is because this time instance falls just after the peak of the flow coefficient, and the backpressure is now rising again, so the flow is rapidly decelerating to respond to the rising backpressure.

At 0.8 span, E (corresponding to minimum backpressure) and D (corresponding to minimum flow coefficient) both have almost uniform static entropy. In comparison, A and B have less average static entropy over all and large difference in static entropy regions between the different blade passages. The regions where SE is lower than the average corresponds to the region of local flow acceleration at the inlet. This is most prominent at 0.9. Again, the disturbances present in A and B are not present at E. It is interesting to assess what static entropy in these specific pockets could be indicating about the overall flow stability. Whereas in the case of E and C the higher static entropy is a consequence of the fact that the flow is overall moving faster, in the case of A and B, these regions are a consequence of the local flow acceleration around the developing stall cells.

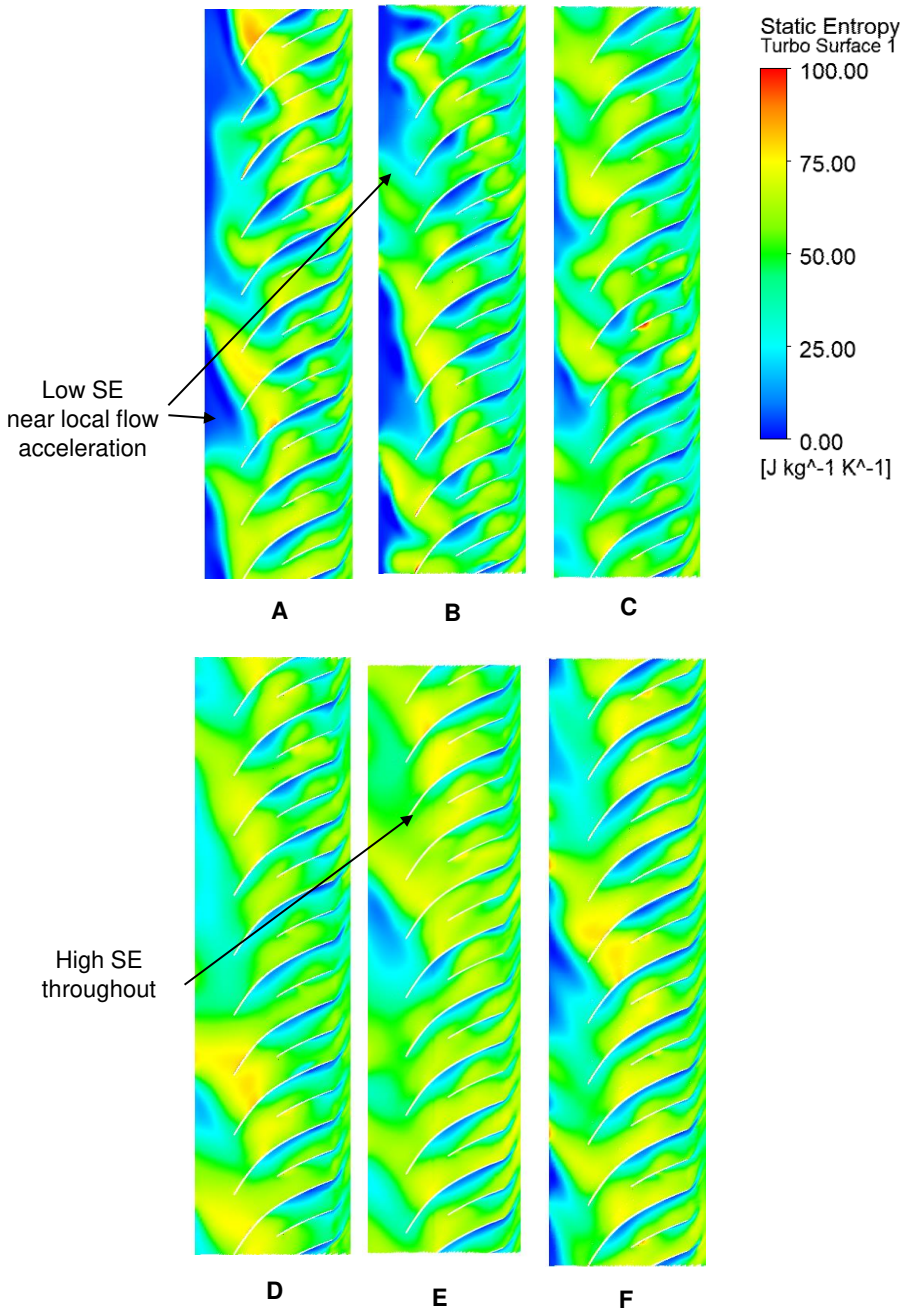


Fig. 5.17 Static entropy contour at blade span 0.8 for timesteps A-F: A (High F_c, High but Rising BP_s), B (Average F_c, High BP_s) C (Low F_c, High BP_s), D (Low F_c, High but Falling BP_s), E (Average F_c, Low BP_s) and F (High F_c, Low but Rising BP_s)

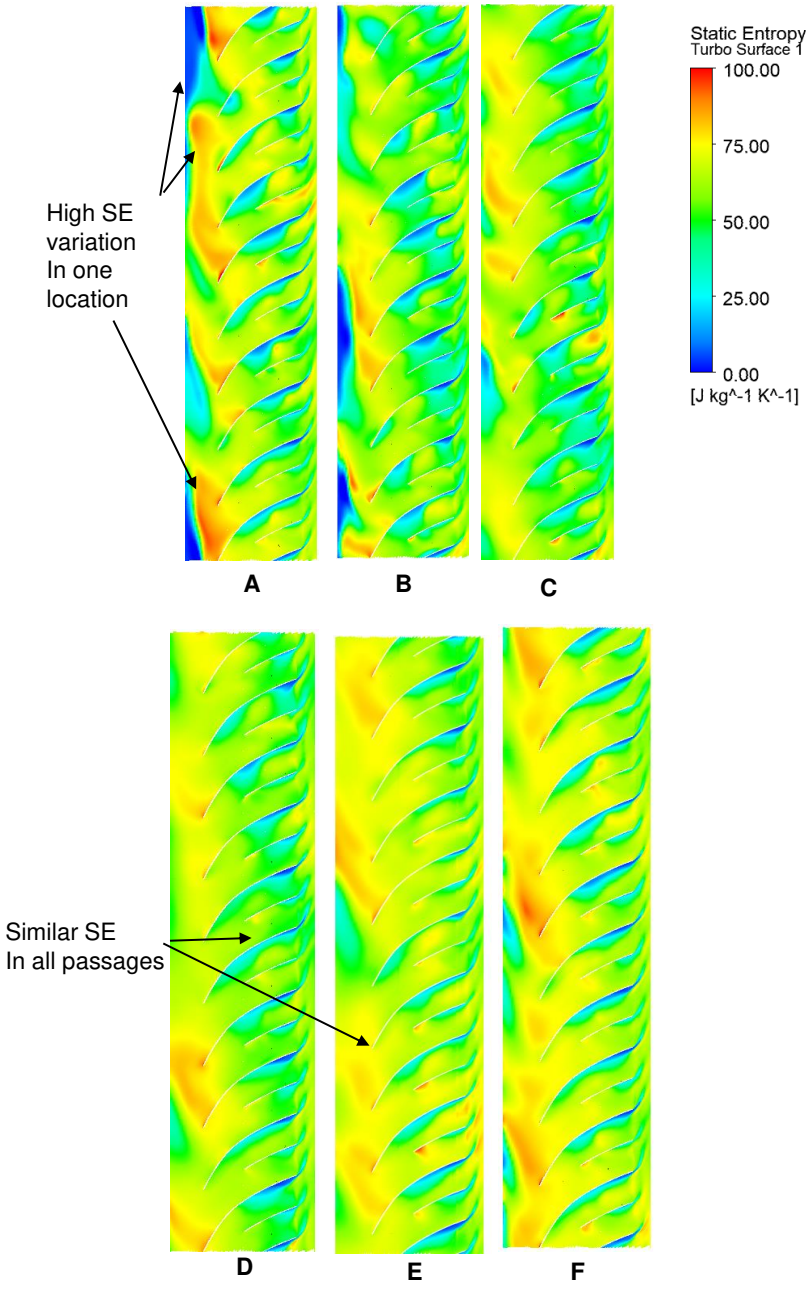


Fig. 5.18 Static entropy contour at blade span 0.9 for timesteps A-F: A (High F_c, High but Rising BP_s), B (Average F_c, High BP_s) C (Low F_c, High BP_s), D (Low F_c, High but Falling BP_s), E (Average F_c, Low BP_s) and F (High F_c, Low but Rising BP_s).Location X and Y indicate high SE in areas of local flow acceleration at the inlet.

5.2.4 Discussion

This investigation studied the local effect of the pulsating flow on the impeller inlet region, however, it is interesting to assess if the surge margin improvement (which is a global system phenomena) is influenced by the local performance that has been discussed in this section. The compressor under study is shown to be able to operate under unsteady conditions in mass flow rates lower than it would have under pure steady flow, see Figure 5.4. For this to be the case, the local flow field and operation must be favourable to the compressor. In other words, the local compressor flow field is promoting stable behaviour of the compressor.

One of the things that should be taken into consideration is the flow inertia, which is different under steady and pulsating flow. In steady situations, as the backpressure rises, the mass flow rate also reduces. The backpressure is never alleviated, so the pressure builds up and acts against the compressor operation. In pulsating conditions, there is an oscillating, dynamic response. Instead of a single operating point, there is a hysteresis in the performance, see Figure 5.5. Although the average mass flow rate drops with rising pressure, instantaneously the mass flow rate rises and falls in response to the changing backpressure. For this particular system, there are inertial 'filling and emptying' effects. It is found that at the impeller there is a lag between the pressure leads and the flow. Because there is a time delay in the response, the minimum flow rate does not coincide with the maximum backpressure, see Figure 5.6. By the time the flow has fully decelerated, the backpressure has already begun to reduce - and it does not act against the compressor with as much intensity as it would in a purely steady case.

The high backpressure regions are more unstable, with more disturbances and therefore much more likely to develop stall cells. In steady and quasi-steady performances, where the backpressure is persistently high, the stall cells have much more time to progress into large blockages and eventually surge. In the pulsating simulation, growing stall cells, which would destabilise the flow field, such as Feature X seen in Figure 5.10, does not seem to develop into a bigger stall cell. When the pressure drops, this stall cells and the corresponding flow acceleration decreases and the flow appears visibly more stable and much less disturbed, such as in D (Low F_c, High but Falling BP_s) and E (Average F_c, Low BP_s). There are some instantaneous states that have more flow disturbances than other states. These states correspond to high backpressure on the impeller exit - and consequently lower flow coefficients. However, these states are instantly alleviated when the backpressure drops. Static Entropy and Mach Number contours show that majority of the disturbances appear near the shroud region in the 90% span.

The findings of this investigation are for a single pulsating frequency, amplitude and compressor speed. There is a relationship between all three factors; a large or smaller pulse amplitude could amplify or reduce the effects that have been seen in the aforementioned sections. For a compressor with a smaller Strouhal number, but relatively large amplitude change, the physical time that the impeller needs to feel the pulse increases, and the growing stall cells may not dissipate fast enough, resulting in no overall benefit in surge margin. If the amplitude is small, the physical time relevance may not matter as the change from mean backpressure would be small. In contrast, for large Strouhal numbers, the physical time the impeller needs to feel the pulse decreases, and if the amplitude is small, the change may be too fast for the impeller to detect it. However, if the amplitude is large, this change may be too abrupt, and trigger instabilities sooner. It can be stated that the impeller behaviour will be different under different pulse conditions - The physical time that the impeller sees the pulse and the amplitude of that pulse are likely to affect the localised behaviour of the impeller.

5.3 Investigation Two: Analysis at Key Operating Points

This section details the results for the computational assessment of the compressor for the three operating points of interest (peak pressure, peak efficiency and large flow). The specific focus of this investigation is to assess the differences in performance at the different operating points. After the initial analysis, the large flow operating point is assessed in further detail to understand the losses in the compressor and the corresponding loss regions. This computational investigation builds on the work presented in the experimental detailed investigation discussed in Chapter 4. In the experimental investigation, it was found that at large mass flow rates, the efficiency reduces from equivalent steady conditions. Studying this operating point computationally can provide further insights into how or why the efficiency drops.

5.3.1 Operating Points

For this analysis, the compressor running speed is set to 40,000 rpm for all the operating points of interest. Figure 5.19 shows a schematic of the key operating points on a typical operating line for 40k rpm. The average pressure ratio, mass flow rate and the governing pulse frequency is also provided on the figure.

	OP B	OP C	OP D
Description	Peak Pressure	Peak Efficiency	Large Flow
Ave. Pressure Ratio	1.73	1.67	1.48
Ave. Flowrate (kg/s)	0.46	0.62	0.78
Frequency (Hz)	30	43.7	66

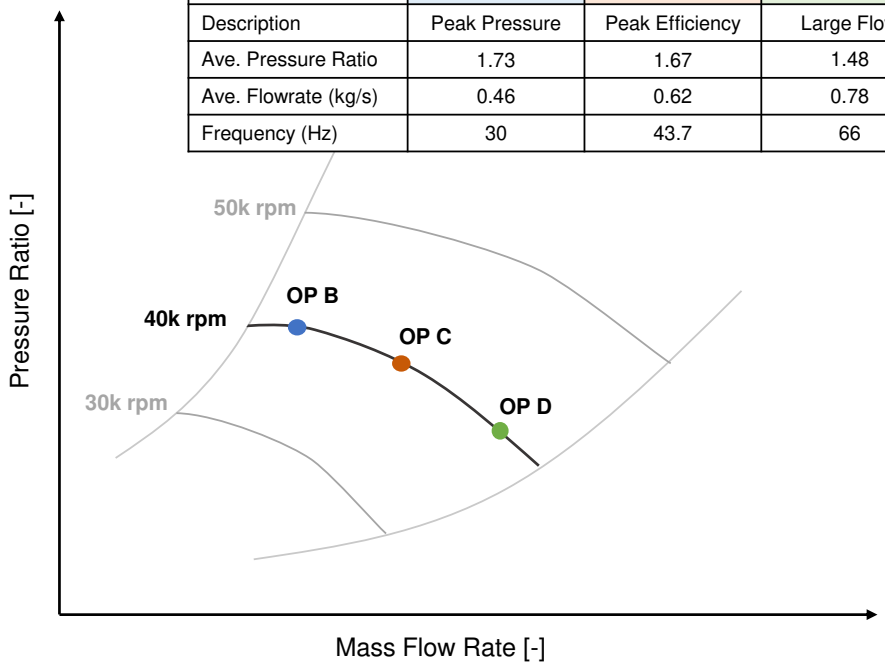


Fig. 5.19 Schematic of the key operating points at the 40k rpm operating line

5.3.2 Validation

The validation of the computational set-up is detailed in this section. Figure 5.20 shows the pressure ratios for 40k rpm under steady and pulsating backpressure conditions experimentally and computationally. As it was possible to study the full operating line experimentally, the experimental results are shown as operating lines. Due to heavy computational time, it was decided to only simulate the operating points of interest. The results from the computational simulation for OP B (Peak Pressure), OP C (Peak Efficiency) and OP D (Large Flow) can be seen in the figure. It can also be seen that OP D is not reached experimentally. As explained in the experimental findings in Chapter 4, the experimental facility is unable to reach the large flow conditions when the pulse generator is on. The mass flow reaches a choking limit due to the restrictions from the piping system. This figure also highlights one of the main reasons for conducting the computational investigation, as it allows for the study of large flow operating points beyond the experimental capacity.

In Figure 5.20, it can be seen that the computationally achieved pressure ratios are greater than the experimental pressure ratios. This is because the experimental facility is not adiabatic and there are losses. Additional differences in the computational model and experimental set-up were mentioned in the previous section and are not repeated here for conciseness.

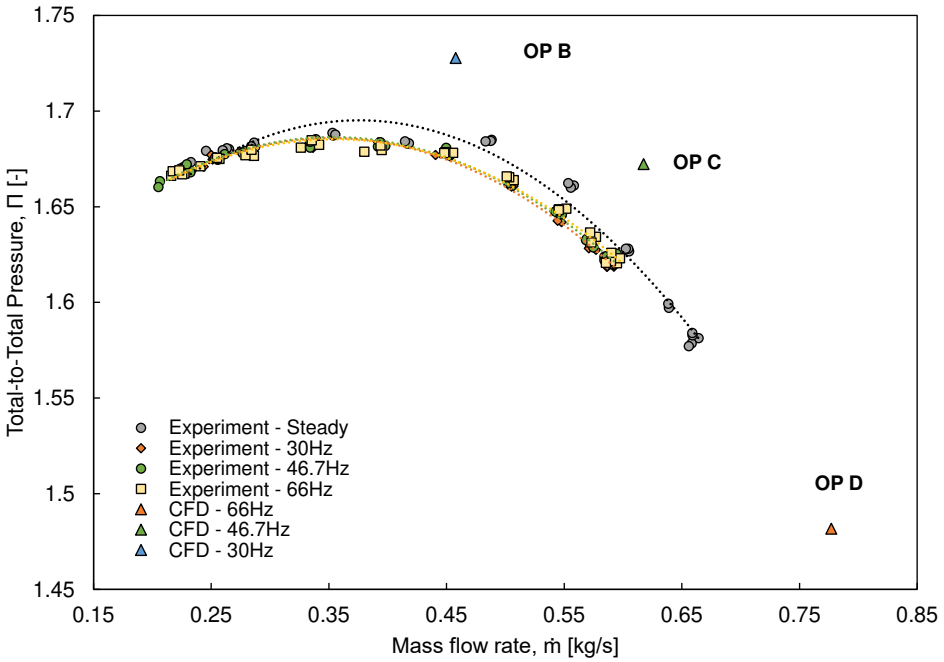


Fig. 5.20 Pressure ratio against mass flow rate for OP B (Peak Pressure), OP C (Peak Efficiency) and OP D (Large Flow) for experimental and computational results; good matching of the results can be seen.

Figure 5.21 shows the instantaneous behaviour in the experimental and computational results for the key operating points. It can be seen that there is good matching of the hysteresis behavior for the peak pressure (OP B) and peak efficiency (OP C) points. Both hysteresis loops have a similar inclination; the hysteresis loops have a negative slope and lean towards the pressure ratio axis. The main difference between the peak pressure (OP B) and peak efficiency (OP C) experimentally and computationally is the mass flow range in the hysteresis loops. In the experimental results, the hysteresis in mass flow is larger. Furthermore, the computational result for peak pressure (OP B) shows a much smaller mass flow range compared to the corresponding experimental result. This is expected because simulations need to be within the stable limits to enable convergence. Experimental systems can extend into dynamic states that are difficult to achieve in computational simulations. The peak efficiency (OP C) results for the computational and experimental results are the most closely matched; the amplitude and range of the hysteresis loops are similar. Overall, the instantaneous behaviour of the operating points are matched well.

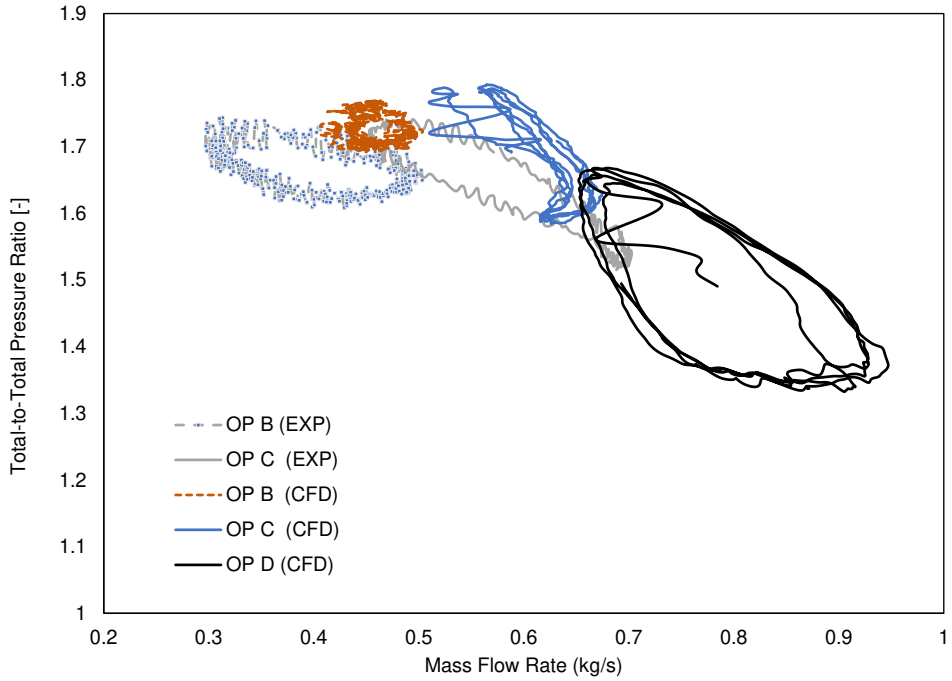


Fig. 5.21 Hysteresis loops for key operating points in CFD results compared to experiments for OP B (peak pressure), OP C (peak efficiency) and OP D (large flow)

5.3.3 Computational Results

In this section, the computational results for the key operating points are discussed. For ease of comparison, a similar approach to the first investigation is followed: The output files are sampled at selected instantaneous times of each of the operating points (OP B - OP D).

This results in nine instantaneous outputs for each operating point that are representative of a full pulse cycle.

The inlet and outlet measurement planes from which the data is extracted is shown in Figure 5.22. The measurement planes are in the same position as in the experimental facility.

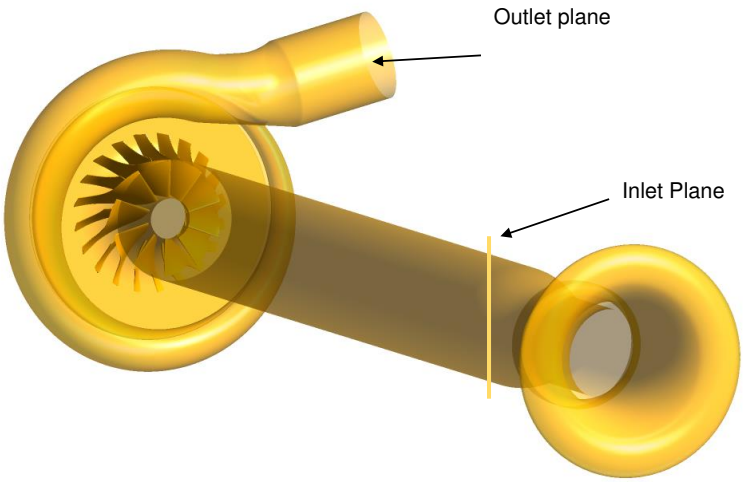


Fig. 5.22 Inlet and outlet measurement planes in CFD positioned to match the experimental facility

Overall PR and Efficiency Results

Figure 5.23 and 5.24 show the pressure ratio and efficiency results from nine instantaneous times have been recorded over a full pulse cycle as above for all three operating conditions. The large flow operating point (OP D) spans a much larger mass flow and pressure ratio than the peak pressure point (OP B). This was also seen in experimental results shown in Chapter 4. Additionally, at OP D, the loop results in a large pressure ratio variation, it is more vertically aligned compared to the peak pressure point (OP B) which is flatter. The experimentally obtained data shown in Chapter 4 also showed similar trends (See Figure 4.7 for reference). The large flow operating point sees a much larger pressure variation instantaneously and spans a much larger mass flow rate. The reason this occurs is because in the large flow operating condition, a large amount of mass flow is subject to the throttle closure - this generates a pressure wave with high amplitude and consequently a large mass flow is locally accelerated and decelerated, resulting in a large hysteresis loop. In

comparison, in the peak pressure operating region, the average mass flow is small resulting in a smaller hysteresis loop.

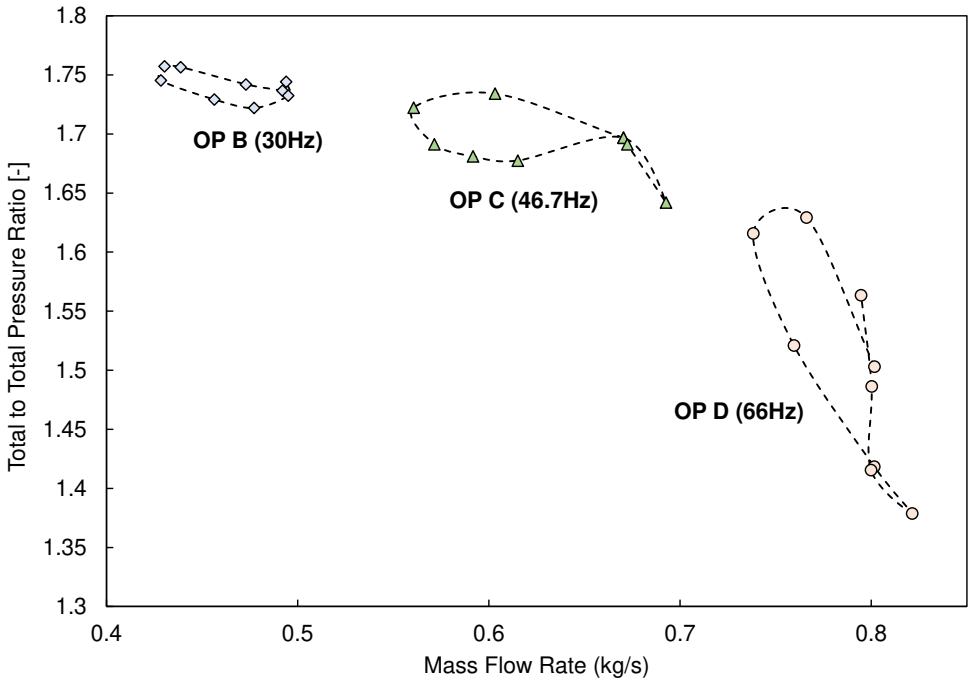


Fig. 5.23 Pressure ratio and mass flow rate results for peak pressure (OP B), peak efficiency (OP C) and large flow (OP D) - instantaneous outputs within a pulse cycle

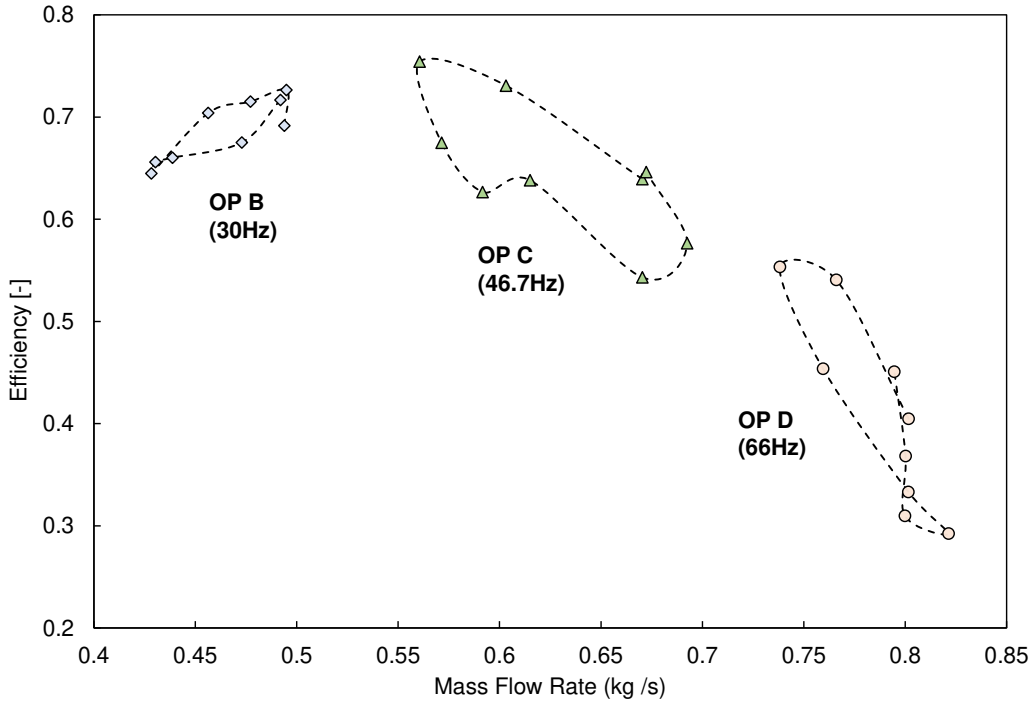


Fig. 5.24 Efficiency and mass flow rate results for peak pressure (OP B), peak efficiency (OP C) and large flow (OP D) - instantaneous outputs within a pulse cycle

Figure 5.24 shows the efficiency variation. Similar to before, the peak pressure point (OP B) shows a small variation in efficiency. The hysteresis at peak efficiency (OP C) is comparatively larger than OP B and similar to OP D. Additionally, it can be seen that the hysteresis behaviour is slanted. At peak pressure (OP B), the instantaneous efficiency tends towards high mass flow rates. At peak efficiency (OP C) and large flow (OP D), the instantaneous efficiency tends towards low mass flow rates. It is known that for this compressor the peak efficiency is around DP2 (the equivalent steady peak efficiency), which explains why both instantaneous efficiencies are tending towards the peak efficiency region. As seen in experimental findings, OP D has the lowest efficiency of all operating points, and has the largest inclination. In the full pulse, the efficiency varies by from 0.55 at instantaneous max. condition to 0.3 at instantaneous min. condition, which is a difference of 0.25 (25%).

The instantaneous behaviour at the peak pressure operating point (OP B) leaning towards the peak efficiency region shows that instantaneously, the dynamic operation wants the compressor to be in more stable operating conditions. When the compressor is in steady operation, there is no dynamic driver due to a single operating state. This tendency for the compressor to move towards peak efficiency matches the results in the previous investigation (at the near surge operating point). It was shown in previous sections that surge is

delayed because there are instantaneous operating states that are more stable than others and in pulsating operation, the compressor does not stay in an unstable operating state for long.

Pressure rise in the volute

Figure 5.25 shows the average pressure rise in the volute, the static pressure at the diffuser exit interface is plotted alongside the static pressure at the compressor outlet for each of the operating points. The position of the interface is also shown in Figure 5.25 for reference. Two things can be seen. First, there is a visible pressure wave at the diffuser - volute interface indicating that the pressure pulse has not dissipated by the time it reaches the diffuser. The pressure wave can be felt by the upstream components. This matches the experimental investigation as it was shown in Chapter 4 through static pressure measurements within the compressor that the pressure wave propagates upstream.

Secondly, the average pressure wave at the diffuser to volute interface is similar to that imposed at the compressor exit. For each of the operating points, the pressure wave peak to peak amplitude is also similar to the imposed output wave, with some damping. For peak pressure (OP B) and peak efficiency (OP C), there is a clear pressure rise through the volute - this indicates that there is diffusion taking place in the volute component and the volute is behaving as intended. However, for large flow condition (OP D), there is no clear pressure rise in the volute component. In fact, there is a slight pressure drop in the compressor exit, indicating that there may be an acceleration process taking place. This indicates that rather than promoting diffusion, the volute component is acting as a nozzle in some instantaneous output states due to the very low pressure at the compressor outlet.

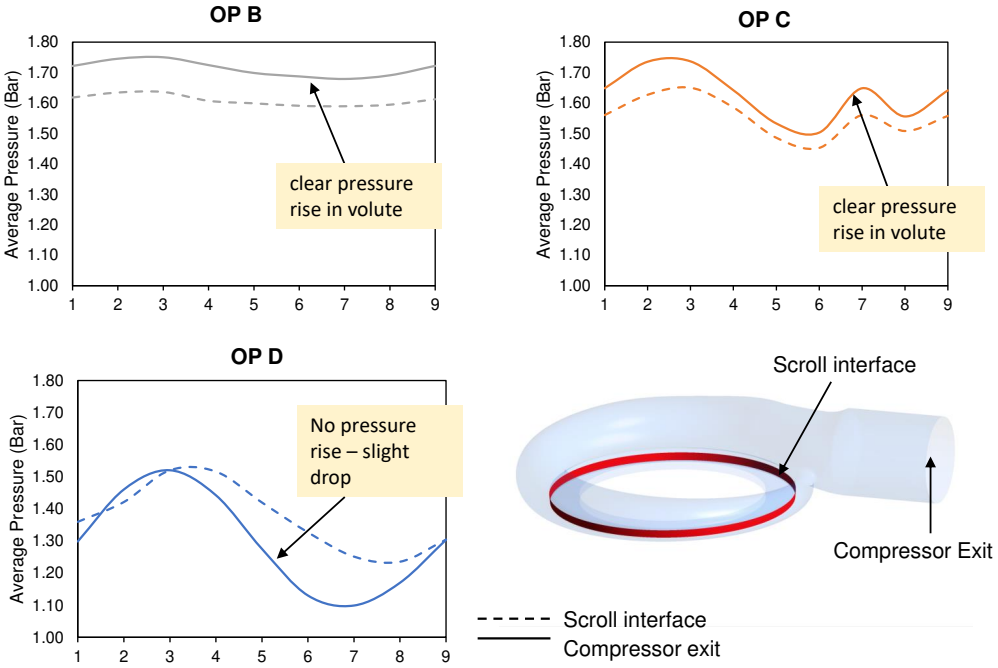


Fig. 5.25 Static pressure rise in the volute component for operating points: OP B - Peak Pressure; OP C - Peak Efficiency, OP D - Large Flow

Entropy Generation Rate

The entropy generation rate is a measure of dissipation rate of useful energy and can be used to estimate losses. This is a useful term for understanding the rate at which losses are taking place and has been shown to be useful in assessing losses in turbomachinery [91]. There are two ways the entropy generation rate can be calculated: direct or indirect methods. In the direct calculations, the convective entropy term, which is the entropy of the flowing medium, is ignored since the convective entropy term is a measure of reversible entropy and does not contribute to losses. Thereofore, an estimation of the entropy generation rate is made by calculating the irreversible entropy generation alone [91]. The direct entropy production is estimated using the dissipation rate and heat conduction rate for the laminar and turbulent flow regimes; the total entropy is the sum of the laminar and turbulent dissipation rate and the laminar and turbulent heat conduction.

In the indirect method, the entropy generation is estimated using source terms in a control volume. The indirect method works for steady flow calculations but does not work in transient calculations due to the mass flux term. For this reason, the direct method of entropy generation has been used. Note that one of the limitations of calculating entropy generation rate in the direct method is that it is an estimation of the entropy through

calculation. However, this estimation is sufficient for the purposes of this analysis as it is being used here as a preliminary indicative measure of losses.

The entropy generation rate (EGR) for all the operating points is shown in Figure 5.26. It can be seen that the greatest EGR takes place at the large flow operating point (OP D), whereas the entropy generation rate is minimum at the peak efficiency design point. The first observation that can be made is that this is an expected result; the losses should be minimum at the peak efficiency point of the compressor. Figure 5.26 indicates that the most amount of losses are generated at the large flow operating point, based on the measure of the dissipation rate of useful energy. The larger EGR at the high flow conditions links to the drop in efficiency at this operating point. The hysteresis plots in Figure 5.24 show that there are certain instantaneous states where there the efficiency is higher than others, indicating that there are some instantaneous states where the compressor has a better performance. This is reflected in the lower entropy generation rate in some instantaneous states of the large flow operating point (OP D) in Figure 5.26.

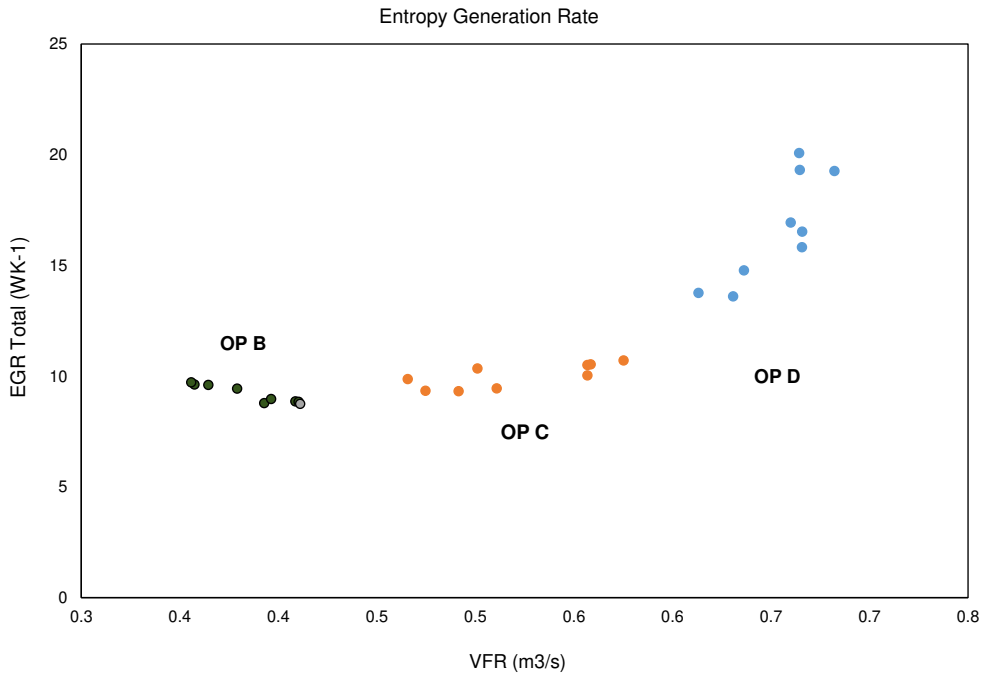


Fig. 5.26 Entropy generation rate for operating points: OP B - Peak Pressure; OP C - Peak Efficiency, OP D - Large Flow

One of the benefits of this calculation is that entropy generation rate can also be calculated for each of the components of the compressor. The breakdown contribution of each of the components for each of the operating points is shown in Figures 5.27 to Figure 5.29. In each of the figures the entropy generation rate (EGR) for the components is analysed and denoted as follows: D1 - inlet, D2 - impeller, D3 - diffuser and D4 - volute.

It can be seen that the impeller domain (D2) has the greatest entropy generation for all of the operating points. A large proportion of impeller losses are due to the generation of secondary flows - a more detailed assessment of the entropy generation at the impeller would require study of the impeller loss profile. This loss profile is not studied in this research as it is out of scope, but background on impeller losses has been provided in the literature review.

It is clear to see that in the large flow operating point (OP D), the volute domain had a significantly greater contribution to the entropy generation rate, compared to the peak pressure and peak efficiency operating points. The impeller has a similar contribution for all of the operating points in comparison. The pulsation effect can be seen in the diffuser results; the diffuser contribution increases with each of the operating points and is higher in OP C. Additionally, there is a clear effect of the pressure pulse. Due to the high pressure pulse amplitude in the large flow condition, the entropy generation increases and decreases with the pressure amplitude, and this effect is visible in Figure 5.29.

From this analysis, the key takeaway is that there is a significant contribution of the volute contribution to the entropy generation rate in the large flow operating point (OP D), which is not seen in the other two operating points. It was seen in Figure 5.25 that there is some flow acceleration in some of the instantaneous output states in the volute component. This high flow velocity and acceleration contributes to the high entropy generation rate and lower efficiency. Interestingly, there are some states where the effect is minimal.

The difference in operation in pulsating conditions to steady conditions is also highlighted with this analysis. In steady operation, there is only one possible operating point and the entropy generation rate is constant. However, in pulsating conditions, the compressor experiences many different instantaneous operating points - some of which are not beneficial to compressor performance, leading to high entropy generation rates that reduce the overall compressor performance.

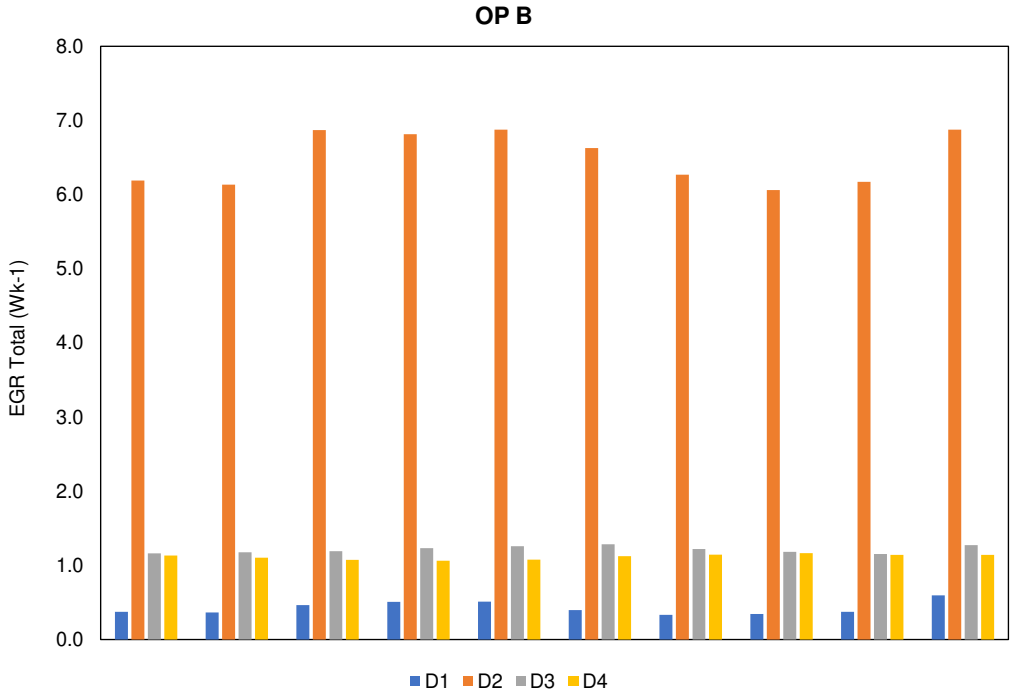


Fig. 5.27 Entropy generation rate for peak pressure operating point (OP B) for domains (D1 - Inlet; D2 - Impeller; D3 - Diffuser; D4 - Volute)

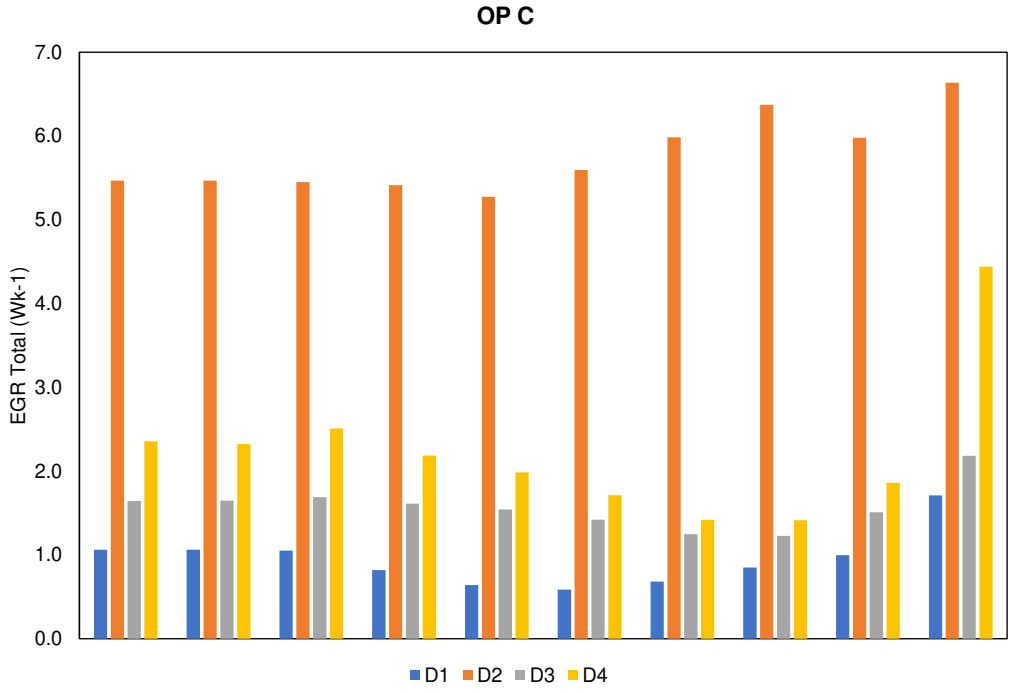


Fig. 5.28 Entropy generation rate for peak efficiency operating point (OP C) for domains (D1 - Inlet; D2 - Impeller; D3 - Diffuser; D4 - Volute)

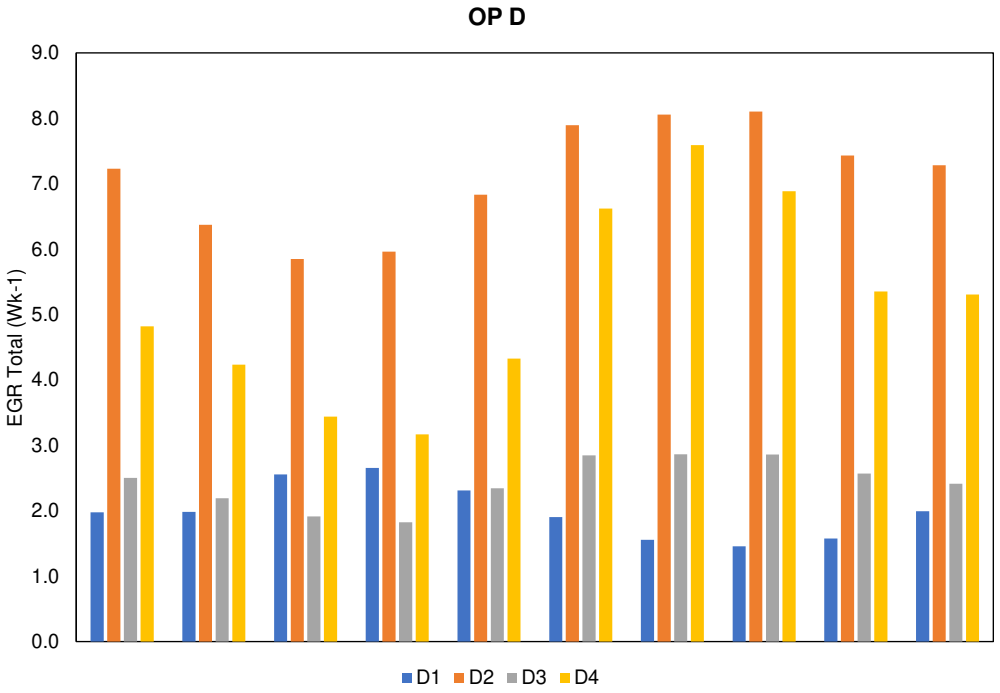


Fig. 5.29 Entropy generation rate for large flow operating point (OP D) for domains (D1 - Inlet; D2 - Impeller; D3 - Diffuser; D4 - Volute)

Detailed Assessment of Large Flow Operating Point (OP D)

In this section, the large flow operating point (OP D) is examined in further detail. The above analysis shows that OP D has a much lower average efficiency, a large negative inclination in hysteresis and the greatest range in efficiencies of around 25%. By studying this operating point further, it can lead to insights on how to improve the compressor performance, particularly under pulsating flow conditions. For this reason, OP D is of particular interest. This subsection focuses on a detailed assessment of the large flow operating point. The objective of the detailed assessment is to gather insights on the efficiency drops.

Figure 5.30 shows the total pressure drop in the volute and diffuser components for the large flow operating point (OP D) at the nine sampled instances in time. It can be seen that the pressure drop in the volute component (blue bars) is larger than the drop in the diffuser component (orange bars). Additionally, it can be seen that the diffuser component has a uniform or near constant pressure drop, indicating that the pulse effect does not affect the losses in the diffuser component. However, the effect of the pulse is felt by the volute component as the pressure drop has a visible waveform. There are are some instances in time where the pressure drop is high and some instances where it is low.

The outlet static pressure has also been plotted in Figure 5.30. When comparing to the outlet static pressure, it can be seen that the greatest pressure drop in the volute component takes place when the static pressure at the outlet is at its lowest, see positions E, F and G. The lowest total pressure drop occurs when the exit pressure at the compressor outlet is rising or at maximum.

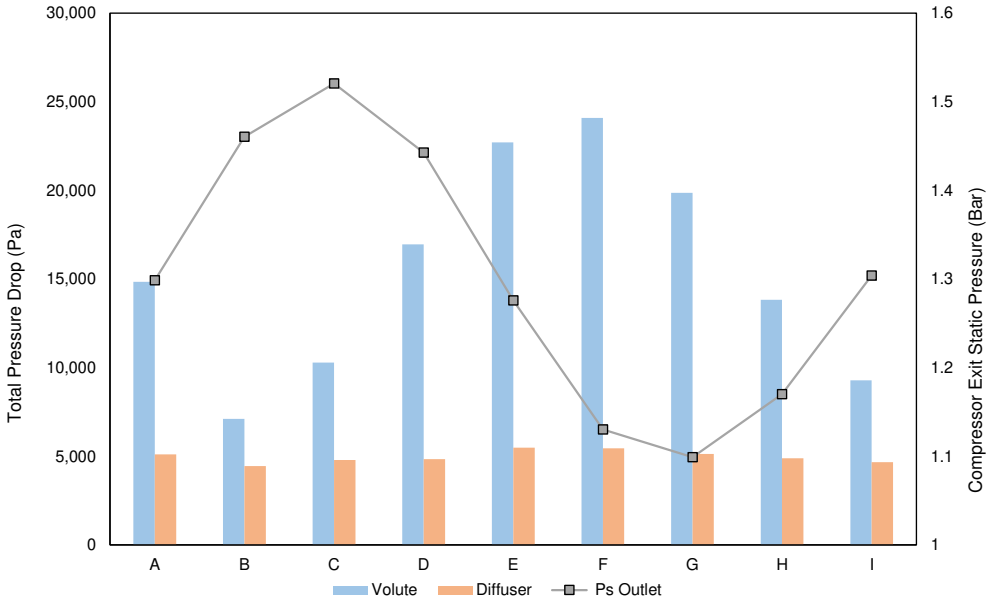


Fig. 5.30 Total pressure drop in the volute and diffuser domain for large flow operating point (OP D)

The volume inside the volute can be split into separation sections. A close approximation of the volume near the tongue was selected using visual approximation. The reason for isolating the tongue was mentioned in the literature review and previous sections; it is thought to be a large region for where the losses in the volute domain is arising. The volume is shown in Figure 5.31. The entropy generation rate was calculated for this volume and compared to the total entropy generation in the volute component. Table 5.4 shows the entropy generation for the tongue. It can be seen that near the tongue, there is a near constant 20% contribution of the tongue. At high backpressure instances (B and C), the tongue contribution drops to 16% but at low backpressure instances (F), the tongue contribution increases to 23%.

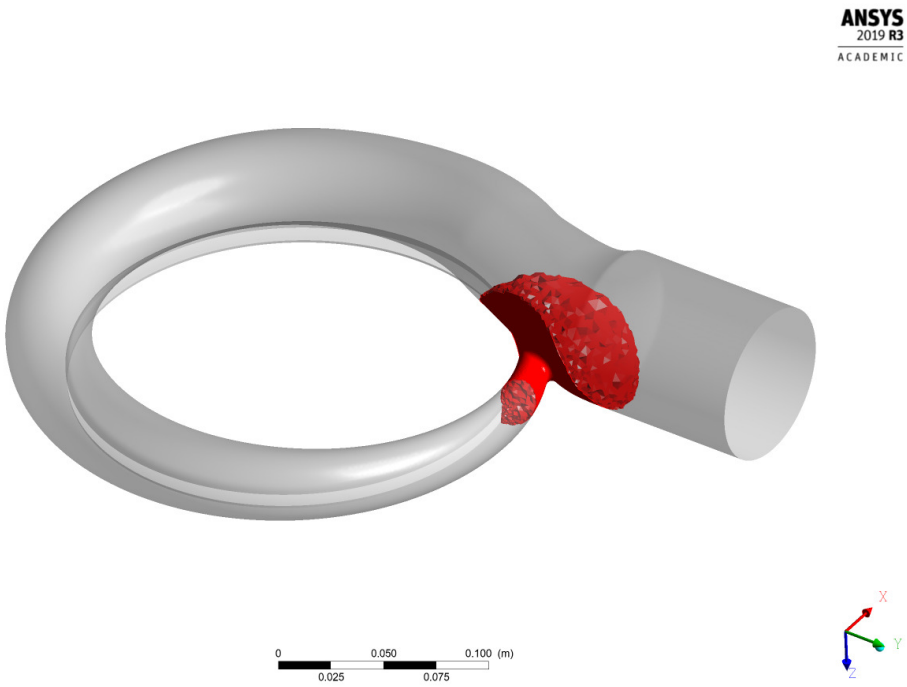


Fig. 5.31 Volute showing the isolation of the tongue volume

Table 5.4 Entropy Generation Rate in volute region contribution from tongue

	Volume 1 - Tongue			Volute Domain			
Time Instance	*Volume Integral (EGR Total) [kg m^2 s^-3 K^-1]*	*Volume Average (Temperature) [K]*	*EGR Total x Temperature [W]*	*Volume Integral (EGR Total)[kg m^2 s^-3 K^-1]*	*Volume Average (Temperature)[K]*	*EGR Total x Temperature[W]*	*Tongue Contribution (%)*
A	0.89	323.80	287.90	4.82	329.60	1588.00	18
B	0.69	337.20	231.00	4.23	338.00	1431.00	16
C	0.54	342.60	185.40	3.44	343.30	1180.00	16
D	0.53	336.70	177.30	3.17	339.90	1076.00	16
E	0.90	322.30	290.90	4.33	330.30	1429.00	20
F	1.61	311.20	500.40	6.62	321.90	2131.00	23
G	1.72	307.90	528.30	7.59	318.70	2419.00	22
H	1.42	313.30	444.70	6.89	320.90	2211.00	20
I	0.95	325.30	307.80	5.35	328.40	1758.00	18

Internal Flow Field Analysis

Figure 5.32 shows the mass flow and pressure ratio at the nine instances in time for the large flow operating point. On the figure, instance B and instance F have been highlighted as the highest backpressure and lowest backpressure instances respectively. The flow fields of instance B and F will be analysed to look at the differences between the two conditions.

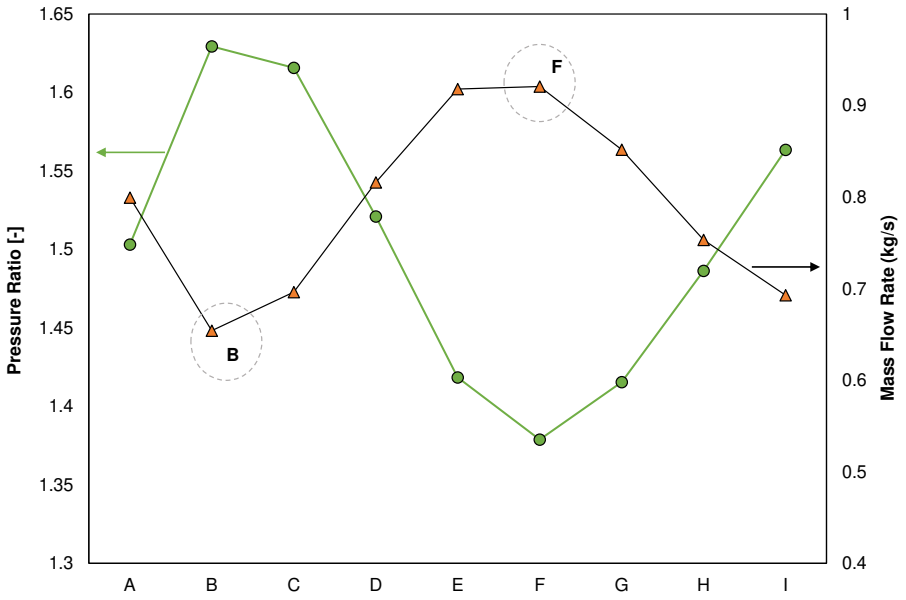


Fig. 5.32 Pressure ratio against mass flow rate at nine instances in time for large flow operating point (OP D)

A cut-plane through the volute is shown in Figure 5.33. The flow field will be shown for this cut plane. For reference, the design flow path of the volute is shown in Figure 5.34.

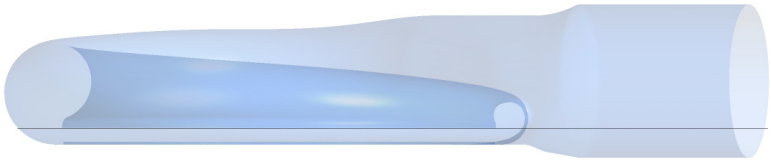


Fig. 5.33 Location of the cut-plane in the volute component

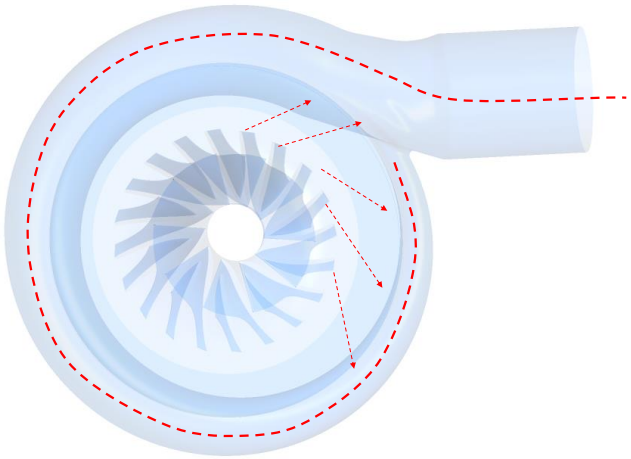
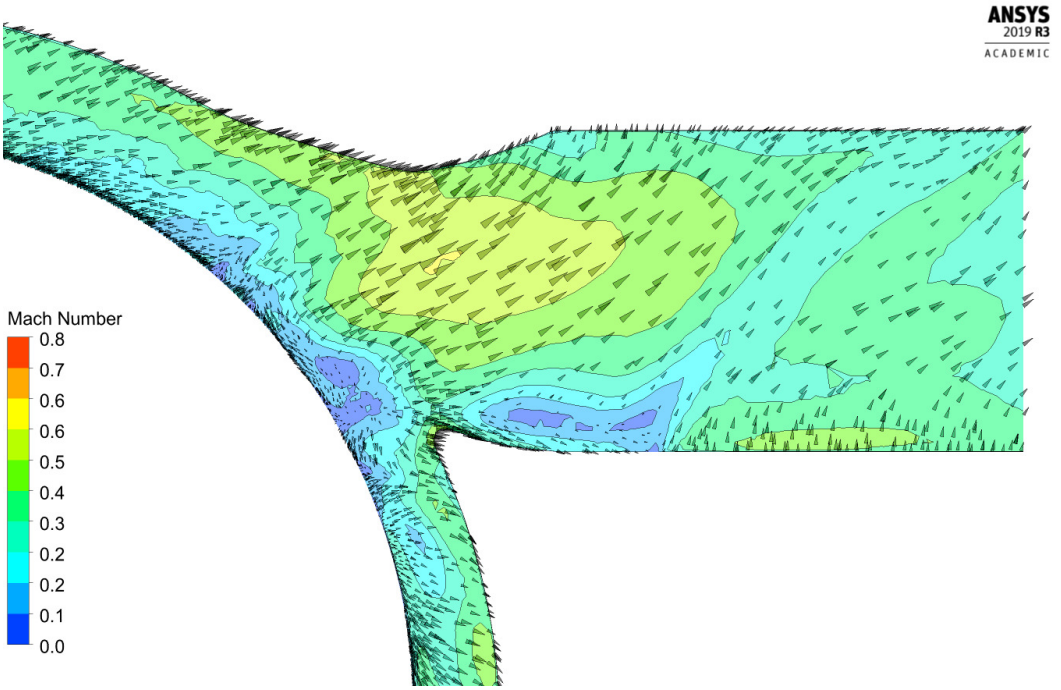
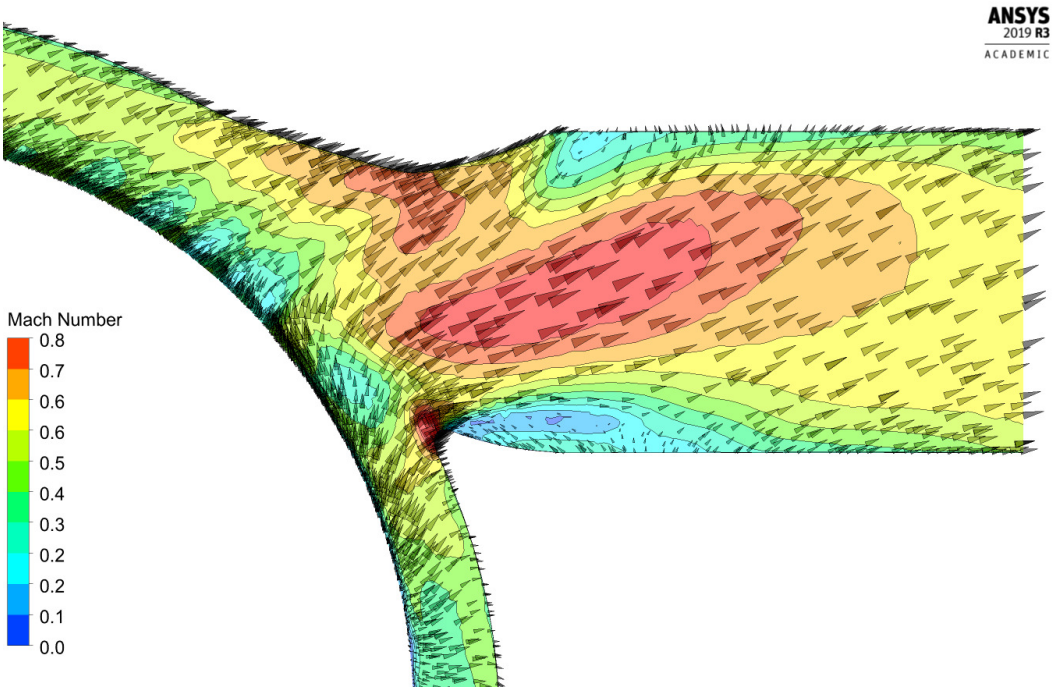


Fig. 5.34 This path schematic shows the flow vectors indicating the design flow path of the volute

Figure 5.35 shows the mach numbers and velocity contours near the tongue for time instances B and F. It can be seen that the circumferential flow field for B, at the tongue, there is a region of low mach numbers (shown by the blue contours), indicating that there is either no main flow in this region or the flow in this region is stagnated or just at low velocity. The flow path entering the volute follows the design flow path, a schematic of which is shown in Figure 5.34. However, the flow field at instance F is very different. It can be seen that there is high speed flow close to the tongue region and the flow is pulled in the opposite direction to design.

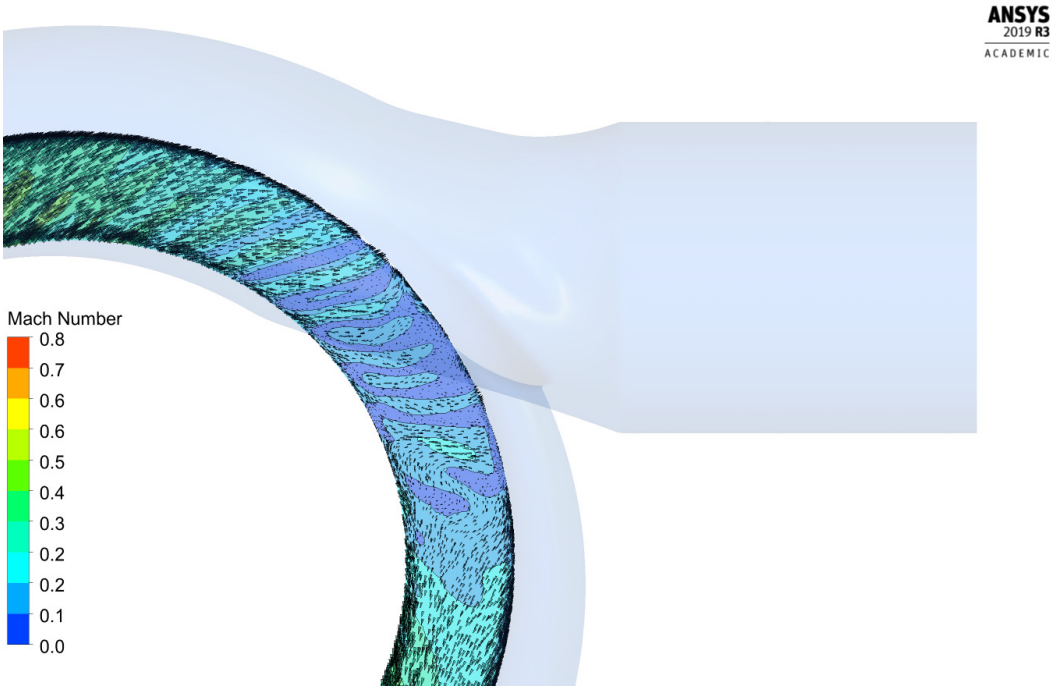


(a) Mach number and velocity vectors (tangential projection) at instance B for large flow operating point (OP D)

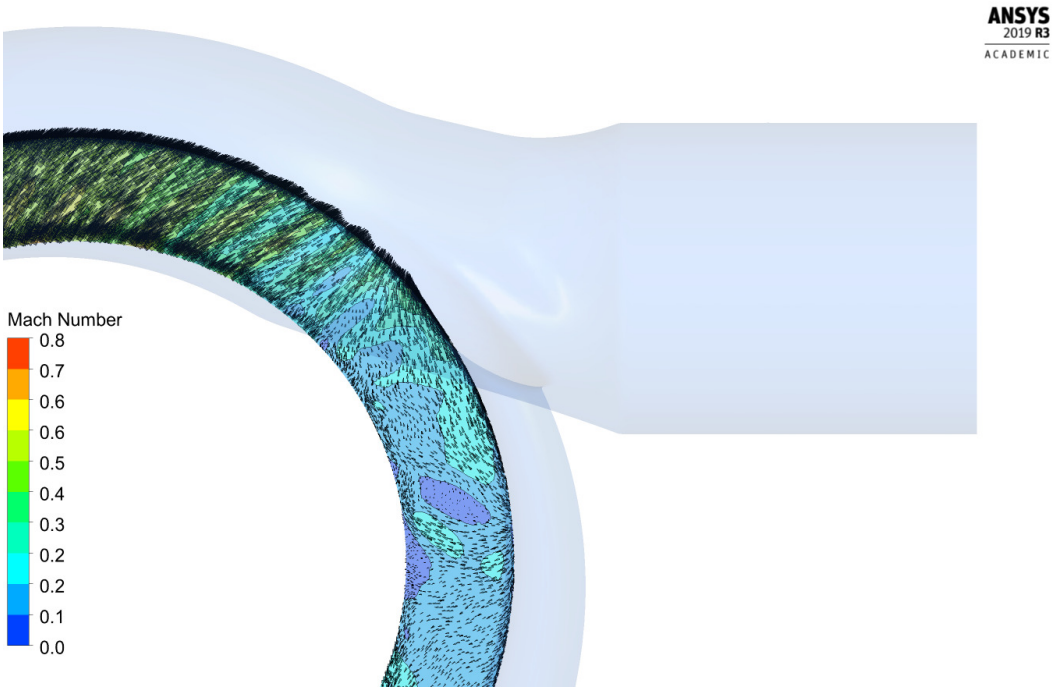


(b) Mach number and velocity vectors (tangential projection) at instance F for large flow operating point (OP D)

Fig. 5.35 Mach number and velocity vectors near the tongue for the volute domain



(a) Mach number and velocity vectors (tangential projection) at instance B for large flow operating point (OP D) at diffuser



(b) Mach number and velocity vectors (tangential projection) at instance F for large flow operating point (OP D) at diffuser

Fig. 5.36 Mach number and velocity vectors near the tongue in the diffuser domain

Figure 5.36 shows the Mach number and velocity contours for the diffuser region. In the diffuser region, for time instance B (high static pressure at the outlet), there are regions of stall near the tongue indicated by the blue contours. This stall region effectively causes the flow to follow the design flow path. At time instance F, there is a stall cell however, this stall cell is placed much lower down from the tongue. As a result, more of the flow is drawn towards the outlet in the opposite direction to the design flow path shown in Figure 5.34.

Discussion

It can be seen that in the large flow case (regardless of the instantaneous point), the pressure variation amplitude is much greater than the peak efficiency and peak pressure points. This causes large inertia fluctuations inside the compressor. The large flow point sees the most changes in performance. There is a steep gradient in comparison to the peak pressure and peak efficiency causes - which are much flatter. The large flow operating point has the largest entropy generation rate and, compared to the peak pressure and peak efficiency operating points, the volute region contributes significantly to the overall entropy generation rate. Additionally, of the two main static components where total pressure loss occurs, the greatest loss in total pressure happens in the volute for the large flow operating point. Furthermore, the total pressure drop in the volute is greatest when there is acceleration in the system due to low pressure at the compressor outlet.

From the instantaneous analysis, there are clear differences between time instance B (worst instantaneous efficiency) and time instance F case (best instantaneous efficiency) and this is to do with a variety of key factors. The circumferential velocity in the time instance F shows that flow is arriving at the tongue region which much higher velocities - due to to the low pressure at the outlet and it is causing the flow to follow the pressure gradient rather than the design path of the compressor. A low outlet pressure compared to the diffuser outlet pressure causes the flow to speed up near the tongue region of the compressor, resulting in loss generation and low instantaneous efficiency.

5.4 Chapter Summary

In this chapter, two computational investigations were conducted.

Investigation One

In the first investigation, the near surge operating point was studied computationally. The Mach number, static pressure and entropy plots were studied in the impeller inlet planes. It was found that there were some instantaneous states that have more flow disturbances than other states. These states correspond to high backpressure on the impeller exit - and consequently lower flow coefficients. However, these states were instantly alleviated when the backpressure dropped. In the low backpressure conditions, the flow was more uniform and had overall less disturbances, lowering the chances of stall cells growing. Static entropy and Mach number contours show that majority of the disturbances appear near the shroud region in the 90% span. It was proposed that if the flow features leading to surge (stall and blockage) are present in some instances but not others, then the surge is delayed.

Investigation Two

In the second investigation, three operating points corresponding to peak pressure (OP B), peak efficiency (OP C) and large flow (OP D) were studied. The large flow operating point (OP D) was found to have the greatest hysteresis in efficiency and had the lowest efficiency overall. The greatest total pressure drop and entropy generation occurred in the volute in the large flow operating point, whereas in the peak pressure and peak efficiency operating points the volute domain was not that significant. The entropy generation rate was also greatest overall in the large flow operating point. The tongue contributed to near 20% of the entropy generation in the volute on average. The flow field analysis showed that instantaneously the low static pressure at the outlet pulls the flow towards the volute exit which is the opposite direction that the pressure rise in the volute should take place.

Chapter 6

Design Modifications to Centrifugal Compressor for Pulsating Flow

In this chapter, the design, development and testing of compressor designs for pulsating flow is detailed. The compressor modifications are based on the analysis in the preceding sections. The objectives of the new designs is to attain better performance of the compressor under pulsating flow conditions, as stated in the Introduction Chapter (Chapter 1).

In the literature review, it was identified that there were critical sub-components and regions which affect the performance of the compressor. In particular, the impeller inlet region and volute exit regions are two key regions which affect performance under pulsating conditions. In Chapter 4 and 5, these regions were also identified to contribute to efficiency deficits. By studying these regions closely, it is possible to develop alternative designs that can improve compressor behaviour.

This chapter describes the development of compressor design modifications that stem from the investigations of the two regions described above. The modifications are detailed in Table 6.1. This chapter describes development of these designs and presents results from preliminary experimental tests. The chapter is broken into two sections for each of the designs.

Table 6.1 Design Modifications for improving the performance of the compressor under pulsating flow

Modification	**Name**	**Location**
Modification 1	Cavity Treatment	Impeller Inlet
Modification 2	Tongue Fillet	Volute Tongue

6.1 Modification 1: Cavity Treatment

The cavity treatment idea was first developed in previous research by Barrera-Medrano & Martos [66] as a design feature that could delay the onset of surge. The cavity is a term used to describe the half-heart shaped cut-out in the shroud at the impeller inlet, see Figure 6.1. Preliminary research on the cavity treatment design has been conducted by Martos [66], and the computational performance under steady flow has been assessed. The outcomes from the preliminary study are described in the literature review. The main findings from literature review show that the cavity achieves a surge margin improvement under steady flow conditions however there is a drop in efficiency.

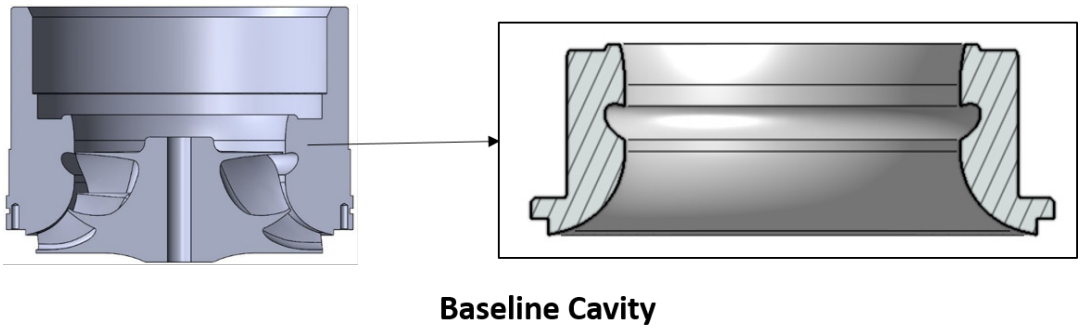


Fig. 6.1 Cavity treatment design developed by Barrera-Medrano and Martos. The baseline cavity position and size is shown in this Figure.

Research and Design objective

The objective of this research and design process is to build on prior knowledge of compressor performance with the cavity treatment with detailed focus on pulsating flow behaviour. The best performing cavity from previous research by Martos [66] is selected as the baseline cavity case to be optimised in order to decrease the efficiency deficit introduced by the cavity. Before doing so, a computational assessment is used to gather insights of the performance deficit under pulsating flow. Similar to the approach followed in Chapter 5 of this thesis, a computational simulation using Unsteady Reynolds Average Navier Stokes equations (URANS) is conducted. To analyse the performance, computational results are sampled at different instances in time along a pulse and analysed.

Methodology

The research methodology is as follows: First, a computational assessment is conducted on a baseline cavity case as well as a no-cavity conditions to obtain insights on the differences and similarities in performance. This is followed by a modified/optimised design based on the insights from the computational assessment. The baseline cavity, optimised cavity and original shroud (without cavity) are experimentally tested. The original shroud is produced with the same manufacturing technique as the cavity cases, this allows for comparison and assessment of the cavity performance against baseline performance. The results are compared and discussed respectively and the research outcome is presented at the end of this section.

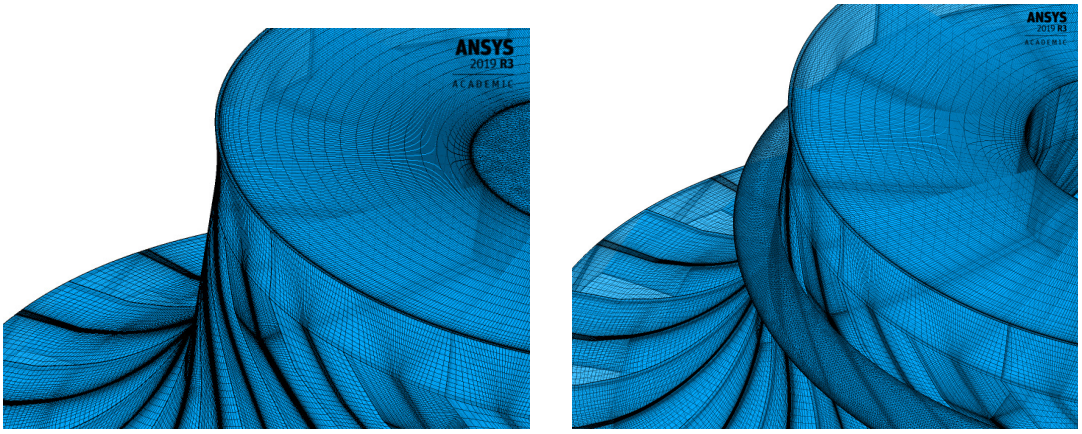
6.1.1 Computational Assessment

Computational set-up

The computational set-up is detailed in Table 6.2. For reference, a figure of the impeller mesh with and without cavity is shown in Figure 6.2. The other domains are hidden from view but in the full simulation the impeller inlet pipe, diffuser and volute is included.

Table 6.2 Computational Set-Up

Software	ANSYS CFX R19
Simulation Type	Full Stage, 3D, RANS and URANS
Computational Domains	Inlet, Impeller, Diffuser, Volute
Impeller Details	10 main blades; 10 splitter blades
Fluid Medium	Air (Ideal Gas)
Walls	Adiabatic, non-slip, smooth
Steady (RANS) boundary conditions	Fixed rotor and stator
Pulsating (URANS) boundary condition	Transient rotor
Pulsating (URANS) boundary condition	Transient rotor-stator at impeller inlet and exit
Interface boundary condition	fluid to fluid
Rotor	Rotating domain at rotational speed of 40,000 rpm
Turbulence model	SST with wall function (k-ω SST)



(a) Impeller Mesh without Cavity **(b)** Impeller mesh with cavity

Fig. 6.2 Impeller mesh without cavity and with cavity

In Chapter 5, the process for defining boundary conditions under pulsating flow for transient computational analysis was explained. The process is a User Defined Function (UDF) where the boundary condition is a data set that varies with time, in this way experimentally obtained static pressure pulse was used as the boundary condition. The baseline cavity and no-cavity simulation cases were run with the same boundary condition. The static pressure pulse was obtained at the peak efficiency operating condition (OP C). This is because the aim of this research is to modify the compressor for increased efficiency in pulsating flow conditions, hence, the peak efficiency operating point is selected as the design point.

Computational Results

The schematic of the operating point for analysis is shown in Figure 6.3. Figure 6.4 shows the compressor exit static pressure and mass flow rate results for the imposed boundary pulse, which drive the corresponding inlet behaviour at the cavity.

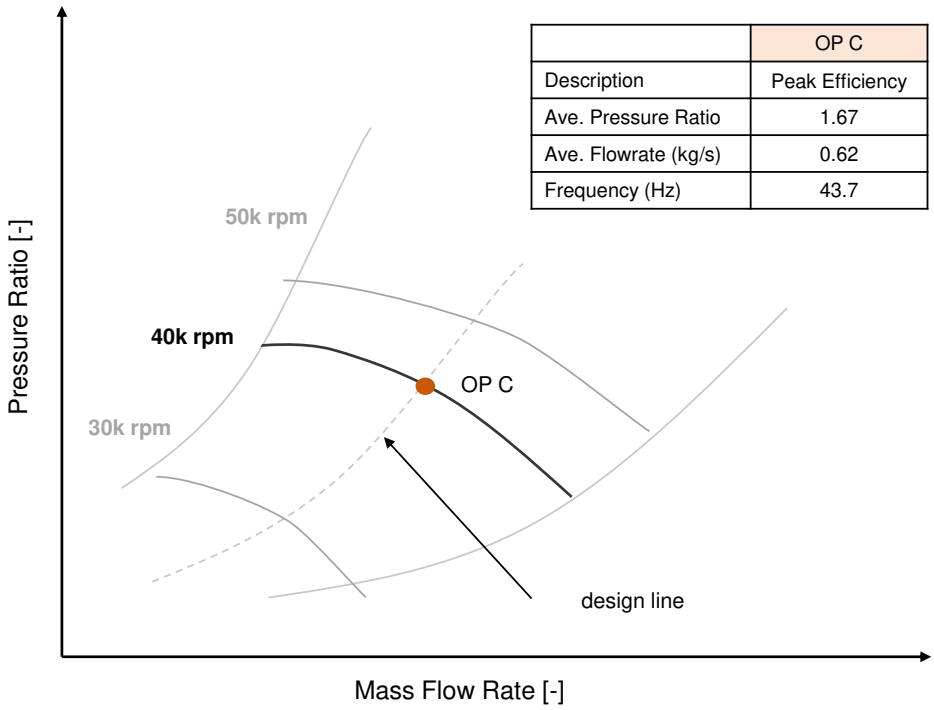


Fig. 6.3 Schematic of the operating point for the cavity flow analysis and design

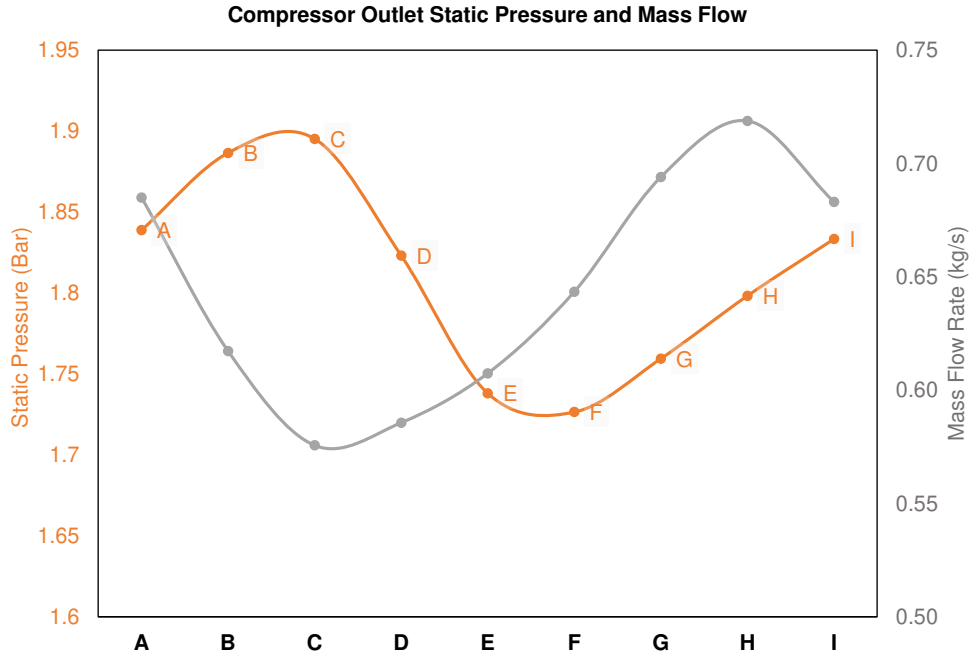
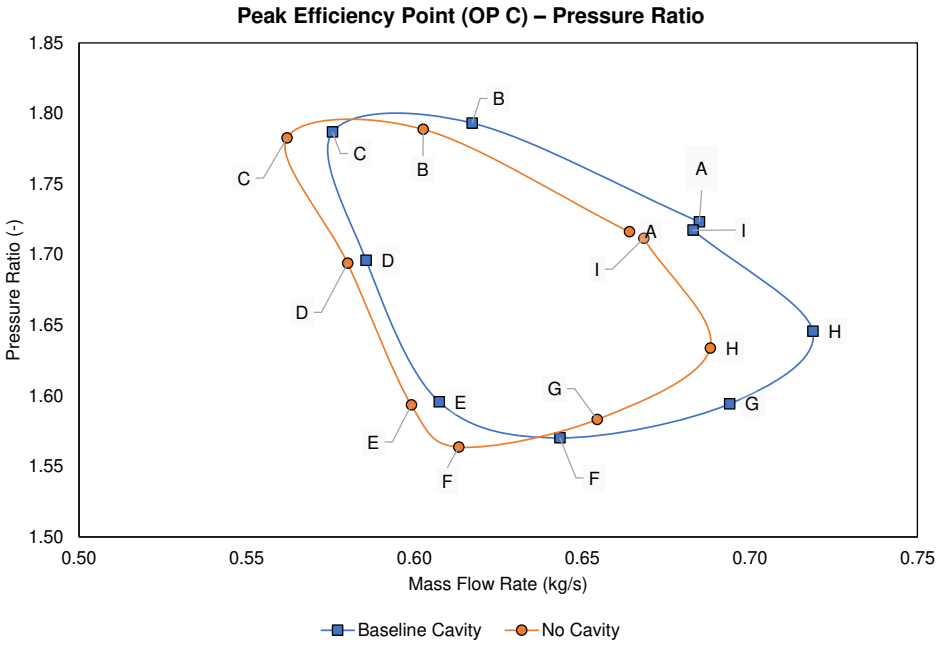
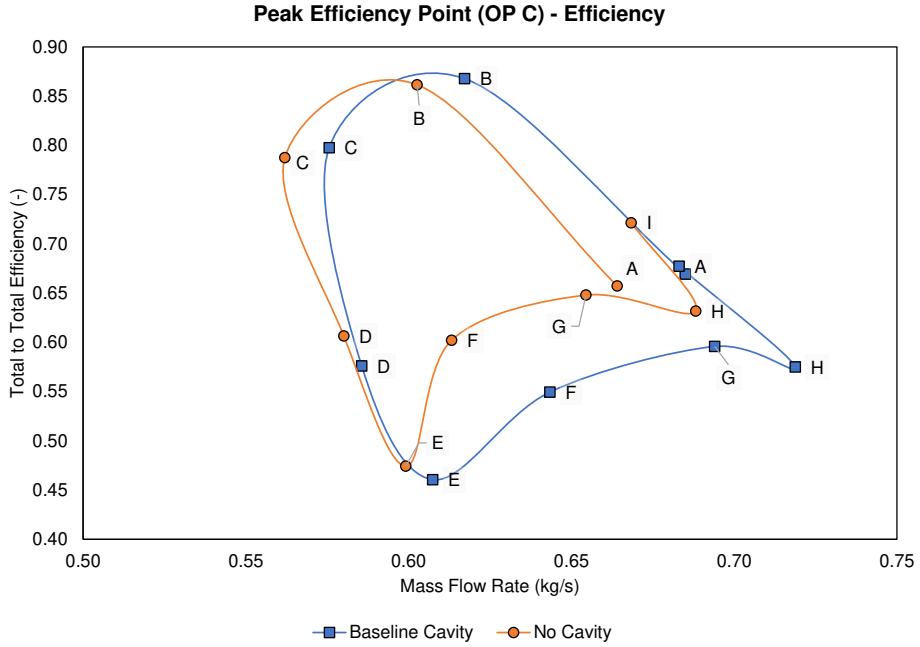


Fig. 6.4 Impeller exit outlet conditions (static pressure and mass flow) for the cavity case at different instantaneous points in time (A-I) for the cavity case simulation. It can be seen that position H corresponds to the case of peak mass flow rate

The simulation results for the cavity and no-cavity case for the peak efficiency operating point were extracted for a full pulse cycle for analysis. Figure 6.5 shows the pressure ratio and efficiency results for the baseline cavity and no cavity simulations against the mass flow rate at different positions along a pulse. In Figure 6.5a, it can be seen that the pressure ratio for the no cavity and baseline cavity cases are similar even though the mass flow rate is shifted to the right for the baseline cavity case. In other words, both loop sizes are similar. In Figure 6.5b, the efficiency in the instantaneous high flow rate conditions for the no-cavity case is higher than the baseline cavity case. This can be seen in points **F**, **G** and **H** in Figure 6.5b. In other words, it can be seen that the no-cavity case has a smaller loop indicating that the range of efficiencies is smaller in the no-cavity case compared to the baseline cavity case.



(a) Pressure ratio vs mass flow for baseline cavity and no cavity cases



(b) Efficiency vs mass flow for baseline cavity and no cavity cases

Fig. 6.5 Pressure ratio and efficiency results for baseline cavity and no cavity case for peak efficiency operating point (OP C)

Another paramater for assessing the performance of a given design is the power. Power is calculated using equations 5.2 and 5.4, presented in Chapter 5. The compressor input

power for the no cavity and baseline cavity case are shown in Figure 6.6. This figure shows the instantaneous power draw for different positions along a pulse. It can be seen that in the baseline cavity case, there are some instantaneous times when the power draw exceeds the power draw for the no-cavity case. The biggest difference in instantaneous power takes place at instantaneous time **G**. The average URANS power is also shown; it can be seen that on average the compressor input power is higher in the baseline cavity case as opposed to the no cavity case.

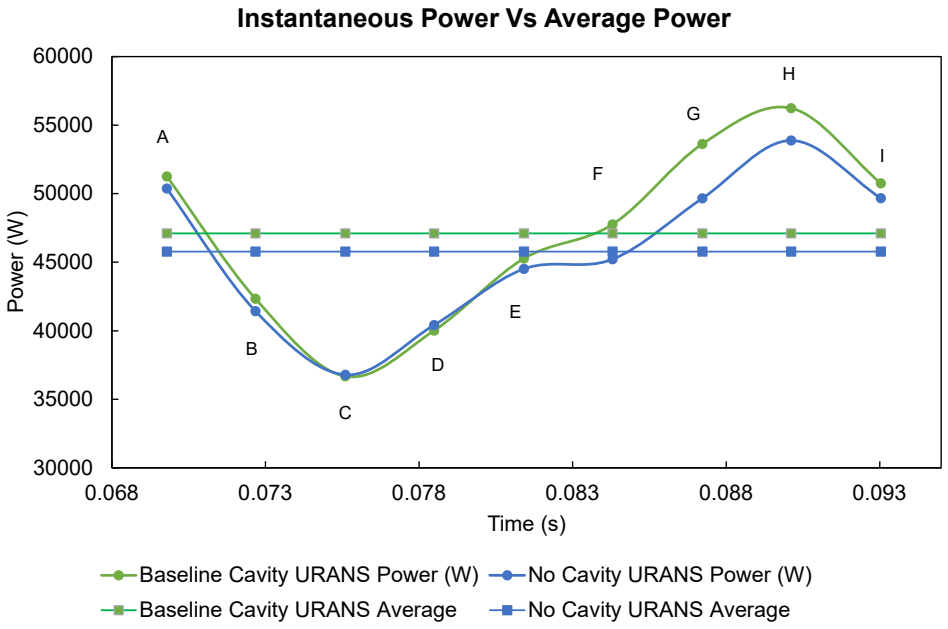


Fig. 6.6 Instantaneous compressor power cavity and baseline case

The differences in efficiency is shown in Figure 6.7 for each of the sampled instantaneous results for the cavity and no-cavity case. The mass flow rate is also plotted to show that the highest efficiency drop occurs when the mass flow rate is increasing, as can be seen in Figure 6.5b. When the mass flow rate is low or dropping, the efficiency between the baseline cavity and no-cavity cases are similar (see times (A-C). At time **G**, corresponding to the largest power difference between no cavity and baseline cavity case, there is an efficiency difference of around 8% at time **G** and around 9% at time **H**. In the low momentum regions, the efficiency in the baseline cavity case is improved by 2%. This is indicative of the cavity treatment mechanism working. The design objective of the cavity treatment is to delay the onset of surge at low mass flow rates by redirecting reversed flow in the right direction through the compressor, see Figure 6.8. An improvement in efficiency at instantaneous low flow rate regions indicates that the reversal mechanism of the cavity is beneficial to the performance of the compressor, as expected.

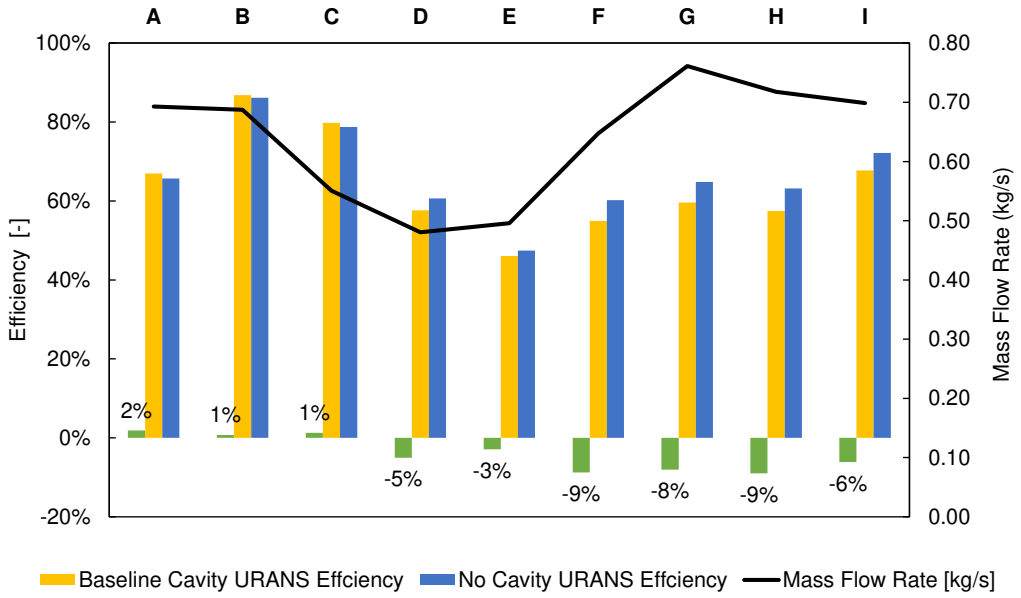


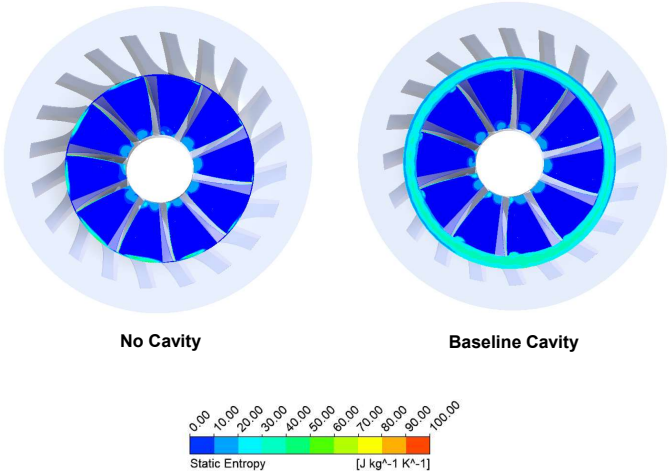
Fig. 6.7 Instantaneous difference in efficiency for baseline cavity and no cavity case



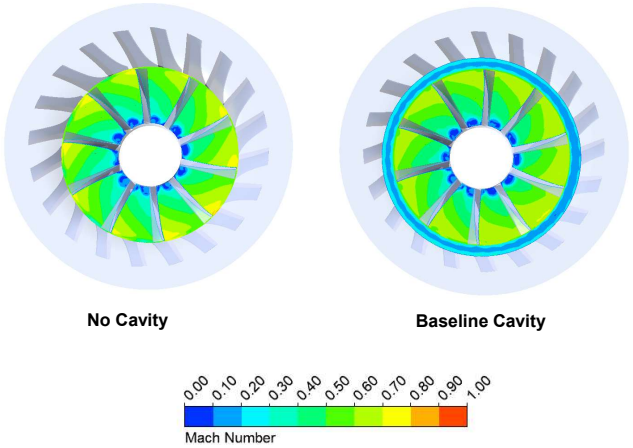
Fig. 6.8 Schematic flow vectors demonstrating the reversal mechanism of the cavity

Since the greatest drop in power occurred at time **G**, the flow field is assessed more closely to study the effects in this region. Figure 6.9a and 6.9b shows entropy and Mach number contours in the cavity plane at time **G**. It can be seen that in the cavity plane there is an

entropy generation in the cavity due to the flow entering the cavity, resulting in frictional losses from shear work between the fluid - fluid layer and fluid - wall layers. Figure 6.9b shows the Mach number. The Mach number in the cavity plane is low because the cavity allows for an accumulation of low momentum fluid. This could also be an indication that in the instantaneous high flow rate condition, the cavity is an area of increased frictional losses.



(a) Static entropy at instantaneous time G for no cavity and baseline cavity case



(b) Mach number at instantaneous time G for no cavity and baseline cavity case

The velocity vectors in the cavity plane for time **G** is shown in Figure 6.10. The top of the figure is the cavity case, the bottom figure is when no cavity is present. This velocity vector provides insight into the flow exiting the cavity. In the cavity case, the velocity vectors of the flow entering the cavity and leaving the cavity can be seen and there is a clear interaction between the returning flow and the main flow. It can also be seen that the returning flow

is of a lower velocity and the main flow, indicating that this is a low momentum region as seen in the Mach number figure 6.9b.

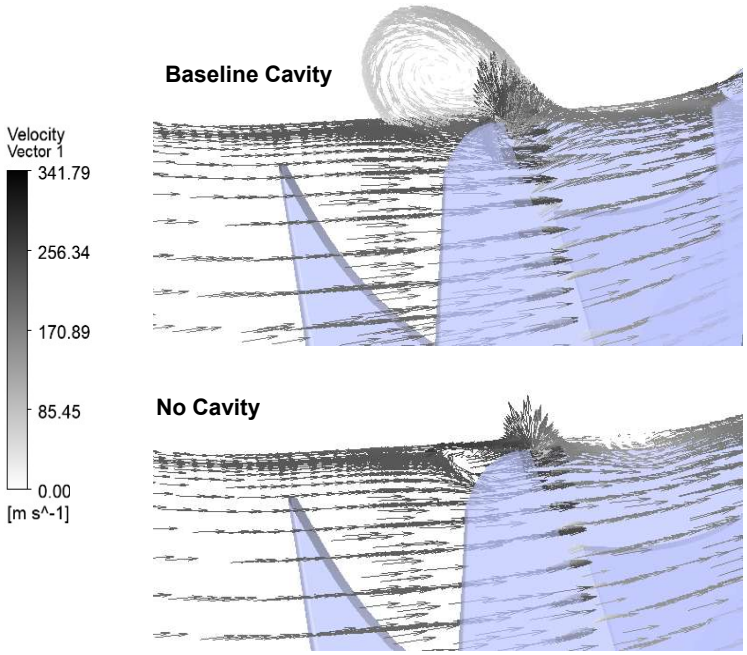


Fig. 6.10 Velocity Vectors for time **G**. Top - Baseline cavity case. Bottom - No cavity case

From this initial analysis it can be seen that the efficiency deficit in the baseline cavity case appears when the mass flow rate is high. The static entropy and mach number contours show that there is entropy generation in the cavity plane. The velocity vectors also show that there is interaction between the low momentum flow leaving the cavity with the main flow - this is where the frictional losses could also be taking place. From this, it is possible to consider a new design or an improved design of the cavity such that the loss in efficiency is reduced.

Design of the optimised Cavity

The design of the optimised cavity is based on the investigation conducted in the preceding section. First, it is clear to see that flow is entering the cavity results in a local static entropy rise around the cavity region. The cavity is beneficial for surge margin improvement as it is the process of reversal of the recirculating flow back towards the main flow that causes the surge margin to be improved. However, in instantaneous high flow conditions, the cavity is not beneficial as there is an efficiency drop of near 8% due to the interaction of the reversing fluid and main flow, resulting in frictional losses and entropy generation.

Modification to the cavity shape could help reduce the efficiency drop in the instantaneous high flow conditions. Figure 6.11 shows a modification of the cavity. First, the size of the cavity has been reduced, this will mean that, at the high flow rates, there will be less flow entering the cavity. As a result, the interaction between the main flow and the reversed flow in the vicinity of the cavity will be reduced. Secondly, the leading edge of the heart-shaped cavity needs to be angled such that it promotes recirculation in the direction of the impeller forward flow. Previously, the baseline cavity, see Figure 6.1, had a curvature that would redirect the flow towards the impeller blades. Because of the shape of the curvature, the redirected flow would directly interact the main flow, rather than merge with the main flow. Figure 6.11 shows a schematic of the angular change that has been implemented to allow the flow efficiently merge with the main flow upon reversal.

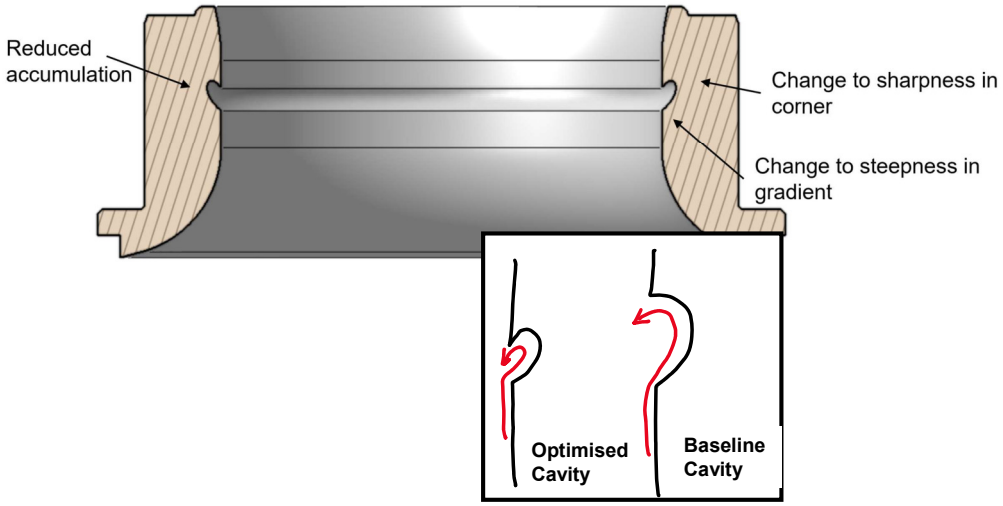


Fig. 6.11 Optimised shape of cavity based on CFD insights - the change to shape is based on the velocity vectors

The optimised cavity shape has been designed to reduce the losses in the cavity but still promote flow recirculation near surge. Due to the limited time available for this research, a computational investigation of the optimised cavity would have taken much longer; to be time-efficient, it was decided to experimentally investigate the baseline and optimised cavities on the test facility, which at this point had all the improvements and modifications for accurate efficiency investigations. This would provide key insights which could be used in future computational investigations.

6.1.2 Experimental Investigation

In this section the experimental research on cavities is detailed. It is worth noting that during Martos's research, the four initial positions were also experimentally studied under pulsating conditions. The results from the initial tests conducted by Martos are available in Martos [66]. However, these results were on a different experimental facility and since there have been many changes to the experimental facility, such as the change in inlet pipe, v-cone flow meter, insulation, and changed instrumentation, there is a need to recreate the experimental research as well. Additionally, comparisons will not be made between the research conducted in this study to the previous study - because this comparison is not valid - the experimental approach, design of the cavity and the experimental test set-up is too different to compare, even though the baseline cavity is tested in this research again.

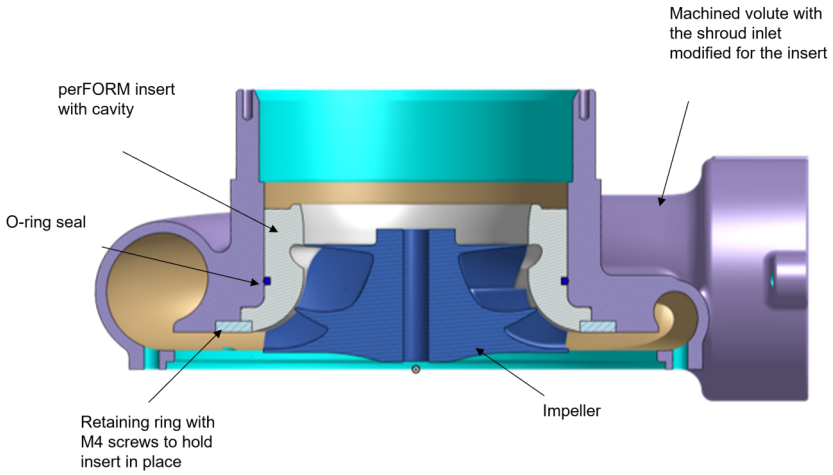


Fig. 6.12 Cad model of the cavity insert and volute assembly

To allow the experimental assessment of the optimised cavity design, a modular compressor has been used. This type of compressor allows for testing of different cavity cut-outs in the shroud. Traditionally, volutes are made in cast-aluminum through a process of sand casting. The process of creating a cast is expensive and lengthy, and usually not worth the time and effort for one-off R&D design. An alternative option for production is 3D printing as it is a convenient choice for prototyping and exploration. 3D printing is a process by which powdered resin is melted together and built upon layer by layer. The research group is familiar with 3D printing bespoke turbocharger designs for testing. Previously, the group has printed ducts, fans and scrolls in SOMOS perFORM, a high temperature grade resin. The selection of this material was based on its suitability under high temperature operation, material roughness (surface finish very smooth), its relatively low cost and manufacturing time when compared to common casting methods for this type of components. However, one of the caveats of using a 3D printed material is that the material properties are different to cast-aluminium. For this reason, the experimental comparisons cannot be made to aluminium results as the results would not be valid. The volute was modified to include a

perFORM insert, which would have the cavity removed from the shroud. A section view of the volute with the cavity treatment insert is shown in Figure 6.12. The printed geometry is shown in Figure 6.13.



Fig. 6.13 Pictures of the cavity insert in the modified volute assembly

Experimental Results

Three perFORM inserts were tested: no cavity, baseline cavity and optimised cavity. The properties of perFORM are different to that of cast aluminium, so for a comparison to

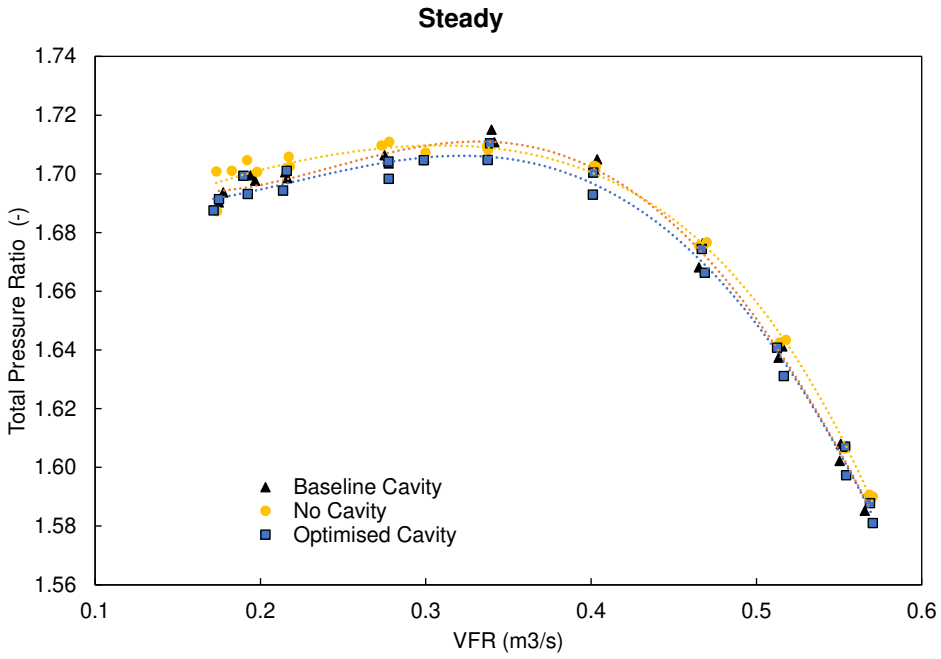
be made to the no cavity cases, it was important that the comparison would be made to perFORM.

The experimental results for total to total pressure ratio and efficiency are shown in Figures 6.14, 6.15, 6.16 and 6.17. Three pulsating frequencies are tested: 30Hz, 46.7Hz and 66Hz. For the steady and all pulsating frequency cases, the optimised cavity has a higher peak efficiency point, and has a higher efficiency in the high flow regions. At low mass flow rates, the steady and pulsating flow efficiencies are similar so the presence of the cavity does not affect efficiency in the low flow rate regions. The efficiency improvement at the peak efficiency point is shown in Table 6.3. It can be seen that at the peak efficiency point being compared, the improvement in the optimised cavity to the no cavity case is around 1.2% to 1.7%. The baseline cavity case has a similar efficiency to the no cavity case.

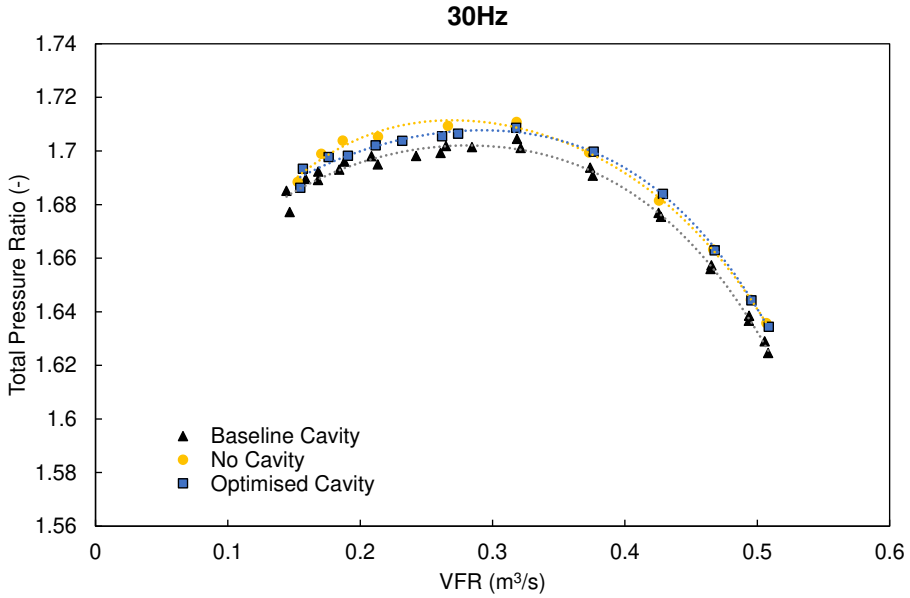
Table 6.3 Efficiency difference at peak efficiency point (OP C)

Operation	**No Cavity**	**Baseline Cavity**	**Optimised Cavity**	**Improvement**
Steady	0.835	0.830	0.845	1.2%
30Hz	0.825	0.824	0.838	1.7%
46.7Hz	0.825	0.823	0.837	1.7%
66Hz	0.835	0.834	0.845	1.3%

This result adds to the understanding that the slight efficiency deficit in the baseline cavity is because there is a flow rate effect, due to the increased frictional losses coming from the shear work generated between the fluid layers and wall layers. Interestingly, the optimised cavity case shows better efficiency than no-cavity cases. This could indicate that the presence of a cavity might capture some of the tip losses that were seen in Figure 6.10 for the no-cavity case, hence, it is beneficial in that region. Note that the cavity results are presented in terms of volume flow rate (VFR), as a requirement from the industrial sponsor.

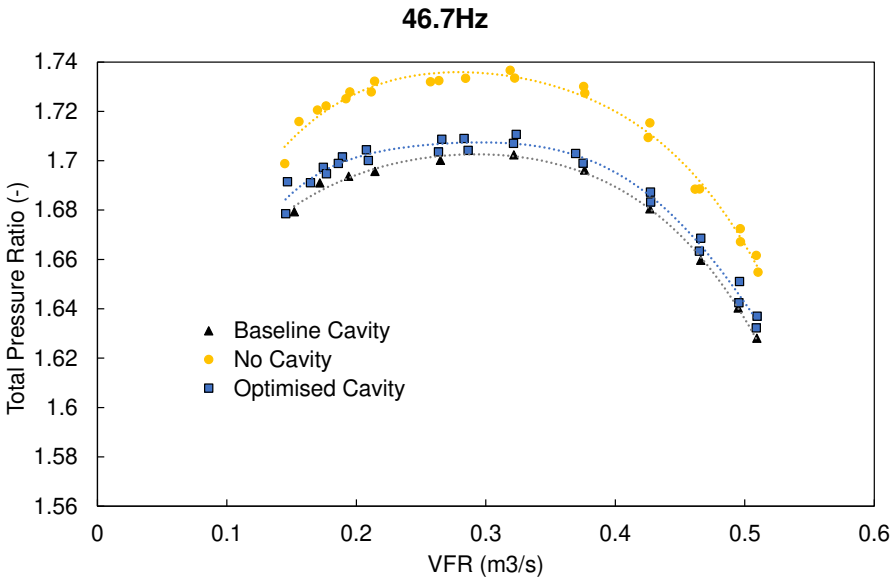


(a) Pressure Ratio vs mass flow rate for baseline cavity, no cavity and optimised cavity - steady flow

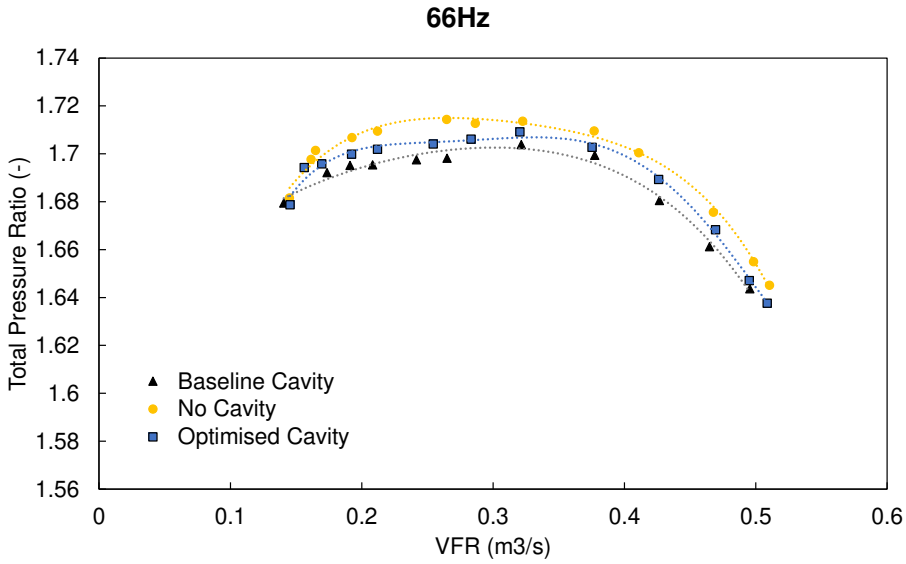


(b) Pressure Ratio vs mass flow rate for baseline cavity, no cavity and optimised cavity case - pulsating flow at 30Hz

Fig. 6.14 Total to total pressure ratio for steady and pulsating (30Hz) cases

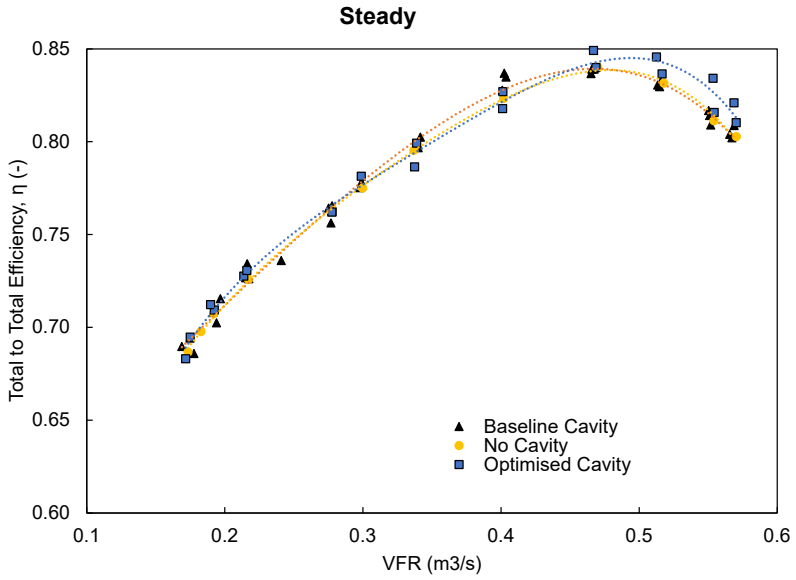


(a) Pressure ratio vs mass flow rate for baseline cavity, no cavity and optimised cavity case - pulsating flow at 46.7Hz

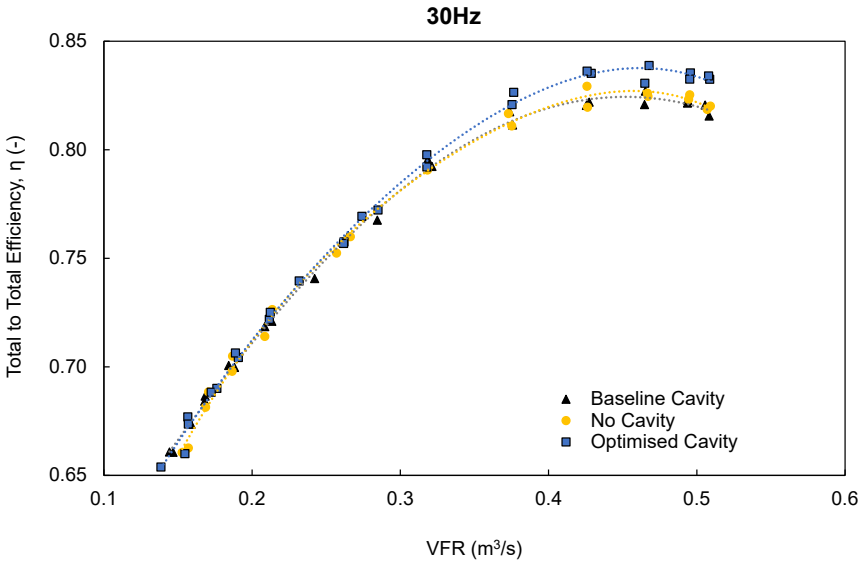


(b) Pressure ratio vs mass flow rate for baseline cavity, no cavity and optimised cavity case - pulsating flow at 66Hz

Fig. 6.15 Total to total pressure ratio for pulsating flow 46.7Hz and 66Hz cases

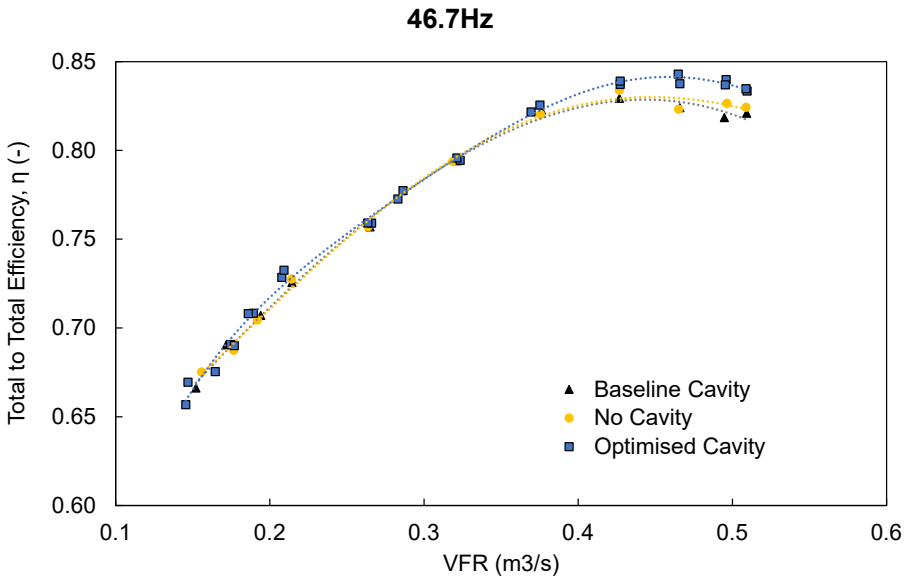


(a) Efficiency vs mass flow rate for baseline cavity, no cavity and optimised cavity - steady flow

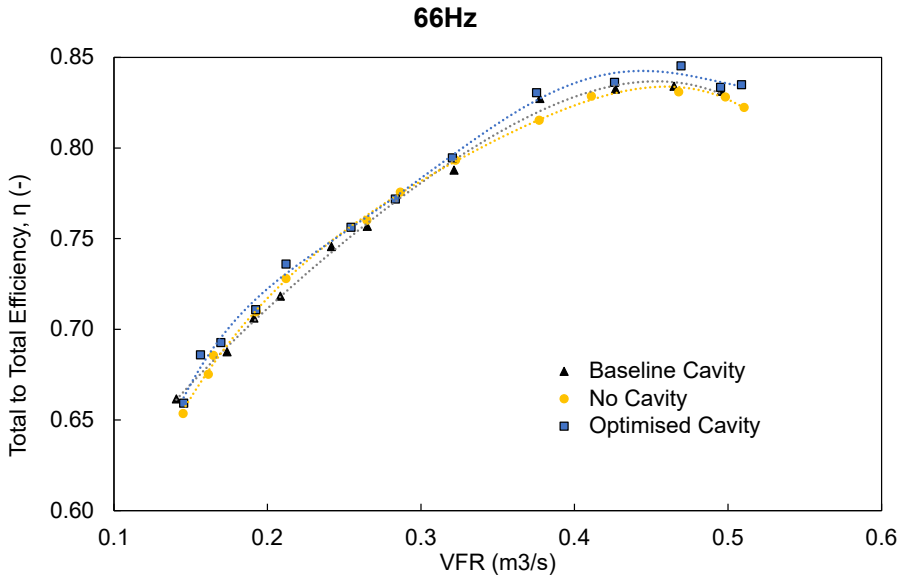


(b) Efficiency vs mass flow rate for baseline cavity, no cavity and optimised cavity case - pulsating flow at 30Hz

Fig. 6.16 Total to total efficiency for steady and pulsating (30Hz) cases



(a) Efficiency vs mass flow rate for baseline cavity, no cavity and optimised cavity case - pulsating flow at 46.7Hz



(b) Efficiency vs mass flow rate for baseline cavity, no cavity and optimised cavity case - pulsating flow at 66Hz

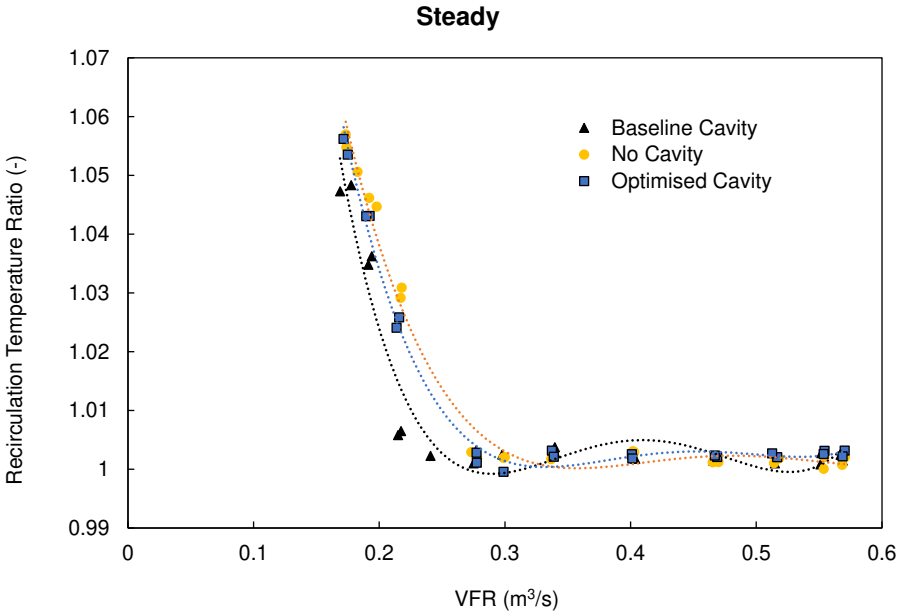
Fig. 6.17 Total to total efficiency for pulsating flow 46.7Hz and 66Hz cases

Effect on surge margin

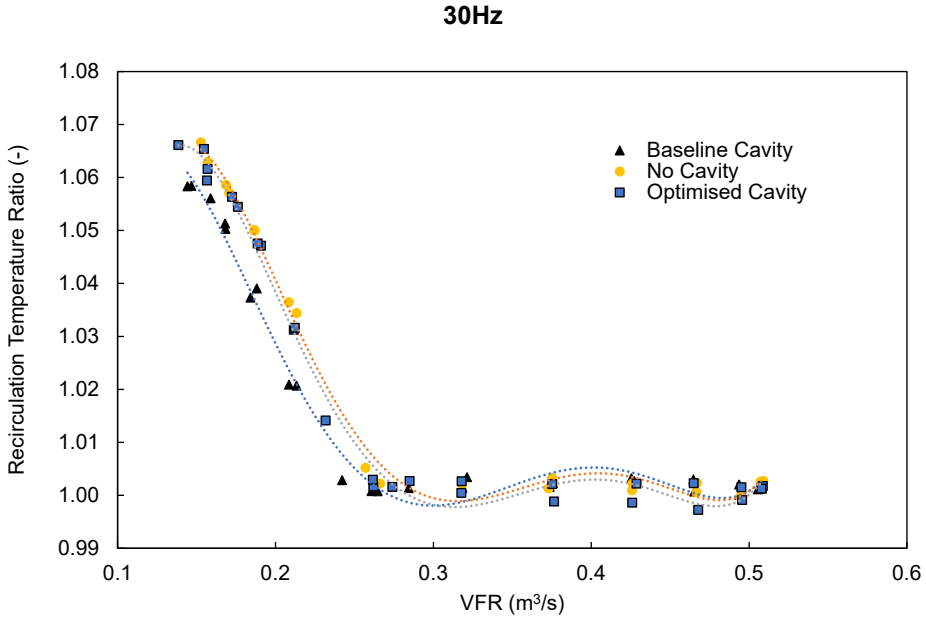
In this experimental campaign, as the effect of high temperature on the perFORM inserts were unknown the compressor was not taken to surge. Therefore, the exact point of the surge margin is not known. However, the recirculation temperature probe (placed a distance of one diameter away, 100mm) from the compressor inlet picks up recirculation temperature. This effect usually happens on the low momentum fluid near the shroud tip. The temperature increases because the fluid has been partially compressed before it is returned.

If a ratio of the recirculation temperature is taken with the inlet temperature, it provides a non-dimensional recirculation temperature ratio. The higher the ratio, the more the temperature has risen at the measurement location, indicating that more fluid has been returned. When the recirculation temperature ratio is plotted against the mass flow rate, it can provide information of the flow rate at which recirculation starts to occur. This has been shown for the steady and 30Hz case Figure 6.18. When the ratio is 1 or below, it means that there has been no recirculated fluid. When the ratio begins to rise, there has been some recirculation.

The mass flow rates for the recirculation are lower for the baseline cavity case compared to the no cavity and optimised cavity case. In the latter, the recirculation mass flow rate seems to be similar, although there is still a slight shift in the return mass flow rates for the optimised cavity case (black squares) compared to no cavity case (yellow circles) in Figure 6.18. In comparison, there is a clear drop in the mass flow rate for the baseline cavity case (black triangles). This means that in the baseline cavity case, the mass flow rate dropped further before flow recirculation began. This indicates that the surge margin would actually have been improved (had it been possible to measure it). This means that the optimised cavity improves the efficiency but perhaps does not result in a sufficient improvement of the surge margin as the cavity size has been reduced. Whilst the optimised cavity does not provide as clear a benefit on surge margin as the baseline cavity, it is worth emphasising that the mass flow range has not been affected by the reduced cavity size. This shows that there is no detrimental impact on the overall compressor operating range as a result of the cavity.



(a) Steady flow recirculation temperature ratio for baseline cavity, no cavity and optimised cavity



(b) Pulsating flow (30Hz) recirculation temperature ratio for baseline cavity, no cavity and optimised cavity case

Fig. 6.18 Recirculation temperature ratio for steady and unsteady case of 30Hz

The results from the compressor cavity testing are interesting. Designers can take away that there is an efficiency drop in the baseline cavity case due to the size of the cavity. Reducing the size of the cavity improves the efficiency, and in fact, the efficiency is improved such that it is even greater than the steady efficiency in cases. However, reducing the size of the cavity does not seem to effect the surge margin - not enough of the fluid gets captured by the cavity to prevent inlet flow recirculation.

6.2 Modification 2: Compressor Tongue

6.2.1 Compressor Tongue

The compressor tongue is a region between the scroll exit duct and the inlet of the scroll, as shown in Figure 6.19. It was shown in Chapter 2 and Chapter 5 that the compressor tongue is an important region for the compressor as the diffuser exit flow is influenced by the pressure fluctuations in the vicinity of the tongue. The shape of the tongue is critical in the way the pressure fluctuations travel upstream. The position and angle of the tongue has local effects on mixing and flow distortion, reducing the performance of the compressor.

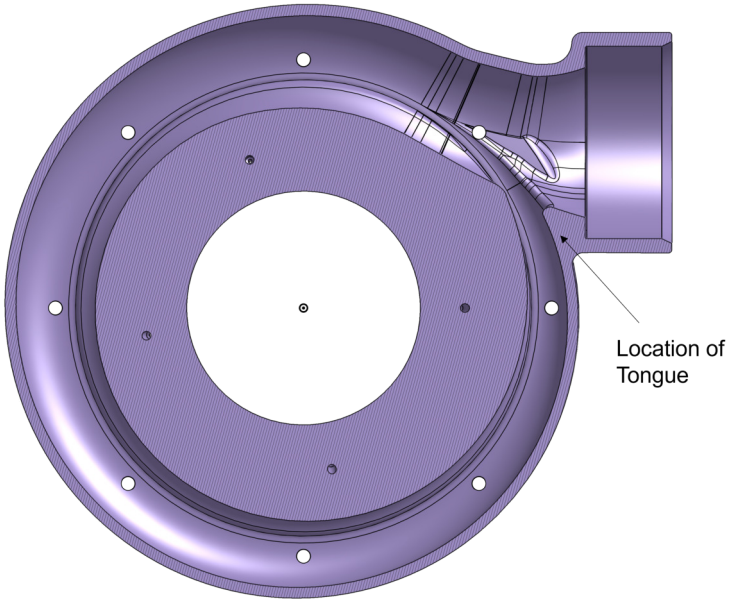


Fig. 6.19 Location of the tongue on the baseline compressor

Figure 6.20 shows two design ideas to modify the tongue shape. This is based on the analysis of the flow around the tongue as shown in Chapter 5. When there is low pressure at the outlet, there is interaction of the exit flow on either side of the tongue region, resulting in flow stagnation and mixing losses. Subsequently, the tongue region is an area of high entropy rise, contributing to the entropy generation rate of the total volute by around 20%.

In this design process, it is hypothesised that the tongue curvature needs to match the fluid motion when it is in an off-design situation. In particular, tongue should aim to capture the flow behaviour at the worst performing instantaneous states for the large flow design point. The worst performing state is the condition when the backpressure instantaneously drops; the low pressure at the compressor outlet in the system drives the mass flow in the incorrect direction through the tongue gap. If the tongue gap is designed such that the flow

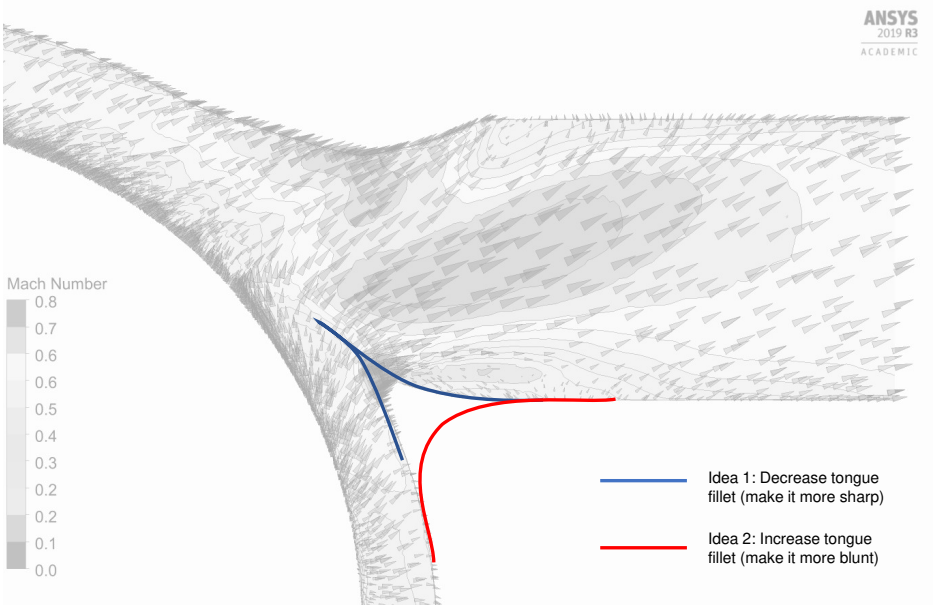


Fig. 6.20 Design ideas for modifying the tongue shape to accommodate the flow at off-design conditions

through the gap is limited, there would be less mixing and interaction between the flow in that region of the tongue.

Figure 6.20 demonstrates the two design ideas. In idea 1, where the fillet radius is reduced and the sharpness around the tongue increases. As a consequence, it is hypothesised that this modification will block the flow path further, preventing the flow from leaving the incorrect way around the tongue. An alternative approach to this proposal is to accommodate the incorrectly leaving mass flow. In idea 2 shown in Figure 6.20, the fillet radius is increased and the fillet radius is made more blunt. It is hypothesized that this alternative modification will accommodate the incorrectly leaving flow and consequently reduce the mixing losses.

6.2.2 Design Process for Compressor Tongue Modification

In order to to test the hypothesis, the tongue geometry was modified. The investigation involved creating a computer aided design (CAD) model of the the baseline MHI volute due to its complex shape. The CAD model would also be used to create of new mesh or volute surface for manufacture of the new geometries.

However, the creation of new geometries was initially difficult. In order to be true to the original design as best as possible, it was important that all parameters matched the baseline compressor and only the tongue region was modified. The original MHI volute

provided to us as a CAD 'volume' file was a complex geometry to dissect. Since the original design sketches were not available, it was difficult to modify just the tongue. Figure 6.21 shows one of the key issues that arose when modifying the volute tongue geometry. When trying to modify the tongue fillet, by making it larger or smaller, there were uneven surfaces created that were difficult to smooth. Even if a smoothing process was applied, due to this clash, the tongue geometry would remain patchy and the resulting mesh would be ill-defined in this region. These local uneven surfaces are unsuitable for computational analysis and even after several attempts, it was difficult to remove this clash.

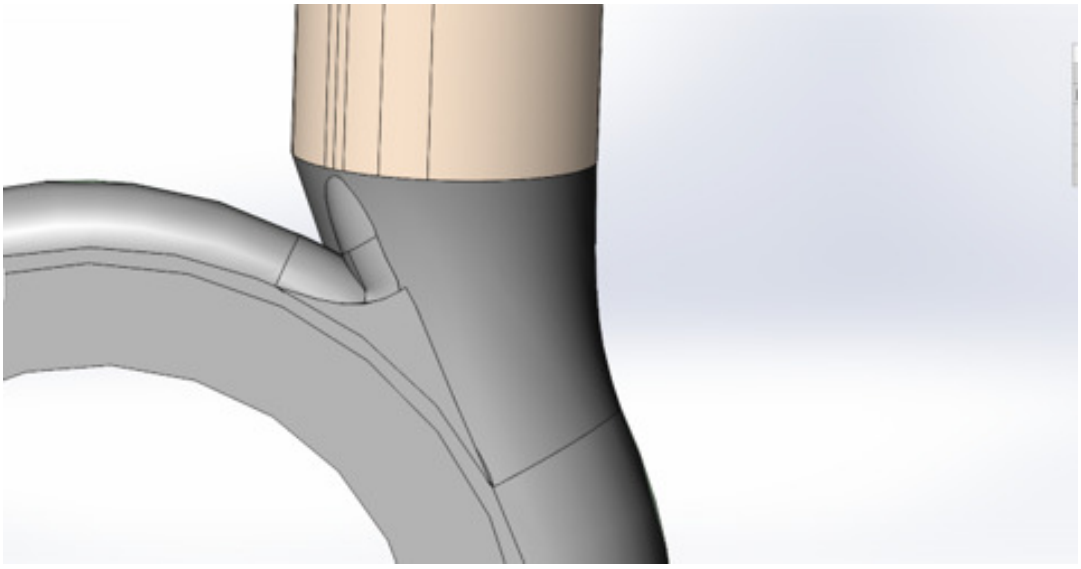


Fig. 6.21 CAD screenshot of the key issues with modifying original MHI geometry

However, it was still important to test this geometry to see the significance of the tongue under pulsating conditions. It was decided to recreate the entire volute geometry maintaining the original Area to Radius (A/R) Ratio and exit duct diameter using a parameterisation process, so that it is possible to control the geometry of the tongue.

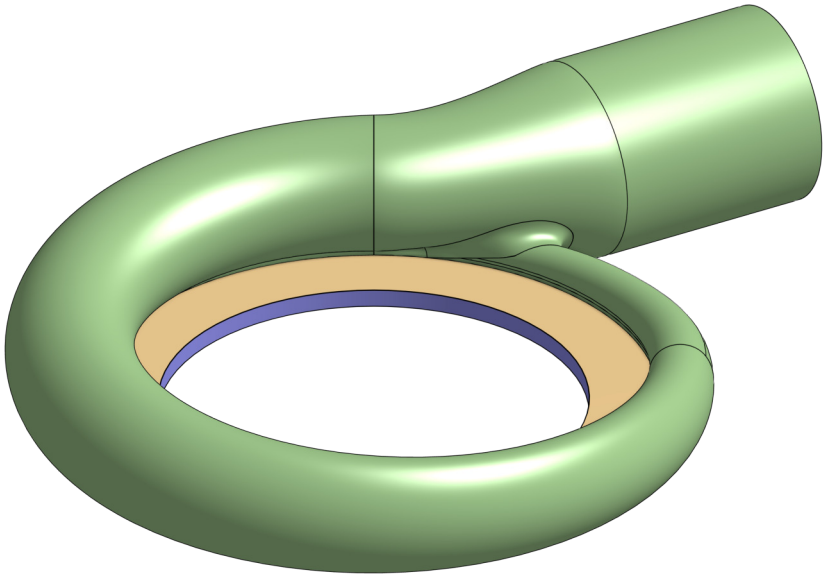
Parametric Volute Design

In order to overcome the aforementioned difficulties and create a volute geometry where the tongue region could be easily modified, a parametric modelling process was applied. This is a useful design technique to create multiple geometries that are similar to each other. Software tailored to parametric modelling assigns geometrical features with equations, rather than just lengths, radii or arcs. Taking a simple example of a rectangle can help explain this scenario, instead of assigning numerical values to the length or breadth of a rectangle, the two lengths can be entered into the model as parameters, x or y. Additionally, one of the lengths could be made into a dependent parameter, for example y = 2x. This would make x the manually adjustable parameter and length y automatically adjust to the

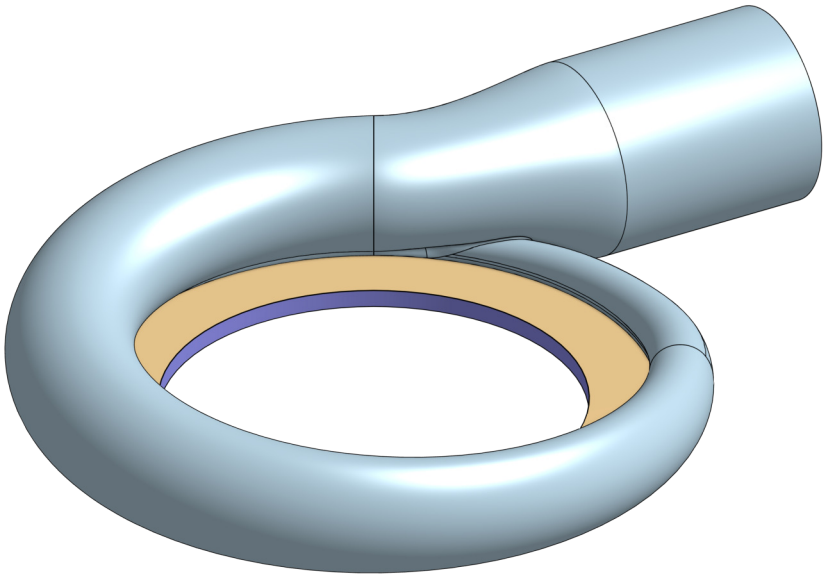
value of x. In this way, it is common to fix some geometrical features as fixed parameters. Aspects of the design that require optimisation or modification are created as design parameters instead.

The MHI volute was parameterised following the same method but albeit to a more complex geometry; however this design is much more complex than the rectangle example above. The parametric model of the compressor volute was developed within the research group for the MHI baseline compressor in conjunction with colleague, C. Freytag, who has previously developed the parametric model for a similar Turbine geometry. For this model, all of the tongue geometry including the scroll exit diameter and the A/R ratio was kept the same and the tongue fillet was chosen as a design parameter.

Figures 6.22a and 6.22b show the two tongue designs in the recreated geometry. This parametric model shows the internal surface of the volute. A computational mesh can be created directly using this internal surface. The computational mesh for both geometries were developed with careful consideration - the mesh in the critical region around the tongue was analysed to ensure that the mesh quality remained similar in both cases, to allow for comparison.



(a) Parametric design of the volute internal surface showing large tongue fillet modification



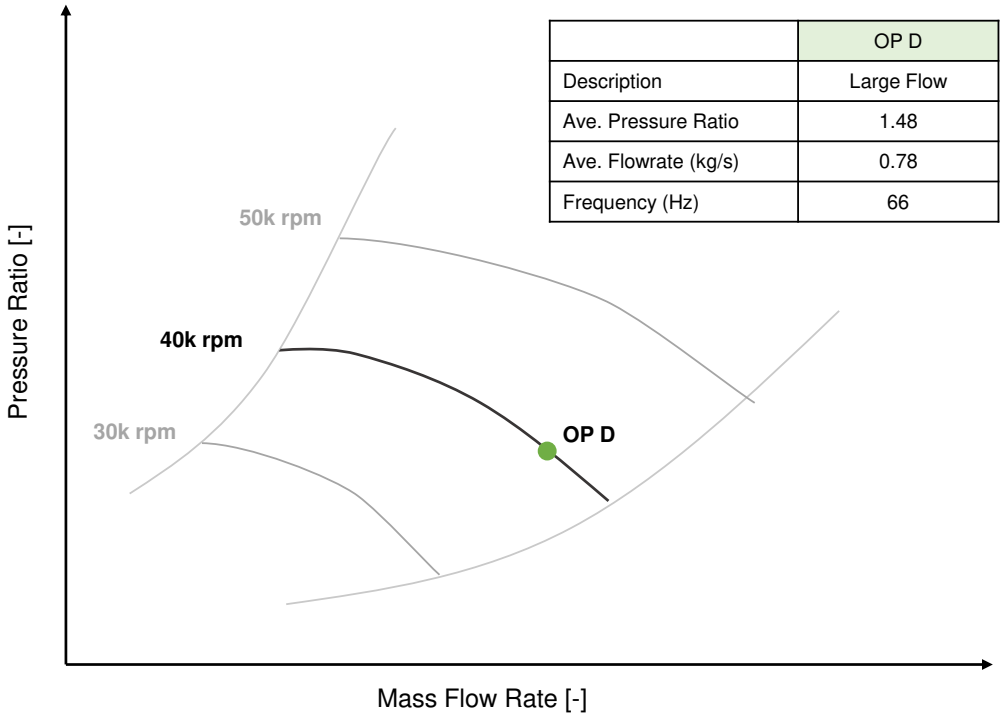
(b) Parametric design of the volute internal surface showing large tongue fillet modification

6.2.3 Computational Results

Operating Point

As previously mentioned, for this study, the compressor runs at 40,000rpm and the frequency of the imposed pulse is 66.6Hz. Three computational simulations are conducted with different geometries for each simulation. The first simulation uses the internal surface of the baseline compressor volute. The results of the sharp and blunt tongue are compared to this baseline volute.

The position of the operating point on the compressor map is shown in the schematic shown in Figure 6.23. It can be seen that this operating point corresponds to the large flow operating condition (OP D), which is the main operating point of interest.



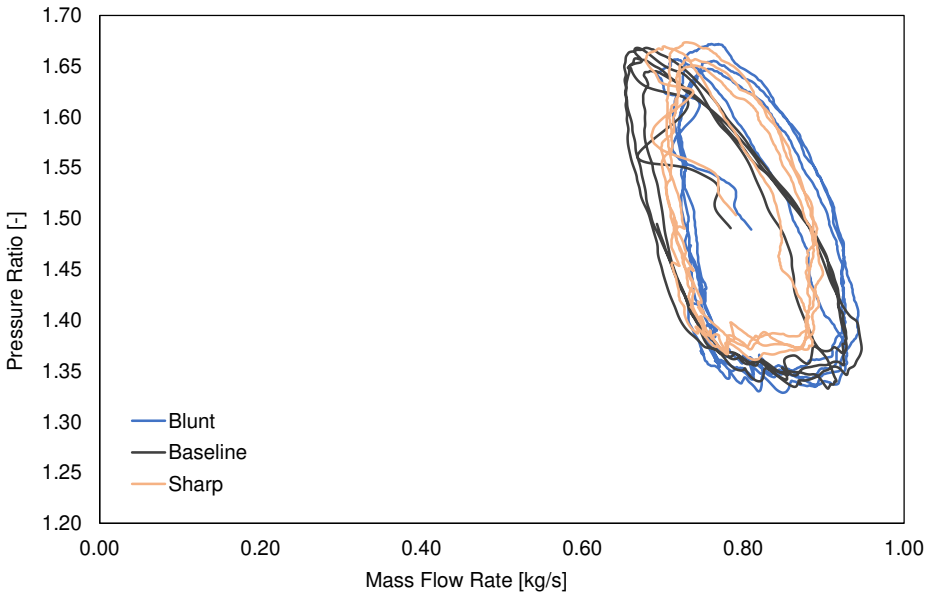
	OP D
Description	Large Flow
Ave. Pressure Ratio	1.48
Ave. Flowrate (kg/s)	0.78
Frequency (Hz)	66

Fig. 6.23 Schematic showing the operating point

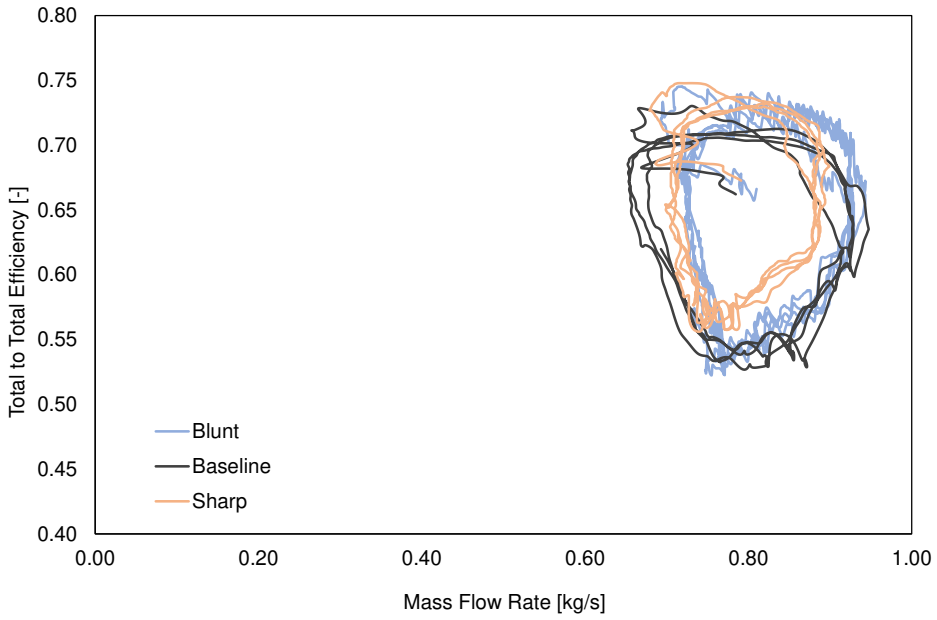
Note that the process of setting up the computational set-up, mesh and boundary condition was described in Chapter 5 and is not repeated here for conciseness.

Computational results at operating point

In this section the results of the computational simulation are described. The pressure ratio and efficiency results compared to mass flow rate are shown in Figure 6.24. Whilst not immediately clear, some differences can be seen. The instantaneous performance within the pulse cycle for the blunt and sharp case is slightly higher when the mass flow rate is instantaneously high.



(a) Pressure ratio and mass flow rate for sharp and blunt tongue volute modifications compared to baseline



(b) Efficiency and mass flow rate for sharp and blunt tongue volute modifications compared to baseline

Fig. 6.24 Pressure ratio and efficiency computational results for large flow operating point (OP D)

A closer look at the efficiency results can provide more insights. The efficiency results comparing the sharp tongue, baseline and blunt tongue is shown in Figure 6.25 and 6.26 for the large flow operating point conducted in CFD, the baseline tongue is shown in black. The

numerical investigation shows that there is an improvement in the sharp case (pulsating as well as average) of around 3.2% in the instantaneous efficiency results. In comparison, the blunt tongue shows an efficiency of around 1.3%. The results show that the sharp tongue and blunt tongue modifications both improve the computational efficiency compared to the baseline average cases, but the sharp tongue shows a higher improvement compared to the blunt tongue case.

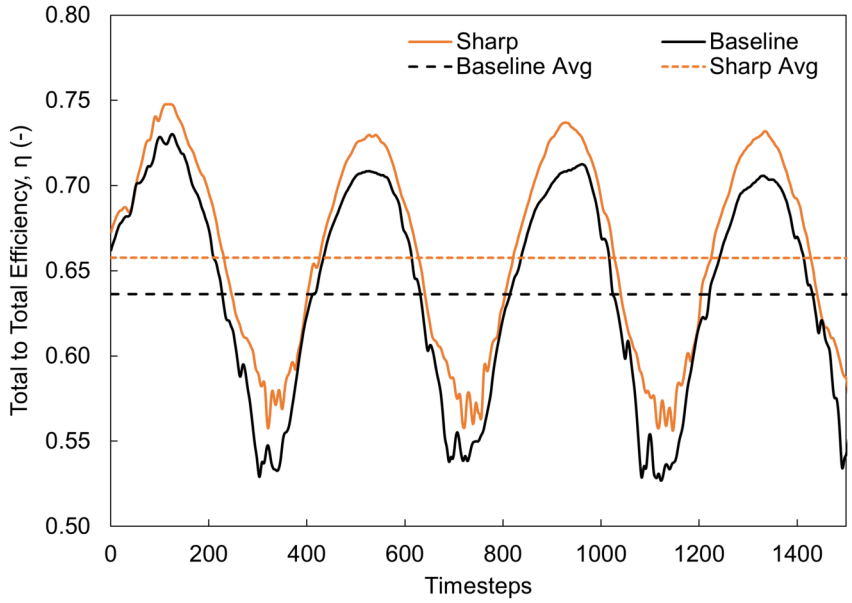


Fig. 6.25 Instantaneous and average efficiency results against time for sharp tongue modification

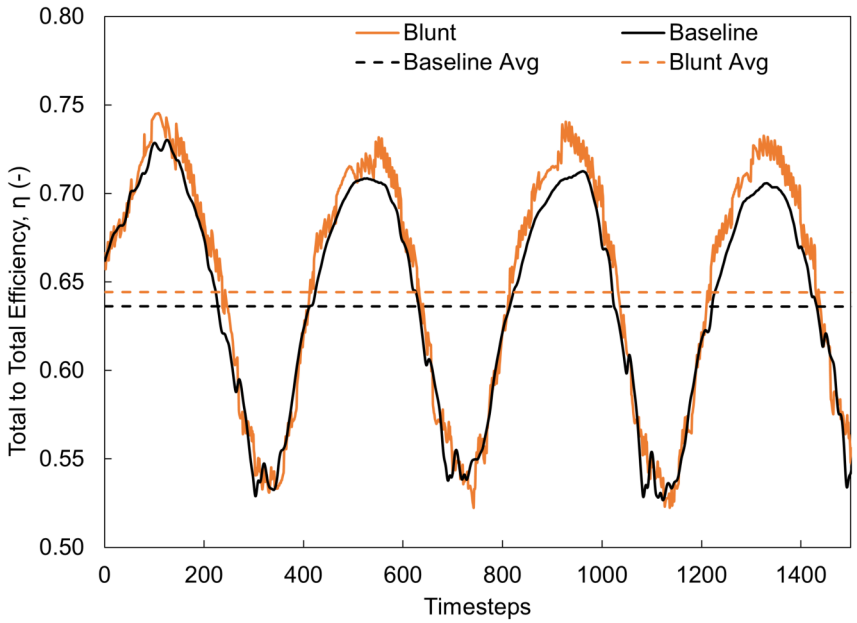


Fig. 6.26 Instantaneous and average efficiency results against time for blunt tongue modification

6.2.4 Experimental Investigation

The computational assessment was conducted on a single operating point, corresponding to the large flow operating point (OP D). A single operating point cannot be sufficiently relied upon for the true performance of the volute designs. However, computational modelling of multiple operating points for such a complex and dense mesh under pulsating flow is not cost-effective, as it requires a large amount of computational time and resources. Therefore, further investigation on this modification was to be complimented with experimental investigation. This section explains the design, manufacture and testing of the compressor tongue modifications experimentally.

The parametric modelling process described above was used to create the internal geometry of the compressor. This is effectively the 'negative' space of a manufactured part, as it is the geometry of the flow. In order to manufacture a volute with the designed internal geometry, the machining profile also needed to be created. The volute needed to have a similar thickness to the baseline volute to retain the heat transfer properties, but it would also need to have similar interfaces to match the requirements of the experimental facility such as the interfacing flanges at the compressor exit.

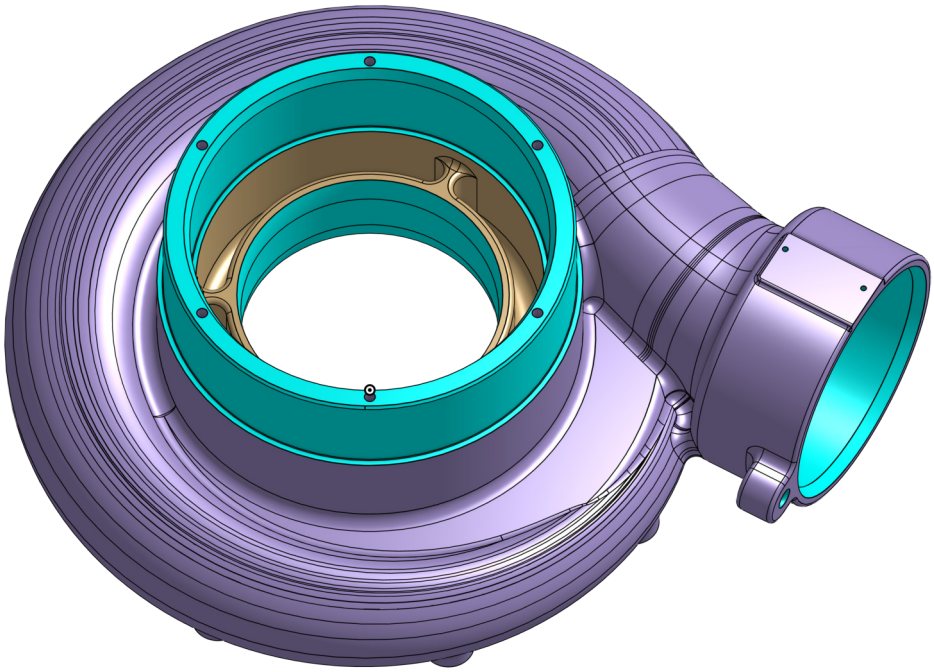


Fig. 6.27 CAD assembly of volute geometry design with the new tongue fillets

The volute corresponding to the modified designs above was created by lab manager and technician C. Noon. The volute was created on CAD package **'Onshape'** and shown here in Figure 6.27. A closer look at the two sharp and tongue modifications in the manufactured volute is shown in Figures 6.28 and 6.29.

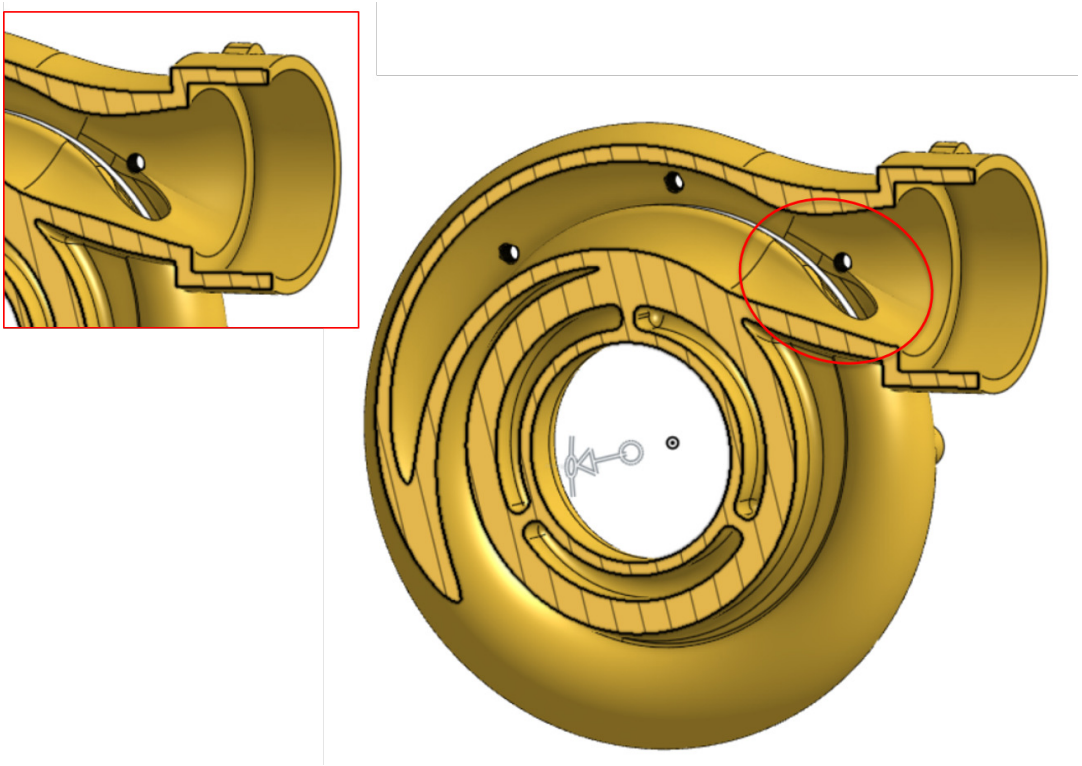


Fig. 6.28 Section view of the CAD model showing the sharp tongue fillet radius

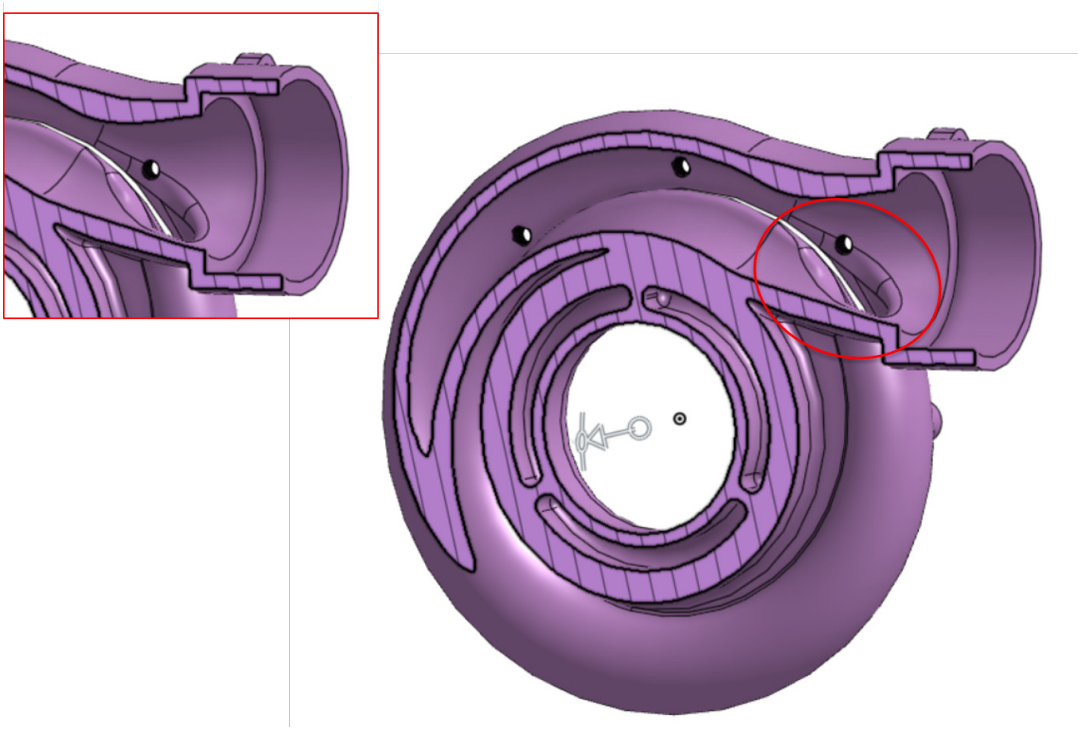


Fig. 6.29 Section view of the CAD model showing the sharp tongue fillet radius

The modified volutes were 3D printed as it is a convenient choice for prototyping and exploration. Previously it was explained that a suitable 3D printing material for this application is SOMOS perFORM, a high temperature grade resin. This material has a smooth surface finish, is cost-effective compared to casting methods and has a small lead time, allowing for fast prototyping.

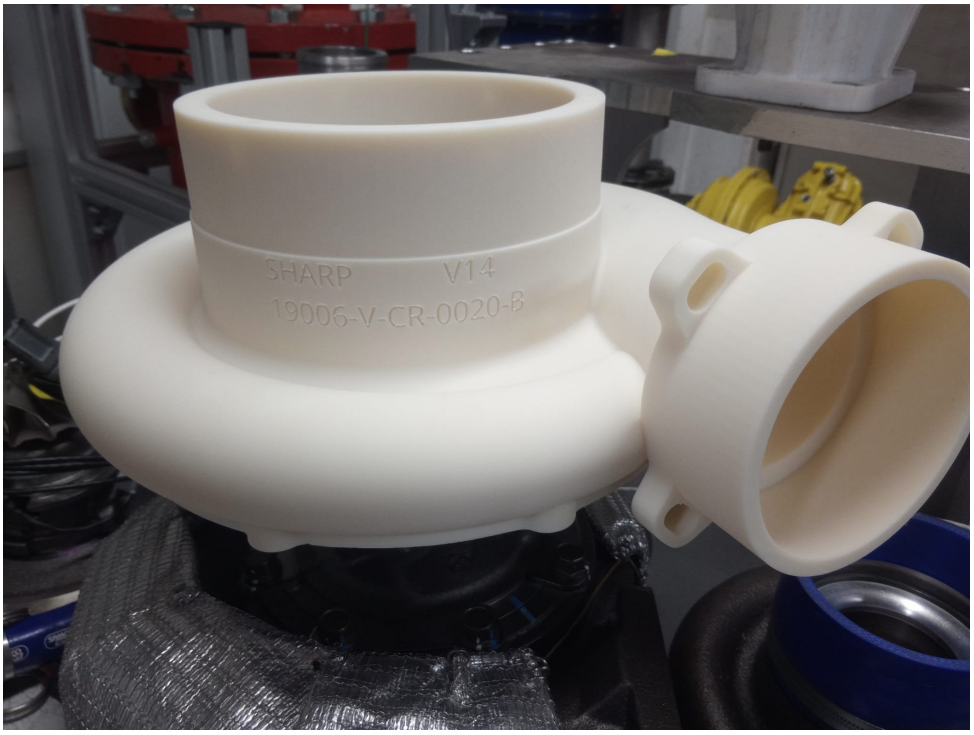


Fig. 6.30 Picture of the printed perFORM volute

The 3D printed perFORM volute for the 'sharp' tongue modification is shown in Figure 6.30 as an example of the completed print. The rest of the experimental set-up matches the original experimental test case and procedure. The inlet pipe is re-installed and the compressor volute is insulated. The measurement planes are kept the same at the inlet and outlet of the compressor and as this was a performance test, no internal measurements are taken.

Testing in perFORM

Although this was the best possible option, there were some issues that arose when working with perFORM volutes of this size and there were some failures. There was a lengthy process of investigation of the failures to assess the key issues. The figure below shows some of the first prints failing at the interfacing bolts and showing signs of touch-down of the shroud region with the impeller.



(a) Damaged tongue perFORM 1



(b) damaged tongue perFORM 2

Fig. 6.31 Pictures of the damaged perFORM volutes after initial testing

The initial investigation led to some key learnings which enabled future testing with perFORM.

1. It was seen that the compressor volute was much larger than previously tested parts. Previous prints in perFORM were for smaller turbocharger scrolls and this meant that there was an element of unfamiliarity of the behaviour of the perFORM volute for a compressor of this size. Therefore, a process of trial-and-error was expected. Additionally, the usage of 3D printed materials for turbocharger testing applications is in itself uncommon.

2. It is well known that the 3D printing tolerances often cannot match traditional machining tolerances. This can affect the position of some of the interfacing geometry. Knowing exactly where the tolerences are affected requires an initial print so that the nominal values for the print can be adjusted to match the expected nominal values from traditional manufacturing. It is also common for 3D printed parts to change their geometry slightly when a 3D printed part is cooled. There is often some associated shrinkage and the geometry is sometimes sub-nominal.

3. For a large 3D printed part like this, it is also common for there to be some sort of print misalignment. This, was possibly the leading cause of interference in some locations near the impeller and the shroud. When layers are built layer upon layer, it is possible that in some positions the compressor radius changes and is not completely uniform, resulting in some internal surfaces having a smaller or greater radius than the nominal condition.

4. There is a natural process of expansion when the material is heated. When the compressor is running, it is natural for the bearing housing, in the vicinity of the interface, to see temperatures as high as 100-120C. This will cause material expansion which needs corresponding space to accommodate. The expansion of perFORM was happening at near half the rate of metal. Additionally, whilst metals have a high ductility, especially under heat, perFORM behaved differently. There are clear fractures at the joints, see figure 6.31a. The fracture is clean, indicating that there was no yielding or shearing in the perFORM material. Under applied heat, the behaviour of perFORM is brittle, like a ceramic, and therefore is unable to accomodate the expansion of the thread insert. Multiple failures of the thread inserts were seen. A solution around this was to avoid overtightening the bolts and keeping the torque loading at a minimum. This worked for the later tests.

5. When an aluminium volute is placed in the test facility, our results showed that there was a high level of repeatability. A test conducted on one day, could be repeated the next day if everything was kept the same. Multiple such tests in aluminium were conducted and it was found that there was a high reliability in the test set up when the aluminium volutes were used. In comparison, when perFORM volutes were tested, there was a heat-dependency. The perFORM volutes were internally expanding when the temperatures were high and the tip-clearances between the impeller and the shroud were changing. This meant that several attempts were made to ensure that there was some sort of repeatability possible. It was found that testing had to be much slower than aluminium. A perFORM volute tested on one day could not be retested at least until the next day at the same time and at the same inlet conditions.

The above discussion highlights the difficulties that arose when testing with a large perFORM volute. The knowledge attained as part of this research sheds some insight for future researchers, within or outside of the research group, when a similar attempt is made.

After the initial failures, the testing protocol was modified and new volutes were ordered in case of breakages. It was possible for the tests to be completed with the modifications. However, it was not possible to obtain multiple repeat results, due to the degradation of the perFORM material. The tests have been repeated at least twice for each operating line.

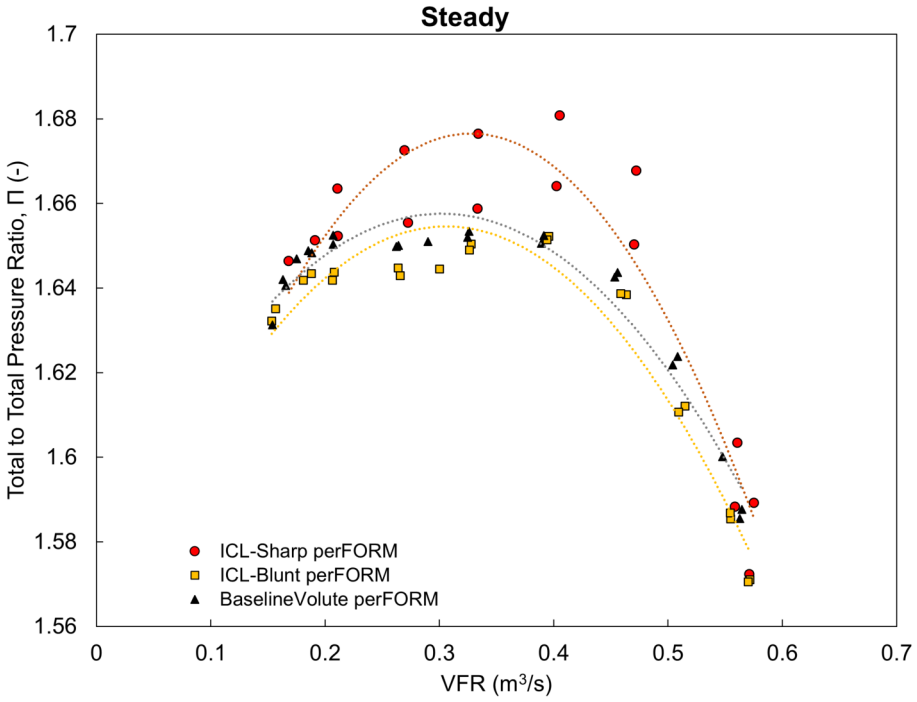
Results

Similar to the computational set-up, the results for the sharp and blunt tongue modifications are compared to a baseline tongue. The baseline tongue has also been printed in perFORM to enable comparision. The absolute values of performance are not representa-

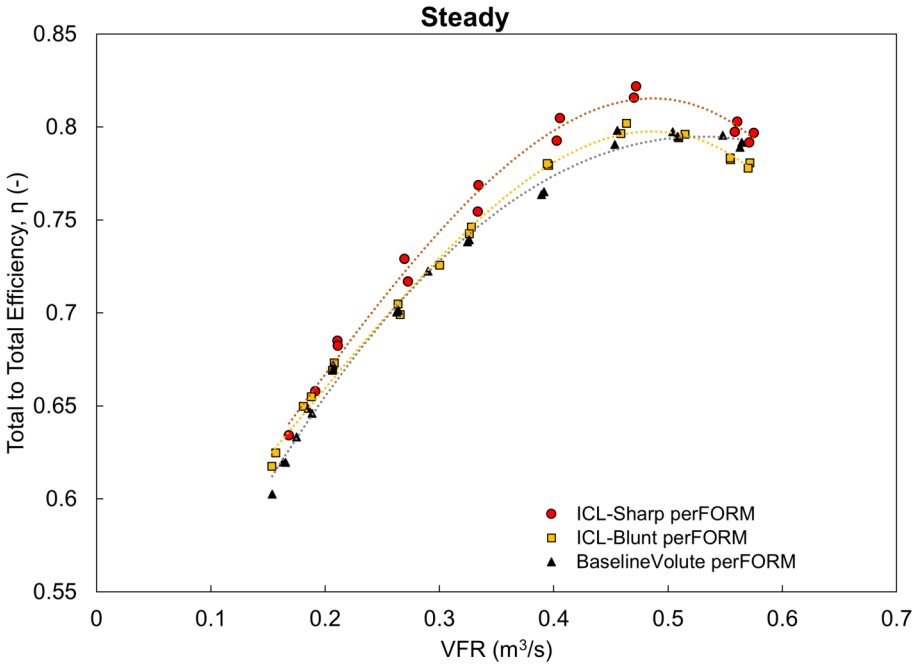
tive of conditions with aluminium. However, for this research, it is critical to compare the performance of the baseline compressor to the modified design.

Figures 6.32 to 6.35 show the results for the experimental performance of the baseline, sharp and blunt tongue modifications for steady flow and three pulsating frequencies: 30Hz, 46.7Hz and 66.7Hz. Results for the full speed-line at a running speed of 40k rpm have been obtained, although it has not been possible to reach the near surge operating point due to material limitations.

The sharp tongue performance for the steady and pulsating cases is greater than the blunt and baseline performance for the full operating line, for all of the tested points. Even though the design case for this modification was the large flow conditions, the performance greatly improved at the peak pressure region. Despite the difficulties in testing with perFORM, it is clear to see that the sharp tongue performed better throughout, leading to confidence that the performance of the compressor with this design modification is better than the baseline compressor. The blunt tongue modification is also found to improve the efficiency, as seen in the computational case, however, the efficiency improvement in the compressor with the blunt tongue is not as distinct as the sharp case.

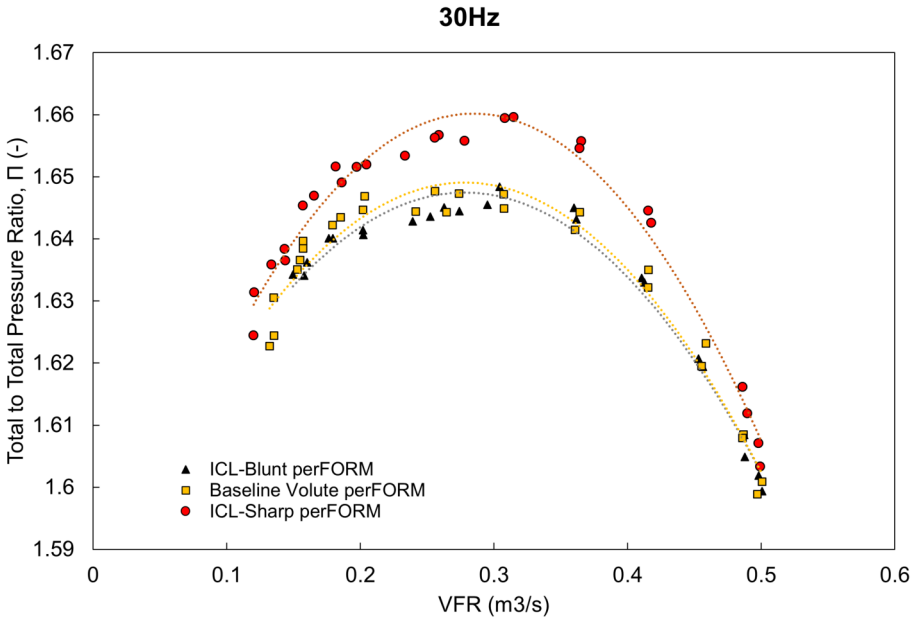


(a) Pressure ratio vs mass flow rate for compressor tongue modifications - Steady flow

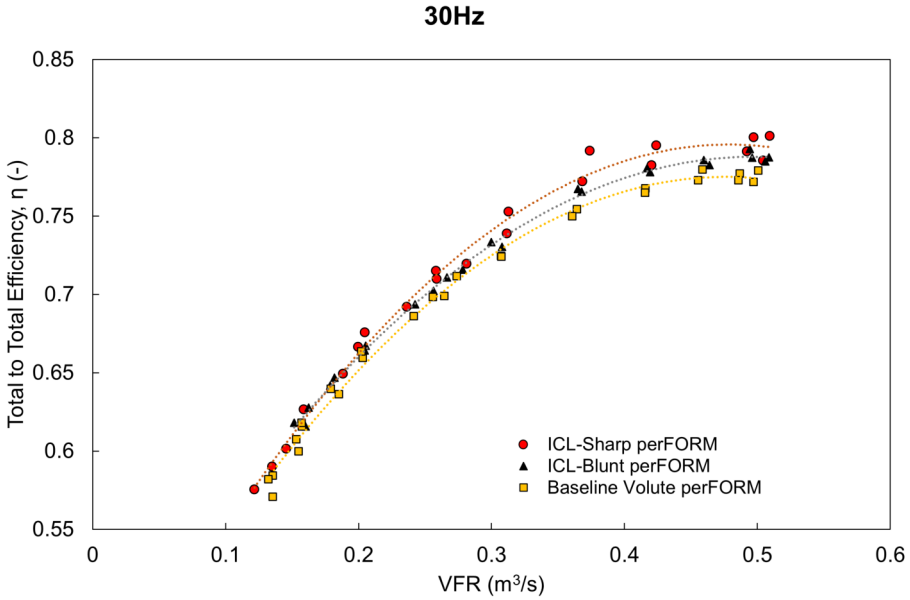


(b) Efficiency vs mass flow rate for compressor tongue modifications - steady flow

Fig. 6.32 Baseline, Sharp and Blunt tongue compressor modification results for pressure ratio and efficiency in steady flow for 40k rpm

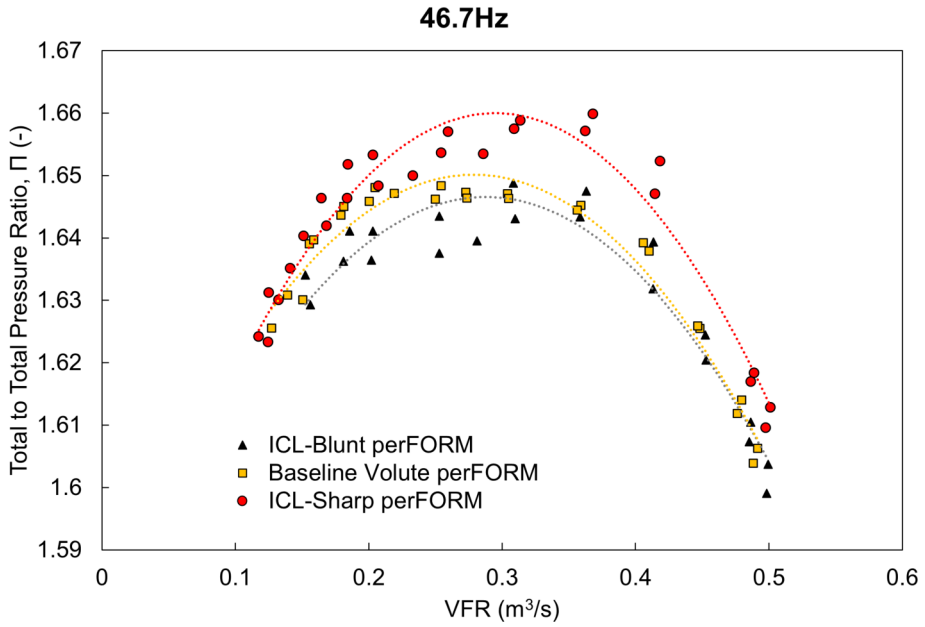


(a) Pressure ratio vs mass flow rate for compressor tongue modifications - 30Hz pulsating flow

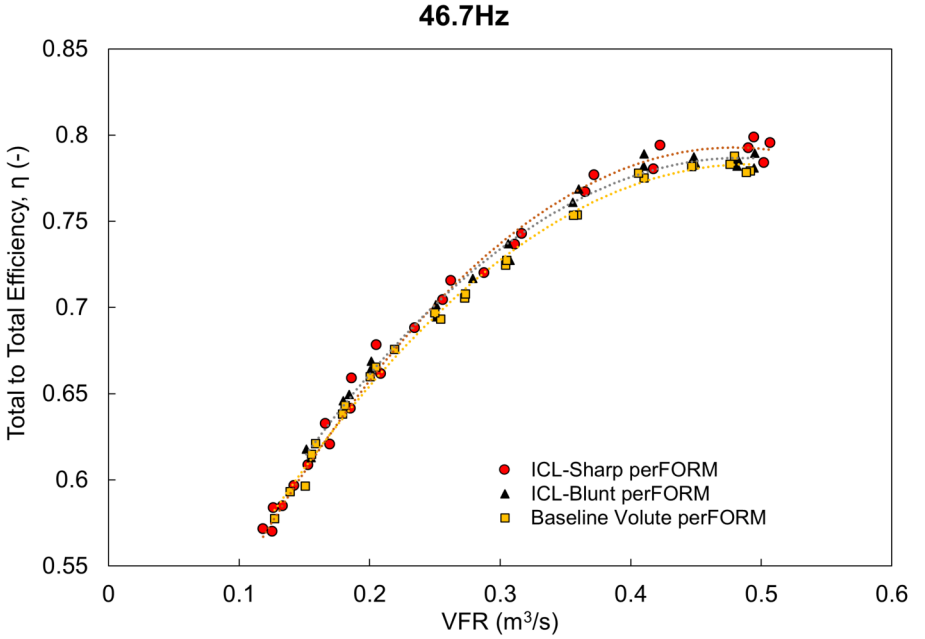


(b) Efficiency vs mass flow rate for compresssor tongue modifications - 30Hz pulsating flow

Fig. 6.33 Baseline, Sharp and Blunt tongue compressor modification results for pressure ratio and efficiency with pulse frequency of 30Hz for 40k rpm

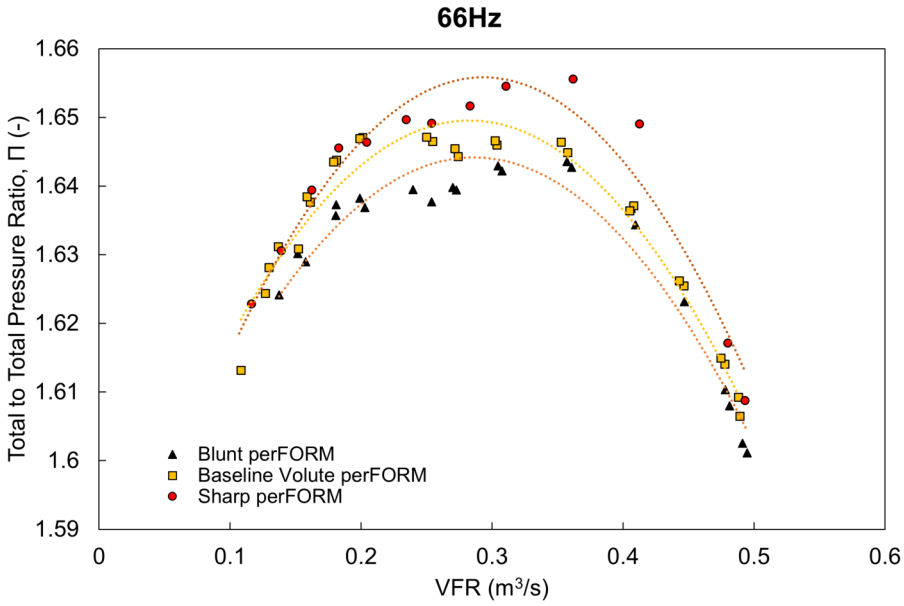


(a) Pressure ratio vs mass flow rate for compressor tongue modifications - 46.7Hz pulsating flow

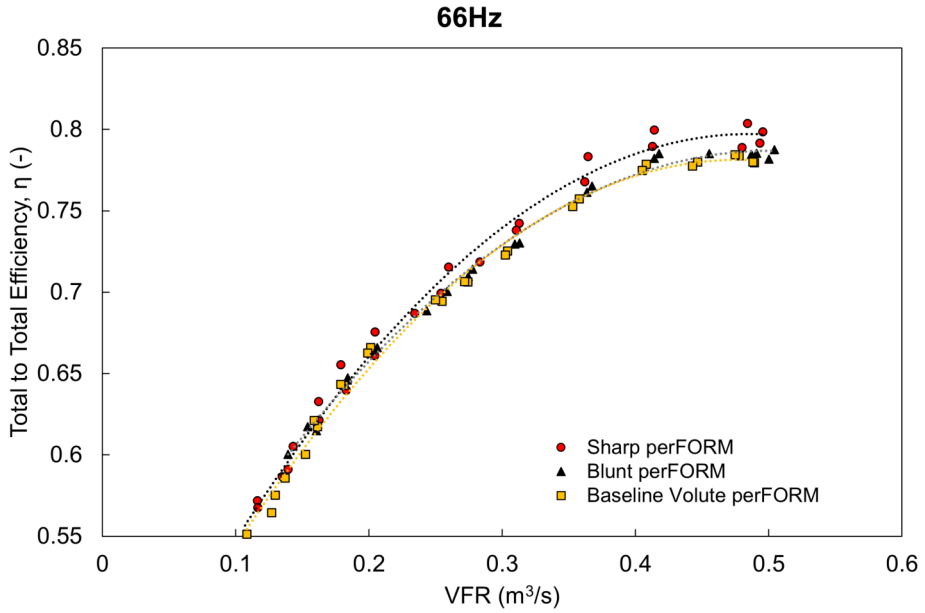


(b) Efficiency vs mass flow rate for compressor tongue modifications - 46.7Hz pulsating flow

Fig. 6.34 Baseline, Sharp and Blunt tongue compressor modification results for pressure ratio and efficiency with pulse frequency of 46.7Hz for 40k rpm



(a) Pressure ratio vs mass flow rate for compressor tongue modifications - 66Hz pulsating flow



(b) Efficiency vs mass flow rate for compressor tongue modifications - 66Hz pulsating flow

Fig. 6.35 Baseline, Sharp and Blunt tongue compressor modification results for pressure ratio and efficiency with pulse frequency of 66.7Hz for 40k rpm

Table 6.4 shows the improvement in peak pressure ratio and peak efficiency for the sharp and blunt compressor tongue modifications compared to the baseline case. It can be seen that at the peak pressure operating point, the sharp tongue compressor modification shows an improvement in total pressure ratio by over 1.6% in the steady flow scenario. When there is pulsating flow in the system, there is an improvement of around 0.6-0.7%. The blunt tongue shows a much smaller improvement in performance of less than 0.5% or lower.

The peak efficiency operating point has an over 2% efficiency improvement in the steady and pulsating flow scenarios for the sharp tongue compressor modification. The blunt tongue compressor modification shows an efficiency improvement of around 1% in the pulsating cases but only 0.5% in the steady flow scenario.

Table 6.4 Improvement of the modified tongue performance at peak pressure and peak efficiency operating points

		Peak Pressure (OP2)	Improvement	Peak Efficiency (OP3)	Improvement
	Sharp	1.676	1.64%	0.821	2.88%
Steady	Blunt	1.653	0.24%	0.802	0.50%
	Baseline	1.649		0.798	
	Sharp	1.659	0.73%	0.801	2.82%
30Hz	Blunt	1.648	0.06%	0.787	1.03%
	Baseline	1.647		0.779	
	Sharp	1.658	0.61%	0.795	2.05%
46.7Hz	Blunt	1.648	0.00%	0.789	1.28%
	Baseline	1.648		0.779	
	Sharp	1.654	0.67%	0.798	2.44%
66.6Hz	Blunt	1.646	0.18%	0.787	1.03%
	Baseline	1.643		0.779	

6.2.5 Discussion

The experimental results show that there was a near 2% efficiency improvement with the sharp tongue compressor modification, and there was also an increase in the peak performance region of the compressor, indicating that the compressor was able to generate a slightly higher pressure rise when the tongue fillet had been reduced. In comparison, the blunt case has a similar efficiency, and even in some cases, has an efficiency improvement of around 1% but the performance is similar or less than the pressure rise in the baseline case. From these experimental results, a clear benefit with the sharp tongue fillet modification can be seen, however, the benefit of the blunt tongue is unclear. It is worth remembering

that these tests are conducted in perFORM, and whilst it has been possible to replicate the aluminium volute performance trends with perFORM, there are insufficient data sets at the present moment, and it is recommended that the tests are repeated with the correct material, such as the cast aluminium volute. The prototype designs of compressors, both computationally and experimentally, have some promise in improving the performance of the compressor with the sharp tongue due to the distinct and clear trends seen in the sharp tongue experiments.

6.3 Chapter Summary

In this chapter, two compressor design modifications were explored and tested.

Modification 1: The first modification to the compressor tested was the compressor cavity. Cavity treatment is a method of taking a shroud cut out in the compressor to re-direct recirculating flow. Previous research had shown that cavity treatment leads to a surge margin improvement, but there is a deficit to the efficiency of the compressor. To investigate, the baseline cavity was studied computationally under pulsating flow, and results within a single pulse cycle showed that the efficiency dropped when the flow rate was instantaneously high. In contrast, the efficiency in the low flow rate conditions was similar to that of the original compressor without a cavity. The cavity size and shape was optimised, and experimental tests on a modified compressor with cavity inserts was conducted. The no-cavity case, baseline cavity and optimised cavity was tested under steady flow and pulsating flow conditions. The optimised cavity showed a higher efficiency and had a higher peak efficiency on average compared to the baseline cavity and no-cavity case. However, as the size had been reduced, there was no benefit on the surge margin. The optimised cavity treatment was resulting in an increase in efficiency because it was accommodating some of the flow vectors that were captured in Fig 6.8, in the no-cavity case, however, the size was not large enough to retain the benefit of surge margin improvement. Further optimisation of the compressor cavity is required to improve both the efficiency and surge margin of the compressor.

Modification 2: The second compressor design modification that was studied was the volute tongue. From computational flow field analysis, the region near the tongue is a high entropy region, particularly at off-design states, when a low pressure at the compressor outlet was causing the flow to travel incorrectly in that region. To rectify, two different tongue fillet radius modifications were trialled: the fillet radius was increased (sharp) and reduced (blunt) to see if this could improve the efficiency under off-design states. A parametric model of the tongue was created such that the fillet radius could be controlled and modified. From this, it was possible to complete the design and re-create the geometry

in CAD. A computational simulation was conducted at the large flow operating point with the modified compressor and it was seen that for the pulsating flow conditions, it was seen that there was an improvement in efficiency with the sharp tongue in some operating points, whilst for the blunt tongue the efficiency was similar to the baseline case.

Experiments were conducted on the baseline tongue, sharp tongue and blunt compressor tongue modifications. There were some issues in testing with perFORM and these have been reported in the chapter. Tests were conducted with new volutes for a limited operating range, and some initial experimental insights have been obtained. The experimental results for efficiency have been presented and discussed. From these experimental results, a clear benefit with the sharp tongue fillet was obtained as well at near 2% for the full operating line at all pulsating flow frequencies, however, the benefit of the blunt tongue was unclear. There is a 1% improvement in efficiency with the blunt tongue, but the performance is similar or slightly worse than the baseline case.

In this research, the two modifications were tested separately and benefits from both modifications were seen. In future research, combine both modifications to create a more optimised design, with the benefits from both modifications.

Chapter 7

Torque Meter Design, Development and Preliminary Results

The final objective of this research was to assess performance in pulsating flow conditions using a torque meter. This would not only provide an alternative method for assessing compressor performance but it would also capture instantaneous data that was not possible to obtain with the previous instrumentation capabilities of the experimental facility.

Outline of Requirement

There are two main reasons a torque meter is required. The first reason is that a torque meter, placed in-line with the shaft, can be used to determine the response of the impeller to the outlet pulse. The previous chapters have shown that the measurements of performance are usually conducted using measurements at the compressor outlet. The pressure pulse at the impeller is not of the same magnitude or phase as that at the compressor outlet. This is a consequence of the physical time taken for pressure to travel upstream through the compressor system and the damping of the pressure wave through the volute. A torque meter that is installed on the compressor shaft which is in-line with the impeller can directly measure the impeller response.

Secondly, torque meters can be used to calculate instantaneous efficiency. Instantaneous efficiency cannot be calculated using thermocouples because to do so would require temperature data at the rate of the fluctuations. Temperature sensors do not currently have the capacity to respond to the changing flow conditions in the same way that high-speed pressure transducers can. In contrast, instantaneous pressure measurements using high-speed pressure transducers are possible both due to the advances in measurement

capabilities of transducers as well as the availability of required data acquisition modules. Therefore, although the facility was improved for thermal equilibrium and heat losses, instantaneous efficiency, which would provide insight on the losses, was still difficult to assess without a torque meter. The purpose of the torque meter is therefore to determine the actual impeller response and also estimate instantaneous efficiency.

As there was no torque meter present at the time of this research that met the specifications of the project, a torque meter needed to be procured. Commercially available torque transducers for high speed, high-torque operation in this specification range were around £25,000-£30,000. Discussions with leading torque transducer manufacturers were initiated and no suitable devices within range and budget were found. A bespoke torque meter would have to have been developed by the manufacturer which was deemed unsuitable at this early stage of development.

Since torque measurements were deemed an essential improvement to the experimental facility, an innovative, low-cost bespoke torque meter was designed and developed in parallel. This project took over 3 years to complete and included a number of collaborators due to the complexity and challenge. Final year student, G. Singh, developed an initial prototype based on the required operating conditions. The initial prototype was further developed in conjunction with lab manager C. Noon and research technician, H. Flora. The build, design and initial calibration of the in-house torque meter can be found in Parikh et al. [92]. The outcome of this parallel project was an initial prototype of a torque meter that is currently installed on the compressor testing facility.

In this chapter, the design and development of a bespoke torque meter for the measurement of unsteady torque has been outlined, including the calibration and validation process for the use of the torque meter in assessment of compressor performance.

This chapter is divided into two parts. The first section summarises the design and development of the torque meter to provide the necessary background and context to the reader. Part of this first section is published in Parikh et al [92]. The second section outlines the validation of the torque meter for research on compressor efficiency. It presents the experimental methodology for unsteady thermodynamic assessments and presents the preliminary results with the torque meter installed. The results detail instantaneous, unsteady compressor performance, torque and efficiency. Finally, a discussion on the current limitations of the torque meter and conclusion is presented.

7.1 Torque Meter Design and Development

7.1.1 Torque Meter Design

The operating principle of the torque meter is through the measurement of phase shift between two ends of a shaft. From a measurement point of view, if the shaft exhibits a higher (elastic) angular twist for a given applied torque, it is easier to measure but would require a material with a low shear modulus. However, it is also important to transmit the expected maximum torque without yield or failure, therefore the correct combination of low shear modulus with high shear strength are critical in the effective material selection of the shaft. Once an appropriate material has been selected, the shaft diameter and length can be selected. Specifically, the shaft diameter should allow for the transmission of the expected maximum torque within the elastic limit of the material, and the shaft length should be sufficient to ensure that the exhibited torsional strain is within the resolution of the device.

The principle stresses on a circular shaft can be given by Equation 7.1. In order to design the geometry of the torque meter, this equation is simplified. First, it is assumed that the shaft is loaded only in torsion, see Equation 7.2, and axial stresses are considered negligible. Additionally, it has been assumed that there are no strain variations that result from thermal expansion and any bending forces that result from the mounted instrumentation are also assumed negligible. Furthermore, if it is also assumed that the shaft is only subject to shear stresses and applying the other assumptions ($\sigma_x = 0, \sigma_y = 0$), equation 7.1 simplifies to equation 7.2.

$$\sigma_1, \sigma_2 = \frac{1}{2}(\sigma_x + \sigma_y) \pm \frac{1}{2}\sqrt{(\sigma_x + \sigma_y)^2 + 4s_{xy}^2} \tag{7.1}$$

$$\sigma_1, \sigma_2 = 2s_{xy} \tag{7.2}$$

Equation 7.2 indicates that maximum stress in the shaft is twice the shear stress as a result of the applied torque. The key takeaway from first principal analysis of the torsion on a shaft can be summarized into the following key equations:

$$\sigma = \frac{\tau R}{J}; \tag{7.3}$$

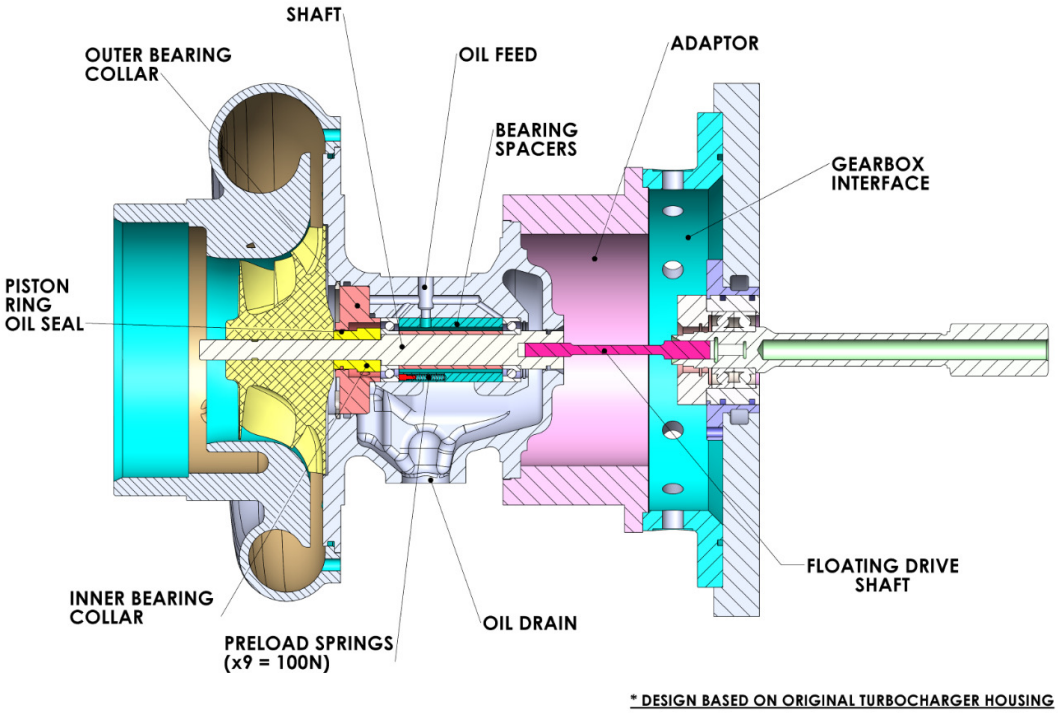


Fig. 7.1 Bearing Housing assembly of the shaft indicating the shaft adapter location as the only plausible placement for the torque meter

$$\sigma_{max} = 2s_{xy}; \tag{7.4}$$

$$\theta = \frac{\tau L}{GJ} \tag{7.5}$$

Constraints and Requirements

In addition to the timeline of the project, the design of the torque meter was constrained by a number of additional aspects. First, there was a spatial limit to where the torque meter could be placed. Figure 7.1 shows the interface between the epicyclic gearbox that drives the compressor and the compressor bearing housing. The adapter (colour 'pink' in the figure) has a connecting shaft. However, the current shaft is too stiff for torque measurements. To reduce the stiffness of the shaft, the shaft needs to be lengthened without compromising dynamic instability at the compressor inlet. As the entire assembly is cantilevered, there is a limitation to the maximum length and dimensions of this shaft.

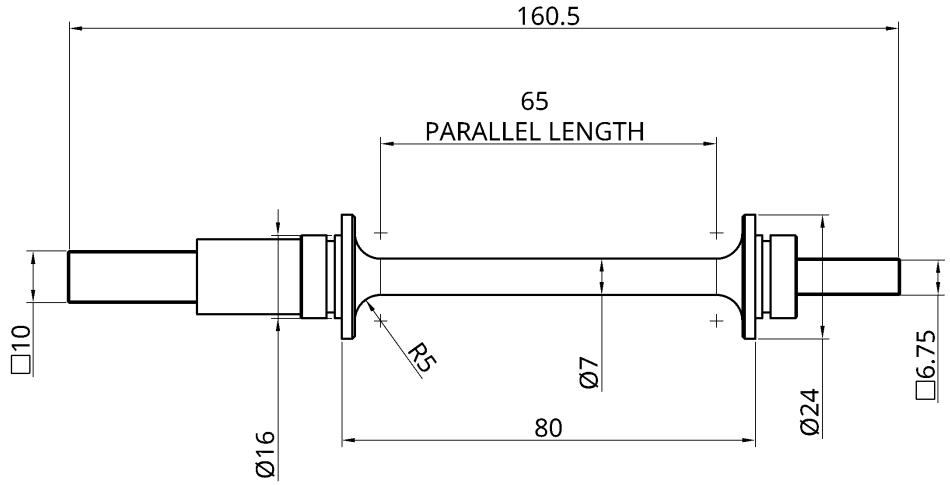


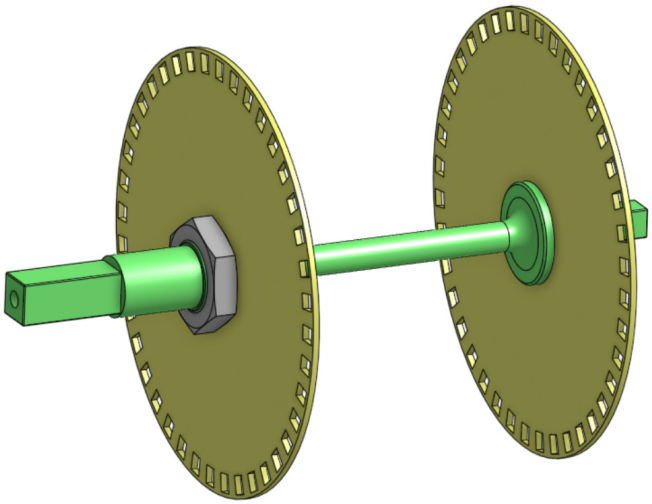
Fig. 7.2 Front-view schematic of the shaft showing critical dimensions

The experimental facility effectively restricts the size and space available for the device as well as interfacing shaft end dimensions. The design constraints on the shaft limit the design to an overall length of less than 175 mm and a diameter of less than 8mm.

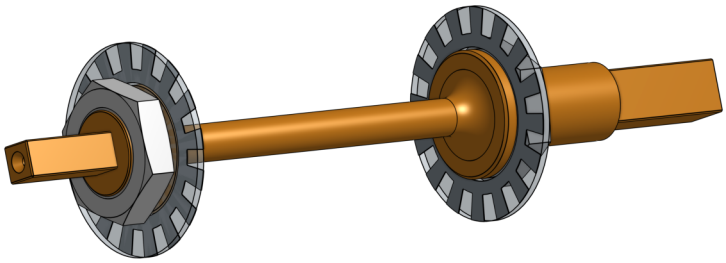
With the upper length of the shaft fixed, the possible phase shift depends on the shear modulus, G, the applied torque, τ, and the polar moment of inertia, J. The current shaft is designed to be solid and has a circular section between the measurement points, the polar moment of inertia, J, is therefore $(\pi r^4)/2$. The shear modulus, G, is dependent on the material. A number of materials were assessed and the final selection of the material was based on a material exploration. The key contenders were cast-Ally alloys, magnesium alloys or Beryllium copper. Beryllium copper (Cu-Br alloy 165) was selected for this proof-of-concept design as it is has a relatively low shear modulus of approximately 50 GPa, with a comparatively high tensile strength and yield, providing good sensitivity and range of torque measurement.

Shaft and Encoder Disc Design

The shaft schematic and assembly can be seen in Figure 7.2 and Figure 7.3a respectively. The shaft design consists of a central parallel length terminated by radiused flanges for mounting the encoder discs. This region forms the measurement section of the device. Outside of the two flanges are square drive sections for interfacing to the test rig.



(a) CAD Model of the first generation shaft and encoder assembly with the large encoder disc



(b) CAD model of the second generation shaft and encoder assembly with the smaller encoder disc

Fig. 7.3 Shaft and Encoder Design Iterations

The torque shaft has a total length of 160.5 mm including square drives. The parallel section of the shaft has a length, L, of 65 mm and a diameter of 7 mm. The flanges have an outer diameter of 24 mm with a locating bore diameter of 16 mm for the encoder disc. The encoders are secured with large locking nuts against the flange face ensuring perpendicularity with the shaft axis. The locking nut torque is sufficient to create high friction preventing encoder wheel slip during high acceleration of the shaft.

The first iteration of the encoder discs were made from stainless steel EN316 and had an equal slot:bar length ratio. The outer diameter of the encoder was 105.0 mm. The encoder disc had 40 slots on a 95 mm nominal diameter track. The encoder disc windows have radial edges to minimise effects of growth and concentricity. It is worth mentioning that since publication ([92]) and initial testing on the first iteration of the shaft, the torque meter has been modified further. The paper contained results from the first iteration and it was found that a one of the losses experienced by the torque meter, which limited its operational reliability, was windage loss caused by encoder flap due to the large size of the disc. To minimise the windage losses, the encoder was reduced in size. Secondly, there were machining tolerences in the initial encoder discs (which were made by laser profiling) resulting in a noisy signal. This is reduced by outsourcing the encoder wheels; producing the encoders externally increased the accuracy in the encoder slots and reduced the machining tolerances.

The second generation encoder discs were purchased from Photo Solutions. The encoder discs have a 40mm in outer diameter and 16mm inner diameter, and a thickness of 1.20mm. The material is a mylar/acrylic composite. The second iteration of the encoder disc is shown in Figure 7.3b , it can be seen that the encoder discs are much smaller. Additionally, the initial tests showed that 40 slot discs were not required for the minimum resolution of the torque and the encoder slot number was reduced to 16.

Optical Swtiches

The optical switch assembly is shown in Figure 7.4. The main requirement for the optical switches is that it needs to have a high-switching speed in order to detect the torque fluctuations. However, to avoid alias effects, the measurement speed needs to be 10 or 20 times greater than the pulse frequency in order to detect it (i.e. if the pulse frequency is 50Hz, the measurement frequency should be 1,000Hz for getting a clear response curve). A high-speed optical switch, Optek OPB9XX series, is selected and deemed suitable for this measurement.

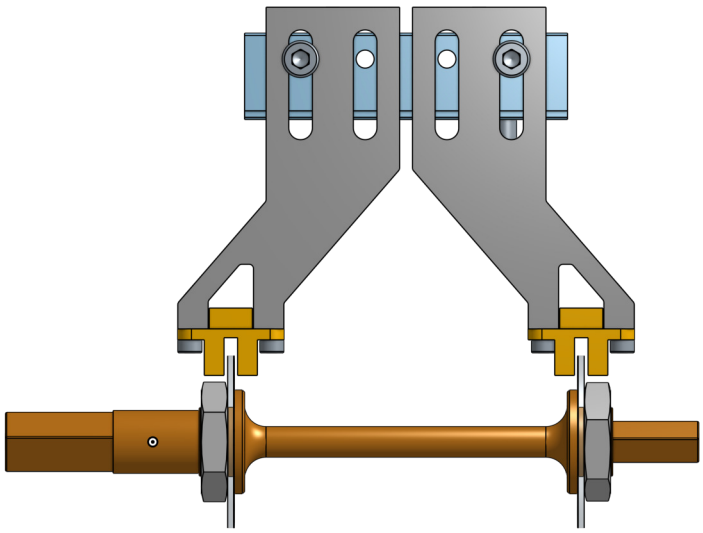


Fig. 7.4 Torque meter shaft and encoder assembly showing the encoder disc and encoder alignment

Operating limits

The operating design range is set as 20,000-60,000 RPM and up to 20 Nm in torque. These design parameters are taken from the current performance envelope of the compressor test rig on which it will be employed. The nominal speed of the device is 30,000 RPM with a torque range of between 10-20 Nm, as this is a typical operating range for the centrifugal compressor being tested. Additional to the maximum operating speed and torque, it is also important to be able to detect the minimum possible torque fluctuation resulting from the unsteadiness or pulsation, as such another performance criteria is resolution sufficient for detection of torque fluctuations at frequencies of 30 - 70 Hz.

Working Principle

The torque meter works by measuring two signals in time. Two time measurements are made by the Field Programmable Gate Arrays (FPGA). The first measurement, t_1, is a measurement of time between each successive pulses on a single encoder. Since there are 16 slots, there are 16 measurements for every rotation of the shaft. The second measurement, t_2, is a measure of edge-separation between the two encoder discs sampled for every edge (i.e. 16 samples per shaft rotation), see figure 7.5. Measurement of t_1 provides the shaft

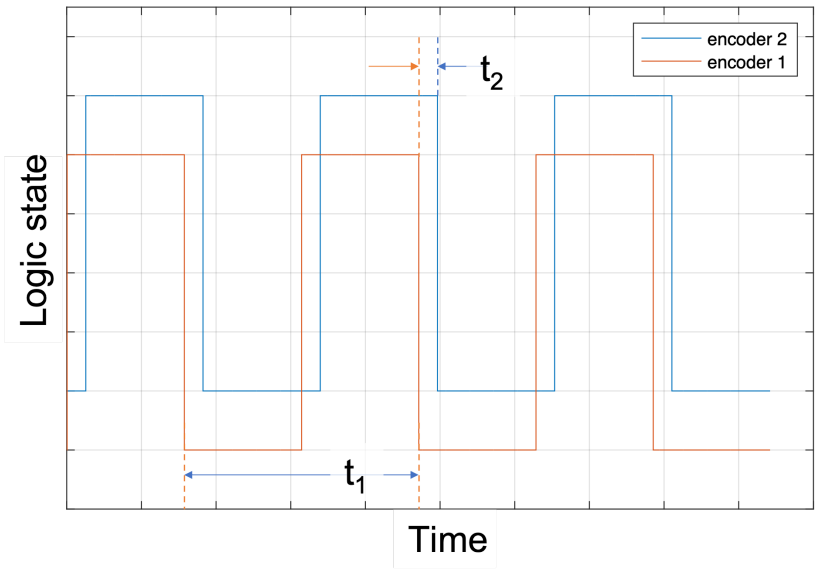


Fig. 7.5 Diagram representing two time measurements required for angular twist measurement - paper reference

speed measurement as the angular separation between the encoder edges are known measurements. The measurement of t_2 is a measure of both shaft speed, ω and relative angle between the two encoder wheels Θ_s in radians.

The speed of the shaft is a function of the number of encoder slots, n, and t_1. The separation angle is a function of the shaft speed and the unloaded offset, K, between the two encoder wheels in radians.

$$\omega = \frac{\frac{2\pi}{n}}{t_1} \tag{7.6}$$

$$\theta_S = \omega t_2 - K \tag{7.7}$$

Minimum resolvable torque

As the angular twist is measured as a function of time, an increased accuracy in the measurement of the time difference between the encoder edges increases the resolution angle and therefore torque measurement. High-speed National Instruments compactRIO data acquisition system with Field programmable Gate Array (FPGA) is used to acquire and measure the pulses at 40MHz. The minimum resolvable torque depends on the shaft

geometry and material and is 0.019 Nm for BeCu for this current shaft geometry, which is suitable for the torque fluctuation range during pulsation.

The angular twist of the encoders is ultimately measured as a function of time; the more accurate the measurement of the time difference between encoder edges, the higher the resolution angle and therefore torque measurement. To maximise the measurement resolution a high-speed National Instruments compactRIO data acquisition system with integrated Field Programmable Gate Array (FPGA) is used to acquire and measure pulses at 40 MHz. The repeatability of the acquisition side of the system is also verified using a bench-top set up of arbitrary waveform generator and oscilloscope to ensure repeatability and stability of measurement time. After verifying that the components can operate at the required speed, the theoretical lower limit of resolution of the system is dependent on shaft speed only.

The minimum resolvable torque depends on the shaft geometry and material. For the given design, the minimum torque for the operating range is 5 Nmm at a speed of 10,000 RPM. This is deemed sufficient for the objective of resolving torque from pulsation (as the absolute torque measured under steady conditions is known to be of the order of 10 Nm).

The method of measurement of angle relies on detection of a change on the logic level of a digital input channel, which must take place within the acquisition time period prior to the actual measurement. As the system checks the signal once per 40 MHz clock cycle, this gives a potential maximum error of 2.5 x$10^{-}8$ seconds on a single edge measurement. When considering the measurement required for a complete torque calculation (edge measurements for speed and edge separation for torque) this equates to a maximum systematic error of ±0.14 Nm on any single measurement at 40,000 RPM shaft speed. This will translate to a band of uniformly distributed noise on the any acquired signal. The systematic error can be used to calculate uncertainty of measurement for any data collected using this device which will define the usable accuracy and resolution of the system [93, 94].

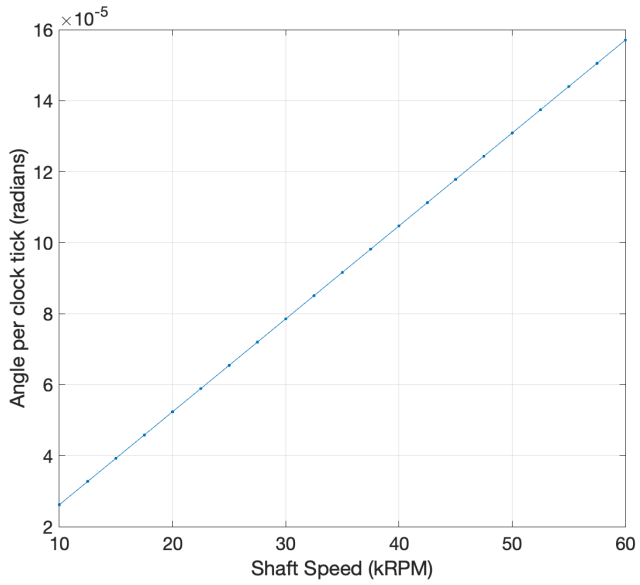


Fig. 7.6 Theoretical minimum resolvable angle as a function of shaft speed

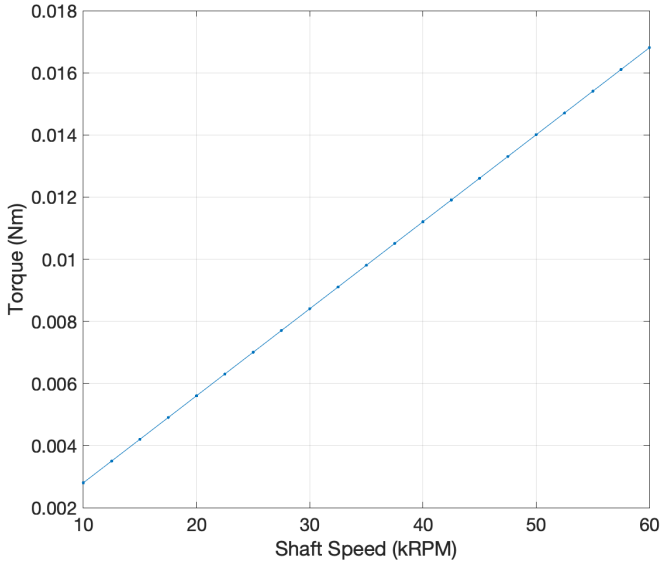


Fig. 7.7 Theoretical minimum resolvable torque as a function of shaft speed

7.1.2 Static Calibration

The raw signal measured by the torque meter is angular change in radians per second. A calibration is required to relate the angular shift to the applied torque. This calibration is done statically. Readers should note that in version 1 of the device (large encoder disc) a dynamic calibration was attempted. The dynamic calibration captures the signal whilst the shaft is at full speed. The dynamic behaviour of the shaft may vary sightly from the static

behaviour, and hence, the dynamic calibration would be a closer approximate to the torque signal in practice. However, the dynamic calibration did not work so well; It was difficult to consistently re-create conditions in the gear pump that was used for the calibration. For this reason, a static calibration is conducted on the shaft instead.

The static calibration rig is shown in figure 7.8. The weights are applied at the end of the calibration arm at 0.3 m away from the pivot centre. From this, the moment or applied torque is calculated. A schematic of the torque meter is shown in figure 7.9.

The torque, τ, is the gravitational force, F, on the applied weights multiplied by the distance of the moment arm, L. The angle of deflection, θ_d is calculated from the deflection distance, d_m and the distance to the point of deflection, which in this case is the diameter of the encoder wheel, A_d. The torque, T, is proportional to the angle of deflection, θ. The calibration runs through a series of different weights in order to find the constant of proportionality between the torque and shaft twist angle. The calibration is done on three loading and unloading cycles. The results from the calibration are shown in Figure 7.10. It can be seen that there is a clear linear fit between the angle of deflection obtained and the torque applied.

$$\tau = Fl \tag{7.8}$$

$$\theta_d = \arctan \frac{d_m}{A_d} \tag{7.9}$$



(a) Static Calibrator Rig for calibrating the angular twist against the applied torque



(b) Figure of the deflection gauge for the static calibration

Fig. 7.8 Static Calibration Machine

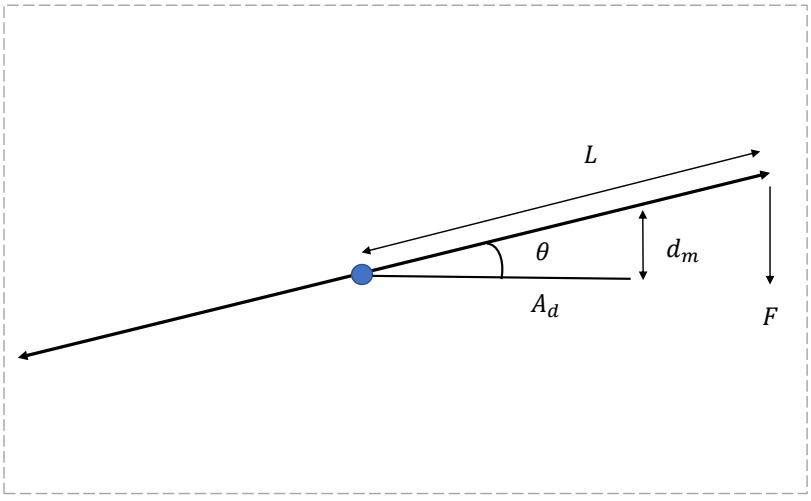


Fig. 7.9 Schematic static torque calibration for the torque meter

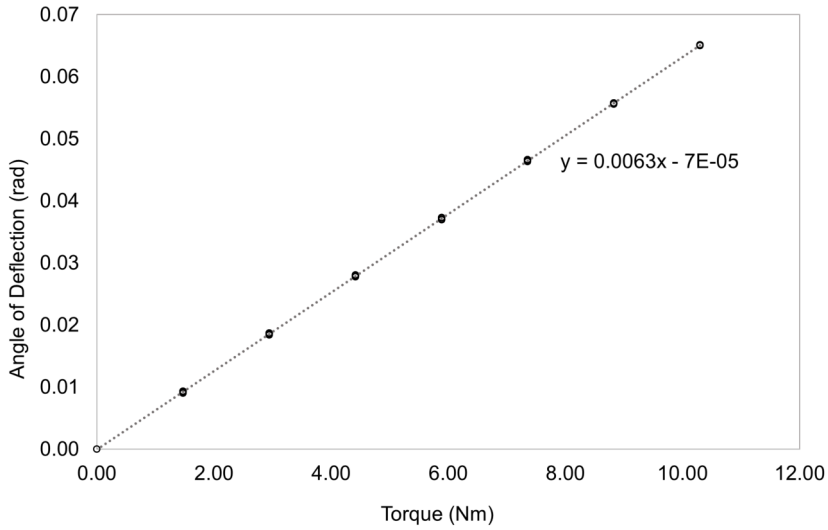


Fig. 7.10 Results from the static calibration of torque meter

Zero-Offsets

The torsional angle is a measure of the calculated angle and offset, K. This offset is a zero-offset introduced due to the misalignment of the encoder wheels. The encoder wheels are deliberately misaligned to increase the sensitivity of measurement, as the measurement of t_2, is inherently in proportion to the edge separation. As this misalignment introduces an arbitary offset and the offset needs to be removed.

To find the zero offset, the torque at zero spped or 0 rpm is required. However, because of the way the the torque meter is designed, it is not possible to obtain a measurement if the compressor rig is not running, in other words, at zero speed. To obtain the zero offset, an extrapolation process needs to take place. For this, the compressor rig was run at very low speeds of 5k, 8k, 10k and 15k rpm.

The graph below shows the zero offset at approximately 39 Nm. It can be seen that the process of generating the offset needs to be improved as it can be seen from the figure that there is not enough data to extrapolate the offset, refer to Figure 7.11. This is one of the main limitations of the current stage of development of the torque meter, as will be seen later.

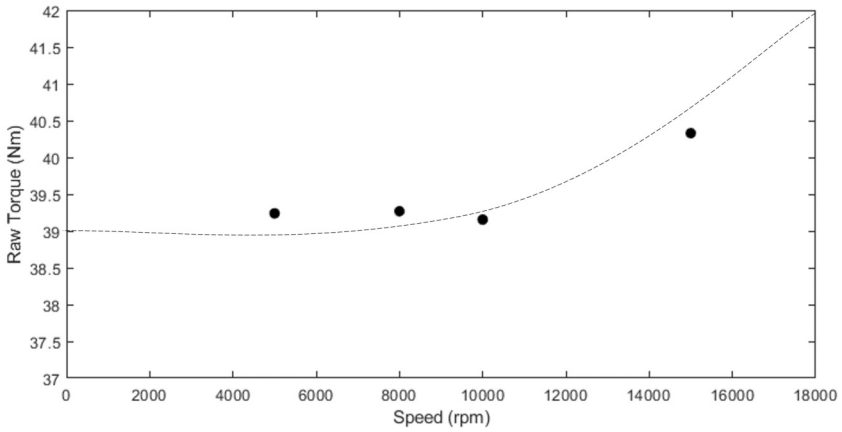


Fig. 7.11 Data from low-speed compressor runs to determine zero offset of torque meter

7.1.3 Experimental Method

The experimental set-up is the same as that outlined in Chapter 3. However, in the time between measurements, some additional changes and improvements have been possible. The outlet sensor has been changed to one that is less noisy than the one that was previously installed. An additional pressure sensor has been placed at the compressor in line with the torque meter. There is also a Constant Current Anemometer (CCA) probe that has been placed at the outlet plane to measure temperature. The CCA probe is more responsive than the thermocouple and it is hypothesized that it might be slightly better at picking up exit temperatures.

The instrumentation is detailed in Table 7.1.

Table 7.1 List of instrumentation for the detailed measurement test

Measurement	Sensor	Location	Type	Range
Ambient Pressure	PTB110 Vaisala Barometer	Lab	Absolute	80kPa-110kPa
Ambient Temperature	K Type Thermocouple	Lab		
Inlet Temperature	K Type Thermocouple	Inlet Plane (Far upstream)		
Inlet Pressure	PX419 Omega	Inlet Plane (Far upstream)	Differential	0-1Bar
Instantaneous Mass Flow	Platinum plated tungsten 10micron wire, CTA, 51.7mm from lower wall - DANTEC	Inlet Plane (Far upstream)		
V-cone differential pressure	Seitrans pressure transducer	differential ports at v-cone	Differential	600mBar
V-cone high pressure	Scanivalve DSA3016/8D in rack enclosure DSAENCL4000; module 16 pressure sensors	upstream of cone	Absolute	0-100PSI
V-cone Temperature	K Type Thermocouple	upstream of cone		
Outlet Temperature	K Type Thermocouple	Outlet measurement plane		
Outlet Pressure	MMV5A Omega	Outlet measurement plane	Absolute	0-3.5Bar
Compressor Torque	Torque meter (in-house)	Drive shaft		0-20Nm

Analytical Method for torque measurements

The efficiency of the compressor is the amount of real work required by the compressor compared to the isentropic work that would be required if the compressor was operating in an ideal manner. An ideal compressor would always require less work than the real compressor as there would be no losses in the compressor operation.

The thermodynamic isentropic Power, $\dot{W}_{is}$ is shown in Equation 7.10 as a function of the mass flow rate $\dot{m}$, inlet temperature, T_{01} and the pressure ratio.

$$\dot{W}_{is} = \dot{m} C_p T_{01} (\Pi^{\frac{k_2-1}{K_2}} - 1) \tag{7.10}$$

The actual power, $\dot{W}_{ac}$ is given by equation using equation 7.11 where T_{02} is the temperature using the thermocouple at the outlet, $T_{02,t}$, or $T_{02,CCA}$

$$\dot{W}_{ac} = \dot{m} C_p (T_{02} - T_{01}) \tag{7.11}$$

The power from torque meter, $\dot{W}_t$ is a function of the angular velocity, ω and the torque, τ_{tm}.

$$\dot{W}_t = \tau_{tm} \omega \tag{7.12}$$

It is also possible to back calculate torque from the thermodynamic relationship between the two powers. In an ideal system the two powers should be equal to each other.

$$\dot{W}_t = \dot{W}_{ac} \tag{7.13}$$

$$\tau\omega = \dot{m} C_p T_{02} - T_{01} \tag{7.14}$$

Since T_{02} is known from experiments, it is possible to calculate the torque that would be achieved at this temperature τ.

$$\tau = \frac{\dot{m} C_p T_{02} - T_{01}}{\omega} \tag{7.15}$$

The efficiency from the torque meter is given by the ratio of the isentropic power and actual power, see Equation 7.16

$$\eta_t = \frac{\dot{W}_{is}}{\dot{W}_t} \tag{7.16}$$

7.1.4 Limitations of Torque Meter

As the torque meter was developed in-house there were a number of tests that needed to be conducted to ensure that the data from the torque meter was consistent and reliable.

Bearing Losses

One of the losses that takes place is bearing losses. The torquemeter measures the torque required to overcome the bearing housing losses plus the torque required to compressor the working fluid. In order to estimate the bearing housing losses, the compressor losses should not be present. This can be obtained if a weight, of the same mass as the impeller, replaces the impeller and does not generate any compression of the gas. Although a representative mass was manufactured, due to time constraints, the test with this impeller was not conducted and hence the loss associated with the bearing housing has not been captured. The main limitation from this is that the compressor efficiency predictions are lower than the thermodynamic predictions because the power requirement also includes the bearing housing loss. Since the bearing housing loss is a constant loss at 40k rpm, it is possible to conduct comparative studies between the steady and pulsating flow results in this preliminary experimental evaluation but it is not possible to get the absolute power of the compressor alone.

Torsional resonance

One of the tests to assess the reliability and suitability of the torque meter was a ramp test. In this test, the motor speed was increased from zero speed to the operating speed of 40,000 rpm (666.7Hz). The pulse generator was disconnected so that the compressor was running at steady conditions. The torque data from this test is shown in shown in Figure 7.12. In ideal conditions, there would be a single line showing the increase in torque for the corresponding increase in speed. The increase in torque is expected as the power draw increases with speed for a compressor system. The thickness of the line in the figure represents variation in the results such as noise. At low speeds, this noise is minimal however as the speed increases to the operating speed of 40k rpm, the torque measurement varies over a wider range. There are two effects taking place. First, there is a large amount of noise at high speeds. Additionally, the 'ballooning' of the line for a specific speed / frequency suggests there is also an amplification in the signal, which can be attributed to resonance. Since this figure is showing the torque signal, this is indicative of torsional resonance in the system.

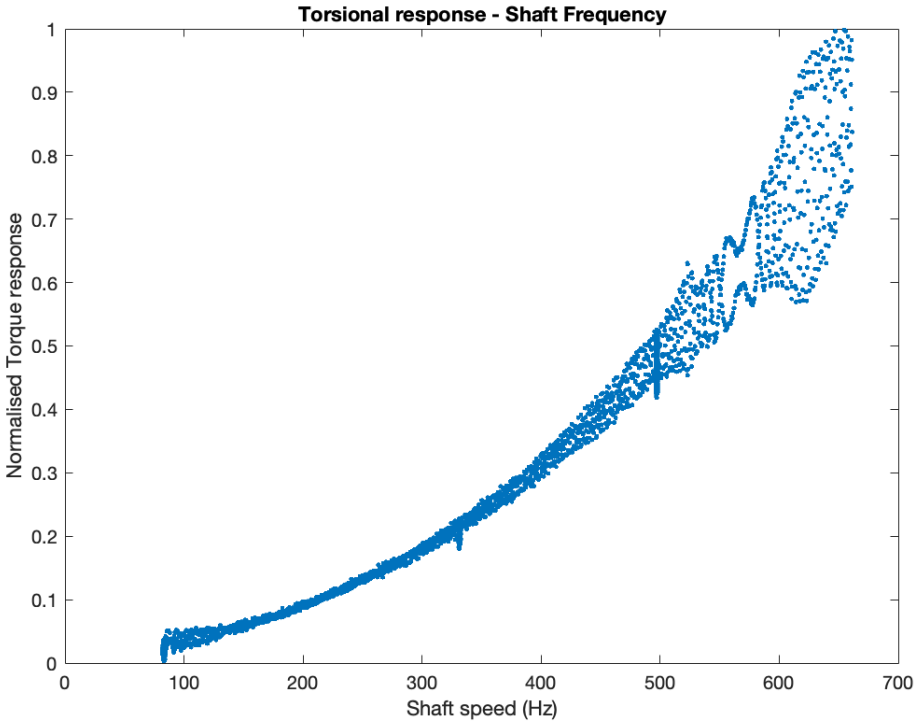


Fig. 7.12 Torsional resonance issue at the operating speed - Result from C.Noon, internal report (2022)

Further investigation of this signal using Fast Fourier Transforms (FFT) indicates that this torsional resonance has a frequency of 73Hz at 40k rpm, this can be seen in Figure 7.13. The figure shows that for a steady run with 40k rpm running speed, there is a spike at 73Hz, even though the compressor is operating in steady conditions. The source of this signal is currently unclear at the time of the assessment. The current hypothesis is that it is arising from the gearbox. Unfortunately, this signal is difficult to decouple and remove from the raw data. One of the options is to change the stiffness of the shaft so that the dynamic behaviour of the torque meter shaft changes, and the shaft has a different stiffness coefficient changing the frequency of resonance. A trial with a stainless steel shaft was undertaken (as opposed to the Beryllium Copper shaft that was developed). Unfortunately although the stiffness coefficient changed, the 73Hz signal remained. In addition, there were additional work-hardening effects taking place in the stainless steel shaft which reduced the reliability of the results. Therefore, the results from the Berrylium copper shaft were retained as they were not affected by work hardening.

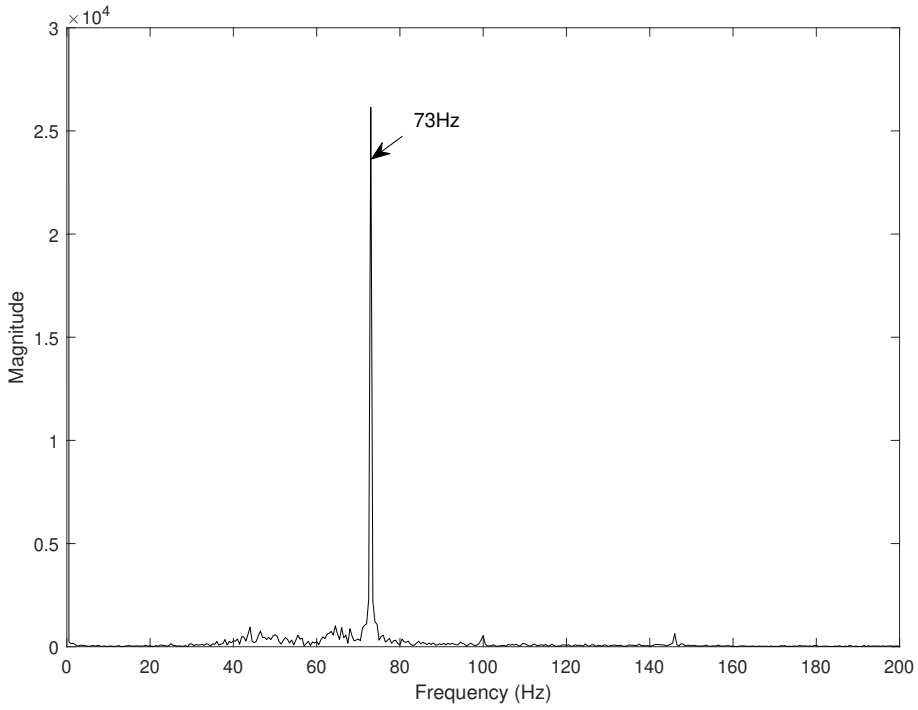


Fig. 7.13 FFT of signal for 40k rpm, Valve Opening - Fully Open, Steady operation, showing torsional resonance at 73Hz

In this case, the difficulty with the torsional resonance of the system is that it is occurring at a frequency that is similar to the operating frequencies that are being tested. Figure 7.14 shows the Frequency Fourier Transforms (FFT) for the experimental results with the pulse generator on. The two pulsating frequencies shown are 30Hz and 66Hz cases. It can be seen that the torque meter picks up the two signals as seen by the corresponding frequency spikes, however, the 73Hz signal is also present in the FFT, indicating that it has also generated in the pulsating flow conditions.

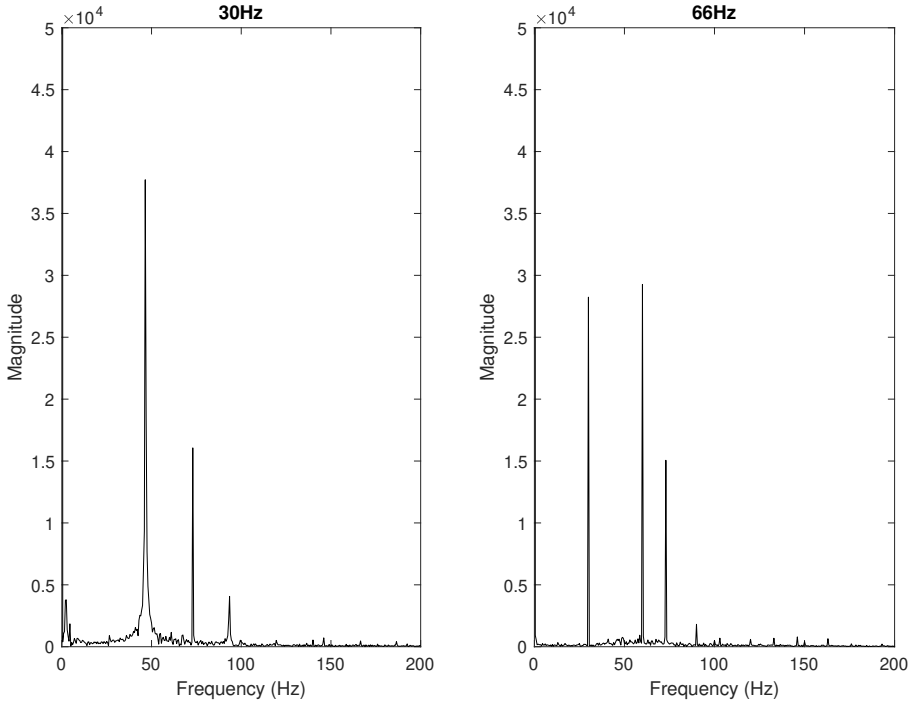


Fig. 7.14 FFT of signal for 40k rpm, Valve Opening - Fully Open, 30Hz and 66Hz operation

The resulting torque signal is affected because of this torsional resonance. Figure 7.15 shows the static pressure and torque measurements with time for steady operation and operation with the pulse generator frequencies set to 30Hz and 66Hz. In the steady operation case, there is a clear ripple due to torsional resonance. This is the ripple that corresponds to the torsional resonance. In the 30Hz and 66Hz case, the torque meter has a torque response (to the imposed static pressure) but is also impacted by the torque ripple.

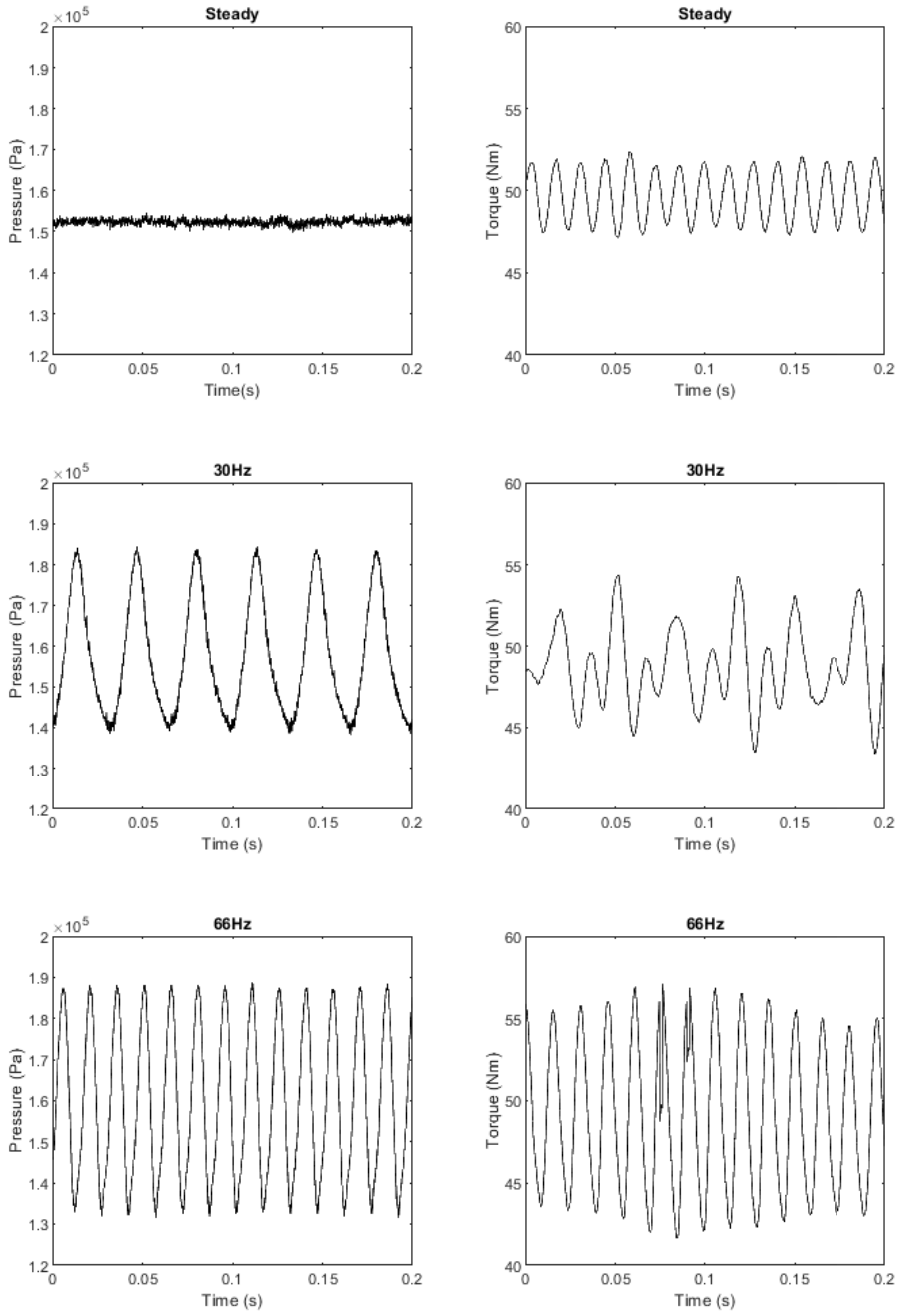
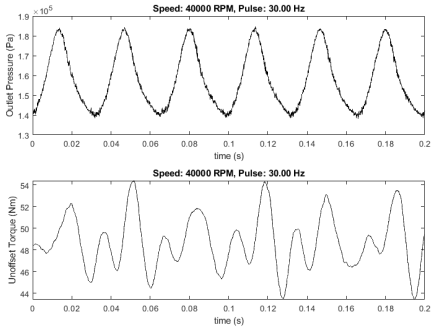


Fig. 7.15 Time signals of the outlet static pressure and the torque signal

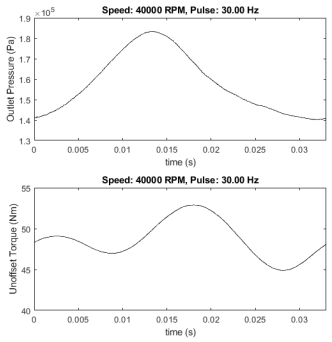
Time synchronous averaging to remove noise and resonant frequencies

Due to the issue with torsional resonance and noise, in order to decipher the torque response of the torque meter as a function of the imposed pressure pulse alone, the signal

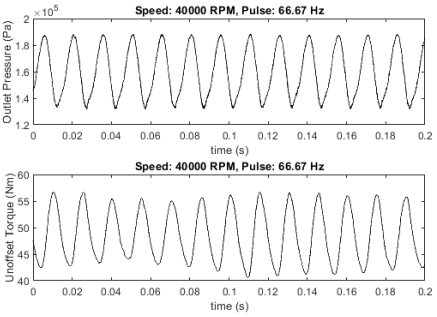
has to be filtered. The approach that is followed is a time-synchronous averaging method. This is the cyclic average process that has been described in the experimental methodology chapter (Chapter 3). The time-synchronous average is a type of narrow-band filtering or ensemble averaging technique. The time synchronous average is taken to match the outlet pressure pulse, this makes it possible to extract the average torque pulse for a given frequency. In effect, the time synchronous average can be conducted by identifying the target frequency using one channel (which is the outlet pressure channel in this case) and then use this frequency to do conduct an average for the other channels. The random noise, such as that from the torsional resonance is filtered out because the average is conducted over several cycles. Figure 7.16 shows the cycle average, time-synchronous signal for the 30Hz and 66Hz torque signal. Since the average is taken over a large number of cycles, the random noise in the signal effectively averages out, leaving the repeatable and traceable signal.



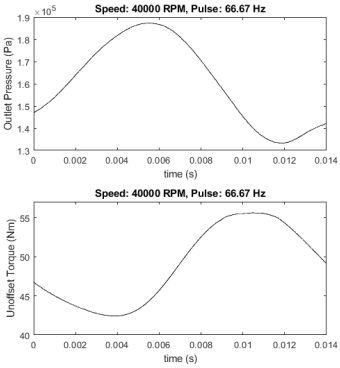
(a) Raw torque signal for compressor running with 30Hz pulse frequency



(b) Cycle average torque of the raw torque signal - 30Hz



(c) Raw torque signal for compressor running with 66Hz pulse frequency



(d) Cycle average torque of the raw torque signal - 66Hz

Fig. 7.16 Time synchronous signal for 30Hz and 66Hz case showing the average pulse signal

7.2 Preliminary Results

In this section, some of the preliminary results obtained with the torque meter are detailed. These initial results are limited due to the capacities of the current installation, as discussed in the previous section. However, the preliminary findings have been presented in this section to demonstrate the value of the torque meter and some insights into compressor performance are discussed.

Over prediction of Compressor Power Draw

Figure 7.17 shows the predicted power in the steady operation for a full speedline operating at 40k rpm. On the figure, there are three power estimations: torque meter power, thermodynamic power (calculated using the average T02 at the outlet), and isentropic power (predicted from the isentropic T02 from the pressure ratio). It can be seen in the figure that the torque meter over predicts the compressor power draw; the power draw calculated at the torque meter is much larger than the power estimated thermodynamically. The reason for this over prediction is the limitations of the current installation as mentioned in the previous section. The reason that the absolute power predicted by the torque meter is much greater than the thermodynamic power can be currently attributed to uncertainty in the zero-offset measurement as well as the current amalgamation of the bearing housing power, whereas the thermodynamic prediction predicts the compressor power alone.

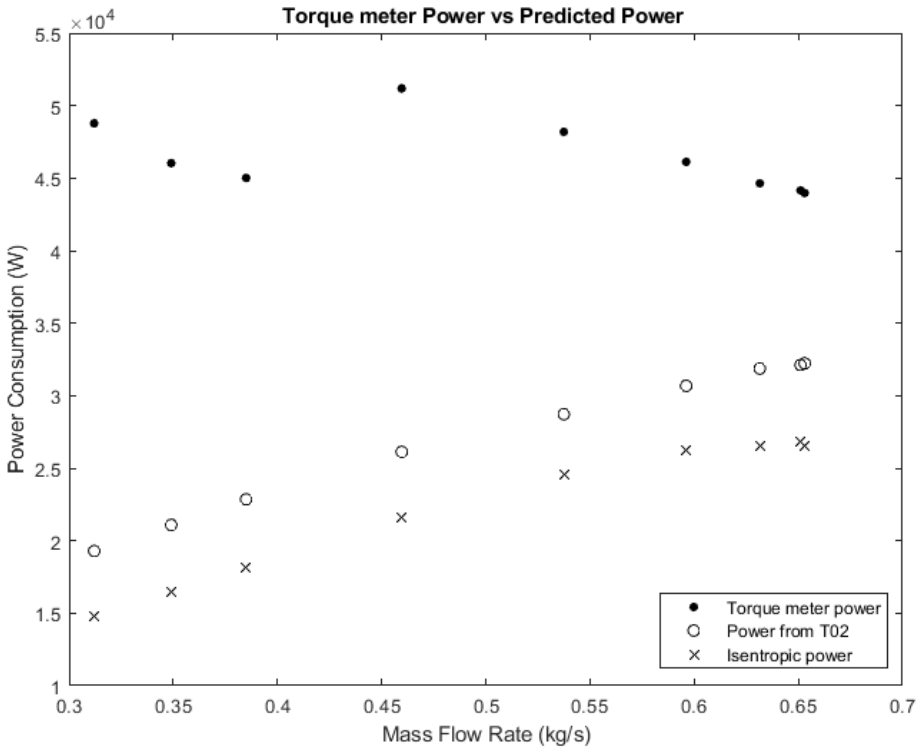


Fig. 7.17 Measured torque meter power compared to predicted thermodynamic power

Capability of tracing instantaneous Power and Efficiency

Figure 7.18 shows the instantaneous efficiency estimated for a single operating point with a 66Hz pulse imposed at the compressor exit. The efficiency is the actual power draw $\dot{W} = \tau\omega$ over the isentropic power draw $\dot{W} = \dot{m}C_p(T_{02,is} - T_{01})$. Equation 7.17 shows the efficiency as a ratio of isentropic power $\dot{W}_{is}$ and actual power, $\dot{W}_{act}$.

$$\eta = \frac{\dot{W}_{is}}{\dot{W}_{act}} \tag{7.17}$$

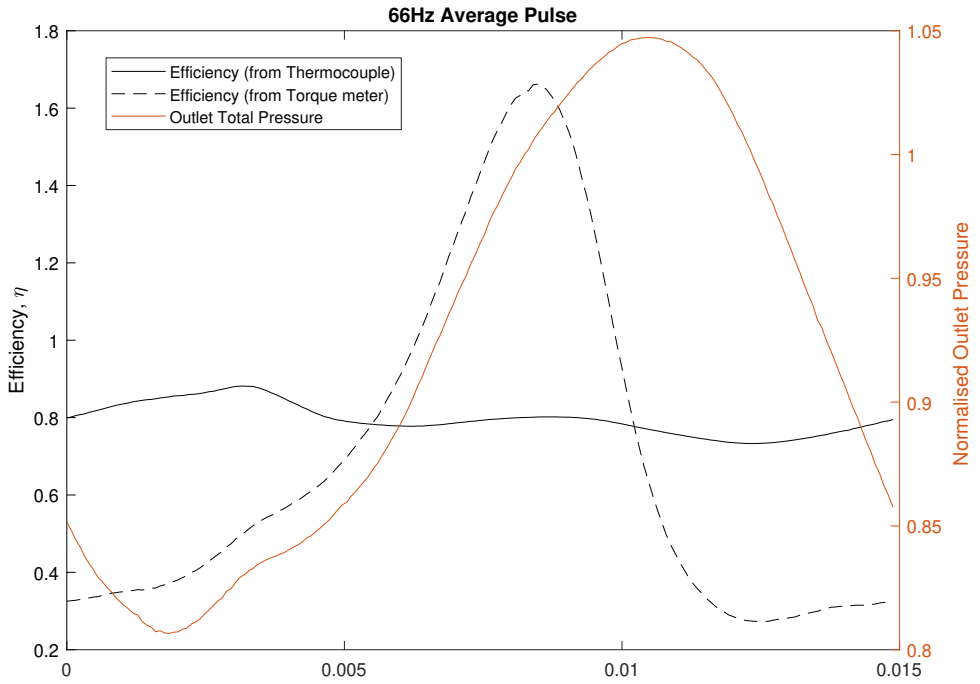


Fig. 7.18 Cycle average efficiency from torque meter compared to thermodynamic prediction for large flow operating point (OP D) at 66Hz

The thermodynamic efficiency is calculated using the temperature measurements at the compressor outlet. First, it can be seen that the thermodynamic efficiency calculated using the temperature probe data is more or less constant despite the changing back pressure condition. The reason for this is as discussed in previous sections: the thermocouple cannot respond fast enough to map the efficiency. The torque meter has a much faster response. Although in the current installation, the absolute values of the two efficiencies cannot be compared because the bearing housing losses are not yet determined.

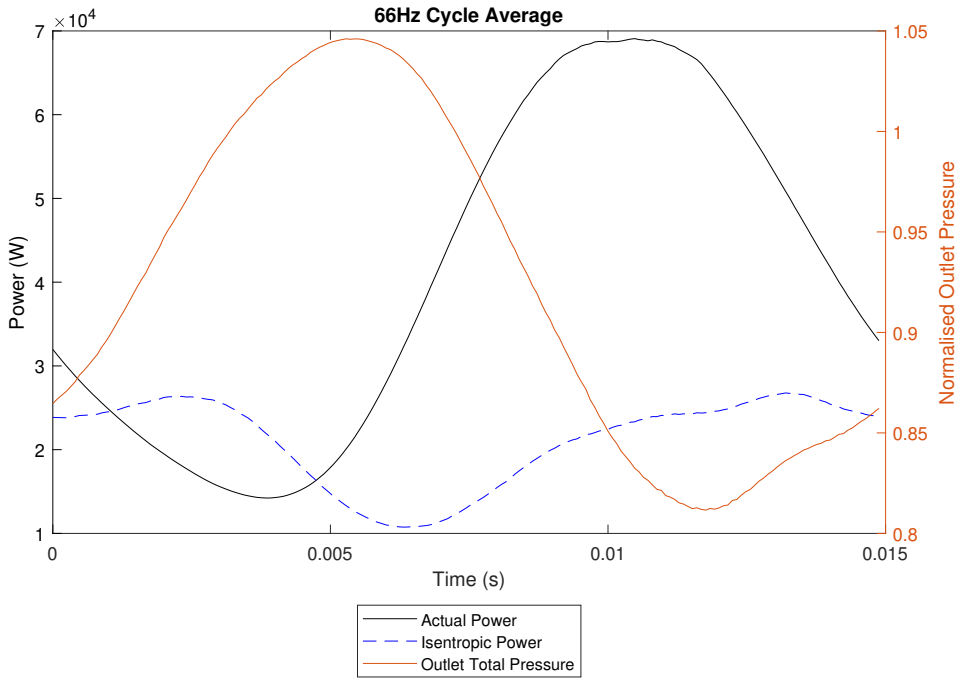


Fig. 7.19 Cycle average power from torque meter compared to thermodynamic prediction for large flow operating point (OP D) at 66Hz

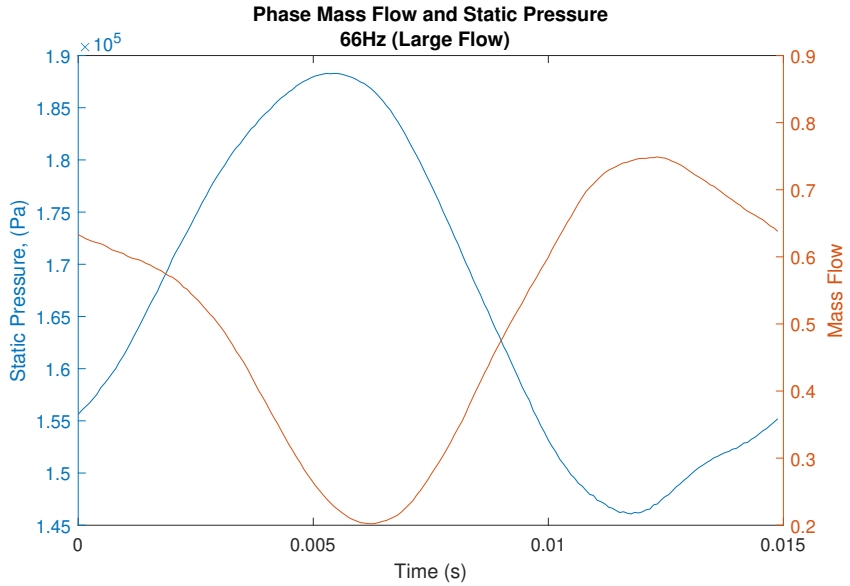


Fig. 7.20 Phase difference in mass flow rate and static pressure measurement

It is interesting that in some cases, particularly for Figure 7.18 the efficiency is much greater than 1. Figure 7.19, the isentropic power and actual power average pulse is shown. As it can be seen on the figure, at certain points in time, the actual power drops below the isentropic power. This is partially due to the phasing between the signals pressure and torque signals, but it is possible that there is also a dynamic response of the shaft, such as wound up in the shaft, which is causing the additional difference in phase.

The isentropic power is calculated using Equation 7.18 and is dependent on the instantaneous mass flow rate as well as the pressure ratio. The phase difference between the mass flow rate and outlet static pressure is shown in Figure 7.20. The two y-axes show the static pressure and mass flow respectively. The x-axis shows the time for the pulse. If there was no inertia in the flow, the mass flow would be directly out of phase with the pressure. However, it can be seen in the figure that the mass flow lags behind the pressure by 1 ms.

Figure 7.19 shows the phase shift between the power and the static pressure at the outlet is approximately 5 ms, which is much greater than 1ms difference between the static pressure and mass flow signals. Even if the power trace is shifted by 1 ms to account for the phase shift introduced by system inertia, there would still be instances in time where the efficiency would be instantaneously greater than one. This further suggests that the absolute value of power may be offset incorrectly due to the zero-offsetting process applied.

Additionally, the calculation of isentropic power is also affected by instrumentation limitations, as it relies on an accurate measurement of temperature. If the temperature measurement is not accurate (as thermocouples have slow response times) then it could also be affecting the instantaneous temperature reading. Therefore, the ratio of actual power to isentropic power leads to estimations of instantaneous efficiency inaccurately being greater than one.

$$P_{is} = \dot{m} C_p T_{01} \left[\Pi^{k_2 - 1/k2} - 1 \right] \tag{7.18}$$

Relative comparisons of average torque for steady and pulsating conditions

Whilst the over prediction prevents comparison with thermodynamic efficiencies to truly validate the torque meter, it is possible to study the compressor torque signals. This can be used to compare the relative torque requirements between steady and pulsating flow using the torque meter signals alone. Since both the data sets are offset by the same systematic errors discussed above, they can still be compared relative to each other for some initial insights. These will be briefly described in this section.

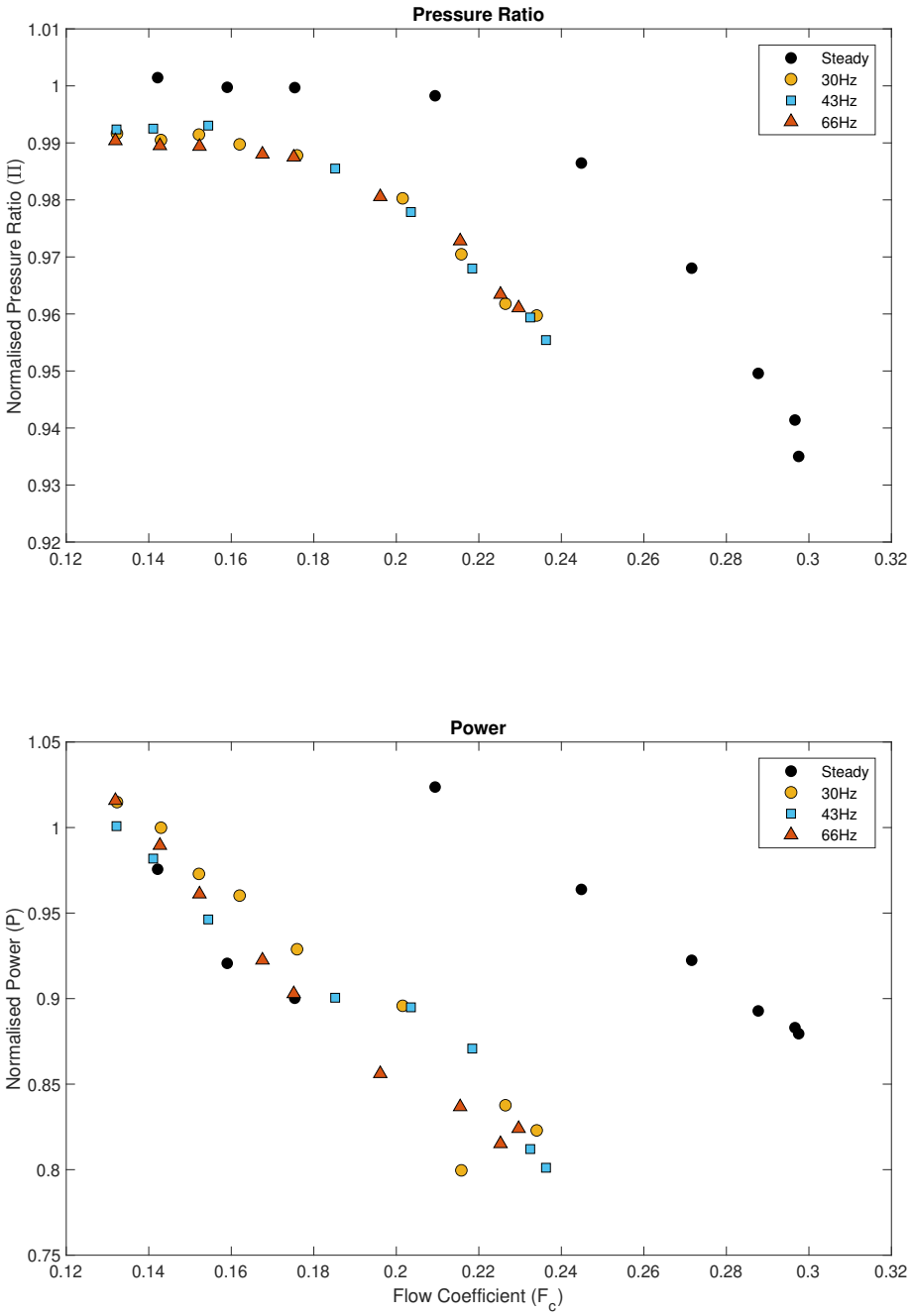


Fig. 7.21 Torque meter power and pressure ratio for steady and pulsating frequencies for full operating line

Figure 7.21 shows the average normalised power and pressure ratio signals for the steady and pulsating frequencies of 30, 43 and 66Hz. The figure shows that the power draw in the pulsating frequency cases drops in pulsating conditions compared to the conditions, as

the mass flow increases. At high flow conditions, the calculated average power is much lower than steady power, a difference of around 15 points is seen between the steady and pulsating case in the worst case. For comparison, the pressure ratio is also shown. It can be seen that at large flow rates, the pressure ratios achieved in the pulsating case are also less than the steady flow conditions. The torque meter and pressure ratio results match. It is clear that the compressor is not able to pressurise the air for the same swallowing capacity in the pulsating conditions as it would in the steady conditions. The performance in large flow conditions is clearly reduced.

Preliminary results of instantaneous torque

As mentioned before, the absolute values of torque are offset due to the systematic errors. However, it is still possible to look at the instantaneous behaviour. Figures 7.22 to 7.24 show the instantaneous power for selected operating points on the operating line for 30Hz, 46.7Hz and 66Hz respectively. The instantaneous operating points are shown in different colours. The black markers are the average results for each of the instantaneous operating points - as before, they do not exist in practice. For comparison the instantaneous pressure ratios are also shown. For both cases, the instantaneous pressure ratio and the power results show a hysteresis. However, the hysteresis in torque is different to the pressure ratio hysteresis.

For example, in the 30Hz Figure (Figure 7.22), the lines cross over, particularly at large flow but this does not happen in the pressure ratio trace. For the full operating line, low flow to high flow, the instantaneous torque response differs and changes shape. The shape at large flow (blue) is different to the shape at mid flow (purple) and both shapes are different from the low flow shape (orange). The pressure ratio hysteresis curves are comparatively different. In the low flow case (orange curve), the pressure ratio curve shows a large hysteresis (much wider curve) however, the power curve is much narrower. The 46Hz and 66Hz case also have a different hysteresis in torque compared to the hysteresis in pressure ratio.

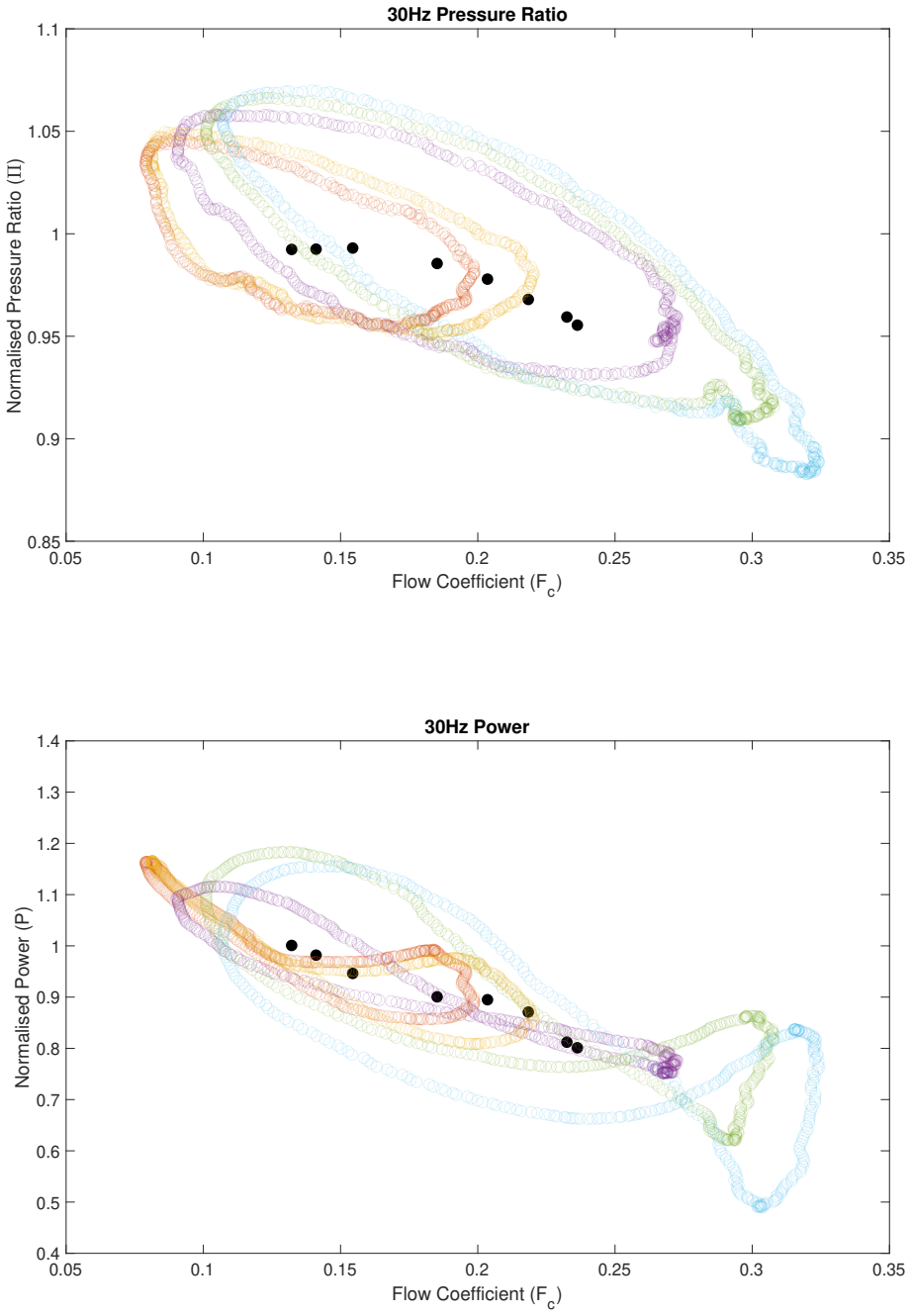


Fig. 7.22 Torque meter power and pressure ratio for instantaneous behaviour at 30Hz for low flow (red) through to to high flow (blue) (from left to right)

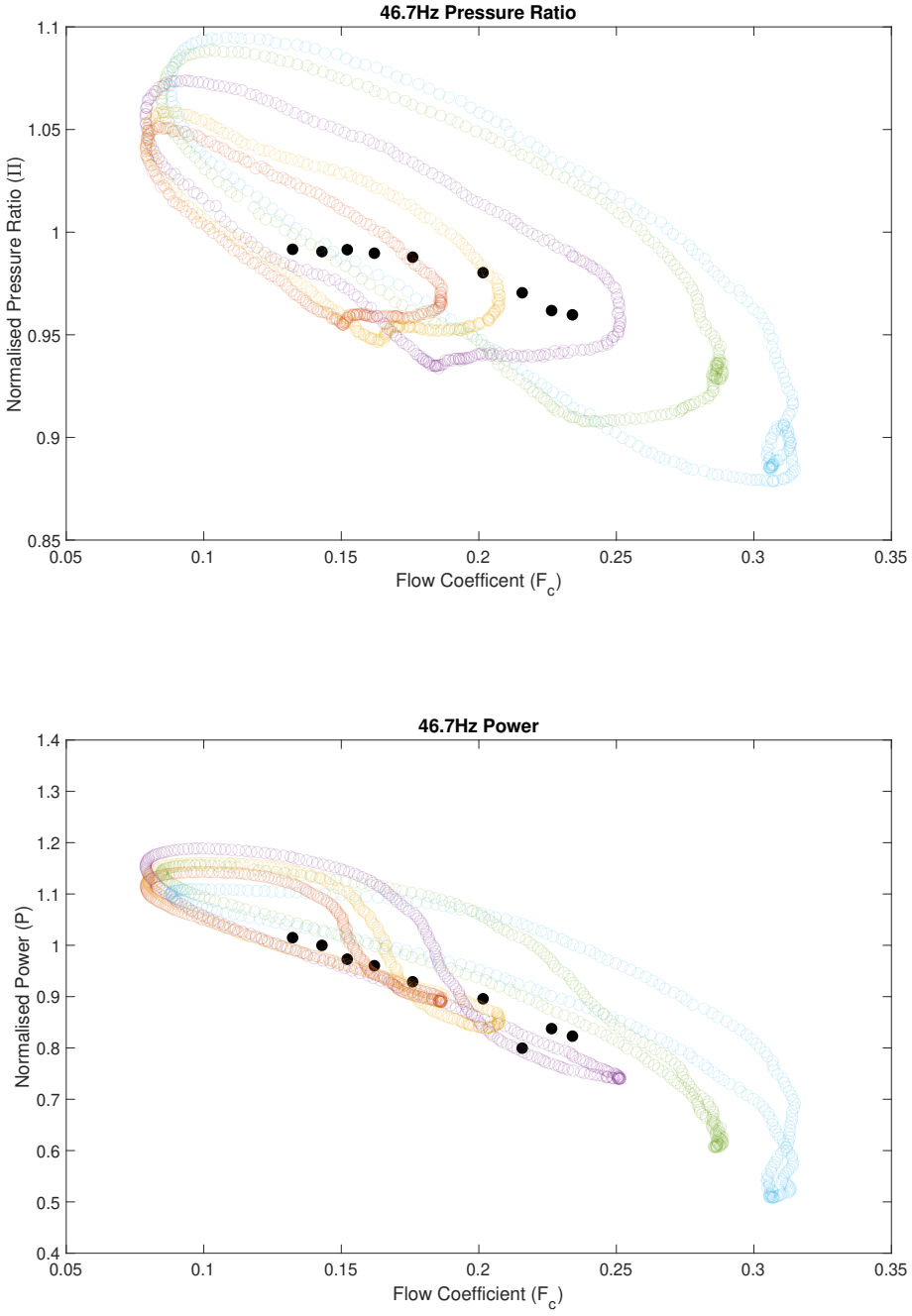


Fig. 7.23 Torque meter power and pressure ratio for instantaneous behaviour at 46.7Hz for low flow (red) through to to high flow (blue) (from left to right)

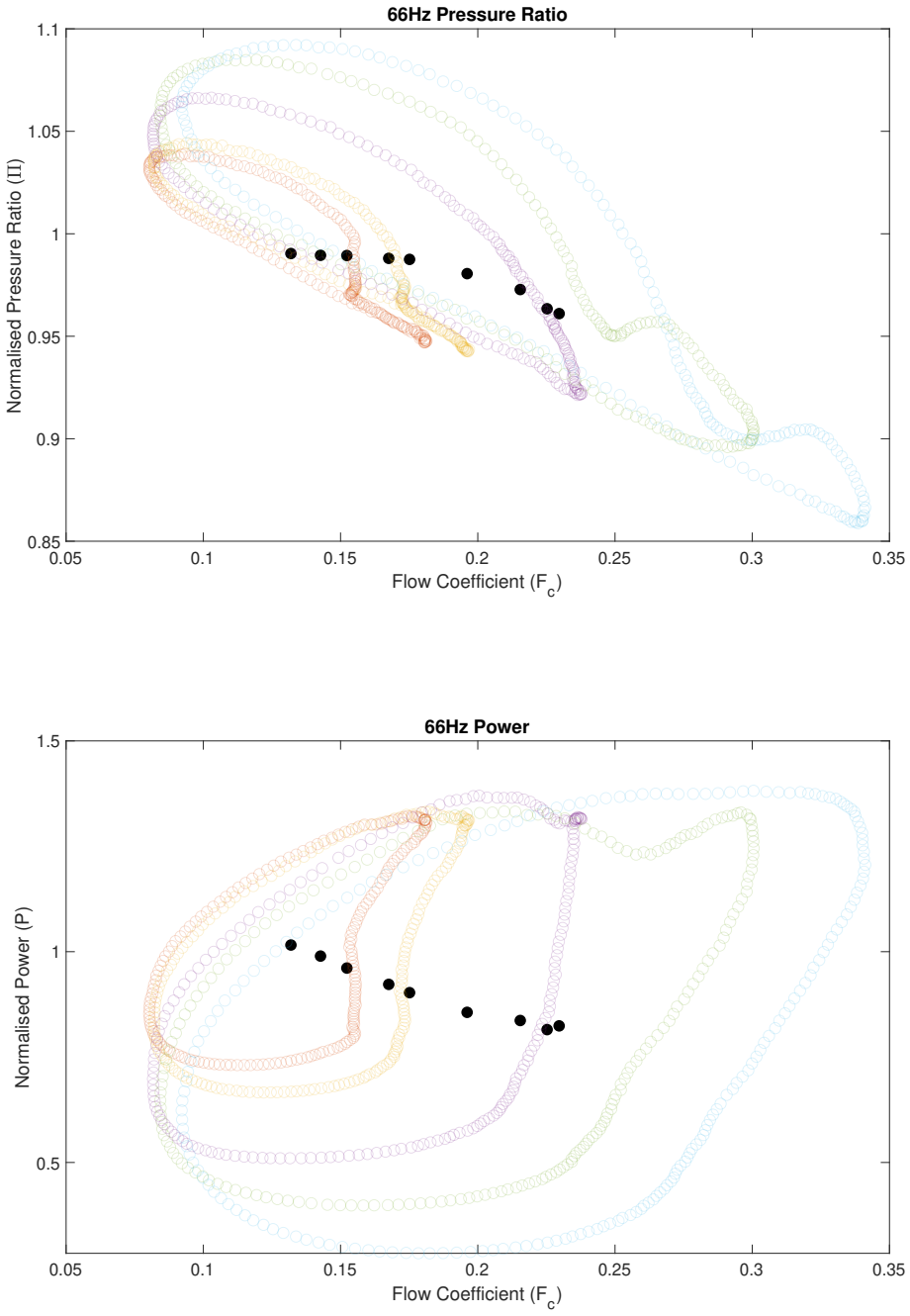


Fig. 7.24 Torque meter power and pressure ratio for instantaneous behaviour at 66Hz for low flow (red) through to to high flow (blue) (from left to right)

Additionally, it can be seen that for each of the pulsating frequencies, not only does the shape of the hysteresis changes with operating point (as discussed above), the hysteresis also changes with frequency. In order to compare the instantaneous response for each of the frequencies, two operating points corresponding to the peak pressure condition and large flow condition respectively are shown for the 30Hz, 46.7Hz and 66Hz case in Figure 7.25 and 7.26. It can be inferred from these figures that there is a different instantaneous response of the compressor depending on the pulsating frequency. The hysteresis in 66Hz case is much larger compared to the 30Hz case.

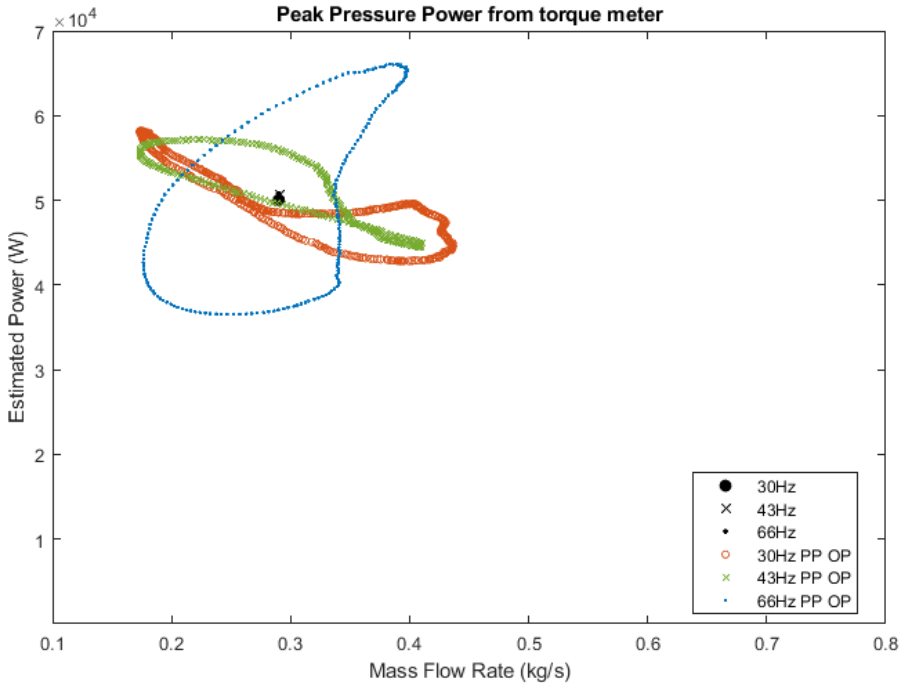


Fig. 7.25 Instantaneous power hysteresis for 30Hz, 46.7Hz and 66Hz pulse frequency cases at peak pressure operating point (OP A)

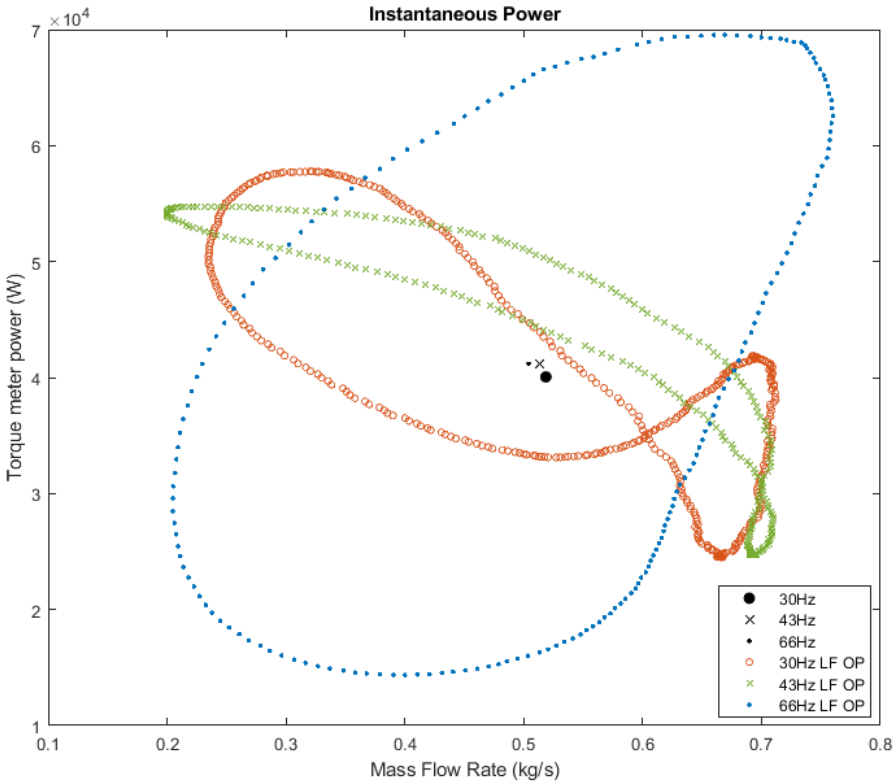


Fig. 7.26 Instantaneous power hysteresis for 30Hz, 46.7Hz and 66Hz pulse frequency cases at large flow operating point (OP D)

Discussion of preliminary results

The preliminary results demonstrate that the torque meter has been an addition to the compressor rig and increased the capabilities as it is now possible to measure torque, which would help further the knowledge of compressor performance in future tests. In addition, the instantaneous power and efficiency can be captured, because the response of the torque meter is faster than the thermocouples. However, the absolute torque values, and estimations of efficiency are not meaningful in the current state, due to the limitations of the instrumentation. The torque meter power is currently over predicted and this results in an over prediction of the instantaneous efficiency as well. There is also an effect of phasing due to the dynamic response of the shaft which also makes it difficult to compare the isentropic power with the torque meter power in the form of a ratio. A relative comparison of the average torque and pressure ratio for the steady and pulsating conditions show similar behaviour that is well matched. The thermodynamic evaluation using pressure ratio and the torque measured at the torque meter both show that there is a reduction in performance at high flow conditions.

The instantaneous response in torque can be captured and a hysteresis in torque is seen. The instantaneous torque measurement more accurately captures the response of the compressor as it is directly in line with the impeller, compared to the instantaneous pressure traces alone. The torque responses also change for each of the operating point. Additionally, it is clear to see that the torque response differs for each of the frequencies. From this, it can be inferred that the frequency has an influence on the torque response of the compressor however currently, without detailed future investigations, it is not possible to comment further on the exact effects that are taking place.

7.3 Chapter Summary

In this chapter, the design and development of a torque meter is detailed and the preliminary results with the torque meter are presented and discussed. The torque meter is designed using the phase shift principle and consists of two encoder discs placed on a Beryllium Copper shaft that has been specifically designed to provide the necessary shear modulus without compromising structural rigidity. This is because the torque measurements are taken on a critical component (driving shaft of the system) and hence, it is important that the compressor rig operation is not compromised with the new installation. The method of extracting torque from the time signals of the two encoders is described, and information of the minimum resolvable torque is provided. The design and assembly of the torque meter is described.

The calibration and offsetting process of the torque meter is described and detailed. The torque meter is calibrated using a static calibration as the previously conducted dynamic calibration is deemed unsuitable. The offsetting process is conducted with with some difficulty and shows limitations. Further limitations of the torque meter include the bearing housing losses (that have not been estimated due to time constraints) and torsional resonance. Both limitations affect the quality and quantity of the results that can be estimated from the torque meter.

An initial assessment of the results obtained from the torque meter show that there is promise in using the device for instantaneous, unsteady assessments of efficiency as the torque meter is more responsive than the thermocouples however it is clear that only a preliminary investigation has been possible.

Chapter 8

Conclusion and Future Work

The overall aim of this thesis is to evaluate the performance of a centrifugal compressor under the pulsating outlet conditions similar to those imposed by the throttling valve of the engine. This section outlines the main conclusions of this research and areas of future work.

8.1 Conclusion

In this study, key operating regions along the compressor performance line were studied for analysis; in particular the low flow (near surge) region and the high flow (near peak efficiency) region which were of particular interest. The research objectives were designed to build on the knowledge of previous researchers and provide computational and experimental insights on the compressor response to an unsteady engine environment. The final and most significant objective, was to design modifications to the baseline centrifugal compressor to improve the efficiency under unsteady, pulsating flow conditions.

Overall, the experimental data showed that the greatest drop in efficiency (around 4%) from steady conditions takes place at large flow rate regions, due to high backpressure pulse amplitude at high mass flow rates. Three of the operating points, peak pressure, peak efficiency and large flow conditions were explored computationally. It was seen that for the large flow operating point, the volute contributed significantly to the loss generation, and that majority of this contribution was due to the tongue, which contributed to 20% of the losses on average in pulsating states. To address this drop in efficiency, modifications to the volute tongue were designed. Two variations, blunting the tongue and sharpening the tongue, both improved the efficiency at the large flow operating point in experimental

and computational results. The greatest improvement was for the sharp tongue variation which improved the efficiency by over 2% for all operating points studied. At the time of writing, the sharp tongue modification is being filed for patent due to this noteworthy improvement.

The area near the impeller inlet is also a significant area that affects the performance of the centrifugal compressor. It is known in literature that for certain compressor systems the surge margin is improved, and the flow range shifts, however, the reasons for this enhancement are still an active area of research. The near surge operating point was computationally studied at different times along a pressure pulse. It was shown that at high backpressure conditions, critical stall-inducing flow states are created, however, these flow states are instantaneously alleviated when the backpressure drops. This dynamic response, and release of backpressure possible when flow is pulsating could explain the shift in flow to lower flow conditions, hence enhancing the surge margin. The cavity concept, a patented design developed by previous researchers, was modified in this thesis to improve the efficiency. The modified design reduced the cavity and tweaked the angular tilt of the cavity inlet, allowing the flow captured by the cavity to smoothly return to the main inlet flow. In the experimental tests, the efficiency was found to be improved by 1.7% for some pulsating frequencies, and up to 1.3% just under steady conditions. It is worth noting that these outcomes are significant in the context of turbomachinery. For example, a 2% efficiency improvement as a result of sharpening the tongue region of the compressor is a valuable improvement and worth investigating in future research. This is because improvements in efficiency for each component of turbocharger and propulsion system, such as the compressor in this case, add up, leading to an overall improved engine efficiency. Additionally, performance of the turbocharger is heavily sensitive and limited by the design and aerodynamic behaviour, such that minor improvements, even as low as 0.5% can lead to substantial improvements in fuel economy for the full life cycle of the product.

Fuel economy is an extremely important consideration for OEMs, particularly as climate change, emissions regulations that manufacturers must comply to are being controlled tightly. The reduction of greenhouse gas emissions from transport fleets are critical to minimising the effects of climate change. When turbochargers are rolled out for a given fleet, turbocharger efficiency has an impact on the overall engine efficiency and therefore directly impacts the fuel consumption through optimising the combustion of fuel.

Although turbochargers are an extremely mature technology, that have been optimised for many decades, the aforementioned concerns regarding climate change has prompted designers to change their design approach. Turbocharger components were historically matched based on their steady performance, but it is clear that the flow range, pressure ratios and efficiencies achieved under pulsating flow engine conditions differ to those under steady flow conditions. The pulsating flow behaviour is therefore becoming more

and more relevant. Designs that improve the turbocharger component under pulsating flow are the last remaining improvements that take highly mature turbocharger to a further optimised and well-matched design.

Summary of Research Objectives

In order to meet the overall aim of the research, the study was broken into key research objectives, as described in the introduction. The summary and key conclusions for each of the research objectives are presented in the subsections below in relation to the obtained outcomes.

1. To increase the capability of the existing compressor rig testing facility for reliable efficiency measurements

It was shown in the literature review (Chapter 2) that whilst performance, particularly with respect to surge and stability limits, had been extensively researched by previous researchers, there were a limited number of assessments conducted on compressor efficiency under pulsating conditions. An important reason for this was the operational difficulty in conducting instantaneous measurements.

An evaluation of the capabilities of an existing compressor test rig was conducted. The current capabilities included pulse generation at different frequencies as well as a variable plenum for assessments of the volume impact on the stability limit. Both the pulse generator and plenum were maintained. Most of the instrumentation, such as pressure transducers, were also kept the same.

It was found that whilst the compressor rig was capable of conducting performance measurements accurately, changes had to be made for efficiency measurements to be possible. Additionally, improvements to the mass flow measurements were also required due to the number of test measurements that were going to be conducted in this study.

Overall, the improvements that were made to allow the efficiency calculation by means of highly accurate and robust data acquisition system, included test processes for thermal equilibrium, insulation, replacement of the Resistance Temperature Detectors (RTDs) to thermocouples. The addition of a thermal insulation sleeve also improved the reliability and consistency of the insulation. A new inlet pipe was also manufactured to move the inlet measurement plane away from the compressor inlet, as it was found to be affected by certain deep surge conditions. A bespoke v-cone was also designed and installed to improve the reliability of the mass flow readings between different test days. The v-cone was used

to calibrate the hot-wire in-situ so that the calibration process was always representative of the test conditions. The updated facility was tested for reliability and repeatability and was found to be suitable.

2. To determine the performance differences of the baseline compressor at key operating points using internal measurements

In order to achieve this objective, as it was key to the research question, an instrumented compressor was designed and tested at the improved compressor testing facility. The details on the instrumentation used for this detailed experimental campaign are outlined in chapter 4. The purpose of the instrumented compressor was to enable measurements internal to the compressor at key components and locations such as the impeller, the diffuser and the volute, including sensors at the vicinity of the tongue. To do so, an existing compressor housing was modified using machining tools for creating measurement ports. Static pressure and temperature measurements were taken at the selected locations.

The instrumented volute was placed in the computational facility and pressure ratio and efficiency results were assessed. It was found that the compressor operating lines varied between the pulsating and steady flow cases. For comparisons to be made between the steady and pulsating flow conditions, key operating points (Labelled A-D in Figure 4.5) were selected for comparison within the comparable range. It was found that the biggest difference in calculation performance between the steady and pulsating flow cases was at large flow rates, peak efficiency condition (OP C), with the 30Hz showing on average a lower performance than the 66Hz case.

Both 30Hz and 66Hz pulses showed the greatest impact on efficiency drop under pulsating flow as well as a drop in performance because the compressor was unable to produce the same amount of work as in steady case. The drop in efficiency was much more significant at high mass flow rates because at high mass flow there was an increase in system flow inertia - more "mass" is moved within the system. This was investigated further by looking at the static pressure measurements internally at all the measurement ports. At the peak efficiency operating point (OP C), there were clear differences in the static pressure profiles compared to near surge operating point (OP A) and peak pressure (OP B). This pressure pulse deviation was attributed to the energy of the large pressure pulse amplitude potentially reflecting at the tongue, as it was possible that the pressure wave was proceeding in opposite directions and interacting in this region. This deviation did not take place at the low flow condition (OP A), despite the pulse frequency and size of the pulsator disc being the same, indicating that the high mass flow region and large pressure pulse amplitude contributed to the deviation of the pressure wave near the tongue.

Additionally, it was found that there were differences in the filling and emptying of the compressor volume for different frequencies. The flow accumulated at different regions within the volume for different frequencies and this impacted the performance of the compressor because different impeller passages saw different static pressures and localised mass accumulation. The impeller exit (in the passage close to the tongue) was also impacted by the pressure deviation in the region of the tongue.

The cycle average performance showed a deviation from the quasi-steady (QS) predictions as the mass flow rate increases for the 30Hz and 66Hz cases. In both cases for large flow conditions, the cyclic average performance is higher than the QS predictions because instantaneously the pressure rise exceeds the steady performance, resulting in a higher average than predicted. At low mass flow rates, the cycle averaged behaviour closely matches quasi-steady approximations as the mass flow spans a smaller range and the cycle behaviour, if present, is uniformly distributed around the QS prediction.

When comparing the quasi-steady to pulsating (unsteady) operation for the selected operating points, it was found that in the pulsating case, the instantaneous pressure ratio reached pressure ratios that would never be seen in the steady case, particularly for the large flow operating point. The unsteady performance in 66Hz case was in some instances higher than the 30Hz case despite spanning a much larger mass flow range. This is why the cycle average result showed that the 66Hz case had a better performance than the 30Hz case. This shows that the mathematical average result is not truly representative of the true performance in unsteady conditions. The cycle average efficiencies between the 30Hz and 66Hz case are similar, so perhaps the performance is much closer than the cycle average predicts. Furthermore, the fact that the 30Hz pulsating frequency cannot match the instantaneous performance of the 66Hz case (instantaneously, the maximum pressure ratio achieved in the 30Hz case is lower than the 66Hz case), could be attributed to the internal reflections and localised mass accumulation. The 30Hz case shows much more mass accumulation than the 66Hz case and has a much stronger pressure wave deviation near the tongue.

3. To conduct computational investigation of the compressor under pulsating conditions and gather insights on the compressor loss mechanisms

Computational investigations have been conducted on the compressor for pulsating flow conditions at certain key operating points and the internal flow fields are studied. Two separate simulations are conducted based on the specification requirement of the industrial sponsor, as they correspond to key conditions experienced by the compressor.

Investigation 1: Near Surge

As mentioned, centrifugal compressors in turbochargers are subject to pulsating flow conditions due to the opening and closing of the engine inlet manifold. Studies have shown that this pulsating condition leads to a surge margin improvement but it is not universally clear as to how or why the surge margin has improved. To investigate further, a URANS simulation for the near surge operating point is conducted on a computational model representative of the experimental facility for which boundary condition data is obtained. The pulsating flow static pressure is imposed as a user defined function in the simulation. The computational result is compared to the experimental result and good correlation is found between them. The transient URANS equations have been solved and six instances in time corresponding to high, low and average backpressure and flow coefficients have been studied. It has been found that there are some instantaneous states that have more flow disturbances than other states. These states correspond to high backpressure on the impeller exit - and consequently lower flow coefficients. However, these states are instantly alleviated when the backpressure drops. In the low backpressure conditions, the flow is more uniform and has overall less disturbances, lowering the chances of stall cells growing.

Investigation 2: Peak Pressure, Peak Efficiency and Large Flow

Another computational investigation is conducted with the improved experimental facility. Data from this facility (obtained during internal measurement tests) is used to validate a computational model and three key conditions are studied. Similar to experimental results, it is shown that there is a hysteresis in performance. The hysteresis is largest in the large flow cases, due to the high pressure amplitude. Correspondingly, the efficiency deviation is also largest in the large flow 66Hz case.

Looking at the large flow case closely, it can be seen that there are certain instances where the loss is greatest in the volute and these correspond to instantaneous high mass flow rate conditions. The positions with the greatest total pressure drop correspond to the largest entropy generation in the component.

Studying the computational fields in the large flow case for the best performing and worst performing case with respect to the total pressure drop in the volute leads to key insights with respect to the flow development near the tongue, as this region is found to be critical for the loss.

4. To design, develop and test compressor designs for improved efficiency

This objective aimed to develop modified compressor designs for increased efficiency under pulsating flow. Two design modifications were developed in total; they were cavity treatment modification and and compressor tongue modification. The designs were tested computationally and experimentally where possible.

Cavity Treatment

The cavity treatment concept was initially developed by Barrera-Medrano and Martos. Martos conducted studies and found the region corresponding to peak Mach number at the blade to be the region where the cavity should be placed. Computational results on the initial cavity under a pulsating boundary condition showed that instantaneously, there was a higher power draw in the case of the cavity to the no-cavity case, and the efficiency reduced by around 9% in some time instances. Further investigation showed that the size of the cavity was too deep and that the cavity shape needs to be altered such that the flow leaving the cavity does not interact with the main flow.

In the optimised cavity the size of the cavity was reduced and the cavities were manufactured experimentally. It was found that the optimised cavity had an improved efficiency in the peak efficiency point for steady and all pulsating frequencies. However, it was difficult to ascertain the effect on the surge margin. Because the experiments were conducted on perFORM (a type of 3D printed polymer material), it was difficult to push the compressor into deep surge as high temperatures could melt the polymer and deform the shape of the cavity. Using temperature measurements at the inlet of the impeller, reverse flow temperatures were used instead to estimate the mass flow at which flow reversed. The mass flow was lower in the baseline cavity case compared to the no cavity and optimised cavity case, suggesting that although the efficiency had been improved, the improvement in surge margin was not seen. This is due to the fact that the purpose of the cavity is to prevent reverse flow, if the cavity is too small, then the reverse flow bypasses the cavity and is not re-circulated back towards the impeller.

Tongue

The compressor tongue modification was designed based on the CFD investigations at the large flow operating point (OP D). The CFD investigations showed certain flow behaviour from which two different modifications to the tongue were suggested. This was evaluated computationally and it was found that the sharp tongue had a better efficiency compared to the baseline case.

The compressor tongue modifications were also experimentally assessed. The tongue parts were created in perFORM due to the flexibility of the material in R& D applications. However, perFORM caused difficulties in the measurement. In the end, it was difficult to conduct the experiment reliably and repeatably more than once or twice. The results showed that the sharp tongue performed better than the blunt tongue case. At the time of

writing, the tongue modification is currently being patented, as there were clear benefits in performance.

5. To enable torque measurements as part of the test facility and assess instantaneous, unsteady torque of compressor

In order to improve the measurement capabilities further, a bespoke torque meter was designed and developed in-house after it was found that a torque meter of similar operating specifications would have high costs, with little benefit as it would not be useful. The torque meter was designed using the phase-shift design principle. Two encoder discs were placed on either ends of a Berrylium Copper shaft (which was specifically designed to have a high shear modulus and high tensile strength) due to the operating range of the compressor. Two iterations of the shaft and encoder discs were conducted. The encoders work through the encoding of two time signals, the phase of which can be used determine the angular shift of the two measurements (as geometrical data is known).

The torque meter was statically calibrated using a static calibration machine and a good correlation between the angular shift and the imposed torque was found. This meant that the torque meter was suitable for estimating torque on the machine. However, there were a few limitations. First, the bearing housing losses were not estimated and as such, the true compressor power and corresponding efficiency has not been estimated. Second, the torque meter suffered from torsional resonance. The torsional resonance had a frequency of 73Hz which was close to the imposed measurement frequencies and interfered with the signal. A time-synchronous averaging process was used to decipher the compressor signal and filter out the noise that resulted from the torsional resonance.

Initial results of compressor power and efficiency are shown to demonstrate the capabilities of the torque meter. It is possible to study instantaneous efficiency because the response time of the torque meter is greater than that of the thermocouples. However, it is found that the instantaneous efficiency cannot be accurately estimated at this current stage because the bearing housing losses have not been recorded. The instantaneous efficiencies therefore provide a misleading calculation. However, it is possible to focus on the compressor power and compare the power requirements between the pulsating results. The average power in the pulsating frequencies is found to be much lower than the steady frequencies for high mass flow conditions, which correlates with the previous investigations within this research (as well as those cited in literature). It can be seen therefore that there is a power drop in the pulsating cases because the compressor is not able to generate the required performance at high mass flow conditions when the pulsator is on.

The instantaneous power hysteresis behaviour is different to the pressure ratio behaviour. When the two hysteresis results are compared, the hysteresis is different compared to the

pressure measurements. As the torque meter is in line with the impeller, the hysteresis in power is due to the delay in the response time of the shaft to the imposed outlet conditions. There is also a hysteresis between the imposed outlet pressure and the torque response.

The hysteresis is different for the different frequencies; showing that the instantaneous response changes with the different frequencies. In some cases, the power rises with rising static pressure, in some cases it falls. Despite the initial early stage of the progress, a major outcome of this research objective was the design and development of a torque meter that could be suitably fitted on the compressor rig at low cost, for the specific requirements for the testing. This addition will be beneficial to future research.

8.2 Future Work

This research has resulted in a number of key outcomes and has met the overall objective of assessing the performance of the centrifugal compressor. However, because of the breadth of the work that was conducted in this research, it acts as the starting point for future research in a number of areas. The key areas of future work are detailed below.

One of the main things to acknowledge is that the research was conducted during the COVID-19 pandemic. Due to the experimental research facilities being closed on many occasions, the research aims and objectives had to be tailored and altered. Whilst this research has achieved some key outcomes, further experimental findings in the focus areas below would greatly benefit this research area.

Experimental Improvements

Whilst a number of key improvements were made such as the addition of thermal insulation and mass flow sensors, few more improvements are necessary. Some of these include, adding a bespoke thermal insulation sleeve around the piping and conducting more internal investigations.

The way this would be done would be through the design and manufacture of a sleeve that could fit over the piping.

Torque meter improvements

A major outcome of this research study is the development of the torque meter, which is currently in place on the compressor rig. However, the initial results show that there is still a large amount of work to be done in order to improve the torque meter measurements. This includes conducting the bearing housing assessments, creating a dynamic model and addressing the issue of torsional resonance. With these improvements it will be possible to assess the instantaneous thermodynamic efficiency. The results can then also be compared to the thermodynamic efficiency.

For future work, first, a bearing loss test is recommended. The bearing loss test can be conducted with a mass attached at the end of the shaft (in place of the impeller) so that no compression takes place and the torque that is measured corresponds to the bearing losses alone. Then, once the impeller is replaced, the test is repeated. The difference in the two measurements would be the compressor torque, corresponding to the thermodynamic power required to compressor the mass flow through the system. Assume all other losses are accounted for in the 'no-impeller/dummy impeller' test.

Additionally, offset or overcome the torsional resonance in the system by manufacturing and using a different shaft or changing the operating frequencies. This is a large task however and requires a closer look at the gearbox, which may have to be sent for recommissioning.

A dynamic model would help assess the system inertia and provide information on the time lag in the system response to the outlet pressure.

Computational Assessments

Detailed computational flow field assessments can also be conducted at different operating points to provide further guidance on the areas of loss.

Compressor Design Modifications

Although the initial process of developing new compressor designs was tested, there is still some outstanding work. In particular, in the cavity case, a number of new cavity designs were developed. These designs are detailed below. However, these were not possible to test due to time constraints. It would be useful to test the new compressor designs with the improved torque meter. Secondly, other designs were also proposed, such

as the development of a honeycomb damper, or non-symmetric diffuser. Both of these design ideas were initially trialled but time constraints limited the progress. For more high efficiency designs, more development and prototyping is required.

Optimisation of the compressor tongue

Since a parametric model had been created, it would be possible to study several different tongue fillet radii and not just the two ideas proposed. With a parametric model, it is possible to optimise the tongue region to find the best performing shape. However, this is a computationally demanding process. It would require the creation of multiple geometries and each geometry would have to be tested against the transient pulsating boundary conditions.

As a compromise between computational power and time for research, since a major aspect of this stage in the research is exploration rather than detailed optimisation, it was decided that only the two design ideas were tested alone. In the two design ideas, the tongue fillet was increased to the maximum possible radii (i.e. an increase in bluntness of the tongue) and reduced to the minimum possible radii (i.e. an increase in sharpness of the tongue) as explained in Figure 6.20.

The compressor tongue modification is being patented so it is possible for more research in this area to lead to more fruitful designs, especially since a parametric model exists.

Mass accumulator concept

The mass accumulator concept is based on the idea of damping the pressure pulse amplitude. In the large flow case, the mass flow fluctuations take place because there is a high pressure pulse amplitude. An additional 'volume' at the exit of the compressor acts is intended to act as a pressure damper and reduces the amplitude of the pressure pulse to the compressor.

The mass accumulation concept design is shown in Figure 8.1. Figure 8.1 represents the internal volume that the working fluid would occupy when it passes through the compressor. The additional manufacturing and design considerations are not shown in the figure in order to focus on the fluid volume.

As discussed in the previous chapters of this thesis, the largest efficiency drop occurs in the high mass flow rate regions of the compressor. In the high flow rate region, as the flow

inertia of the system is quite large, restrictions in the flow caused by the pulse generator, result in a backpressure wave of high amplitude. The effect of a travelling backpressure wave is stronger pulse amplitude in the high flow rate regions than in the low flow rate regions.

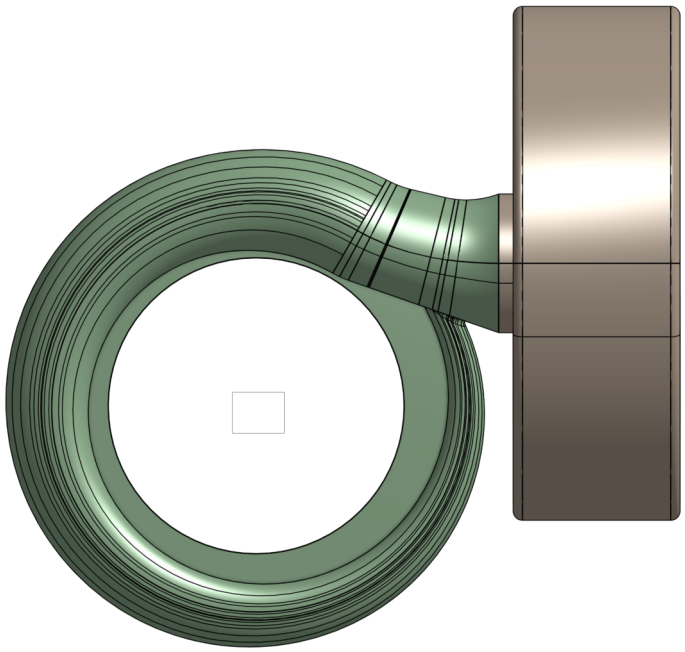


Fig. 8.1 CAD schematic of mass accumulation concept

One of the ways in which we can reduce the amplitude of pulsation is by damp the pulse. Similar to how piping systems have overflow valves to regulate pressure, damping reservoirs can act as an overflow volume; allowing the pressure amplitude to dissipate and regulate such that the pressure at the exit of the compressor is uniform. In chapter 4 and 6, it is shown how the tongue region, which is in the vicinity of the compressor exit, is highly affected by the pressure fluctuation. Hence, if the pressure wave is dissipated before the tongue, the compressor will behave as if it is closer to steady flow conditions.

Figure 8.1 shows the original designed concept. However due to time constraints, and the geometry of this concept, it was not possible to test the design. Some experiments were conducted by using the plenum as a volume instead to prove the concept. The appendix shows the results of some of the initial tests that were done. In the proof of concept tests with the plenum, the pressure was damped as a result of the volume and an improvement in pressure and efficiency was found. However, it is clear that there is a lot more work that is required and this could be a considerable area for future work.

Testing all the cavity ideas

In design process, multiple cavities were designed and these are shown below in Figure 8.2. However, due to time constraints, only one cavity was tested. The other ideas are shown below, in order of increasing size and shape. The changes include reducing the cavity size, repositioning the cavity, changing the shape and changing the depth as these would all have an impact. For example, the size of the cavity would have an impact on the amount of flow that would be recirculated, whereas the shape or angle of the cavity would influence the way the flow captured by the cavity is redirected into the main flow. The depth of the cavity could have an overall impact on the amount of flow captured and returned. Although the cavity is a small modification to the impeller shroud, it is in a critical region of impeller performance and therefore these modifications could result in significant differences to the overall performance. Since the cavity concept has been patented, it is possible to explore these other ideas and find the best performing cavity.

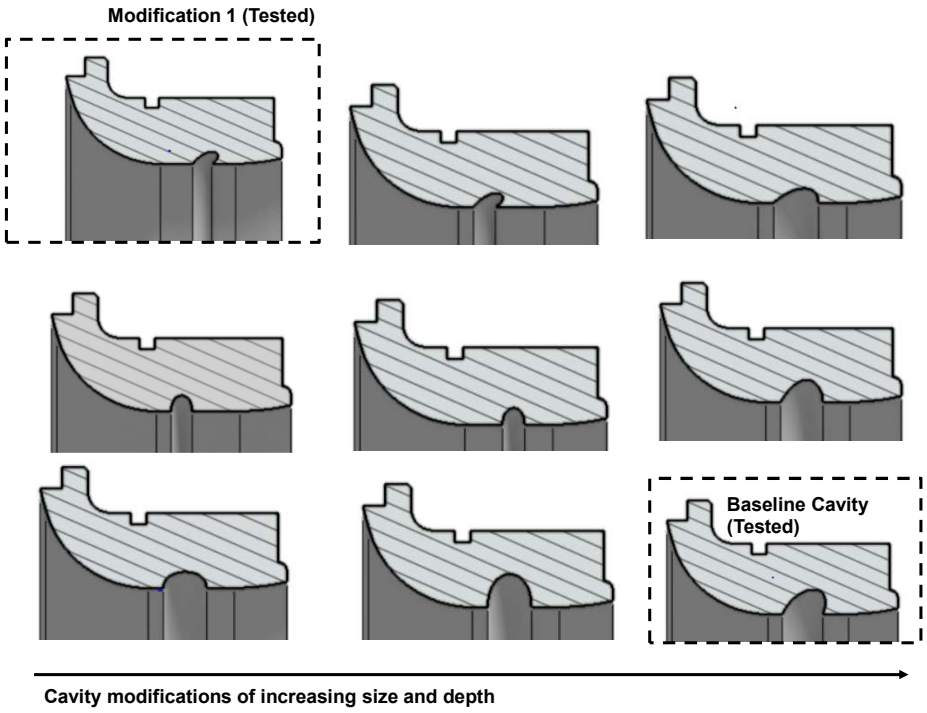


Fig. 8.2 Different cavity modifications for optimisation of baseline cavity

Closing Remarks

The objective of this research was to increase the understanding of the compressor behaviour under pulsating flow conditions and identify the corresponding sources of efficiency deficit. The objectives outlined in the introduction have been met and this research

has led to a number of outcomes, such as, detailed assessments of compressor loss mechanisms, a compressor torque measurement device, conceptual designs, a new patent and four publications. The obtained results provide new insights into compressor behaviour under pulsating flows and will additionally help steer future research endeavours in this field.

References

[1] United Nations. *What is Climate Change*, n.d. [Accessed 1st January 2024].

[2] NRDC. *Global Warming 101*, 2021. [Accessed 28th July 2023].

[3] World Wide Fund. *What are climate change and global warming?*, 2022. [Accessed 28th July 2023].

[4] Earth Observatory. *What's behind California's surge of large fires*, 2021. [Accessed 12th February 2022].

[5] IPCC. *IPCC Press Release*. April 04, 2022.

[6] NCEI. *Assessing the Global Climate in 2021*. 2022. [Accessed 28th July 2023].

[7] Jamie Edkins. *Ban on petrol and diesal cars pushed back to 2035*, September 2023. [Accessed 01 January 2024].

[8] European Commission Joint Research Centre. *Global CO2 emissions rebound in 2021 after temporary reduction during COVID lockdown*, October 2022. Accessed 28th July 2023.

[9] EV market. *EV market stats 2023*, May 2023. [Accessed 28th July 2023].

[10] Statista. *Distribution of carbon dioxide emissions worldwide in 2021, by sector.*, 2021. [Accessed 28th July 2023].

[11] Statista. *Distribution of carbon dioxide emissions produced by the transportation sector worldwide in 2021, by subsector*, 2022. [Accessed 28th July 2023].

[12] Department of Transport. *Transport and Environmental Statistics 2022*, October 2022. [Accessed 28th July 2023].

[13] x engineer. *How turbocharging works*, 2023. [Accessed 28th July 2023].

[14] Turbodynamics. *How does a turbocharger work*, n.d. [Accessed 28th July 2023].

[15] Macián V., Luján J., Bermúdez V., and Guardiola C. Exhaust pressure pulsation observation from turbocharger instantaneous speed measurement. *Measurement Science and Technology*, 15:1185, 2004.

[16] Japikse D. *Centrifugal compressor design and performance*. Concepts ETI, Inc, Wilder, Vt, 1996.

[17] PetroSkills. *Important Aspects of Centrifugal Compressor Testing – Part 2*, September 2010. [Accessed 28 July 2023].

[18] Japikse D. and Baines N. *Introduction to turbomachinery*. Concepts ETI [u.a.], White River Junction, Vt, reprint with problems edition, 1997.

[19] Zambonini G. *Unsteady dynamics of corner separation in a linear compressor cascade*. PhD thesis, 2016. University of Lyon.

[20] ETA Energy Solutions. *How Suboptimal Performance of Centrifugal Compressors causes Damage*, 2022. [Accessed 28th July 2023].

[21] Yahya S. *Turbines, Compressors and Fans*. McGraw-Hill Education, New York ER, 4th ed. edition, 2011.

[22] Tatar O., Ozturk A., and A. Pınarbaşı. Flow analysis in centrifugal compressor vaneless diffusers. *Journal of Scientific & Industrial Research*, 67:348–354, 2008.

[23] Barrera-Medrano M. *The effect of exit pressure pulsation on the performance and stability limit of a turbocharger centrifugal compressor*. PhD thesis, Jul 2017.

[24] Tamaki H. Enhancement of centrifugal compressor operating range by use of inlet fins. *IHI Engineering Review*, 49:44–55, 01 2016. https://doi.org/10.1115/1.4033187.

[25] Cumpsty N. *Compressor aerodynamics*. Longman, Harlow, 1. publ., reprinted edition, 1999.

[26] Brun K. and Kurz R. Analysis of secondary flows in centrifugal impellers. *International Journal of Rotating Machinery*, 2005, 01 2005.

[27] Kang S. and Hirsch C. Numerical simulation and theoretical analysis of the 3d viscous flow in centrifugal impellers. *Task Quarterly*, 5:433–458, 01 2001.

[28] Abel M., Martinez-Botas R., and M. Müller M., Wöhr, and J. Leweux. 3D Computational Loss Analysis of a Compressor for Heavy Duty Truck Engine Turbochargers. Volume 2B: Turbomachinery, 06 2019. V02BT44A001.

[29] Khoshkalam N., Mojaddam M., and Pullen K. Characterization of the performance of a turbocharger centrifugal compressor by component loss contributions. *Energies*, 12(14):2711, Jul 16, 2019.

[30] Gong X. and Chen R. Total pressure loss mechanism of centrifugal compressors. *Mechanical Engineering Research*, 4(2), Oct 18, 2014.

[31] Velasquez E. Determination of a suitable set of loss models for centrifugal compressor performance prediction. , 30(5):1644–1650, 2017.

[32] Semlitsch B. and Mihăescu M. Flow phenomena leading to surge in a centrifugal compressor. *Energy*, 103:572–587, 2016.

[33] Tosto F. Investigation of performance and surge behavior of centrifugal compressors through cfd simulations. 2018.

[34] Zhang H., Yang C., Yang D., Wang W., and M. Qi C., Yang. Investigation on the Stall Inception Circumferential Position and Stall Process Behavior in a Centrifugal Compressor With Volute. *Journal of Engineering for Gas Turbines and Power*, 141(2), 10 2018. 021030.

[35] Fink. D., Cumpsty N., and Greitzer E. Surge Dynamics in a Free-Spool Centrifugal Compressor System. *Journal of Turbomachinery*, 114(2):321–332, 04 1992.

[36] K. Brun and R. Kurz. Analysis of secondary flows in centrifugal impellers. *International Journal of Rotating Machinery*, 2005(856141):8, 2005.

[37] Vacula J. and Novotný P. An Overview of Flow Instabilities Occurring in Centrifugal Compressors Operating at Low Flow Rates. *Journal of Engineering for Gas Turbines and Power*, 143(11), 09 2021. 111002.

[38] I. Trébinjac, N. Bulot, and N. Buffaz. Analysis of the flow in a transonic centrifugal compressor stage from choke to surge. *Proceedings of the Institution of Mechanical Engineers, Part A: Journal of Power and Energy*, 225(7):919–929, Nov 2011.

[39] Gancedo M., Gutmark E., , and Guillou E. Piv measurements of the flow at the inlet of a turbocharger centrifugal compressor with recirculation casing treatment near the inducer. *Experiments in Fluids*, 57(2):1–19, Feb 2016.

[40] Eck B. *Fans; Design and Operation of Centrifugal Axial-Flow and Cross-Flow Fans*. Pergamon Press, Oxford, 1st edition, 1973.

[41] Heinrich M., , and Schwarze R. Genetic algorithm optimization of the volute shape of a centrifugal compressor. *International Journal of Rotating Machinery*, 2016:4849025, Apr 2016.

[42] Pan D., Whitfield A., and Wilson M. Design considerations for the volutes of centrifugal fans and compressors. *Proceedings of the Institution of Mechanical Engineers, Part C: Journal of Mechanical Engineering Science*, 213(4):401–410, 1999. PMID: 10581967.

[43] Ayder E., Van den Braembussche R., and Brasz J. Experimental and theoretical analysis of the flow in a centrifugal compressor volute. June 1992.

[44] Gulich J. *Centrifugal Pumps*. 01 2008.

[45] Braembussche R. Flow and loss mechanisms in volutes of centrifugal pumps. page 27, 11 2006.

[46] Greitzer E. Surge and Rotating Stall in Axial Flow Compressors—Part II: Experimental Results and Comparison With Theory. *Journal of Engineering for Power*, 98(2):199–211, 04 1976.

[47] Hansen K., Jorgensen P., and Larsen P. Experimental and Theoretical Study of Surge in a Small Centrifugal Compressor. *Journal of Fluids Engineering*, 103(3):391–395, 09 1981.

[48] He X. and Zheng X. Mechanisms of sweep on the performance of transonic centrifugal compressor impellers. *Applied Sciences*, 7(10), 2017.

[49] Yano T. Performance of centrifugal blower under pulsating flow. *Bulletin of JSME*, 6(23):478–486, 1963.

[50] Yano T. and Nagata B. A study on surging phenomena in diesel engine air-charging system. *Jsme International Journal Series B-fluids and Thermal Engineering*, 14:364–376, 1971.

[51] Benson R. and Whitfield A. An experimental investigation of the non-steady flow characteristics of a centrifugal compressor. 1965.

[52] Benson R. and Whitfield A. Paper 20: Application of non-steady flow in a rotating duct to pulsating flow in a centrifugal compressor. *Proceedings of the Institution of Mechanical Engineers, Conference Proceedings*, 182(8):184–196, 1967.

[53] J. Galindo, H. Climent, C. Guardiola, and A. Tiseira. On the effect of pulsating flow on surge margin of small centrifugal compressors for automotive engines. *Experimental Thermal and Fluid Science*, 33(8):1163–1171, 2009.

[54] Marelli S., Carraro C., and M. Capobianco. Effect of pulsating flow characteristics on performance and surge limit of automotive turbocharger compressors. *SAE International Journal of Engines*, 5, 01 2012.

[55] Barrera-Medrano M., Martinez-Botas R., Tomita I., and S. Ibaraki. On the effect of engine pulsations on the performance of a turbocharger centrifugal compressor. *Journal of Engineering for Gas Turbines and Power*, 141(8), Aug 1, 2019.

[56] Barrera-Medrano M., Newton P., Martinez-Botas R., Rajoo S., Tomita I., and Ibaraki S. Effect of exit pressure pulsation on the performance and stability limit of a turbocharger centrifugal compressor. *Journal of Engineering for Gas Turbines and Power*, 139(5):052601–9, May 1, 2017.

[57] Shu M., M. Yang, Zhang K., Deng K., Yang B., and Martinez-Botas R. Experimental study on performance of centrifugal compressor exposed to pulsating backpressure. *Aerospace Science and Technology*, 95:105450, Dec 2019.

[58] Marelli S., Capobianco M., and Zamboni G. Pulsating flow performance of a turbocharger compressor for automotive application. *International Journal of Heat and Fluid Flow*, 45, 2013.

[59] Shu M., Yang B., Yang M., Martinez-Botas R., and Deng K. Investigation on the unsteadiness of centrifugal compressor exposed to pulsating backpressure. *Proceedings of the Institution of Mechanical Engineers, Part D: Journal of Automobile Engineering*, 235:2212 – 2225, 2021.

[60] Strouhal V. Ueber eine besondere art der tonerregung. *Annalen der Physik*, 241:216–251.

[61] Newton P. *An Experimental and Computational Study of Pulsating Flow within a Double Entry Turbine with Different Nozzle Settings*. PhD thesis, Feb 2014.

[62] Y. Hayashi R. Martinez-Botas I., Tomita and M. Barrera-Medrano. Flow field analysis of a turbocharger centrifugal compressor under pulsating conditions. *Mitsubishi Heavy Industries Technical Review*, 56, 07 2019.

[63] Shu M., Yang M, Martinez-Botas R., Deng K., and Shi L. Unsteady responses of the impeller of a centrifugal compressor exposed to pulsating backpressure. *Journal of Engineering for Gas Turbines and Power*, 2018.

[64] Yang M., Cai R., Shu M., Pan L., Zhuge W., and Yang B. Effects of pulsating backpressure on performance of stability of a centrifugal compressor. *Aerospace Science and Technology*, 130:107926, 2022.

[65] Leichtfuß s., Bühler J., Schiffer H., Peters P., and Michael M. A casing treatment with axial grooves for centrifugal compressors. *International Journal of Turbomachinery, Propulsion and Power*, 4(3), 2019.

[66] Martos P. *Centrifugal Compressor Casing Flow Field Analysis and Optimization*. PhD thesis, Jul 2021. Embargo.

[67] Suzuka T. Sakai T.-Whitfield A Okauchi, H. The effect of volute tongue and passage configuration on the performance of centrifugal fan. *International Compressor Engineering Conference*, 2002.

[68] Mohtar H., Chesse P., Chalet D., Hetet J-F., and Yammine A. Effect of diffuser and volute on turbocharger centrifugal compressor stability and performance: Experimental study. *Oil Gas Science and Technology*, 66:pp. 779–790, 09 2011.

[69] Xu C. and Müller M. Development and design of a centrifugal compressor volute. *International Journal of Rotating Machinery*, 2005, 01 2005.

[70] Taher M. Asme ptc-10 performance testing of centrifugal compressors — the real gas calculation method. page V03BT25A019, 2014.

[71] Arenz M., Weigel B., Habermann J., Staudacher S., Rose M., Berns W., and Ewald L. Development and Application of a Fast-Response Total Temperature Probe for Turbomachinery. *Journal of Turbomachinery*, 139(5), 01 2017. 051010.

[72] Tropea C., Alexander A. Yarin, and Foss J. *Springer Handbook of Experimental Fluid Mechanics*. 01 2007.

[73] Zappalá D., Bezziccheri M., Crabtree C., and Paone N. Non-intrusive torque measurement for rotating shafts using optical sensing of zebra-tapes. *Measurement Science and Technology*, 29(6):065207, may 2018.

[74] Fleming W. Automotive torque measurement: A summary of seven different methods. *IEEE Transactions on Vehicular Technology*, 31(3):117–124, 1982.

[75] Torquemeters Limited. *Torquetronic ET Test Bed Torquemeter*, 2021. [Accessed 28th July 2023].

[76] Van Millingen R. and Van Millingen J. Phase shift torquemeters for gas turbine development and monitoring. 1991.

[77] Ward J., Silvey J., and Roberge J. High-accuracy optical torquemeter, 1976.

[78] Ohigashi S., Ono G., S., and Machida. A new electronic device for measuring torque. *SAE Technical Paper 650041*, 1965.

[79] Omega. *Temperature Probes*, September 2023. [Accessed 28th July 2023].

[80] Omega. *Fast response insulated thermocouples with connectors*, September 2023. [Accessed 28th July 2023].

[81] ISO 5389-2005. *Turbocompressors. Performance test code*, December 2005. [Accessed 28th July 2023].

[82] RS Stock No 137-2239. Rs pro superwool fibre thermal insulating sheet, 2.4m x 610mm x 25mm, December 2023. [Accessed 28th July 2023].

[83] Stasyshan R. *How Inlet Conditions Impact Centrifugal Air Compressor Performance*. [Accessed 28th July 2023] https://www.airbestpractices.com/.

[84] McCrometer. *V-cone Flow Meter Technical Brief*. 2013.

[85] ISO 5167-5:2022. Measurement of fluid flow by means of pressure differential devices inserted in circular cross-section conduits running full — part 5: Cone meters, September 2022. [Accessed 28th July 2023].

[86] Incropera F. and DeWitt D. *Fundamentals of Heat and Mass Transfer*. John Wiley Sons, Inc., New York City, New York, 4th edition edition, 1996.

[87] Dantec Dynamics. *Measurement Principles of CTA*, 2023.

[88] Kirkup L. and Frenkel R. *An Introduction to Uncertainty in Measurement: Using the GUM (Guide to the Expression of Uncertainty in Measurement)*. Cambridge University Press, 2006.

[89] Marelli S., Capobianco M., and Zamboni G. Pulsating flow performance of a turbocharger compressor for automotive application. *International Journal of Heat and Fluid Flow*, 45:158–165, Feb 2014.

[90] Wesserman S. Choosing the right turbulence model for your cfd simulation, 2016.

[91] Heinz H. and Kock F. Direct and indirect methods of calculating entropy generation rates in turbulent convective heat transfer problems. *Heat and Mass Transfer/Waerme- und Stoffuebertragung*, 43:207–215, 01 2007.

[92] Parikh A., Singh G., F. Harminder C., Noon, and Martinez-Botas R. Design and Development of a Fast Response Torque Meter for Unsteady Flows in Turbocharger Applications. Volume 7: Industrial and Cogeneration; Manufacturing Materials and Metallurgy; Microturbines, Turbochargers, and Small Turbomachines; Oil Gas Applications, 06 2022. V007T18A014.

[93] K. Birch. Estimating uncertainties in testing. *Measurement good practice guide*, 2003.

[94] M. Goldsmith. A beginners guide to measurement. *Good Practice Guide No. 118*, 2010.

Appendix A

Mass Accumulator Concept

The initial results from the mass accumulator concepts are shown here. The benefit of this initial assessment is to validate the mass accumulation concept.

Experimental set-Up

The considered volumes ("mass accumulation") for the experimental validation of the concept are 8L, 12L and 16L. This volumes are implemented by a plenum with adjustable volume, as depicted in figure A.1. The experimental facility for the mass accumulator concept is similar to the facility for the baseline testing. The pulse generator has been moved behind the plenum instead of before the plenum. This moves the pulse generator further away from the compressor outlet and as a result, the pulse reaching the compressor outlet passes through the volume and is damped. In order to test the impact of the different volumes and pulse amplitudes, a total of 3 volumes (8L, 12L and 16L) has been tested with a large disc and medium disc size.

Figure A.2 shows the experimental set-up of the facility. Sensors are placed before and after the plenum for measurements of temperature and pressure. Temperature measurements are conducted as an average temperature of the measurement plane, recorded with thermocouples. Static pressure measurements are taken with Omega fast response pressure transducers. The facility is completely insulated, including insulation around the plenum. The insulation is a glass-fibre insulating material similar to other measurements during this research. The experiments are repeated three times to ensure that the results are repeatable.

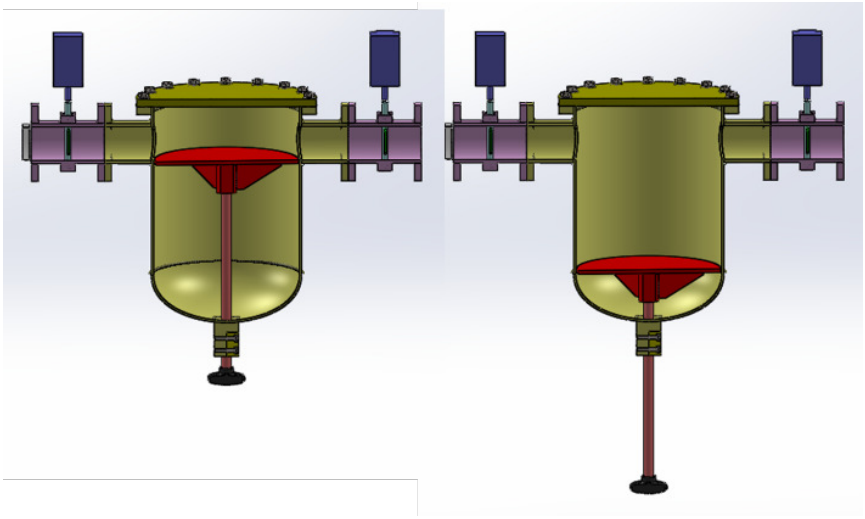


Fig. A.1 Current conceptualised mass accumulation concept using existing plenum

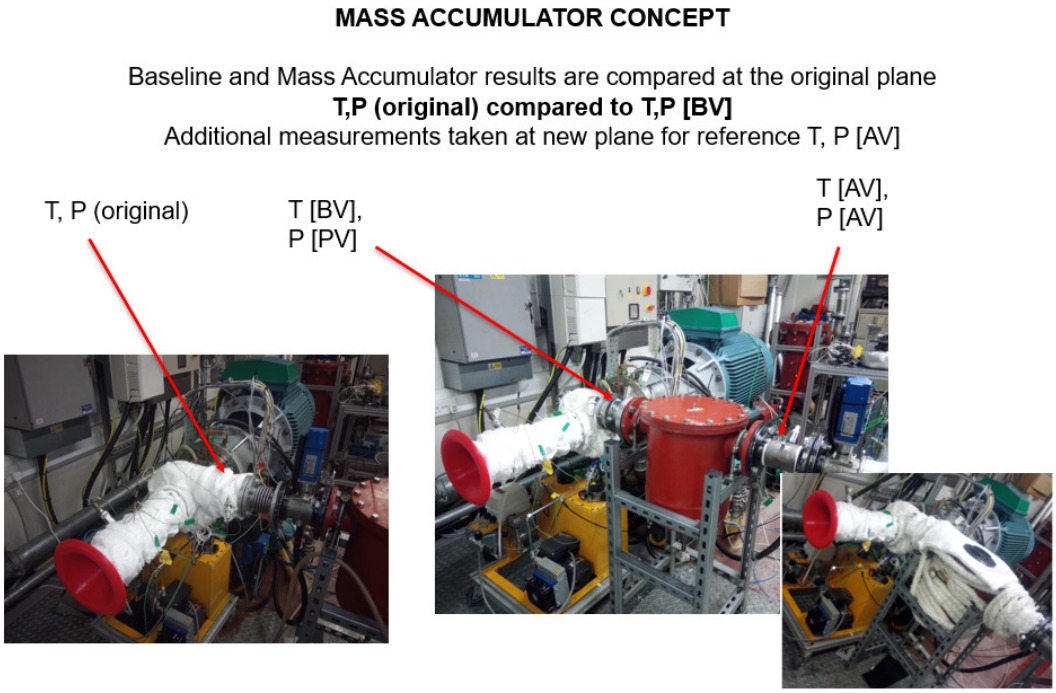


Fig. A.2 Experimental set-up to test the mass accumulation concept

Experimental results for mass accumulator concept

The experiments showed promising results for the mass-accumulation concept.

Figure A.3 shows the instantaneous hysteresis behaviour for some selected operating points at high and low mass flow rates at 66Hz. The hysteresis behaviour for the high mass flow rate case shows how much the pressure ratio varies for a given operating point. In the low mass flow rate case, the pressure ratio does not vary so significantly, but a hysteresis

loop can none the less be seen in the baseline, no-volume case. The effect of the mass accumulation concept can be seen clearly in the instantaneous pressure ratio for both operating points. In all three volumes tested, the hysteresis behaviour is much smaller than the no-volume case. Although the 16L hysteresis loop is the smallest, the difference between the three loops is minor in comparison to the baseline case. The mass flow rate no longer fluctuates. What this demonstrates is that the volume acts as a pressure damper. Although the pressure pulse is present in reality, the volume dampens the effect and the compressor behaves in close-to-steady behaviour.

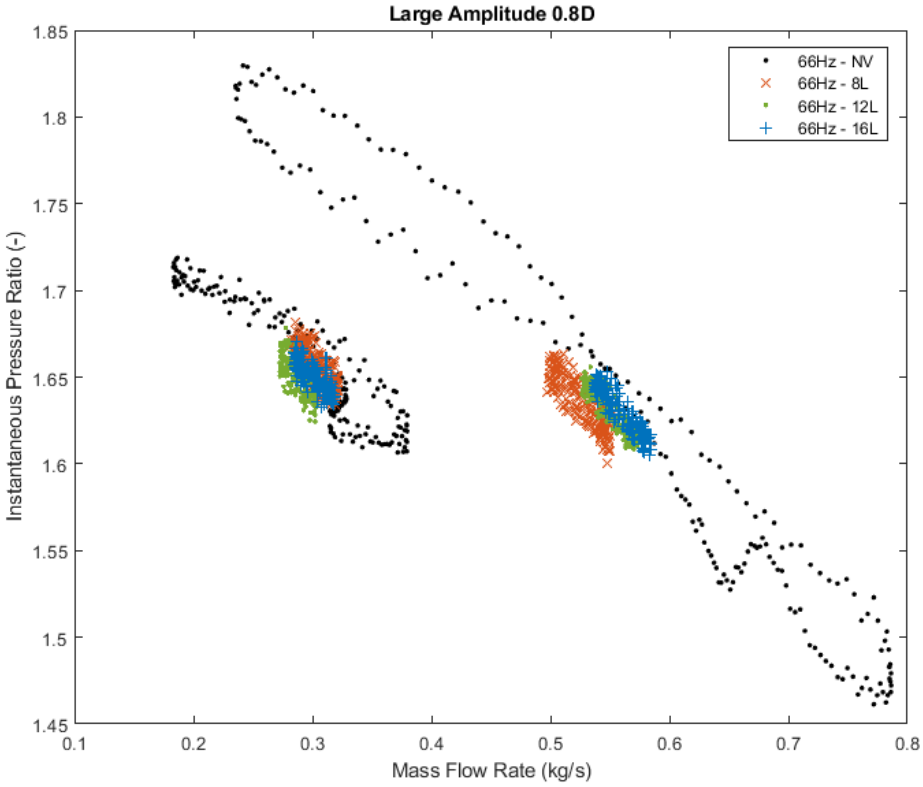


Fig. A.3 Pressure ratio vs mass flow for Large flow (OP D) and peak efficiency (OP C) operating Points

The extent of pressure pulse reduction is demonstrated in Figure A.4. This is a cyclic average or ensemble average of static pressure sensor at the outlet plane of the compressor - and the point at which the thermodynamic calculations are conducted. The static pressure variation is much smaller when there is a mass accumulation volume than without the volume. The dynamic signal remains nonetheless which could help the compressor gain some benefits in the low flow region, for instance for surge margin improvement.

Mass Accumulator Preliminary Results - Summary

As presented and discussed when introducing the hypothesis behind this concept, the static pressure amplitude variation in the large flow state is large, this causes the flow to

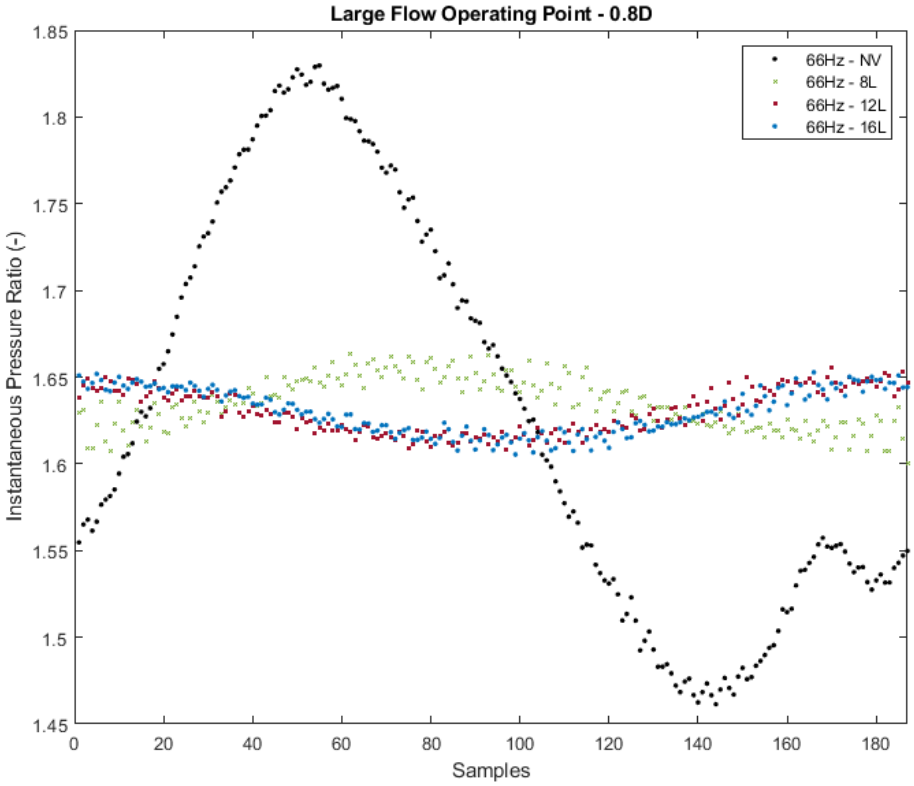


Fig. A.4 Static pressure pulse reduction at compressor outlet

instantaneously fluctuate between many states - causing a large efficiency deviation. The mass accumulation concept aims to reduce this variation.

Generally, a volume reduces the pressure pulse amplitude simply because it acts as a damper. The larger the volume, the more effective this will be. This hypothesis is proven during the performance experimental campaign of this concept, where different ranges of pulse frequencies and amplitudes combined with different "mass accumulator" volumes were tested. However, a large amount of further research is required to further test this concept.

Experimental Protocol - Compressor Rig 18/01/22

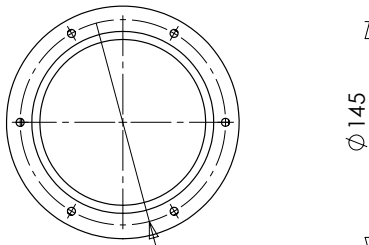
	TRR		
A	Ensure mechanical interface definition is completed* [on onshape or otherwise]		Document only valid after TRR
B	Instrumention for the test is defined & available		
C	Ensure all sensors are calibrated and scaling factors are correct in the software*		Calibration procedure X should be followed; important to have the correct reference (reference device required)
	Mechanical and Instrumentation Set up	Safety check	Notes
1.01	Install the compressor, mechanical connections and corresponding sensors required for the test;	Ensure bearings, seals and flanges are correctly tightened and secured	Only possible after mechanical set up and instrumentation requirements are approved [TRR]
1.02	Insulate rig		
1.03	Check the installation physically to check for clearance on the compressor and ensure that the compressor is properly placed. To do this, you need to physically turn the engine motor by hand, and you should see the compressor move as a result. You should not be able to hear any sounds that suggest there is friction or contact. There needs to be a clear sound. Do not proceed if there is a sound otherwise you could damage the compressor.		
	Pre-test procedure		
2.01	Turn on the cooling water supply		
2.02	Connect the oil cart for lubricating the bearing housing & switch it on	Ensure oil cart hoses are properly connected with the seals properly placed & the hoses securely clamped. Prime the pump; visually inspect hose to see if oil is free of oil bubbles - adjust speed for flow rate according to test	
2.03	Turn on cabinets + air supply		
2.04	Switch on the lubricating oil supply for the motor (on the compressor rig controller)		
2.05	Check that the pulsating device is in the correct position.		
2.06	Ensure sensor connections are all correctly placed, and connected + reading		
2.07	Ensure that the butterfly valve is fully open before a run		physically check this by looking at the valve position
2.08	Check all the seals are correctly in place (oil seal, volute/exit duct gasket)		
2.09	Check that there are no air leaks in the system (physically whilst the rig is running - at low speed around 20k - feel leaks)		
2.10	Ensure all the bolts are tightened (Especially if the compressor system had reached surge in previous run)		
2.11	Check that the hotwire signal is reading correctly (load hotwire live data on VI, ensure the dantec system is showing 'operating' not 'standby'		
2.12	Check that the ventilation system is on to ensure room is at correct temperature		
	Test procedure		
3.01	Warm up the rig and allow for surface thermocouple to reach thermal equilibrium at the speed of test	Check for unfamiliar noise/vibration before reaching full speed	
3.02	Turn off motor (speed to 0) and Zero-offset sensors		
3.03	Take zero reading data log		At 0 speed of the compressor
3.04	Insert speedline .csv file if available, re-start the motor to speed		
3.05	Perform trial run by closing butterfly valve from fully open to surge	Always go down 1% at a time. You don't know the surge point of the compressor - so it's important to ensure that you do not miss it & the situation can change very fast.	Check everything is connected and recorded correctly
	Check the trial data is sensible - does the speedline make sense?		
3.06	Log 10 points for the trial run that cover fully open to surge		
3.07	Calculate speed line performance [and other necessary calculation checks]		
	Test Quality Assurance		
4.01	Conduct test measurements 3 times		
4.02	Calculate speed line performance		Refer to performance calculation procedure
	Shut-down procedure		
5.01	Turn off the cooling water, oil cart and lubricating oil and air supply		
5.02			

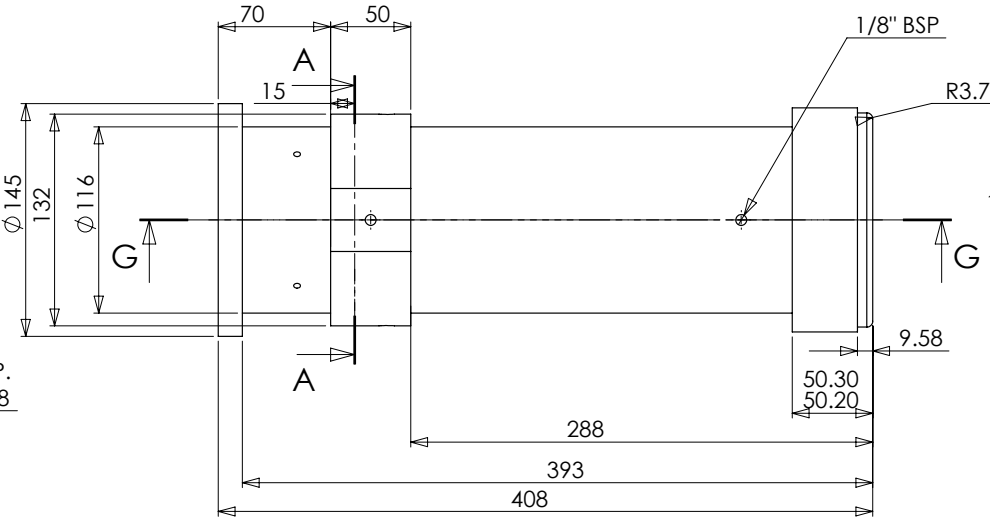
Appendix B

Attached Drawings

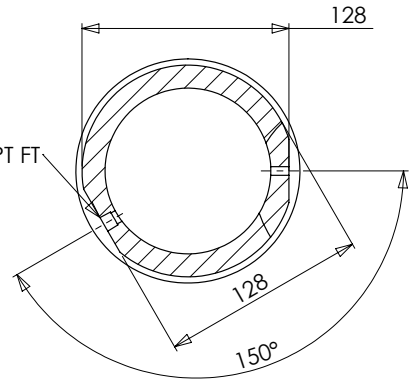
The following drawings are appended.

1. Intake pipe
2. Instrumented Volute
3. Instrumented Bearing Housing
4. Modified volute for cavities insert



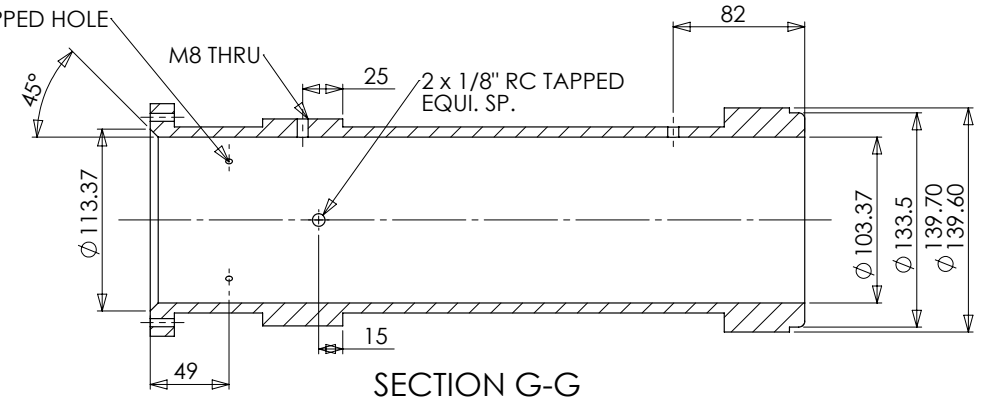


6 x M5 EQUI. SP.
ON PCD Ø128

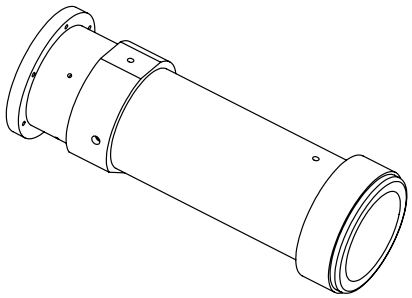


SECTION A-A
SCALE 1 : 3

4 x M5
EQUI. SP.
AT 45° TO 1/8 RC TAPPED HOLE



SECTION G-G
SCALE 1 : 3



TOLERANCES		THIRD ANGLE PROJECTION
X = ± 0.5	ANGULAR ± 1°	
X.X = ± 0.1	SURFACE FINISH MACHINED FACES Ra 6.3	
X.XX = ± 0.02		

	NAME	DATE
DRAWN	A.Parikh	28/07
CHECKED		
APPROVED		

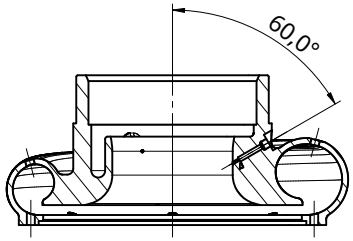
MATERIAL: Aluminium	TITLE: Long Intake
ALL DIMENSIONS ARE IN MILLIMETRES	
DO NOT SCALE DRAWING	DWG No. T6-001
A3 SCALE 1:3	

Imperial College London
Department of Mechanical Engineering

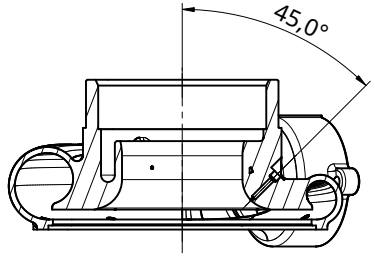
SHEET 1 OF 1 REVISION 01

REFER TO SHEET 5 AND 6 FOR HOLE DETAIL

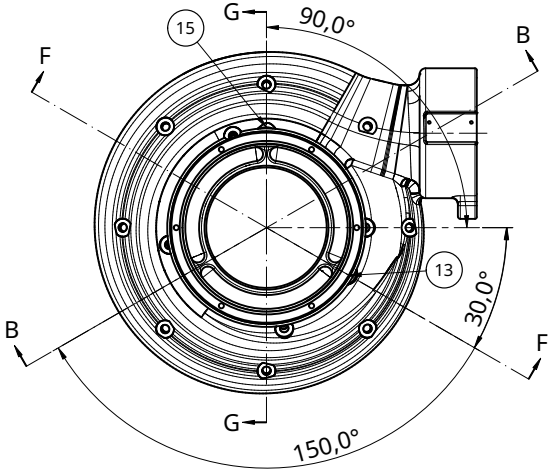
FOR HOLES 13-15 USE EXACT BREAKOUT LOCATIONS
SPECIFIED ON BLANK INSERT TO GUIDE ENTRY POSITION

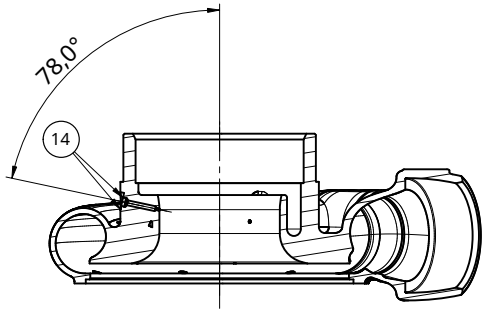


G - G

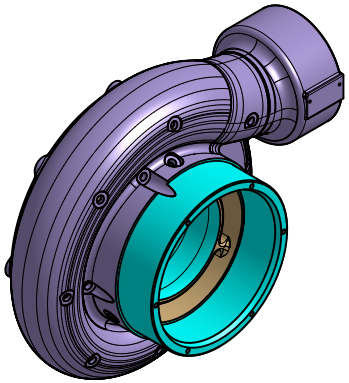


F - F





B - B



Impeller holes
13-15

UNLESS OTHERWISE SPECIFIED, DIMENSIONS ARE IN MILLIMETERS X = ±0.5 X.X = ±0.1 X.XX = ±0.02 ANGULAR = ± 1° SURFACE FINISH 1.6		NAME	SIGNATURE	DATE
	DRAWN	AAKEEN PARIKH		2021-03-18
	CHECKED			
	APPROVED			
DO NOT SCALE DRAWING				
BREAK ALL SHARP EDGES AND REMOVE BURRS				
THIRD ANGLE PROJECTION	MATERIAL		FINISH	

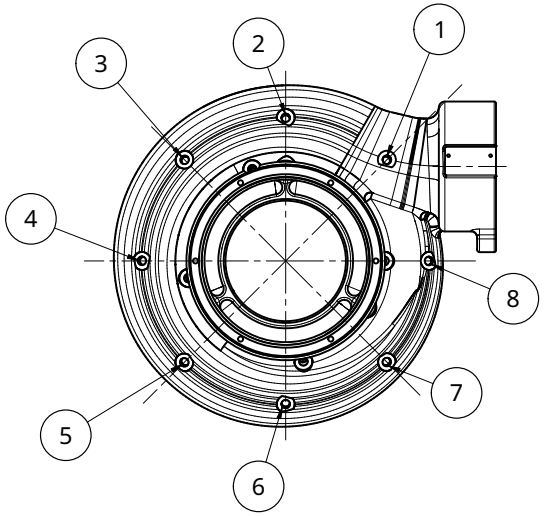
Imperial College London

TITLE
MHI THEME 6
VOLUTE HOUSING
INSTRUMENTATION POSITIONS

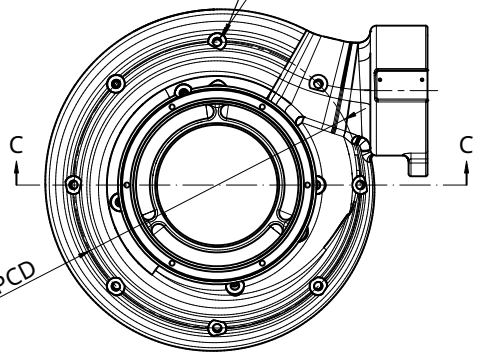
SIZE	DWG NO.	REV.
A3	19006-IF-CR-0003	1

SCALE	WEIGHT	SHEET
1:4		1 of 6

Volute holes 1-8

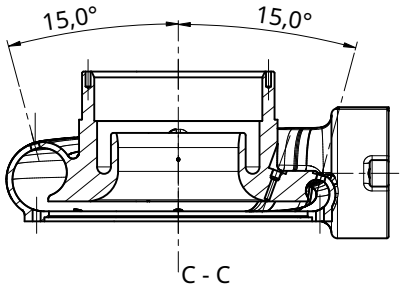


HOLES 1-8
Ø15 SPOTFACE
Ø7
M8x1,00



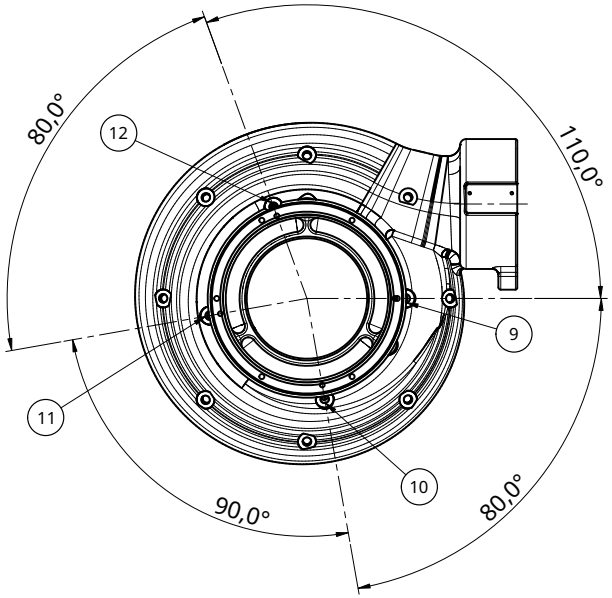
Ø237,67
ALL HOLES ON SAME PCD

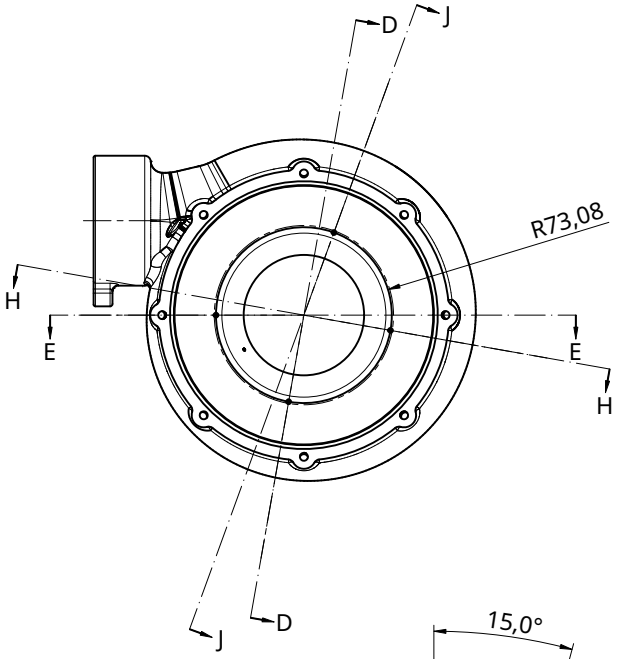
NOTE: holes 1-8
angle drill at 15° from normal vertical

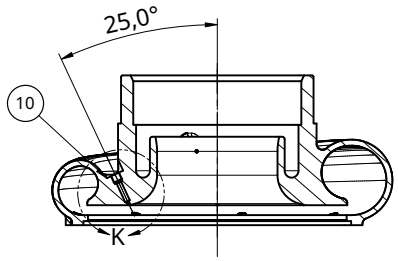


Imperial College London

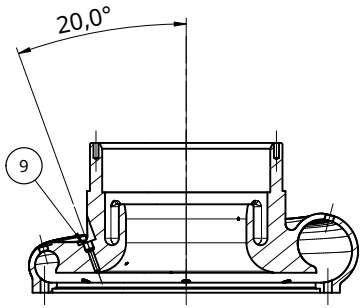
DWG NO.	SIZE	SCALE	SHEET	REV.
19006-IF-CR-0003	A3	1:4	2 of 6	1



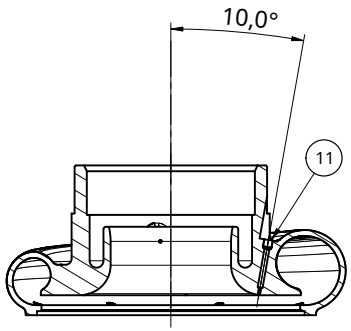




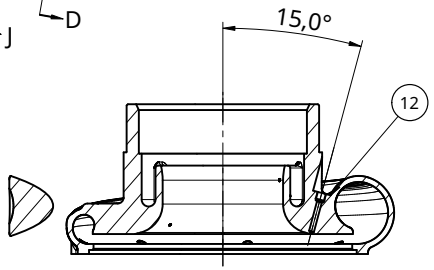
D - D



E - E



J - J



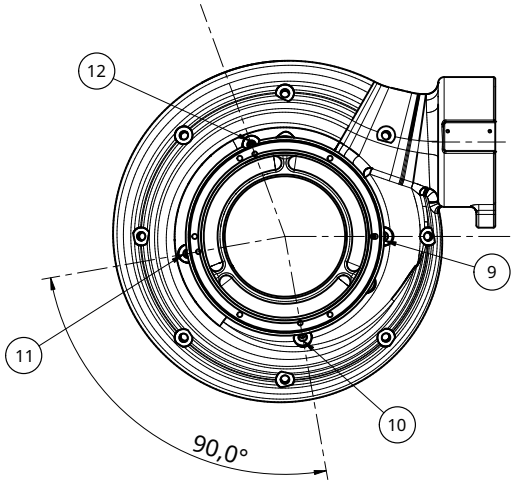
H - H

REFER TO SHEET 5 FOR DETAILED DRAWING K

FOR HOLES 9-12 USE EXACT BREAKOUT LOCATIONS
SPECIFIED ON BLANK INSERT TO GUIDE ENTRY POSITION

Imperial College London

DWG NO.	SIZE	SCALE	SHEET	REV.
19006-IF-CR-0003	A3	1:4	3 of 6	1

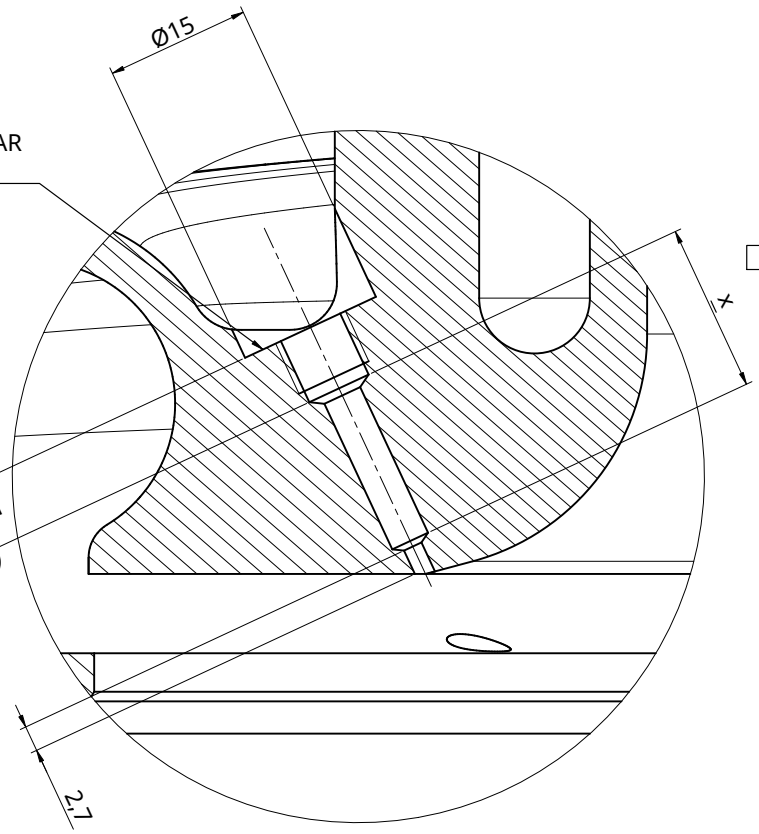


REFER TO SHEET 5 FOR DETAILED DRAWING K

FOR HOLES 9-12 USE EXACT BREAKOUT LOCATIONS
SPECIFIED ON BLANK INSERT TO GUIDE ENTRY POSITION

Imperial College London

DWG NO.	SIZE	SCALE	SHEET	REV.
19006-IF-CR-0003	A3	1:4	4 of 6	1



K

4 POCKET DEPTH
MINIMUM TO CLEAR
OUT Ø15.0

1 ALL M8 TAPPED HOLES TO BE:
Ø6.8 ↧7
M8 x 1.0 ↧6
(REFERENCE SURFACE = POCKET)

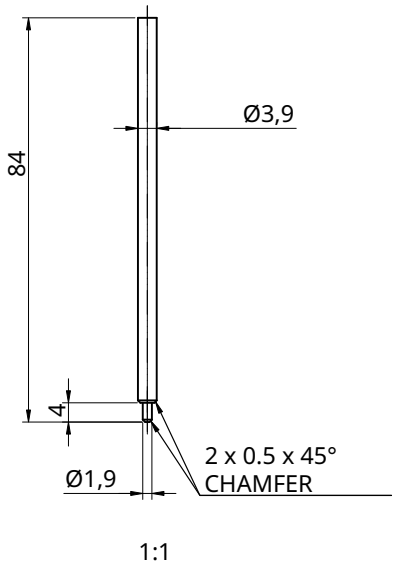
2 DEPTH OF Ø2 HOLE TO BE:
2.0 MIN
3.5 MAX

3 DEPTH OF Ø4.1 HOLE TO VARY
ACCORDING TO REQUIREMENTS
OF NOTES 1 AND 2
USE PENCIL GUIDE TO APPROXIMATE DEPTH.
USE POINT AT WHICH PENCIL GUIDE
PROTRUDES AT INTERNAL SURFACE AS MAX
DEPTH OF 4.1mm HOLE

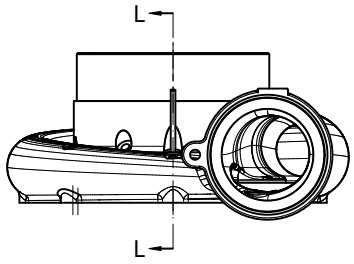
SEE SHEET 6

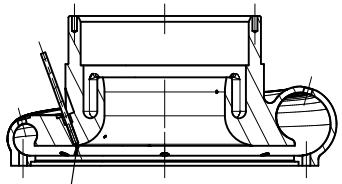
Imperial College London

DWG NO.	SIZE	SCALE	SHEET	REV.
19006-IF-CR-0003	A3	2:1	5 of 6	1



1:1





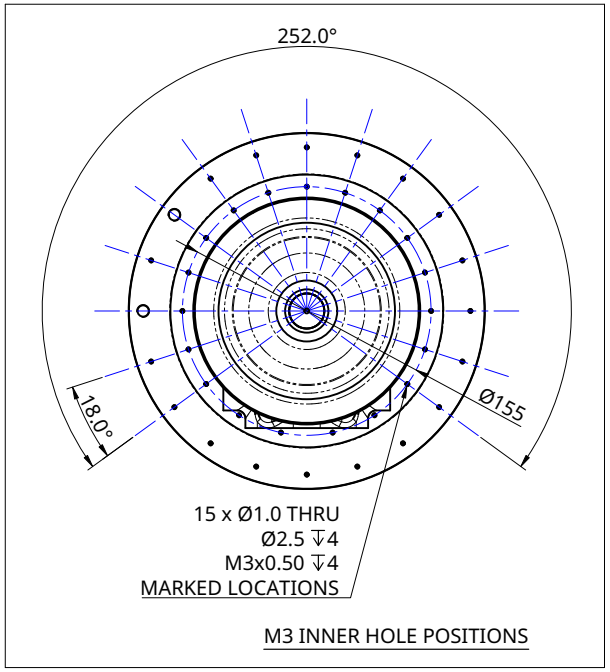
EXAMPLE POSITIONING OF PENCIL GUIDE BOTTOMING OUT AT END FACE OF 4.1mm HOLE

TO BE USED TO DETERMINE THE DEPTH OF 4.1mm HOLE

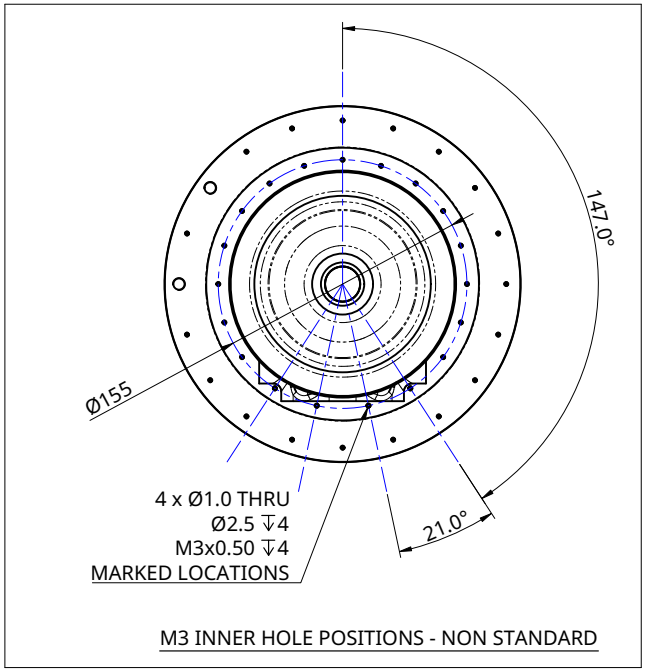
SEE SHEET 5 FOR DETAILED HOLE CALLOUT

Imperial College London

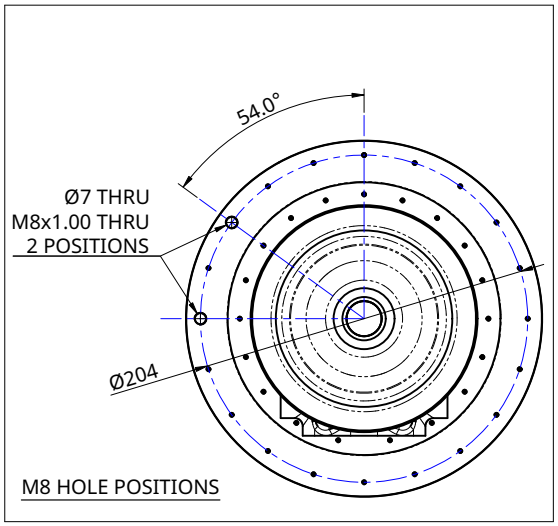
DWG NO.	SIZE	SCALE	SHEET	REV.
19006-IF-CR-0003	A3	1:4	6 of 6	1



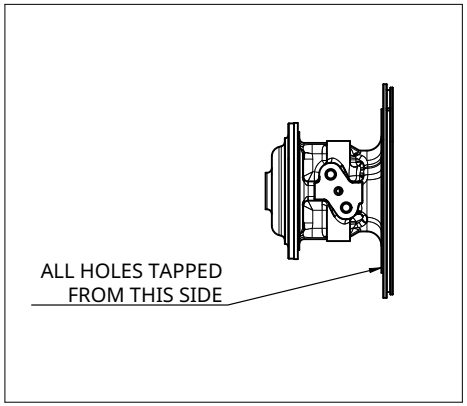
M3 INNER HOLE POSITIONS

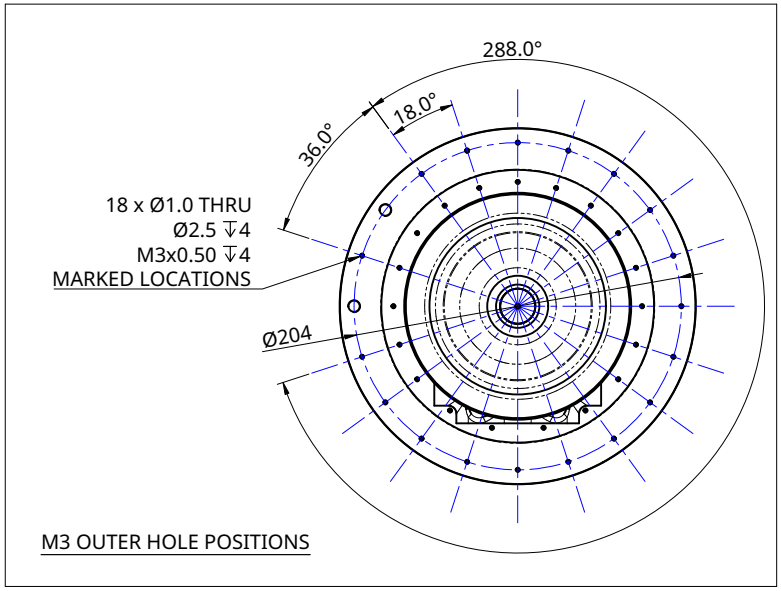


M3 INNER HOLE POSITIONS - NON STANDARD



M8 HOLE POSITIONS





M3 OUTER HOLE POSITIONS

	NAME	SIGNATURE	DATE
DRAWN	AAKEEN PARIKH		2021-03-26
CHECKED	CHRIS NOON		07/04/21
APPROVED			

UNLESS OTHERWISE SPECIFIED, DIMENSIONS ARE IN MILLIMETERS

X = ±0.5
X.X = ±0.1
X.XX = ±0.02
ANGULAR = ± 1°

SURFACE FINISH 1.6

DO NOT SCALE DRAWING

BREAK ALL SHARP EDGES AND REMOVE BURRS

THIRD ANGLE PROJECTION

MATERIAL: AS SUPPLIED

FINISH:

Imperial College London

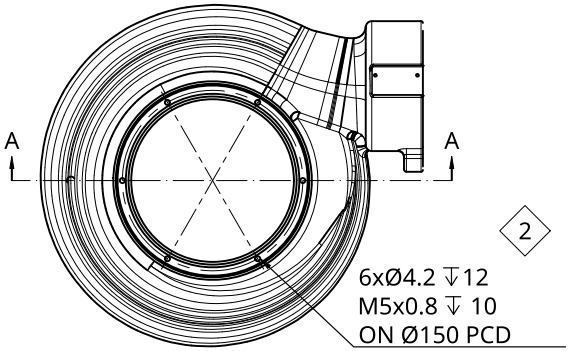
TITLE: MHI THEME 6 BEARING HOUSING INSTRUMENT POSITIONS

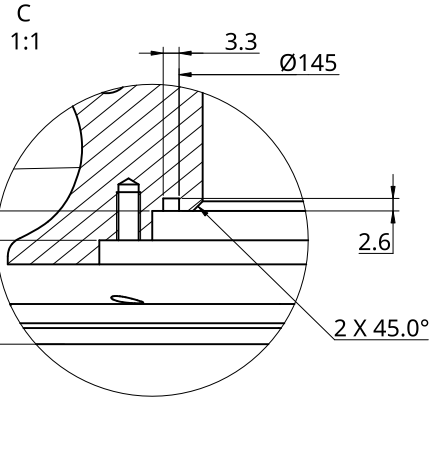
SIZE	DWG NO.	REV.
A3	19006-IF-CR-0002	1

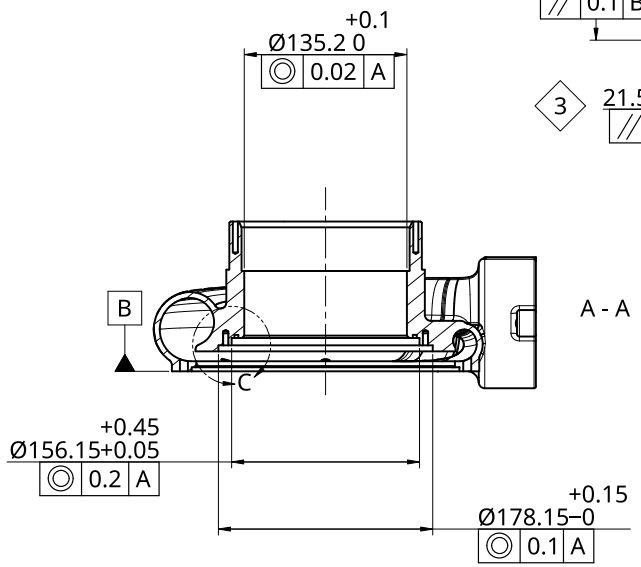
SCALE	WEIGHT	SHEET
1:3		1 of 1

2 ADDED INLET HOLE DETAILS

3 UPDATED TOLERANCE

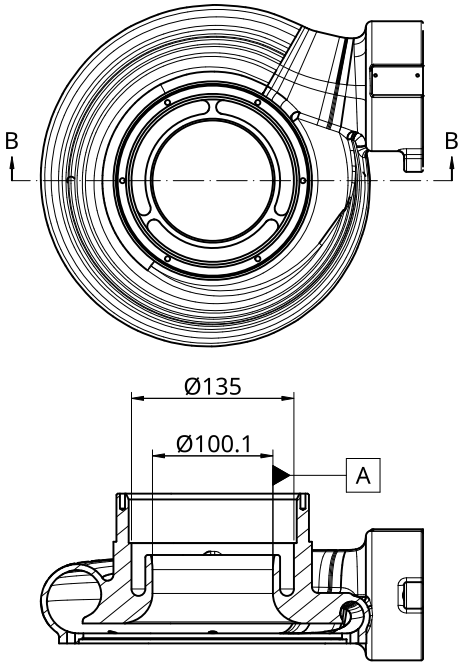






A - A

ORIGINAL
PART FOR
REFERENCE



B - B

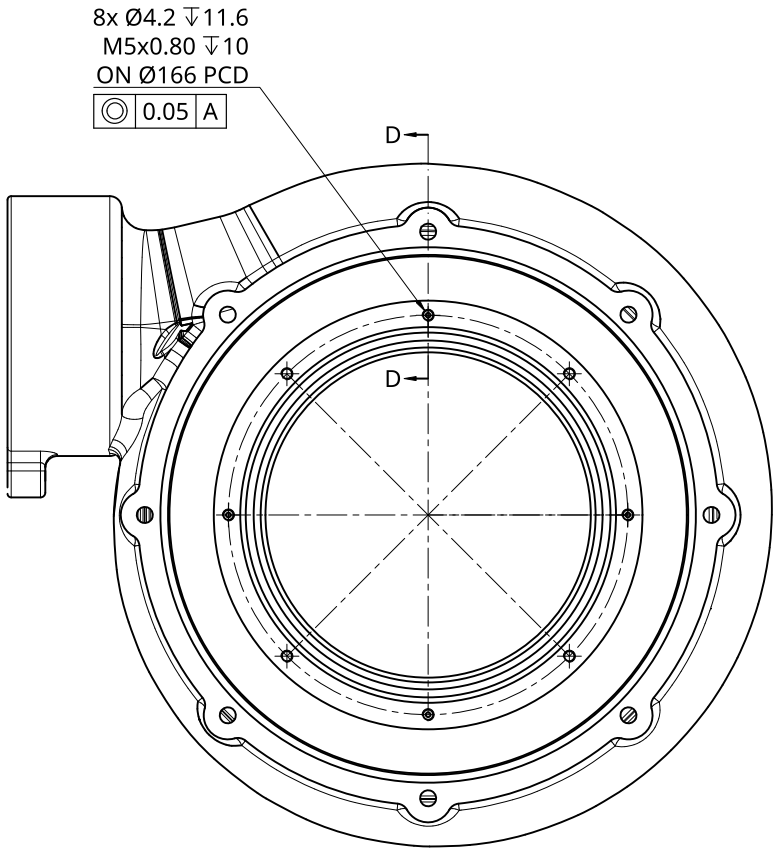
UNLESS OTHERWISE SPECIFIED, DIMENSIONS ARE IN MILLIMETERS		NAME	SIGNATURE	DATE
X = ±0.5 X.X = ±0.1 X.XX = ±0.02 ANGULAR = ± 1°	DRAWN	AAKEEN PARIKH		2021-12-21
SURFACE FINISH √1.6	CHECKED			
DO NOT SCALE DRAWING	APPROVED			
BREAK ALL SHARP EDGES AND REMOVE BURRS				
THIRD ANGLE PROJECTION	MATERIAL	CAST ALLY	FINISH	

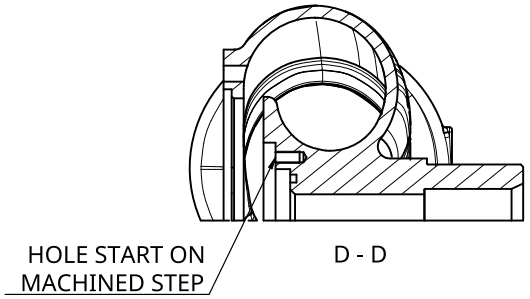
Imperial College London

TITLE: VOLUTE RUNOUT HOLES IN VOLUTE

SIZE	DWG NO.	REV.
A3	19006-V-CR-0017	3

SCALE	WEIGHT	SHEET
1:4		1 of 4

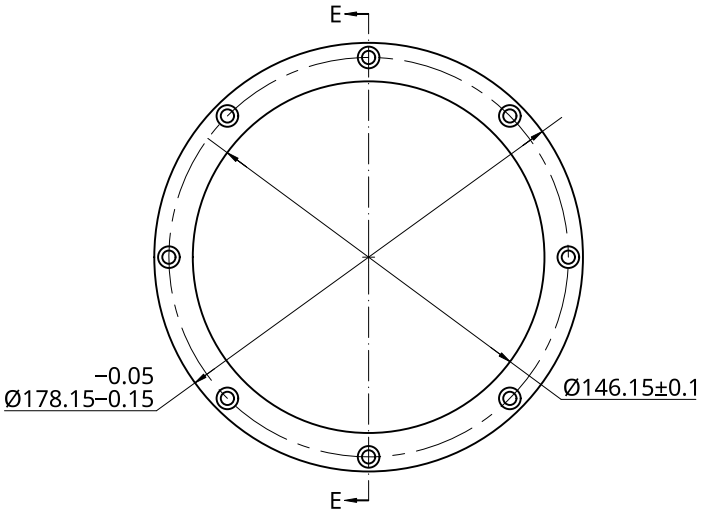


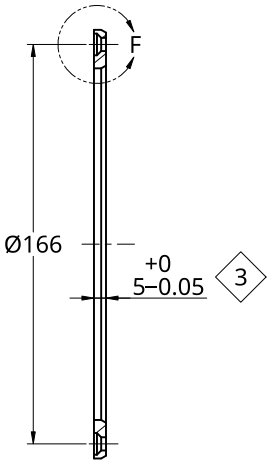


Imperial College London

DWG NO.	SIZE	SCALE	SHEET	REV.
19006-V-CR-0017	A3	1:2	2 of 4	3

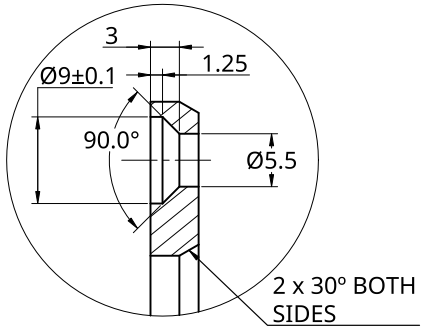
3 ADDED MISSING DIMENSION



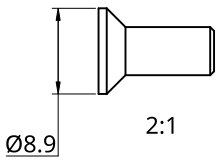


E - E

MODIFIED M5 COUNTERSINK
WITH Ø9.0 POCKET
8 LOCATIONS



F
2:1



2:1

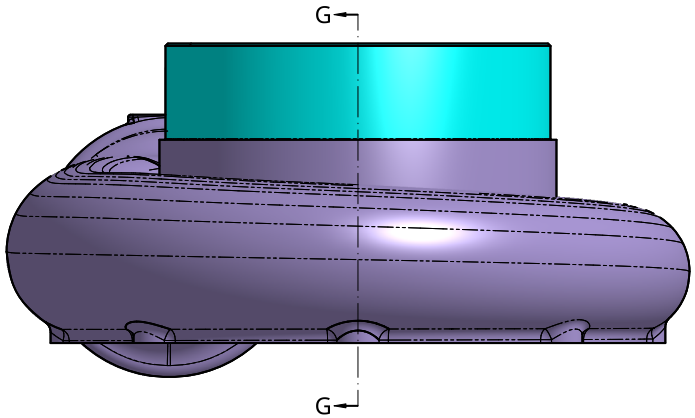
8 OFF M5 x 0.8 x 12
COUNTERSUNK SOCKET HEAD SCREW

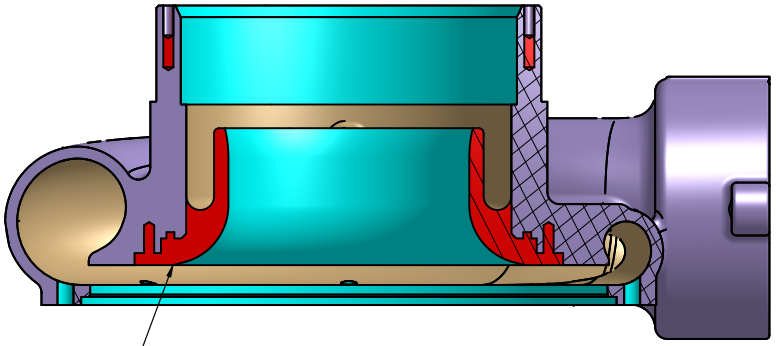
MODIFIED WITH REDUCED HEAD
DIAMETER

Imperial College London

DWG NO.	SIZE	SCALE	SHEET	REV.
19006-V-CR-0017	A3	1:2	3 of 4	3

MODIFICATION TO VOLUTE





MATERIAL REQUIRED
FOR REMOVAL
HIGHLIGHTED IN RED

G - G

Imperial College London

DWG NO.	SIZE	SCALE	SHEET	REV.
19006-V-CR-0017	A3	1:2	4 of 4	3